Laser-based aerosolized nanoparticle diagnostics: Enhancing the spectroscopic model

by
Sina Talebi-Moghaddam

A thesis
presented to the University of Waterloo
in fulfillment of the
thesis requirement for the degree of
Doctor of Philosophy
in
Mechanical and Mechatronics Engineering

Waterloo, Ontario, Canada, 2020

Examination committee membership

The following served on the Examining Committee for this thesis. The decision of the Examining Committee is by majority vote.

External examiner	Christopher M. Sorensen Distinguished Professor
Supervisor	Kyle J. Daun Associate Professor
Internal member	Serhiy Yarusevych Associate Professor
Internal member	Jean-Pierre Hickey Assistant Professor
Internal-external member	Peter Levine Associate Professor

Author's declaration

I hereby declare that I am the sole author of this thesis. This will be a true copy of the thesis, including any required final revisions, as accepted by my examiners.

I understand that my thesis may be made electronically available to the public.

Abstract

The distinct properties of nanoparticles compared to their bulk counterparts makes them a suitable candidate for the development of many emerging technologies, and this presents a demand for scalable production routes. Gas-phase nanoparticle synthesis is the most scalable method to achieve this goal, but developing these techniques requires diagnostics that can characterize nanoparticle morphology in situ. On the other hand, the incidental release of nanoparticles to the environment contributes to climate change and severely influences human health. Therefore, effective and robust diagnostics for assessing the morphology of aerosolized nanoparticles are essential for understanding and mitigating its impacts, assessing and developing environmental regulations, understanding how nanoparticles are formed in combustion and gas-phase synthesis systems, and providing feedback for closed-loop control systems for nanoparticle production.

In situ optical methods such as multi-angle light scattering (MALS) and time-resolved laser-induced incandescence (TiRe-LII) have a robust temporal and spatial resolution, which are less expensive and time-consuming compared to transmission electron microscopy, and permit online control. Both of these methods depend on precise spectroscopic models to connect the observed signals to the aerosol properties. In the case of MALS, the morphological parameters of polydisperse aerosolized soot can be found by regressing modeled angularly-resolved elastic light scattering to experimental measurements, but this is an ill-posed problem in the presence of measurement noise or model error. Rayleigh-Debye-Gans Fractal Aggregate (RDG-FA) theory provides a closed-form solution for the light scattering kernel in the measurement model but can be subject to as much as 30% model error compared to the exact solution, which is amplified by the ill-posedness of the inference problem into significant errors in the recovered morphological parameters. More precise approaches, e.g. the multi-sphere T-matrix method (MSTM), are too expensive for inference problems, which require repeated evaluation of the forward model. The efficiency of RDG-FA and the accuracy of MSTM can be combined by modeling the approximation error. The error function is derived from a

principal component analysis on error matrices generated using randomly-sampled aggregates. The error model is then used to correct the RDG-FA kernel in the forward model for a particular set of fractal parameters. The model is then used to estimate probability densities of the size distribution and aggregate fractal parameters via Bayesian inference. Alternatively, an artificial feed-forward multi-layered neural network (ANN) can be trained using MSTM scattering simulations on randomly-generated soot aggregates. The ANN is then used to approximate the light scattering kernel in the measurement model, which is incorporated into the Bayesian inference procedure. The Bayesian/ANN approach is shown to be more accurate compared to the Bayesian approximation error technique. The Bayesian/ANN is then applied to in-flame measurements of soot and results are compared with transmission electron microscopy results from the literature.

While MALS is mainly used to infer the size distribution of aggregates and usually a deterministic primary particle size is assumed in the model, TiRe-LII is increasingly applied to characterize the size distribution of soot primary particles and non-carbonaceous nanoparticles as well as the thermophysical properties of the bulk material. However, there exist several measurement phenomena, particularly from signals generated from metal nanoaerosols, that cannot be explained using traditional models. This thesis shows that some of these phenomena may be due to errors caused by using the Rayleigh approximation of Mie theory, which is a standard approach for modeling the spectral absorption of carbonaceous nanoparticles but is generally invalid for metal nanoparticles.

There has also been speculation that several commonly-observed measurement phenomena in TiRe-LII measurement data may be caused by bremsstrahlung emission from a laser-induced plasma, a phenomenon known to occur at higher fluences typical of laser-induced breakdown spectroscopy. This thesis presents the theoretical framework to investigate a laser-induced plasma formation under LII measurement conditions and explores how this plasma may affect time-resolved spectral intensity measurements. At fluences larger than 8 mJ/mm^2, the absorption cross-section of the laser-energized nanoparticle is enhanced due to inverse bremsstrahlung absorption, and bremsstrahlung emission results in an overestimation of the nanoparticle temperature due to the corruption of the incandescence signal.

In the case that aerosolized nanoparticles with a low absorption cross-section at the laser wavelength, the neutral bremsstrahlung emission can be detected during the experiments due to the absence of nanoparticle incandescence emission contingent on electron emission to the gas phase from the nanoparticle. Measurements carried on silver (Ag) and gold (Au) nanoparticles within the size range of 30 nm to 60 nm excited with a 1064 nm nanosecond Nd:YAG laser pulse. Assuming that the detected

signals are due to incandescence from the nanoparticle a pyrometric temperature is defined which varied with buffer gas molecule type and showed a linear relation with laser fluence that suggests that the signal is not, in fact, incandescence. A new model is proposed based on plasmonically-enhanced photoemission of electrons from the nanoparticles. The interaction of the electrons with buffer gas neutral species leads to inverse neutral bremsstrahlung absorption of the laser pulse as well as neutral bremsstrahlung emission.

In summary, this thesis not only improves the spectroscopic models of two aerosol metrology techniques but also proposes new methods that could lead to a faster inference of aerosol properties and presents a set of new approaches to explain the TiRe-LII model deficiencies. Also, newly proposed models for TiRe-LII could connect the field to other research areas such as laser-induced plasma diagnostic, LIBS on aerosols, and nanoantenna study.

Acknowledgements

Without the support and help of numerous people, this PhD thesis would not have been possible to be established.

First and foremost, I would like to express my sincere gratitude to my supervisor and mentor, Kyle Daun, for his continuous support throughout my PhD study. His constructive feedback and ideas were extremely valuable. His observations and comments helped me to establish the overall direction of the research. His approach of teaching has led me to be an independent researcher myself. I thank him for providing me with the opportunity to work with a talented team of researchers in a progressive workspace. I am aware of the fact that this is not an end, but the start of a lifelong research cooperation and friendship.

I would like to thank my fellow researchers and colleagues, for their feedback, thoughtful insights and of course, friendship. To name just a few: Stephen Robinson-Enebeli, Timothy Sipkens, Paul Hadwin, Samuel Grauer, Rodrigo Bener, Stanislav Musikhin, Nigel Singh, Ned Zhou, Mohit Verma, Kaihsiang Lin, Cory Yan, Roger Tsang, Natalie Field, Weizhi Zhu, Fatima Suleiman, Tom Zhao, and Cameron Klassen. Thanks again Dr. Kyle Daun for creating such a diverse and wonderful group of people, namely my Waterloo Laboratory for Inverse Analysis and Thermal Sciences (WatLIT) family, which had made my journey more enjoyable.

Of particular note, many thanks to Stephen Robinson-Enebeli for his devotion and immense help with the experiments which provided relevant data for the analysis depicted in this thesis.

I want to express my sincere gratitude to Dr. Timothy Sipkens, Nigel Singh, Dr. Franz Huber, Prof. Kyle Daun and Prof. Stefan Will as this thesis is a partial continuation of their high-quality research.

I am incredibly grateful to Prof. Stefan Will and many others at the University of Erlangen-Nuremberg (Friedrich-Alexander-Universität Erlangen-Nürnberg), Germany, for the insightful discussions and providing me with access to your outstanding laboratory and research facilities. It would not have been possible to complete this work without your precious support and collaboration.

Special thanks to Dr. Prem Lobo and many others at National Research Council (NRC) Canada for the many long-lasting discussions and guidance, especially during my stay in Ottawa.

Special thank you to Dr. Anna Klinkova and her team at the Chemistry Department of the University of Waterloo for their invaluable assistance and providing access to their laboratory and research facilities. I extend this thank to Kseniia Mosina and Xenia Medvedeva for many helpful discussions and their aid for nanoparticle synthesis.

I would also like to extend thanks to the members of my examination committee, including Prof. Kyle Daun, Prof. Christopher Sorensen, Prof. Jean-Pierre Hickey, Prof. Serhiy Yarusevych, and Prof. Peter Levine. Your willingness to review and comment on this thesis is greatly appreciated.

I would like to thank the Natural Science and Engineering Research Council (NSERC) of Canada and the University of Waterloo for granting me this opportunity by funding my research.

This work was made possible by the facilities and support by (Shared Hierarchical Academic Research Computing Network) (SHARCNET:www.sharcnet.ca) and Compute Canada (www.computecanada.ca).

Last but not least, I would like to thank my family for their never-ending support. From the bottom of my heart, I say big thank you to all of you for being there for me, even from thousands of miles away. Your love gave me the strength to accomplish this not-so-easy task.

To my family,
My parents, Manzar and Hamid
And my siblings, Kaveh and Mahnaz

Table of contents

List of figures

List of tables

Nomenclature

This section reviews the nomenclature used throughout the remainder of this thesis. As this thesis draws from multiple bodies of literature, there are occasionally overlapping symbols. In these cases, the *chapter restriction* indicates the chapters in which a specific definition applies. In cases where no chapter is specific, the symbol applies universally throughout the document.

Latin characters

Symbol	Chapter Restrictions	Unit	Definition
A	4	-	Clausius-Clapeyron equation coefficient
A_R	-	electrons·nm^{-2}·s^{-1}·K^2	Richardson-Dushman constant
b	1, 2, 3	-	Measured MALS signal
$\mathbf{b}$	1, 2, 3	-	Measured MALS signal in vector format
c_0	-	m/s	Speed of light in vacuum
c_g	-	m/s	Mean thermal speed of the gas
c_p	-	J·K^{-1}·kg^{-1}	Specific heat capacity
c_v	-	m/s	Mean thermal speed of the vapor
$C_{abs,\lambda}$	-	m^2, nm^2	Spectral absorption cross-section
D_f	1, 2, 3	-	Fractal dimension
d_p	-	nm	Nanoparticle diameter
$d_{p,v}$	-	nm	Volumetric mean
E_F	-	J, eV	Fermi energy
$E(\mathbf{m}_\lambda)$	-	-	Absorption function
e_{elec}	-	coulombs	Electron charge, $1.60217662 \times 10^{-19}$
e_{ph}	-	J, eV	Photon energy
$F(\mathbf{m}_\lambda)$	2, 3	-	Scattering function
f	4	-	Oscillator strength of plasmon frequency
$f(E)$	-	J^{-1}	Electron energy distribution function

f_V	-	-	Volume fraction
f_0	4, 5, 6	1/s	Temporal laser fluence profile
F_0	-	mJ/mm^2	Laser fluence
$g_{e\text{-}i}$	-	-	Gaunt factor
H°	4	J/kg	Enthalpy
h	-	$kg \cdot m^2 \cdot s^{-1}$	Planck's constant
Δh_v	-	J/kg	Specific latent heat of vaporization
ΔH_v	4	J/mol	Molar latent heat of vaporization
i	-	-	Constant, $(-1)^{1/2}$
I	-	W/cm^2	Laser intensity
$I_{b,\lambda}$	-	$W \cdot sr^{-1} \cdot m^{-1}$	Spectral blackbody intensity
J_λ	-	-	Spectral incandescence intensity
J_{th}	-	electron/s	Rate of thermionic electron emission
K	1, 2, 3	-	Kernel of the light scattering
k	-	-	Index of refraction, imaginary component
k_B	-	$m^2 \cdot kg \cdot s^{-2} \cdot K^{-1}$	Boltzmann's constant
k_f	-	-	Fractal prefactor
k_g	-	$W \cdot m^{-1} \cdot K^{-1}$	Thermal conductivity of the gas
$\mathbf{K}$	-	-	Kernel of the light scattering in matrix format
Kn	-	-	Knudsen number
L_c	-	m, nm	Characteristic length for mean free path calculations
L_{hi}	3	-	Neural network internal layer
L_{in}	3	-	Neural network initial layer
L_{out}	3	-	Neural network output layer
m	-	kg	Mass
m_{elec}	-	kg	Electron mass, $9.10938356 \times 10^{-31}$
$\mathbf{m}_\lambda$	-		Complex index of refraction
n	-	$molecules/m^3$	Molecular number density
n_n	-	-	Near field enhancement
n_v	-	$molecules/m^3$	Number density of evaporated species
n_λ	-	-	Index of refraction, real component
N_A	-	molecules/mole	Avogadro constant, $6.02214086 \times 10^{23}$
N_p	-	-	Number of primary particles in an aggregate

N''	-	molecules·m^{-2}·s^{-1}	Molecular number flux
N''_g	-	molecules·m^{-2}·g^{-1}	Incident gas molecule number flux
N_p	-	-	Number of primary particles
$p(\cdot)$	-	-	Probability density function
p_{ref}	-	-	Reference pressure
q	-	-	Modulus of scattering
q_{laser}	-	W	Rate of laser absorption
q_{cond}	-	W	Rate of conductive heat transfer
q_{evap}	-	W	Rate of vaporization heat transfer
$Q_{abs,\lambda}$	-	-	Spectral absorption efficiency
r	-	m	Radius of a primary particle
r_{ic}	-	m	Distance between primary particle center to the cluster's center of mass
r_e	-	m	Classical electron radius
R	-	J·mol^{-1}·K^{-1}	Universal gas constant
R_g	1, 2, 3	m	Radius of gyration
S	2, 3	-	Structure factor
$\mathbf{S}$	2	-	Scattering amplitude matrix
t	-	ns, s	Time
T	-	K	Temperature
T_{cr}	4, 5, 6	K	Critical temperature
T_p	4, 5, 6	K	Nanoparticle temperature
T_{ref}	4, 5, 6	K	Reference temperature, Clausius-Clapeyron equation, fluence curves
U	4	J	Internal energy of a nanoparticle
U_b	-	J, eV	Nanoparticle potential barrier
V	-	m^3	Volume of the aerosol
W_{MPI}	-	Molecule/s	Multi-photon ionization rate
W_{ion}	-	J, eV	Ionization potential
W	-	J, eV	Work function
x_p	-	-	Size parameter
$\mathbf{x}$	-	-	Unknown quantities vector
Z	-	-	Partition function

Z	-	-	Ionic charge number

Greek characters

Symbol	Chapter Restrictions	Unit	Definition
α	4,5,6	-	Thermal accommodation coefficient (TAC)
α	3	-	Neural network number of output elements
$\alpha_{f\text{-}s}$	6	-	Fine structure constant
δ	3	-	Neural network number of input elements
$\boldsymbol{\varepsilon}_{\lambda}$	-	-	Complex dielectric function
$\varepsilon_{I,\lambda}$	-	-	Real component of dielectric function
$\varepsilon_{II,\lambda}$	-	-	Imaginary component of dielectric function
Γ	-	s	Damping coefficient of plasmon
γ	-	-	Specific heat ratio
γ_s	-	N/m	Surface tension
η_{λ}	-		Calibration constant
φ	3	-	Fuel to air equivalence ratio
$\boldsymbol{\Phi}$	-	-	Vector of additional parameters inside the kernel of light scattering
Φ	4	V	Electrostatic potential
Φ_e	-	J, eV	Ionization potential
λ	-	nm	Wavelength
λ_g	-	nm	Mean free path of the gas
λ_l	-	nm	Laser wavelength
Λ	-	-	The intensity scaling factor (ISF)
μ	-	-	Mean, often for normal distribution
μ_g	-	nm	The geometric mean of the aggregate lognormal size distribution
μ_p	-	nm	Geometric mean of primary particle lognormal size distribution
ν_g	-	Hz	Frequency of gas-nanoparticle collisions
π	-	-	Constant, 3.1415...

θ	-	degree	Scattering angle
Θ	-	-	Dimensionless temperature
ρ	-	kg/m^3	Density
σ	-	-	Standard deviation
σ_g	-	-	Standard deviation of aggregate lognormal size distribution
σ_s	-	m^2, nm^2	Scattering cross-section
σ_p	-		Standard deviation of primary particle lognormal size distribution
σ_{MPI}	-	$cm^{2N}s^{N-1}$(N-photon ionization process)	Multi-photon ionization cross-section
τ	-	s	Plasma relaxation time
ω	-	rad/s	Angular frequency of the electromagnetic field
ω_p	-	rad/s	Angular plasma frequency
ζ	-		Thermodynamic degrees of freedom
ζ_{rot}	-		Rotational thermodynamic degrees of freedom
χ	-		MALS calibration constant
ψ_l	4	-	Riccati-Bessel function of order *l*

Common subscripts and superscripts

Supscript	Definition
elec	electron
g	Gas
LSQ	Least-squares
meas	Measured
mod	Modeled
p	Nanoparticle
pl	plasma
s	Surface
v	Vapor

Abbreviations

Abbreviation	Definition
DDA	Discrete dipole approximation
HAB	Height above burner
ISF	Intensity scaling factor
LII	Laser-induced incandescence
LOSA	Line-of-sight attenuation
MAP	Maximum a posteriori estimate
MLE	Maximum likelihood estimate
pdf	Probability density function
QoI	Quantities of interest
TAC	Thermal accommodation coefficient
TEM	Transmission electron microscopy
TiRe-LII	Time-resolved laser-induced incandescence
RDG-FA	Rayleigh-Debye-Gans fractal aggregate
MSTM	Multi-sphere T-matrix

Chapter 1
An Introduction to laser-based aerosolized nanoparticle metrology

The unique chemical and electromagnetic properties of nanoparticles underlie advancements in many areas of engineering and science [1], including drug delivery [2], photothermal cancer therapy [3], ultra-sensitive biosensing [4], and photovoltaic devices [5]. Nanoparticles are usually categorized based on their dimensionality, morphology, composition, uniformity, and agglomeration [6]. They come in a variety of shapes; for example, nanospheres are spherical shaped nanoparticles or nanoaggregates which are formed as a result of the aggregation process between the nanoparticles in a colloid or an aerosol, cf. Figure 1-1. The size and morphology of the nanoparticle or nanostructure strongly affect their physical properties. For instance, the plasmonic behavior of gold nanoparticles causes the color of a colloid solution to change from deep red to black, depending on the size and shape of the constituent nanoparticles [7].

Nanoparticles may be synthesized purposefully, such as the production of gold (Au) nanoparticles for medical applications [8,9] or commercially-produced soot (carbon black) used in painting, rubber, and printing industries [10]. On the other hand, they can be unintentionally created as a byproduct of mechanical or industrial processes. For example, atmospheric soot is formed as a result of the imperfect combustion of hydrocarbons [11], which contributes to climate change by increasing radiative forcing and severely impacts human health in ways that continue to be understood [12–17].

There is a keen interest in the mass-production of synthetic nanoparticles due to their growing applications in many emerging technologies. Gas-phase synthesis offers the opportunity for producing controlled high-purity nanostructures in the continuous flow [18]. By varying reaction settings such as

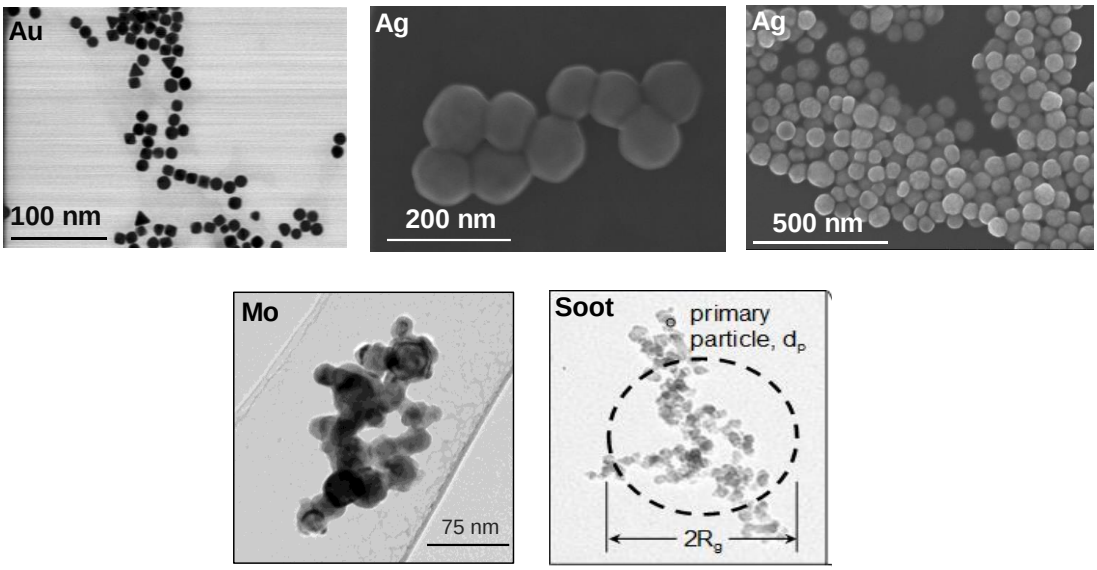

Figure 1-1 Silver (Ag), molybdenum (Mo), gold (Au), and soot nanoparticles (BC). Molybdenum (Mo) image is used with permission from P. 8 of Ref. [21].

stoichiometry or pressure, individual particles of different sizes, agglomerates, and aggregates could be produced. Controlling nanoparticle morphology is of fundamental importance for exploiting their properties. However, to mass-produce nanostructures, robust techniques with a high temporal and spatial resolution to measure morphology and size during the fabrication is indispensable. Measuring nanoparticle size and morphology is also essential for assessing their impact on the environment and human health [19,20].

Typically, nanoparticles are defined as a collection of atoms and molecules that form a structure having a size dimension in the range of 1-100 nm. They can be composed of one or more species of atoms or molecules and can exhibit a wide range of size-dependent properties. Often the atoms assemble into nanospheres having diameters described by a particular probably density. In the case of diffusion-limited transport, the nanoparticle sizes, d_p, often obey a lognormal distribution [22]

$$p\left(d_p;\mu_p,\sigma_p\right)=\frac{1}{\sqrt{2\pi}d_p\ln\sigma_p}\exp\left(\frac{-\left(\ln d_p-\ln\mu_p\right)^2}{2\left(\ln\sigma_p\right)^2}\right), \tag{1.1}$$

where μ_p and σ_p are the geometric mean and geometric standard deviation of d_p, respectively.

In some cases, the nanospheres assemble into fractal-like aggregates. The radius of gyration R_g for a homogeneous aggregate is defined as

$$R_g^2 = \frac{1}{N_p}\sum_{i=1}^{N_p} m_i \; r_{ic}^2 + r_i^2 \;, \tag{1.2}$$

where m_i, r_i, and r_{ic} are the i^{th} primary particles mass, radius and distance to the cluster's center of mass, respectively. The primary particle diameters are frequently sufficiently narrow to be modeled as monodisperse [23]. The number of primary particles per aggregate, N_p, and the radius of gyration, R_g are empirically related by [24]

$$N_p = k_f \left(\frac{2R_g}{d_p} \right)^{D_f} , \tag{1.3}$$

where D_f and k_f are the fractal dimension and prefactor, respectively, which together define the aggregate morphology. In the case of soot, each aggregate contains tens to hundreds of primary particles, while the fractal dimension and prefactor usually vary between $1.4 \le D_f \le 1.9$ and $1.2 \le k_f \le 3.0$, respectively [25–30]. The wide range of these parameters is attributed, in part, to variations in the type of fuel, local stoichiometry, and ambient conditions, as well as differences in the methodology used to analyze the aggregates. The aggregate size range R_g can also often be modeled as a lognormal distribution

$$p\left(R_g;\mu_g,\sigma_g\right) = \frac{1}{\sqrt{2\pi}R_g \ln\sigma_g} \exp\left(\frac{-\left(\ln R_g - \ln\mu_g\right)^2}{2\left(\ln\sigma_g\right)^2} \right). \tag{1.4}$$

In Eq. (1.4) μ_g and σ_g are the geometric mean and geometric standard deviation of R_g, respectively

One of the possible ways to find information about size distributions, $p(d_p)$, $p(R_g)$, morphology D_f and k_f, is to examine direct images of nanostructures. Transmission electron microscopy (TEM) can be used to directly image nanoparticles at scales approaching a single atom [31]. In this process, first, a sample of nanoparticles is fashioned on a grid micrograph from a colloidal suspension or aerosolized nanoparticles. An example of a sampling method is thermophoretic sampling which adopts thermophoresis for collecting particles with a high spatial resolution in hot gases such as flames [32]. Subsequently, 2D images are formed by the interaction of the electrons with the sample as the beam is transmitted through the sample. While TEM analysis of extracted nanoparticle samples is considered the most accurate approach in determining morphology and size, it is time-consuming, with limited spatial and temporal resolution. Size parameters inferred from TEM analysis may also be biased by the sampling process and by the algorithms used to transform 2D images into 3D morphology [33]. Therefore, there is a pressing need for accurate, reliable *in situ* nano-characterization approaches.

In recent decades, various optical methods have been developed to provide detailed insight into reactive gas-phase systems with high spatial and temporal resolution and for studying soot produced by combustion processes. In particular, non-intrusive laser-based methods have become indispensable for improving combustion technologies and for the mass production of nanoparticles [34,35]. Despite the relative simplicity of laser-optical setups compared to other methods, characterizing nanostructures from the optical signal is a complicated process due to the complexity of the underlying physics of the problem, model uncertainty, signal noise, and imperfect knowledge of phenomena involved during the laser-aerosol interaction.

There is a wide variety of laser-based aerosol diagnostics. Light extinction measurement techniques such as line of sight attenuation (LOSA) [36–38], cavity ring-down laser absorption spectroscopy (CRDS or CRLAS) [39,40], laser-induced breakdown spectroscopy (LIBS) [41,42], X-ray scattering techniques such as small-angle x-ray scattering (SAXS) technique [43], dynamic light scattering (DLS) [44], laser-induced fluorescence (LIF) [45], and Raman spectroscopy [4,46] are just a few examples of diagnostics which apply to aerosols. A detailed description of *in situ* optical diagnostics applicable to aerosols can be found in Ref. [47].

All laser-based aerosol diagnostics are based on irradiating a sample volume of aerosol with a collimated laser beam and then measuring some sort of electromagnetic signal that is determined by the laser-nanoparticle interaction physics. The underlying physics of the laser-nanoparticle interaction is governed by the power of the laser beam, material, stoichiometry conditions, particle size and morphology and so forth. This thesis looks into two laser-based aerosolized diagnostics methods: multi-angle elastic light scattering (MALS) and time-resolved laser-induced incandescence (TiRe-LII). The historical evolution of both methods is presented in the next sections.

During TiRe-LII the aerosolized nanoparticles are heated up to incandescent temperatures by a laser pulse. The subsequent time-resolved incandescence signals, as shown schematically in Figure 1-2 are used to infer volume fraction, size distribution, and thermophysical properties (e.g. thermal accommodation coefficient) of the nanoparticles [11,48–54]. The magnitude of the LII signal is correlated with the volume fraction of nanoparticles in the detection region, and the decay rate of the LII signal could be used to indicate the primary particle size and thermophysical properties of nanoparticles [49]. TiRe-LII has been used extensively for quantitative measurements of soot volume fraction and primary particle size [18,55–59].

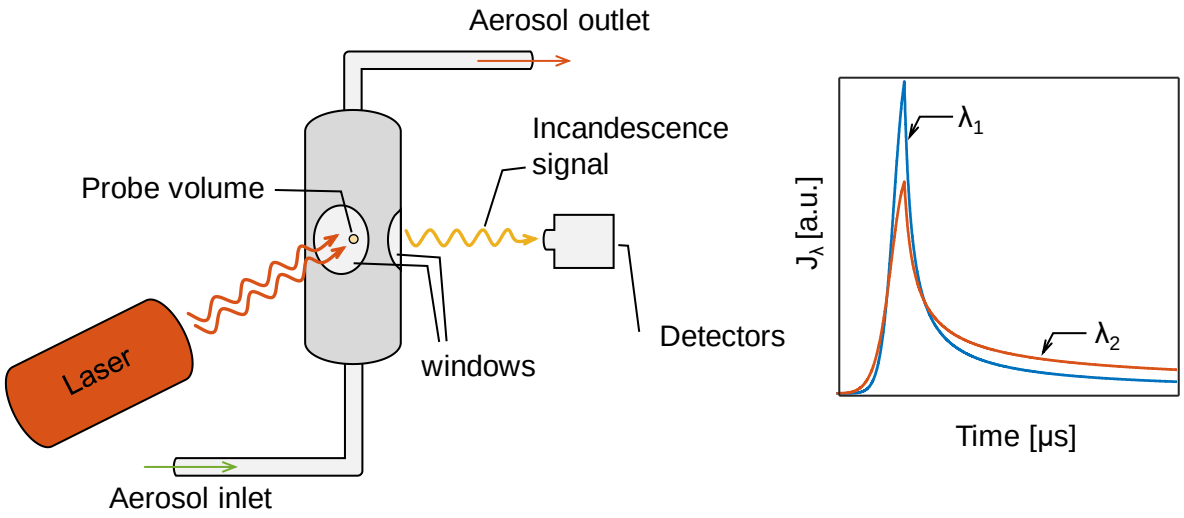

Figure 1-2 Schematic view of a TiRe-LII setup. The detection wavelengths are λ_1 and λ_2.

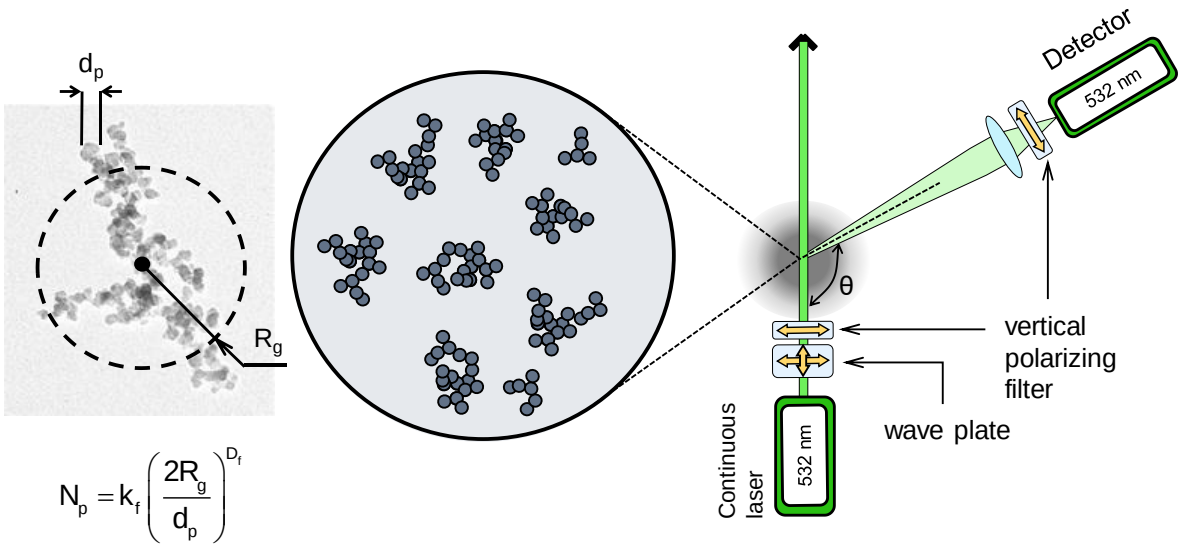

Figure 1-3 Schematic view of a MALS setup.

The laser fluence used in MALS measurements is much lower than what is normally used for TiRe-LII, and it does not induce significant heat up in the aerosol. The angular distribution of scattered light from the interaction of a collimated beam with an aerosol is used to infer information about the morphology of constituent aggregates and as well as the volume fraction [60,61]. For example, a detector bay traverse over a range of angles, or an array of detectors are fixed at specific angular

locations, or an optical device collects scattered light over a wide angular range and focuses it on a detector [62,63]. A schematic of a MALS setup is shown in Figure 1-3.

In the case of aggregates, the fractal parameters such as k_f and D_f and nanoaggregate size distribution can be inferred from MALS data with the assumption of deterministic primary particle size, while TiRe-LII infers primary particle size assuming a fractal geometry, which influences the cooling rate through the aggregate shielding effect [64]. The rest of this chapter will discuss the MALS and TiRe-LII setups measuring principles in more detail, and known problems regarding these methods are discussed.

1.1 Multi-angle light scattering fundamentals

In MALS, information related to the scattering phase function of the laser-nanoparticle interaction is exploited to infer useful information regarding the morphology of aerosolized nanoparticles. In the MALS setup, scattered light from aggregates in a probe volume defined by the intersection of a collimated light source and detection optics is measured as a function of scattering angle, θ, as shown in Figure 1-3. The number density of nanoparticles in the aerosol is sufficiently small so that signal trapping between the probe volume and detector is negligible, and scattering by the gas molecules in the aerosol is accounted for in the calibration constants. Typically, both incident and detected light are vertically-polarized [65]. In this section, we will look into the MALS historical development and basic model principles.

1.1.1 A brief history of multi-angle light scattering (MALS) development

Mainly three different types of experimental MALS setups have been presented in the literature. The first approach uses a scanning goniometer in which the detector mechanically rotates around the probe volume [66–68]. This method allows for a potentially high angular resolution but comes with the disadvantage of sequential and, therefore, slow measurements. Usually, one data acquisition takes several minutes for a 10° angular resolution between the scattering angle range of 10°–150° [69]. Accurate alignment of the goniometer is critical in this setup. In the case of any inaccuracy, the position of the detected scattering probe volume would change with θ, which can cause an artificial change in the measured scattering intensity [66]. The second experimental setup is to use multiple detectors which provides fast measurement at several angles, but with limited angular resolution. In this method, the

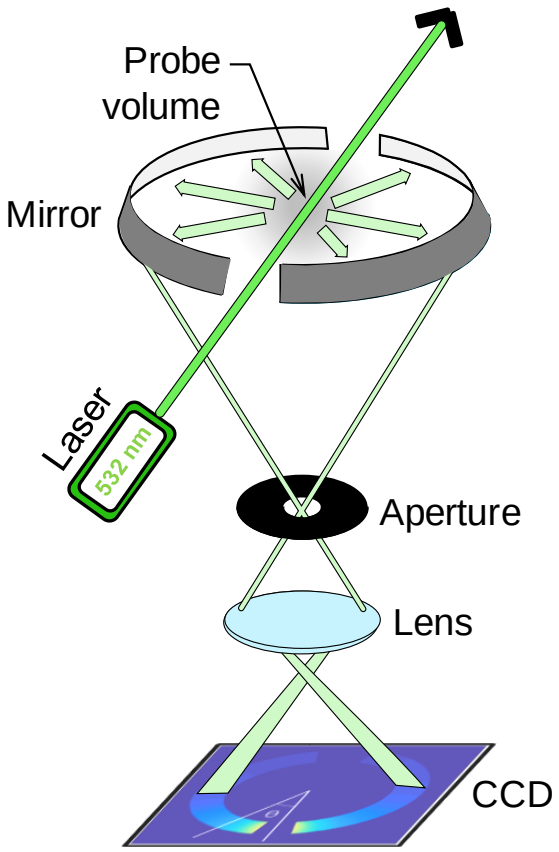

Figure 1-4 Schematics of the WALS apparatus.

scattering intensity is measured by pre-set detectors or optical fibers at fixed angles [68,70–72]. The key idea of the fiber optics instrument was to use optical fiber as a flexible light transmittance tool. Salzman et al. [73] used 32 photodiodes to measure forward light scattering of a flow system. Bartholdi et al. [74] could achieve a complete circular measurement around the probe volume with an angular resolution of 2.91°. This type of setup permits fast measurements compared to the setups using a goniometer. However, angular resolution is limited due to the physical dimension of the detection optics.

The third and the most recent MALS setup was developed by Tsutsui et al. [69] in which a continuous-angle laser light scattering apparatus developed by using an ellipsoidal mirror and a charged-coupled device (CCD) detector. The ellipsoidal mirror collects the scattered light from a wide-angle range and reflects it to the CCD detector. The developed setup could achieve 0.6° resolution and each measurement was reported to be less than 1 second. Oltmann et al. [62] further improved the setup

design and named it the wide-angle light scattering (WALS) apparatus. Also, they demonstrated the performance of the apparatus by performing various *in-flame* soot measurements. Schematics of the WALS setup is shown in Figure 1-4. Since then, the WALS apparatus has been used to perform measurements on metal oxide nanoparticle such as silica aerosol [75], and *in-flame* soot [76,77]. Recently, the setup is used for 2D-MALS measurements on soot [78].

1.1.2 Multi-angle light scattering (MALS) inference fundamentals

Forrest and Witten [24] were the first to demonstrate that cluster aggregates have a fractal morphology with a fractal dimension, which can be quantitatively measured. Further investigations have shown fractal morphology is a universal consequence of aggregation [79]. Sorensen et al. [22] proposed a novel method for *in-situ* optical diagnostics of soot-cluster primary particle size d_p, the number of primary particle N_p, and the fractal dimension D_f by using a combination of scattering-extinction and the scattering phase function measurements. However, their study could not infer N_p and d_p. Köylü and Faeth [68] have improved this approach and evaluated several models to approximate the optical properties of soot aggregates, but with large uncertainties in the inferred soot morphology parameters. Manickavasagam and Mengüç [60,80] investigated the possibility of measurement scattering-matrix (Mueller matrix) elements of soot during laser interaction with the aerosol and discussed possible measurement techniques to identify soot structures from scattering-matrix elements. In the case of an aerosol consisting of monodisperse aggregates, the angular scattering distribution is directly related to R_g [23]. Eriçok and Ertürk recovered particle size and the number of primary monomers per aggregate for a hypothetical aerosol containing identical aggregates through nonlinear least-squares regression [81]. It should be noted that most of the studies mentioned above assumed a monodisperse soot aggregate size.

In the case that the polydispersity of soot aggregate size distribution is not overlooked, the measured scattering signal $b(\theta)$ is due to contributions from all aggregate size classes. The aggregate size distribution $p(R_g)$ is found by deconvolving a first-order Fredholm integral equation

$$b(\theta) = \chi_{exp} \int_0^\infty k\left(R_g, \theta, \mathbf{\Phi}\right) p\left(R_g\right) \mathrm{d}R_g, \tag{1.5}$$

where χ_{exp} depends on the soot volume fraction in the probe volume, incident beam intensity, and detection optics. The light scattering kernel is $k(R_g, \theta, \mathbf{\Phi})$, $p(R_g)$ is the probability density of the radius of gyration, and $\mathbf{\Phi}$ is a vector of additional parameters that includes the complex refractive index of

soot, $\mathbf{m}_\lambda$, primary constituent monomer size, d_p, and morphological parameters, D_f and k_f. The deconvolution problem is ill-posed due to the smoothing action of the kernel, and consequently, a large number of candidate distributions, $p(R_g)$, and parameters in $\mathbf{\Phi}$, exist that could explain the observed data. Accordingly, the measurement data must be augmented with additional information about the estimated parameters known prior to the experiment.

If the radius of gyration, R_g (or, equivalently, the number of primary particles, N_p) is approximated by a lognormal distribution, the distribution parameters are related to the light scattering measurements by a nonlinear Fredholm integral equation of the first kind, similar to Eq. (1.5)

$$b(\theta) = \chi_{exp} \int_0^\infty k\left(\theta, R_g, \mathbf{\Phi}\right) p\left(R_g; \mu_g, \sigma_g\right) dR_g \tag{1.6}$$

In this thesis the primary particle sizes are modeled as monodisperse [63]. With the assumption of a lognormal size distribution $p(R_g; \mu_g, \sigma_g)$ through Eq. (1.5), inferring lognormal distribution size parameters μ_g and σ_g of aerosolized soot aggregates from the angular distribution of elastically-scattered light is a well-posed problem contingent upon possessing definite information about morphology parameters k_f and D_f, primary particle size d_p, and refractive index of soot $\mathbf{m}_\lambda$. In the solution process, the unknown vector $\mathbf{x} = [\mu_g, \sigma_g]^T$ is found by minimizing the sum-of-squares residual between measured and modeled data. However, if the vector of unknowns $\mathbf{x}$ also includes any additional parameters, e.g., k_f, D_f, d_p, and $\mathbf{m}_\lambda$, the solution becomes ill-posed. The ill-posedness of the problem is due to the existence of an infinite set of candidates for $\mathbf{x}$ that, when substituted into the measurement model, can mathematically generate nearly the observed scattering signal. This sensitizes the recovered solution to measurement noise and model error and questions the stability of the solution, which is required for defining a problem well-posed by Hadamard definition [82].

Another complication lies in the required model of electromagnetic wave scattering through nanoaggregates, which is used to derive the kernel $k(R_g, \theta, \mathbf{\Phi})$. In the case of isolated polydisperse spherical nanoparticles, Mie theory [83] can predict an exact solution for the phase function of the nanoparticle. However, in the case of soot or other nanostructures in aggregate form, there is no closed-form analytical solution to the Helmholtz wave equation to predict the optical properties. Thus, approximate models are frequently used to reduce the complexity of the model. In the case of MALS, light scattering is often approximated using Rayleigh-Debye-Gans Fractal Aggregate (RDG-FA) theory [23,84,85], which is an extension of Rayleigh approximation of Mie theory for primary particles scattering by considering the morphology of the scattering aggregate through the Fourier transform of

the density distribution of the scattering aggregate [23]. In the RDG-FA model, self-induced and multiple scattering phenomena between the primary particles are ignored. Compared to the exact solution, the RDG-FA approximation is computationally-efficient but limited in accuracy due to: (*i*) the fundamental Rayleigh approximation error for single primary particles compared to Mie theory, and (*ii*) the fact that reabsorption of the scattered electromagnetic wave between primary constituent particles is neglected. Further details will be provided in *Chapter 2* to relate the RDG-FA predictions to the exact solution for different morphological parameters.

The resulting RDG-FA model errors are amplified by the ill-posed nature of the problem into significant errors in the recovered soot parameters [76]. More precise approaches, like the multi-sphere T-matrix (MSTM) method [86], discrete dipole approximation (DDA) [87] or generalized Mie-solution method (GMM) [85,88] are too computationally-intensive and time-consuming to be used in the inference procedure to find the vector of unknowns **x** through Eq. (1.5). The experimental results on the recovery of soot morphology by MALS shows the RDG-FA model error impairs accurate inference of soot morphological and size parameters [76,89].

The RDG-FA model error is not random, unlike the experimental noise; instead, it is structured due to the correlation between the morphological parameters and the exact electromagnetic wave interaction solution [90–92]. Therefore, predictions about the behavior of the RDG-FA model error as a function of morphological parameters can be made based on statistical analysis. Subsequently, these statistical predictions can be implemented directly into the solution of Eq. (1.5) for correcting the model error in the kernel of light scattering $k(R_g, \theta, \mathbf{\Phi})$.

For achieving a statistical prediction of RDG-FA model error, the exact solution of $k(R_g, \theta, \mathbf{\Phi})$ for different sets of morphological parameters is required. Therefore, a comprehensive study is necessary to determine the applicability of approximating the RDG-FA model error and using it in the solution of the ill-posed light scattering problem to infer nanostructures morphology and size distribution. *Chapters 2* and *3* of this dissertation investigate statistical models that could be added alongside the Bayesian inference to enhance the soot morphology inference compared to using RDG-FA model as the kernel of light scattering.

1.2 Laser-induced incandescence fundamentals

Time-resolved laser-induced incandescence (TiRe-LII) is a technique for characterizing aerosolized nanoparticles that uses a laser pulse to energize aerosolized nanoparticles to incandescent temperatures and then measures the spectral incandescence from the nanoparticles as they return to the ambient gas temperature. In this section, the historical development of LII and basic model principles are discussed.

1.2.1 A brief history of laser-induced incandescence

Weeks and Duley [93] in 1974 presented time-resolved signals of light emission from aerosolized particles (carbon black and aluminum) following laser excitation with pulses from a transversely excited atmosphere (TEA) CO_2 laser and proposed that the detected signal may be related to particle size. They also found an analytical expression of the nanoparticle cooling rate by applying the First Law of Thermodynamics to the nanoparticles. The results agreed with the detected signals qualitatively. Eckbreth [94] in 1977 measured laser-induced incandescence which was called laser-modulated incandescence of soot particles generated by a propane diffusion flame. Eckbreth further developed the TiRe-LII model by including vaporization/sublimation. Also, for the first time, the inferred peak temperature of particles as a function of laser fluence (fluence curve) is reported, and the particle sublimation model is used to justify the plateau regime at high laser fluences. Melton [95] in 1984 further developed the TiRe-LII model and used it for soot particle diagnostics. Rohlfing [96] in 1988 used the model proposed by Eckbreth to measure TiRe-LII signals from carbon clusters.

The development of the LII technique accelerated through the 1990s. Measurements mainly focused on soot produced in engines [58,97–100], laminar flames [100–103] and turbulent flames [103–106]. Also, laser sheets used to investigate the 2D spatial distribution of soot for the first time [102,107,108]. Another development was to use LII in combination with other laser-based diagnostics such as laser-induced fluorescence (LIF) measurements [104,109,110] and elastic light scattering [99]. Some studies also questioned the possibility of non-incandescent laser-induced emission (LIE) during the experiments. Cignoli et al. [111] used the fourth harmonic of the Nd:YAG laser at 266 nm to excite soot. The measurement showed contamination of the LII signal with LIF and also it is noted that interference signals last only 20 ns after the laser pulse.

At the end of the 1990s, LII was already a well-established technique for combustion diagnostics, and researchers once again started applying it to non-carbonaceous nanoparticles. Vander Wal et al. [112] in 1999 applied LII to measure tungsten (W), molybdenum (Mo), iron (Fe) and titanium (Ti) aerosols. They used LII to characterize the metal nanoparticle concentration and showed that the

decay rate could be related to nanoparticle size, however they did not infer the size. In the same year, Filippov et al. [57] applied LII to carbon (graphite), silver (Ag) and titanium nitride (TiN) aerosol with particle sizes below 100 nm. They used the LII model developed previously for soot and compared the inferred size distribution with TEM data along with online measurements employing a differential mobility analyzer (DMA). Eremin et al. [113,114] applied LII to iron and carbon aerosolized nanoparticles, while Sipkens et al. [115] inferred the size distribution of iron, molybdenum and silver aerosols from TiRe-LII signals via Bayesian inference. In recent years and by applying the LII technique to further nanoparticle types and size distributions, several measurement phenomena are reported in the literature in which the traditional TiRe-LII model mainly proposed by Eckbreth [94] and further developed through the 1990s is unable to explain. Some of these measurement phenomena are briefly discussed in the next subsection. *Chapters 4*, *5* and *6* of this dissertation are mainly focused on explaining these measurement phenomena by improving on the existing LII model or implementing models for disregarded phenomena and adding them alongside the LII model.

1.2.2 Laser-induced incandescence (LII) model basics

Many attempts have been made to model the processes involved in generating an LII signal; an overview of these models can be found in Schulz et al. [49], and Michelsen et al. [116]. There are two primary coupled models: (*i*) the heat transfer model that considers cooling by conduction to the surrounding atmosphere, evaporation/sublimation, and radiative cooling, and (*ii*) the spectroscopic model that links the observed spectral incandescence with the nanoparticle temperature.

Accurate determination of the nanoparticle size and volume fraction through TiRe-LII relies on accurate modeling of both heat transfer and spectroscopic models. The standard LII model developed in the literature has certain shortcomings compared to experimental data such as “anomalous cooling” in which the nanoparticle loses sensible energy higher than the prediction of the LII standard model after the peak temperature [21,117], cf. Figure 1-5. Another discrepancy is excessive absorption by the nanoparticle compared to the one predicted by Mie/Drude theory [21,118].

Deriving robust estimates of nanoparticle morphology and volume fraction from LII measurements requires a reliable measurement model grounded in physics. Recent research into LII has focused mainly on the heat transfer submodel; far less effort has been devoted to addressing the accuracy of the spectroscopic model. The spectroscopic model is essential for understanding the amount of absorption in the nanoparticle during the laser pulse; also, it is the link between the detected signal

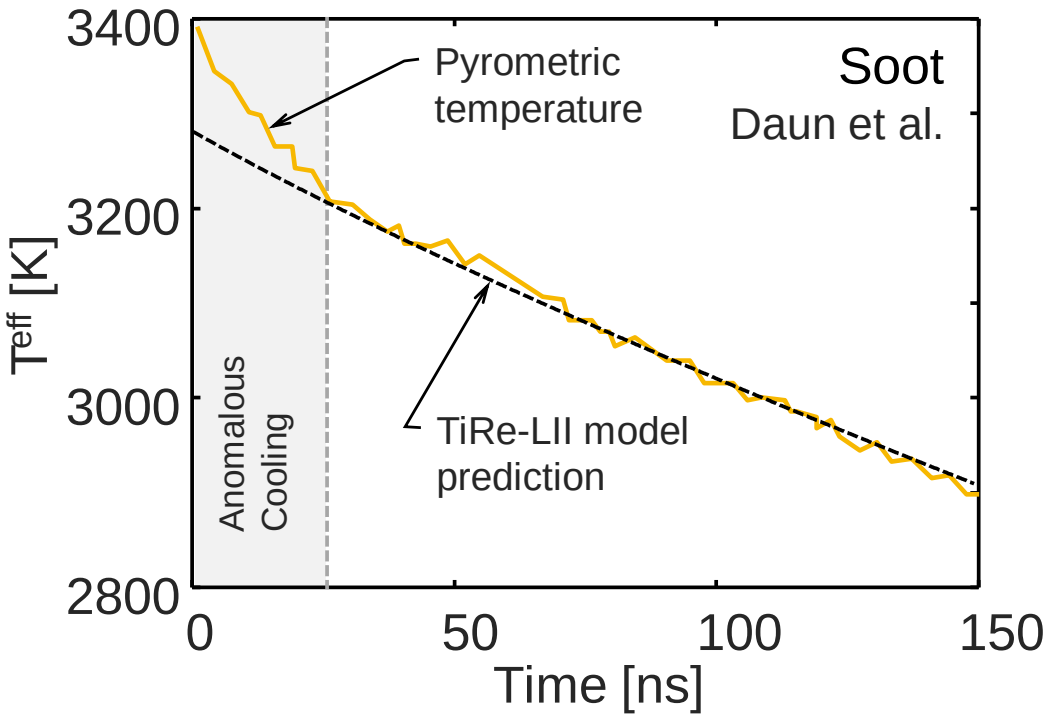

Figure 1-5 Example of the anomalous cooling phenomenon during TiRe-LII experiments on soot [117]. The pyrometric temperature drops faster than what is predicted by the TiRe-LII model.

and the inferred nanoparticle characteristics. Therefore, it is of prime importance to improve the spectroscopic model to improve the LII diagnostic technique.

1.3 Thesis objectives and document overview

The purpose of the thesis is to improve laser-based nanoparticle diagnostics by refining the spectroscopic models used to infer aerosol properties from MALS and TiRe-LII data and performing experiments to test these refined models. In the current study, MALS is used to probe the fractal parameters (D_f and k_f) and size distribution parameters (σ_g and μ_g) of soot-laden aerosols, while TiRe-LII is used for the inference of the primary particle size of metal nanoparticles, $p(d_p)$, although the techniques developed in this work are broadly applicable to many types of nanoparticles.

In the case of MALS, the efficiency of RDG-FA and the accuracy of MSTM can be combined by modeling the approximation error. The error function is derived from a principal component analysis

(PCA) [119] on error matrices generated for randomly-sampled aggregates having morphological fractal parameters sampled from distributions derived from published studies in the literature. The error model is then used to correct the RDG-FA kernel in the forward model for a particular set of fractal parameters. Finally, the corrected model is used to estimate the probability densities of the size distribution and aggregate fractal parameters via Bayesian inference. *Chapter 2* describes how the approximation error technique is used to improve the soot size and morphology inference by correcting the light scattering kernel.

Another approach is to use a computationally-efficient fully-connected multi-layered artificial neural network (ANN) to approximate the MSTM light scattering kernel which is the subject of *Chapter 3*. Accordingly, the fidelity of physics-based models must be sacrificed to achieve a computationally-efficient solution when they are used directly in inference problems. ANNs can avoid this compromise by "front-loading" the computational burden to a one-time training period, potentially reducing the model error. The ANN is trained by using MSTM random samples with morphological fractal parameters expected to occur during the experiments. Afterward, the ANN replaced the kernel of the light scattering as a black-box model. Subsequently, the Bayesian/ANN is compared with Bayesian/AE in a numerical study. Bayesian/ANN outperformed the Bayesian/AE in the accuracy of the inference. Finally, the Bayesian/ANN model is applied to experimental measurements and the results compared with inferred morphological parameters from TEM micrographs. The experimental data collected by using WALS apparatus on a well-defined soot-laden aerosol. The Bayesian/ANN estimates of D_f and k_f values were close to the TEM micrograph analysis of the literature but the size distribution parameters were underestimated.

In contrast to MALS, in the case of TiRe-LII, there are discrepancies between the experiments indicating significant knowledge gaps in the physics underlying the measurement models. The TiRe LII practitioners usually model the spectra; absorption cross-section of the nanoparticles using the Rayleigh limit of Mie theory [120,121] due to the small size of the nanoparticle compared to the wavelength. However, this assumption is questionable for metallic nanoparticles. *Chapter 4* investigates how applying Mie theory, incorporating polydispersity of primary particle sizes, and accounting for the change in the refractive index about the melting point, explain anomalies or reduce the discrepancies in TiRe-LII measurements on metal nanoparticles. *Chapter 4* starts by introducing the spectroscopic and heat transfer models used in TiRe-LII analyses, including a summary of Mie theory as it applies to the absorption of E-M waves by silicon, iron, silver, and molybdenum nanoparticles. Synthetic signals are generated for monodisperse and polydisperse aerosols by applying

Mie theory to modeled nanoparticle temperature decays. The signals are then interpreted using the Rayleigh approximation and a quadrupole approximation to Mie theory to investigate the effect that these approximations have on the inferred properties. It is shown that using Mie theory instead of the Rayleigh approximation and considering polydisperse particle sizes explains the discrepancy between the experimentally-derived and simulated integral scaling factor (ISF) and may partially explain the apparent discrepancy in the $E(\mathbf{m}_\lambda)$ ratio at the detection wavelengths for iron nanoparticles, while these effects combined with the change in refractive index when the nanoparticles melt partially accounts for the apparent enhanced absorption cross-section. Remaining anomalies suggest that some other spectroscopic phenomena must also be occurring to explain the enhanced absorption of laser energy, particularly for silver nanoparticles.

This thesis also proposes entirely new mechanisms to explain some commonly-observed but unexplained features in LII data. The formation of a laser-induced plasma in the aerosol during the laser pulse can potentially heat the nanoparticle due to plasma conductivity. Moreover, were such a plasma to form, it would radiate thermal bremsstrahlung radiation (*brake radiation*) and potentially corrupt the LII pyrometric temperature inference, cf. Figure 1-6. One section of this thesis regarding LII heat transfer and spectroscopic models is to consider the formation, evolution, expansion, and diffusion of the laser-induced microplasma, heat and mass transfer dynamics between the nanoparticle and the microplasma, and the corruption of the LII signal with thermal bremsstrahlung of plasma. The new TiRe-LII enhanced model is then used to predict experimentally observed discrepancies with the traditional TiRe-LII model, such as anomalous cooling and excessive absorption. The possibility of formation of a plasma during TiRe-LII experiments and the plasma bremsstrahlung radiation interference with the nanoparticle incandescence emission is investigated in *Chapter 5*.

In *Chapter 6* the plasma emission model is used to study TiRe-LII data taken on aerosols of silver and gold nanoparticles and measurements carried out on these nanoparticles to test the hypothesis. Due to the small absorption cross-section of both nanoparticles at 1064 nm (the wavelength of the laser), one should not expect significant heat-up during the laser irradiation, yet a detectable albeit weak signal can be observed. Assuming that the detected LII signal is incandescence and is governed by Planck's distribution and the spectral absorption cross-section of the nanoparticle, the inferred pyrometric temperatures are above the boiling temperature of silver (2162 °C) and vary with the buffer gas type used during the experiments. Therefore, the detected signals are more likely due to a non-incandescent laser-induced emission (LIE) source. A new model is proposed to explain the detected signals based on plasmonically-enhanced photoemission of electrons from the nanoparticles

as is shown in Figure 1-7. The interaction of the electrons with buffer gas neutral species leads to inverse neutral bremsstrahlung absorption of the laser pulse as well as neutral bremsstrahlung emission. A linear trend is observed for electron temperatures as a function of laser fluence in which the slope of the trend depends on the buffer gas type. Also, insignificant electron number density variation is observed during the signals, which is expected due to negligible electron diffusion in the studied timescales and no electron-ion recombination.

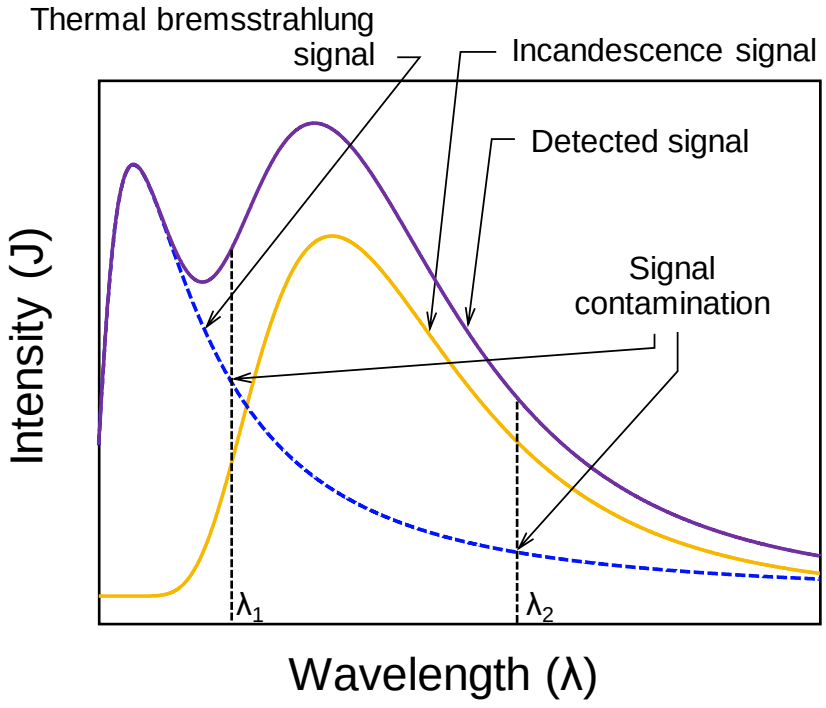

Figure 1-6 The detected signal is a combination of the nanoparticle incandescence and plasma thermal bremsstrahlung emission. The effect could artificially inflate the inferred temperature.

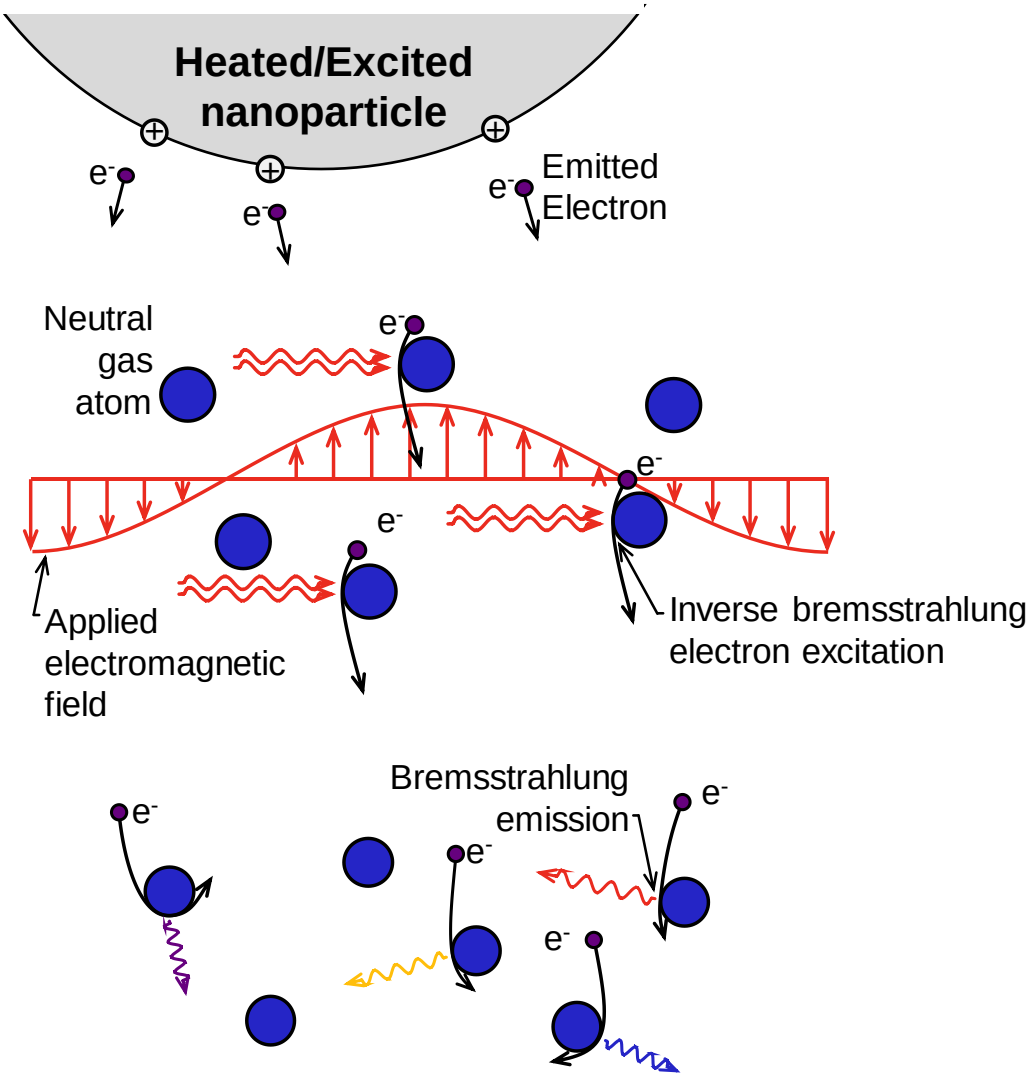

Figure 1-7 Proposed model for electron neutral bremsstrahlung emission from the gas phase. Free electrons after emission from the nanoparticle could both absorb the irradiation by inverse neutral bremsstrahlung and emit neutral bremsstrahlung. In the case of Ag and Au experiments, negligible heat up is expected.

Chapter 2
Error approximation technique for multi-angle light scattering

The content of this chapter is an extended version of a paper published in the *Journal of Aerosol Science* as titled, "Soot aggregate sizing through multiangle elastic light scattering: Influence of the model error [122]."

2.1 Introduction

Using the Rayleigh-Debye-Gans fractal aggregates (RDG-FA) model impairs the inference of soot morphological parameters due to the amplification of model error by the ill-posed nature of the problem. On the other hand, using exact solutions such as multi-sphere T-matrix (MSTM), which solves the electromagnetic wave interaction with the aggregates numerically, is time- and computationally-demanding, which makes it unfeasible. One of the proposed solutions is to use the approximation error to approximate the RDG-FA model error. This is done by constructing a statistical sample of RDG-FA error function, which is derived from a principal component analysis (PCA) on error matrices generated for randomly-sampled aggregates having morphological fractal parameters.

This chapter investigates how modeling the approximation error can improve the accuracy of the RDG-FA light scattering kernel, while maintaining its other advantages. The RDG-FA kernel is used as the forward model to estimate the morphological parameters. The error model is computed by comparing light scattering kernels obtained through the most accurate physical model available and similar RDG-FA predictions for random aggregates constructed from fractal parameters sampled from distributions derived from experimental data. The variation in these samples is then modeled using principal component analysis (PCA) on the error matrices [119,123,124]. Applying PCA to the error of the kernel matrices allows us to write the error matrix as a finite sum of fixed matrices with random coefficients that capture the variations observed within the samples. The approximation error is then

incorporated into the Bayesian inference of the soot aggregate size parameters by simultaneously estimating the random coefficients along with the quantities of interest. A comparison of these posterior estimates with those found by ignoring the model error (currently the most prevalent practice) and masking the model error using white noise highlights the importance of considering this effect and the efficacy of the approximation error procedure.

Initially, the literature for nanoparticle morphology and size distribution inference by multi-angle light scattering (MALS) setup is reviewed, and Bayesian inference as a tool for quantifying the extent of ill-posedness is introduced briefly. Candidate models for light scattering aerosolized from fractal aggregates are then presented; these include the approximate RDG-FA model and two high-fidelity solution methods: the discrete dipole approximation (DDA) and multi-sphere T-matrix (MSTM) methods. The Bayesian method is revisited as a way to introduce prior information into the inference process and to understand the impact of model error on the inferred aerosol parameters. Finally, the error approximation technique is applied to account for the RDG-FA model error. The improvement with implementing model approximation error in the soot size and morphology inference is evaluated. The results showed that the approximating model error corrects the RDG-FA model error in the inference process without the need for a computationally expensive exact light scattering solution.

2.2 A review on multi-angle light scattering inference

In *Chapter 1*, the measurement model for a polydisperse aerosol is presented in Eq. (1.5), and it is discussed that the aggregate size distribution probability density function $p(R_g)$ is usually approximated as a lognormal distribution as is shown in Figure 2-1. This assumption introduces a significant amount of information into the problem and simplifies the size distribution inference to find μ_g and σ_g. However, Burr et al. [65] attempted to recover size distribution without any shape assumption for $p(R_g)$ in Eq. (1.5), cf. Figure 2-1. In their study Eq. (1.5) was transformed into a matrix equation, $\mathbf{Ax} = \mathbf{b}$, where $\mathbf{x}$ represents $p(R_g)$ in discretized form and $\mathbf{\Phi} = [k_f, Df, \mathbf{m}_\lambda, d_p]^T$ was assumed to be perfectly known. The $\mathbf{A}$ matrix is ill-conditioned due to the underlying ill-posed nature of the problem, which Burr et al. attempted to overcome using linear regularization techniques that promoted a smooth $p(R_g)$ distribution.

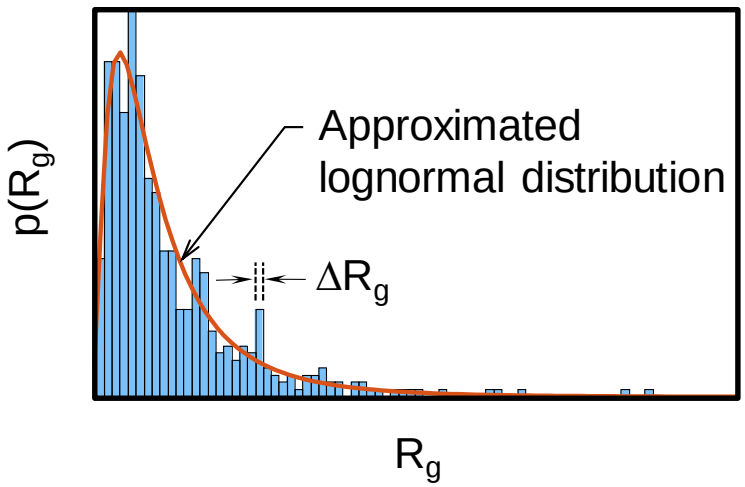

Figure 2-1 The deconvolution problem can be converted into a linear problem by discretizing $p(R_g)$ in which the width of the strips are ΔR_g.

The extent of ill-posedness can be quantified directly via Bayesian inference [125,126]. In this approach vector **x**, which contains the unknown model parameters (including μ_g, σ_g, and often some of the parameters in **Φ**), and **b**, which contains the measurement data, are treated as random variables that obey probability densities. These equations are related by Bayes' equation

$$p(\mathbf{x}|\mathbf{b}) = \frac{p(\mathbf{b}|\mathbf{x})\, p_{\mathrm{pr}}(\mathbf{x})}{p(\mathbf{b})}, \tag{2.1}$$

where $p(\mathbf{b}|\mathbf{x})$ is the likelihood of the observed measurements (i.e., the probability of observing the data in the context of the measurement noise for a given set of model parameters), $p(\mathbf{x}|\mathbf{b})$ is the posterior probability of **x** based on the observations in **b**, $p_{\mathrm{pr}}(\mathbf{x})$ is a joint probability density that quantifies the information known about **x** before the measurements, and $p(\mathbf{b})$ is the evidence, which scales $p(\mathbf{b}|\mathbf{x})p_{\mathrm{pr}}(\mathbf{x})$ so that the posterior satisfies the Law of Total Probability. The main advantages of this approach are: (*i*) the uncertainties associated with the inferred variables can be interpreted as the probability density widths; and (*ii*) it explicates the crucial role of prior information when solving ill-posed inverse problems. Huber et al. used the Bayesian approach to infer lognormal distributions parameters and associated uncertainties from data collected using the Wide-Angle Light Scattering (WALS) apparatus [76]. In their treatment, the unknown parameters were $\mathbf{x} = [\mu_g, \sigma_g, D_f]^T$, and priors were derived from TEM images of extracted soot aggregates.

Evaluating the posterior probability, $p(\mathbf{x}|\mathbf{b})$, requires the calculation of the likelihood $p(\mathbf{b}|\mathbf{x})$ over a range of **x**, which, in turn, requires the repeated computation of the measurement model, and

consequently $k(R_g, \theta, \mathbf{\Phi})$. While there is no closed-form, exact solution to the kernel of the light scattering, it can be calculated numerically by applying electromagnetic theory to random aggregates generated according to a particular set of morphological parameters $\{d_p, k_f, D_f\}$, which can then be averaged over all sizes and orientations. The MSTM method [86,127] is highly accurate, provided that the primary particles touch without any overlap or necking [128]. The main advantage of MSTM over other techniques, such as the discrete dipole approximation (DDA) [87] is that it avoids repetition of the solution for a particular aggregate over different orientations by performing an integration [127]. Nevertheless, MSTM calculations on fractal aggregates are still computationally-demanding to carry out. To find the light scattering kernel for a particular R_g value, one should average the results over multiple randomly-generated aggregates, which further exacerbates the computational burden.

Due to the high computational demand of MSTM, most practitioners instead derive the scattering kernel using Rayleigh-Debye-Gans fractal aggregate (RDG-FA) theory, which is founded on the assumption that each primary particle scatters in the Rayleigh limit of the Mie theory, and multiple scattering between the primary particles and self-interaction scattering phenomena are ignored [23,120,129]. This approach is closed-form and computationally-efficient compared to MSTM and depends only on a set of morphological parameters specified by D_f and k_f, rather than a particular aggregate configuration. However, RDG-FA predictions can be expected to have errors of around 30% for typical soot aggregates [23,90,91,130]. (The exact error depends on scattering angle, aggregate morphology, and bulk radiative properties.) Some studies have tried to extend the RDG-FA theory by integrating multiple scattering effects on the absorption and scattering of fractal soot aggregates [131] or taking into account the interactions of large monomers [132]. The RDG-FA errors are manageable when predicting angular light scattering from an aerosol of well-characterized soot aggregates, but when light scattering data is used to infer aggregate size and morphology, the ill-posed nature of Eq. (1.5) amplifies small amounts of model error into significant variations in the inferred parameters.

Nevertheless, only Huber et al. [76] has acknowledged this issue by highlighting the different soot aggregate parameters inferred using RDG-FA with three candidate structure factors, arguing that a conservative estimate of the RDG-FA model error compared to a more accurate treatment like DDA or MSTM can be estimated by comparing the parameters recovered using three RDG-FA structure factors. While it is possible to incorporate model error by "masking" it with white noise, which is equivalent to artificially increasing the data uncertainty, doing so significantly increases the uncertainty in the recovered parameters. Huber et al. [76] postulated the Bayesian approximation error technique [124,133] as an alternative way to account for systematic model error in RDG-FA without significantly

increasing the uncertainty of the recovered parameters, while also avoiding the computational expense of the more accurate light scattering models. In this approach, the statistics of the model approximation error is constructed by comparing two models: one that is computationally-efficient but subject to a particular model error (RDG-FA); while the other is considerably more accurate but computationally-expensive (MSTM). These statistics are then used to correct the approximation obtained using the computationally-efficient model.

2.3 Light scattering from aerosolized fractal aggregates

The kernel of the light scattering in Eq. (1.6) can be derived from RDG-FA theory by writing the scattering cross-section regarding the cross-section of primary particles

$$\begin{aligned} k_{\text{RDG-FA}}(R_{\text{g}},\mathbf{\Phi}) &= N_{\text{p}}^2 \frac{d\sigma_{\text{s}}^{\text{m}}}{d\Omega} S_{\text{RDG-FA}}\left(qR_{\text{g}},D_{\text{f}}\right) \\ &= k_{\text{f}}^2 \left(\frac{2R_{\text{g}}}{d_{\text{p}}}\right)^{2D_{\text{f}}} \lambda^2 x_{\text{p}}^6 F\left(\mathbf{m}_\lambda\right) S_{\text{RDG-FA}}\left(qR_{\text{g}},D_{\text{f}}\right)/\left(2\pi\right)^2 \end{aligned} \tag{2.2}$$

where $d\sigma_{\text{s}}^{\text{m}}/d\Omega = \lambda^2 x_{\text{p}}^6 F(\mathbf{m}_\lambda)/(2\pi)^2$ is the differential scattering for primary particles, λ is the wavelength, $x_{\text{p}} = \pi d_{\text{p}}/\lambda$ is the size parameter, $F(\mathbf{m}_\lambda)=|(\mathbf{m}_\lambda^2-1)/(\mathbf{m}_\lambda^2+2)|^2$ is the scattering function derived from the Rayleigh limit of Mie theory [120], and S is the structure factor, which indicates how the angular variation of scattered light depends on the modulus of scattering vector, $q(\theta)$ [23]

$$q(\theta) = \frac{4\pi}{\lambda}\sin\left(\frac{\theta}{2}\right). \tag{2.3}$$

The number of primary particles is related to the radius of gyration via Eq. (1.3). While many structure factors have been presented in the literature, here we use

$$S_{\text{RDG-FA}}\left(qR_{\text{g}},D_{\text{f}}\right) = \left(1+\sum_{m=1}^{M} C_m \left(qR_g\right)^{2m}\right)^{-D_f/2M} \tag{2.4}$$

where $C_1 = 2M/3D_{\text{f}}$ for small values of qR_{g} [134]. Lin et al. proposed using $M = 4$ with $C_2 = 2.5$, $C_3 = -1.52$, and $C_4 = 1.02$. This equation applies to the range of D_{f} proposed for soot aggregtes ($1.4 < D_{\text{f}} < 1.9$).

Although RDG-FA offers a fast, closed-form solution for the light scattering kernel, these predictions are limited in accuracy because they exclude self-induced and multiple scattering phenomena. To find the exact solution, on the other hand, one would need to generate a large population of soot aggregates using morphological parameters sampled from probability densities representative of those that occur within the aerosol [135], and then solve the Helmholtz wave equation solution for each aggregate. The average of these results would represent the light scattered by the ensemble of aggregates in the aerosol. The tuneable cluster-cluster aggregation (CCA) is used to generate the aggregate [64,91]. Examples of aggregates generated by this algorithm are shown in Figure 2-2 for three different fractal dimensions.

The simulated aggregates can be used to obtain the exact numerical solution to the light scattering kernel as a matrix over discrete values of R_g and θ by averaging over samples and orientations of soot aggregates. The complex elements of the scattering amplitude matrix (S_i, i = 1, 2, 3, 4) connect the incident field to the scattered field and depend on the scattering zenith angle θ as well as the azimuthal angle [120]. Due to the vertical polarization of the incident and detected scattered light, S_1 is the only non-zero component. The light scattering kernel is then approximated by

$$k_{\mathrm{exa}}\left(N_{\mathrm{p}}, D_{\mathrm{f}}, k_{\mathrm{f}}, d_{\mathrm{p}}, \mathbf{m}_{\lambda}, \lambda, \theta\right) \simeq \frac{\lambda^2}{N_{\mathrm{s}}^{\mathrm{agg}} N_{\mathrm{orien}}} \sum_{i=1}^{N_{\mathrm{s}}^{\mathrm{agg}}} \sum_{j=1}^{N_{\mathrm{orien}}} \left| S_1\left(\mathbf{r}_{\mathrm{i}}, d_{\mathrm{p}}, \mathbf{m}_{\lambda}, \lambda, \theta_j\right)\right|^2, \tag{2.5}$$

where **r** contains the primary particle centroid coordinates, N_s^{agg} is the number of samples and N_{orien} is the number of orientations. To compare the exact solution and RDG-FA we define an "exact structure factor" consistent with RDG-FA theory and Eq. (2.2) as

$$S_{\mathrm{exact}} = \frac{(2\pi)^2 k_{\mathrm{exact}}}{N_{\mathrm{p}}^2 \lambda^2 x_{\mathrm{p}}^6 F(\mathbf{m})}. \tag{2.6}$$

Note that S_{exact} depends on both the aggregate geometry and complex refractive index, while the RDG-FA structure factor depends only on the fractal parameters. The RDG-FA error, which is an accumulation of geometric error of structure factor and the error introduced through the Rayleigh approximation, is defined as the difference between S_{exact} and the RDG-FA structure factor, $S_{\mathrm{RDG\text{-}FA}}(qR_g, D_f)$.

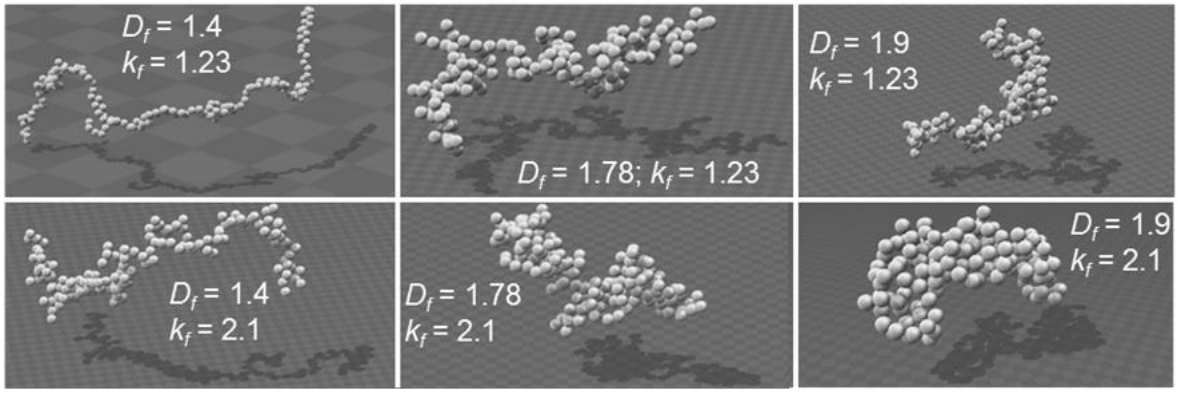

Figure 2-2 Simulated soot aggregates with CCA algorithm. It is observable that the aggregates become more compact as D_f and k_f become larger.

The RDG-FA or exact MSTM light scattering kernel can be incorporated into different numerical integration schemes to solve Eq. (1.6). For a particular scattering angle θ_j , the light scattering is modeled by

$$\begin{aligned} b(\theta_j) &= C_{\exp}\int_0^{\infty} k\left(\theta, R_g, \mathbf{\Phi}\right) p\left(R_g;\mu_g,\sigma_g\right) dR_g \approx \cdots \\ C_{\exp}&\sum_{i=1}^{N_r} w_i k\left(\theta_j, R_{g,i}, \mathbf{\Phi}\right) p\left(R_{g,i};\mu_g,\sigma_g\right) = a_j(\mathbf{x}), \end{aligned} \tag{2.7}$$

where $\mathbf{x}$ contains μ_g, σ_g, and possibly a subset of $\mathbf{\Phi}$, $\mathbf{R}_g = [0, R_{g,2}, \ldots, R_{g,Nr}]^T$ is the discretized set of R_g used to numerically-compute the scattering intensity, w_i are the weights used for the integration scheme, which, in this thesis, is the trapezoidal scheme. For a set of discrete scattering angles, $\boldsymbol{\theta} = [\theta_1, \theta_2, \ldots, \theta_m]$,

$$\underbrace{\begin{bmatrix} b(\theta_1) \\ b(\theta_2) \\ \vdots \\ b(\theta_m) \end{bmatrix}}_{\mathbf{b}} = \underbrace{\begin{bmatrix} a_1(\mathbf{x}) \\ a_2(\mathbf{x}) \\ \vdots \\ a_m(\mathbf{x}) \end{bmatrix}}_{\mathbf{a}(\mathbf{x})} = \begin{bmatrix} C_{\exp}\sum_{i=1}^{N_r} w_i k\left(\theta_1, R_{g,i}, \mathbf{\Phi}\right) p\left(R_{g,i};\mu_g,\sigma_g\right) \\ C_{\exp}\sum_{i=1}^{N_r} w_i k\left(\theta_2, R_{g,i}, \mathbf{\Phi}\right) p\left(R_{g,i};\mu_g,\sigma_g\right) \\ \vdots \\ C_{\exp}\sum_{i=1}^{N_r} w_i k\left(\theta_m, R_{g,i}, \mathbf{\Phi}\right) p\left(R_{g,i};\mu_g,\sigma_g\right) \end{bmatrix} = C_{\exp}\mathbf{K}\left(\mathbf{\Phi}\right)\mathbf{p}\left(\mu_g,\sigma_g\right) \tag{2.8}$$

, where

$$\mathbf{K}(\mathbf{\Phi}) = \begin{bmatrix} w_1 k\left(\theta_1, R_{\mathrm{g},1}, \mathbf{\Phi}\right) & w_2 k\left(\theta_1, R_{\mathrm{g},2}, \mathbf{\Phi}\right) & \dots & w_{N_r} k\left(\theta_1, R_{\mathrm{g},N_r}, \mathbf{\Phi}\right) \\ w_1 k\left(\theta_2, R_{\mathrm{g},1}, \mathbf{\Phi}\right) & w_2 k\left(\theta_2, R_{\mathrm{g},2}, \mathbf{\Phi}\right) & \dots & w_{N_r} k\left(\theta_2, R_{\mathrm{g},N_r}, \mathbf{\Phi}\right) \\ \vdots & \vdots & \ddots & \vdots \\ w_1 k\left(\theta_m, R_{\mathrm{g},1}, \mathbf{\Phi}\right) & w_2 k\left(\theta_m, R_{\mathrm{g},2}, \mathbf{\Phi}\right) & \dots & w_{N_r} k\left(\theta_m, R_{\mathrm{g},N_r}, \mathbf{\Phi}\right) \end{bmatrix} \in \mathbb{R}^{m \times N_r} \tag{2.9}$$

, and

$$\mathbf{p}(\mu_{\mathrm{g}}, \sigma_{\mathrm{g}}) = \begin{bmatrix} p\left(R_{\mathrm{g},1}; \mu_{\mathrm{g}}, \sigma_{\mathrm{g}}\right) \\ p\left(R_{\mathrm{g},2}; \mu_{\mathrm{g}}, \sigma_{\mathrm{g}}\right) \\ \vdots \\ p\left(R_{\mathrm{g},N_r}; \mu_{\mathrm{g}}, \sigma_{\mathrm{g}}\right) \end{bmatrix} \in \mathbb{R}^{N_r} . \tag{2.10}$$

Vector functions $\mathbf{a}_{\text{RDG-FA}}(\mathbf{x})$ and $\mathbf{a}_{\text{exact}}(\mathbf{x})$ denote numerical evaluations of Eq. (1.6) using kernels derived from RDG-FA or the exact scattering kernel, the latter computed using MSTM.

The MSTM method is verified using the discrete dipole approximation (DDA) [87]. The open-source DDA solver package DDSCAT is used for this study [136]. The calculations are for $N_{\mathrm{p}} = 50$, $\mathbf{m}_{\lambda} = 1.6 + 0.6i$, $d_{\mathrm{p}} = 30$ nm, an incident wavelength of $\lambda = 532$ nm and vv-polarization for three different sets of morphological parameters. In the DDA analysis, the GKDLDR polarizability relation [136] is used with approximately 10^3 dipoles representing each monomer and a lattice parameter of 2.4180 nm. The DDA solution is averaged over 7^3 orientations for each of the 150 aggregates generated by the CCA algorithm. Figure 2-3 shows the structure factors, $S_{\text{RDG–FA}}$–S_{exact}, and relative error of RDG-FA and DDA to MSTM method for D_{f} randing from 1.4 to 2.1 and $k_{\mathrm{f}} = 2.3$. The Rayleigh error increases as D_{f} increases, which corresponds to a more compact aggregate and, consequently, higher multiple scattering between the primary particles. The MSTM and DDA results are in good agreement except at high angles; at θ larger than 130º the DDA estimates differ by up to 13% error for $D_{\mathrm{f}} = 1.4$, which is a known shortcoming of DDA for shapes having high aspect ratios [136].

2.4 Bayesian inference method

In most MALS experiments [65,76] the light scattering kernel found by RDG-FA is incorporated into a naïve least-squares analysis to estimate the quantities of interest (QoI). In Bayesian inference, however, the data and unknowns are treated as random variables that obey probability densities, which

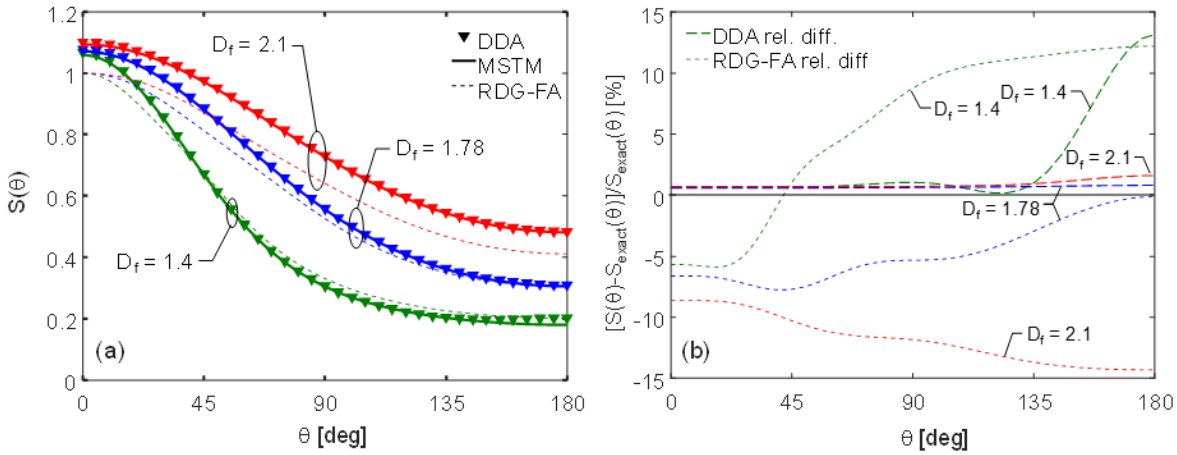

Figure 2-3 (*a*) Exact and RDG-FA structure factors for three different values of D_f with k_f = 2.3. (*b*) The relative error of DDA and RDG-FA to MSTM is calculated for three different D_f values.

directly indicate their uncertainties through their distribution width. The Bayesian framework also facilitates the incorporation of prior knowledge into the inference, which can narrow the posterior distribution.

In this approach, the data vector $\mathbf{b} = [b(\theta_1), b(\theta_1), \ldots, b(\theta_m)]^T$, containing the light scattering measurements made at different angles, and the unknown parameters in $\mathbf{x} = [\mu_g, \sigma_{g,\ldots}]^T$ are modeled as random variables that obey probability densities. (The unknown quantities include the aggregate size distribution parameters, and may also include fractal parameters and other uncertain model parameters.) The measurement signal, $\mathbf{b}$, is contaminated with unbiased noise consisting of electronic noise, $\delta\mathbf{b}_{elect}$, photonic shot noise, $\delta\mathbf{b}_{shot}$, and noise associated with fluctuations in laser fluence and concentration, $\delta\mathbf{b}_{fluc}$ [76]

$$\mathbf{b} = \mathbf{b}_{exact} + \delta\mathbf{b}_{model} + \delta\mathbf{b}_{noise}, \quad \delta\mathbf{b}_{noise} = \delta\mathbf{b}_{shot} + \delta\mathbf{b}_{elect} + \delta\mathbf{b}_{fluc} \tag{2.11}$$

The $\delta\mathbf{b}_{elect}$ and $\delta\mathbf{b}_{fluc}$ terms are independent and normally-distributed for each measurement angle. Photonic shot noise also affects each measurement angle independently but obeys a scaled Poisson distribution that can be modeled as normally-distributed [76]. Huber et al. [76] showed that $\delta\mathbf{b}_{noise}$ is small compared to calibration error $\delta\mathbf{b}_{cal}$, which is reported to be around 2%. Therefore, in this study, a standard deviation of 2% of the maximum value of $\mathbf{b}$ is assumed for $\sigma_{b,i}$ ($\mathbf{\Gamma}_b = 0.02^2 \cdot diag[b(\theta_1)^2, b(\theta_1)^2, \ldots, b(\theta_1)^2]$). The likelihood function is then defined as

$$p(\mathbf{b}\,|\,\mathbf{x}) = \frac{1}{\left(2\pi^{m/2}\right)\left[\det\left(\mathbf{\Gamma}_b\right)\right]^{1/2}} \exp\left(\frac{-\left[\mathbf{b}-\mathbf{a}(\mathbf{x})\right]^T \mathbf{\Gamma}_b^{-1}\left[\mathbf{b}-\mathbf{a}(\mathbf{x})\right]}{2}\right). \tag{2.12}$$

In the absence of prior knowledge about the QoI uninformed priors are used, $p_{pr}(\mathbf{x}) = 1$. In this scenario $p(\mathbf{x}|\mathbf{b}) \propto p(\mathbf{b}|\mathbf{x})$ and the most probable solution is found by maximizing Eq. (2.12), which is the maximum likelihood estimate (MLE)

$$\mathbf{x}_{\mathrm{MLE}} = \arg\max_{\mathbf{x}} p(\mathbf{x}\,|\,\mathbf{b}) = \arg\max_{\mathbf{x}} p(\mathbf{b}\,|\,\mathbf{x}) = \arg\min_{\mathbf{x}} \left\| \mathbf{L}_{\mathrm{b}} \left[\mathbf{b} - \mathbf{a}(\mathbf{x}) \right] \right\|^2, \tag{2.13}$$

where $\mathbf{L}_{\mathrm{b}}$ is a weighting matrix derived from the Cholesky factorization of $\boldsymbol{\Gamma}_{\mathrm{b}}^{-1}$, $\boldsymbol{\Gamma}_{\mathrm{b}}^{-1} = \mathbf{L}_{\mathrm{b}}^{\mathrm{T}}\mathbf{L}_{\mathrm{b}}$.

Due to the ill-posed nature of the problem, the posterior distributions over $\mathbf{x}$ will be wide as many combinations of these parameters could explain the observed data. These distributions can be narrowed by introducing additional information in the form of priors, although it is important that the priors contain only testable information to avoid unduly biasing the estimate. According to the Principle of Maximum Entropy, prior PDFs should be chosen that maximize their information entropy (which minimizes their information content) subject to constraints of testable information. If a point estimate, $\boldsymbol{\mu}_{\mathrm{pri}}$, and an uncertainty estimate, $\boldsymbol{\Gamma}_{\mathrm{pri}}$, are available for the QoI and/or nuisance parameters, the maximum entropy prior is a Gaussian distribution centered at $\boldsymbol{\mu}_{\mathrm{pri}}$ with covariance defined by $\boldsymbol{\Gamma}_{\mathrm{pri}}$ [137,138]. The maximum a posterior estimate (MAP) is then given by

$$\begin{aligned} \mathbf{x}_{\mathrm{MAP}} &= \arg\max_{\mathbf{x}} p\left(\mathbf{x}|\mathbf{b}\right) = \arg\max_{\mathbf{x}} p\left(\mathbf{b}|\mathbf{x}\right) p_{\mathrm{pr}}\left(\mathbf{x}\right) \\ &= \arg\min_{\mathbf{x}} \left\| \begin{bmatrix} \mathbf{L}_{\mathrm{b}}\mathbf{a}(\mathbf{x}) \\ \mathbf{L}_{\mathrm{pri}}\mathbf{x} \end{bmatrix} - \begin{bmatrix} \mathbf{L}_{\mathrm{b}}\mathbf{b} \\ \mathbf{L}_{\mathrm{pri}}\boldsymbol{\mu}_{\mathbf{x}} \end{bmatrix} \right\|^2, \end{aligned} \tag{2.14}$$

where $\boldsymbol{\Gamma}_{\mathrm{pri}}^{-1} = \mathbf{L}_{\mathrm{pri}}^{\mathrm{T}}\mathbf{L}_{\mathrm{pri}}$.

In the case of Gaussian priors and Gaussian measurement noise, the posterior can sometimes be modeled as a normal distribution centered at $\mathbf{x}_{\mathrm{MAP}}$, $p(\mathbf{x}|\mathbf{b}) \sim \mathcal{N}(\mathbf{x}_{\mathrm{MAP}}, \boldsymbol{\Gamma}_{\mathrm{x}})$ with a covariance estimated using the Jacobian at $\mathbf{x}_{\mathrm{MAP}}$ [133]

$$\boldsymbol{\Gamma}_{\mathrm{x}} = \left[\mathbf{J}^{T}\left(\mathbf{x}_{\mathrm{MAP}}\right) \boldsymbol{\Gamma}_{\mathrm{b}}^{-1} \mathbf{J}\left(\mathbf{x}_{\mathrm{MAP}}\right) + \boldsymbol{\Gamma}_{\mathrm{pri}}^{-1} \right]^{-1}. \tag{2.15}$$

The accuracy of this approach depends on the linearity of the measurement model; it is usually reasonably close to the maximum a posteriori estimate, with errors that grow as $\mathbf{x}$ moves further away from $\mathbf{x}_{\mathrm{MAP}}$. The posterior density $p(\mathbf{x}|\mathbf{b})$ can then be marginalized to obtain univariate probability densities for each QoI, e.g.,

$$p\left(\mu_{\mathrm{g}}\,|\,\mathbf{b}\right) = \int_{-\infty}^{\infty} \mathrm{d}D_f \int_{-\infty}^{\infty} \mathrm{d}k_f \int_{-\infty}^{\infty} p\left(\mathbf{x}\,|\,\mathbf{b}\right) \mathrm{d}\sigma_{\mathrm{g}}. \tag{2.16}$$

Finally, these univariate posterior densities can be summarized with credible intervals that correspond to a specified probability, e.g.

$$\sigma_{g,90\%} \in \left[\sigma_{g,MAP} - \alpha, \sigma_{g,MAP} + \alpha\right] \text{ s.t. } \quad 0.9 = \int_{\sigma_{g,MAP}-\alpha}^{\sigma_{g,MAP}+\alpha} p\ \sigma_g \middle| \mathbf{b}\ d\sigma_g \tag{2.17}$$

which are trivial to compute since $p(\mathbf{x}|\mathbf{b})$ is modeled as Gaussian.

The above treatment only considers the measurement error defined in Eq. (2.11), however, and excludes model error. To highlight this effect, we compare the QoI inferred using the RDG-FA and the MSTM models with synthetic data generated using the MSTM model. In this example, we assume that D_f and k_f are perfectly known, so $\mathbf{x} = [\mu_g, \sigma_g]^T$. The incident wavelength is $\lambda = 532$ nm, and the refractive index is $\mathbf{m}_\lambda$=1.6+0.6*i*, typical for soot in the visible spectrum [90]. The CCA-generated soot aggregates satisfy $D_f = 1.80$, $k_f = 1.88$, $d_p = 30$ nm, $\sigma_g = 1.6$ and $\mu_g = 90$ nm, so $\mathbf{x}_{exact} = [90, 1.6]^T$. The MSTM exact numerical kernel is plotted as a function of N_p and θ in Figure 2-4, where $N_p \in \{5, 10, \ldots, 300\}$ and $\theta \in \{1, 2, \ldots, 180\}$, and each point is the average of kernels obtained from 150 randomly-sampled aggregates.

The scattered light is measured at 31 uniformly-spaced angles between 10° to 165° to generate the measurement data, **b**. The range and sample rate of θ is chosen based on wide-angle light-scattering (WALS) apparatus output which will be used in Chapter 3 to perform measurements. The measurement data is then contaminated with Gaussian noise having a standard deviation of 2% of the maximum value, which is typical of many MALS experiments (e.g. [76]). The kernel is also calculated with RDG-FA approximation, which requires far less computational effort compared to the MSTM method. Generating the soot aggregates and modeling the scattering through MSTM required approximately 72 CPU hours on a cluster of 520 2.3 GHz cores. In contrast, the RDG-FA kernel calculation time in serial on a 2.6 GHz clock-rate machine is less than two seconds. After generating **b** we obtain $\mathbf{x}_{MAP}$ through Eq. (2.14) using priors having a standard deviation of 15% centered at $\boldsymbol{\mu}_{pri} = [85.5, 1.68]^T$. Figure 2-5 (*a*) and (*b*) show the posterior density distribution and 90% credibility.

Notably, the credibility intervals obtained using the RDG-FA kernel do not include $\mathbf{x}_{exact}$. This is because of measurement covariance $\boldsymbol{\Gamma}_{b,meas}$, used to derive $p(\mathbf{b}|\mathbf{x})$, does not account for the model error introduced by the RDG-FA scattering model. This is highlighted by plotting the relative error in structure factor, $(S_{RDG\text{-}FA} - S_{exact})/S_{exact}$, as a function of N_p and θ in Figure 2-4 (b) and (c). The average value of the error is 10%, and its distribution on N_p and θ is consistent with the literature [23], but this

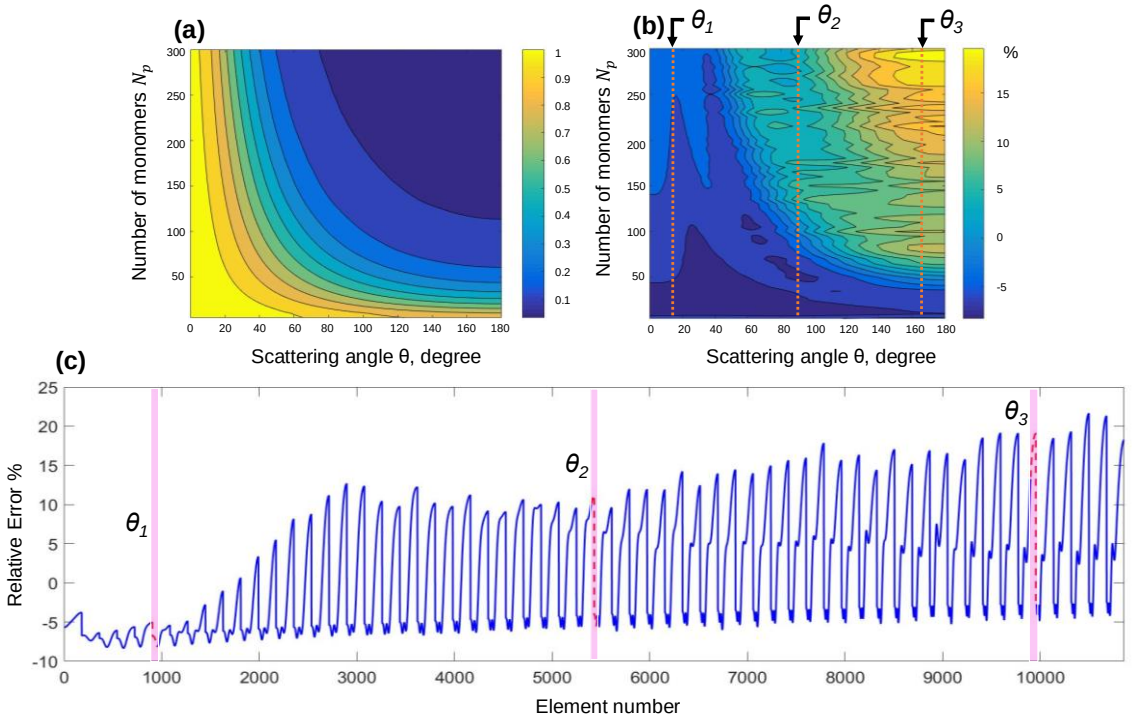

Figure 2-4 (*a*) The exact structure factor S_{exact} calculated by MSTM as a function of θ and N_p (N_p and R_g are connected through Eq. (1.3)). (*b*) The relative error percentage between the exact structure factor and RDG-FA. (*c*) Vectorized version of the 2D relative error plot found by stacking the columns of the 2D error matrix. The values of θ_1, θ_2, θ_3 are 15°, 90°, 165° respectively.

error is amplified by the ill-posed nature of the inverse problem into a significant error in the recovered size parameters.

2.5 Posterior estimation combined with error estimation technique

Ignoring model error severely underestimates the uncertainty in the recovered parameters and introduces a bias in the posterior density distribution. The model error can be incorporated into the inference process regarding the difference between measurements predicted using the exact (MSTM) light scattering kernel and those found with the RDG-FA kernel

$$\begin{aligned}\mathbf{b} &= \mathbf{a}_{\text{exact}}(\mathbf{x}) + \boldsymbol{\delta}\mathbf{b}_{\text{noise}} \\ &= \mathbf{a}_{\text{RDG-FA}}(\mathbf{x}) + [\mathbf{a}_{\text{exact}}(\mathbf{x}) - \mathbf{a}_{\text{RDG-FA}}(\mathbf{x})] + \boldsymbol{\delta}\mathbf{b}_{\text{noise}} \\ &= \mathbf{a}_{\text{RDG-FA}}(\mathbf{x}) + \boldsymbol{\delta}\mathbf{b}_{\text{model}} + \boldsymbol{\delta}\mathbf{b}_{\text{noise}}\end{aligned} \tag{2.18}$$

One approach to accommodate this error is to mask $\boldsymbol{\delta}\mathbf{b}_{\text{model}}$ with white noise [76]

$$\left(\boldsymbol{\delta b}_{\text{noise}} + \boldsymbol{\delta b}_{\text{model}}\right) \sim \mathcal{N}\left(0, \boldsymbol{\Gamma}_{\text{b,meas}}\right) + \mathcal{N}\left(0, \sigma^2_{\text{model}} \mathbf{I}\right) \tag{2.19}$$

To illustrate this method, the likelihood from the previous example is re-evaluated by augmenting the measurement noise with white noise having a standard deviation of 5% of the maximum value to mask the RDG-FA model error, which is representative of the expected error in RDG-FA simulations [23]. By adding white noise, the 90% credibility intervals now contain the exact solution as shown in Figure 2-5 (c), and Table 2-1, but $p(\mathbf{x}|\mathbf{b})$ and the associated credibility intervals are wider, and consequently, $\mathbf{x}_{\text{MAP}}$ is less certain.

The masking approach does not exploit the predictable, structured way with which the model error varies with the aggregate parameters, information that can be used to improve the estimate and narrow the posterior density. This concept is formalized through the approximation error technique in which the model error statistics are constructed by comparing two models: one that is computationally-efficient but subject to a particular model error (RDG-FA), and one that is considerably more accurate but computationally expensive (MSTM). These statistics are then used to correct the approximation obtained using the more efficient model. The goal of the approximation error technique is to approximate the hidden structure of the model error in terms of a multivariate normal distribution, $\boldsymbol{\delta b}_{\text{model}} \sim \mathcal{N}(\boldsymbol{\mu}_{\text{model}}, \boldsymbol{\Gamma}_{\text{model}})$, where $\boldsymbol{\mu}_{\text{model}}$ and $\boldsymbol{\Gamma}_{\text{model}}$ are the mean and covariance of the model error respectively.

A major challenge in this approach lies in the fact that the kernel is a high-dimension function of R_g, θ, and $\boldsymbol{\Phi}$, and, while it may be possible to tabulate the exact kernel as a function of R_g and θ, *cf*. Figure 2-4, it is impractical to do this for all the variables in $\boldsymbol{\Phi}$. Instead, a principal component analysis (PCA) can capture the underlying stochastic nature of the model error for all or a subset of the parameters inside $\boldsymbol{\Phi}$. This information can be utilized alongside the Bayesian inference to enhance estimates and reduce the effect of the model error in estimates, as was seen in Figure 2-5 (b). Specifically, the approximation error is given by

Table 2-1 90% credibility intervals for the posterior density shown in Figure 2-5 with and without masking the model error and for the exact MSTM exact numerical kernel.

	RDG-FA without masking	RDG-FA with masking	Exact numerical kernel
$\mu_{g,90\%}$ [nm]	91.98 ± 1.05	91.99 ± 2.59	90.03 ± 1.02
$\sigma_{g,90\%}$	1.59 ± 0.03	1.59 ± 0.07	1.59 ± 0.03

$$\begin{aligned}\boldsymbol{\delta}\mathbf{b}_{\text{model}} &= \mathbf{a}_{\text{exact}}(\mathbf{x}) - \mathbf{a}_{\text{RDG-FA}}(\mathbf{x}) \\ &= C_{\text{exp}}\mathbf{K}_{\text{exact}}(\boldsymbol{\Phi})\mathbf{p}(\mathbf{x}) - C_{\text{exp}}\mathbf{K}_{\text{RDG-FA}}(\boldsymbol{\Phi})\mathbf{p}(\mathbf{x}) \\ &= C_{\text{exp}}\left[\mathbf{K}_{\text{exact}}(\boldsymbol{\Phi}) - \mathbf{K}_{\text{RDG-FA}}(\boldsymbol{\Phi})\right]\mathbf{p}(\mathbf{x}) \\ &= C_{\text{exp}}\boldsymbol{\delta}\mathbf{K}(\boldsymbol{\Phi})\mathbf{p}(\mathbf{x}),\end{aligned} \tag{2.20}$$

where $\mathbf{K}_{\text{exact}}$ and $\mathbf{K}_{\text{RDG-FA}}$ are the matrices derived from Eq. (2.9) using the MSTM and RDG-FA kernels, respectively. The error in the scattering kernel depends on various unknown variables in $\boldsymbol{\Phi}$, in a highly nonlinear way. (For example, D_f and k_f may not be known without a detailed TEM analysis of extracted soot aggregates.) The approximation error is thus defined regarding the size distribution of the aggregates, $\mathbf{p}(\mathbf{x})$, and $\boldsymbol{\delta}\mathbf{K}(\boldsymbol{\Phi})$, which contains the systematic error induced by the RDG-FA scattering kernel, and the random error induced from using fixed values for the nuisance parameters. If these systematic and random errors in the scattering kernel are not accounted for, the estimates and the associated uncertainties will not represent the true uncertainty.

One approach to account for model error is to estimate it along with the unknown parameters [139]. This is done using a PCA expansion, which relies on the Karhunen-Loève theorem, through which a random field can be represented as a countable linear combination of orthogonal basis functions [119]. In applying this approach to capture the structural and stochastic components in the kernel error, this thesis followed the work of Calvetti et al. [124] who developed the PCA approximation of an operator with nonlinear dependence on unknown parameters. The PCA approximation represents the kernel error as

$$\boldsymbol{\delta}\mathbf{K}(\boldsymbol{\Phi}) \approx \boldsymbol{\delta}\overline{\mathbf{K}} + \sum_{i=1}^{p}\beta_i\mathbf{K}_i \tag{2.21}$$

where $\boldsymbol{\delta}\overline{\mathbf{K}}$ is the expected error (approximated by the average error), $\mathbf{K}_i$ are fixed basis matrices, which capture the variation within the kernel error, and β_i are unbiased stochastic coefficients to be estimated along with the QoI.

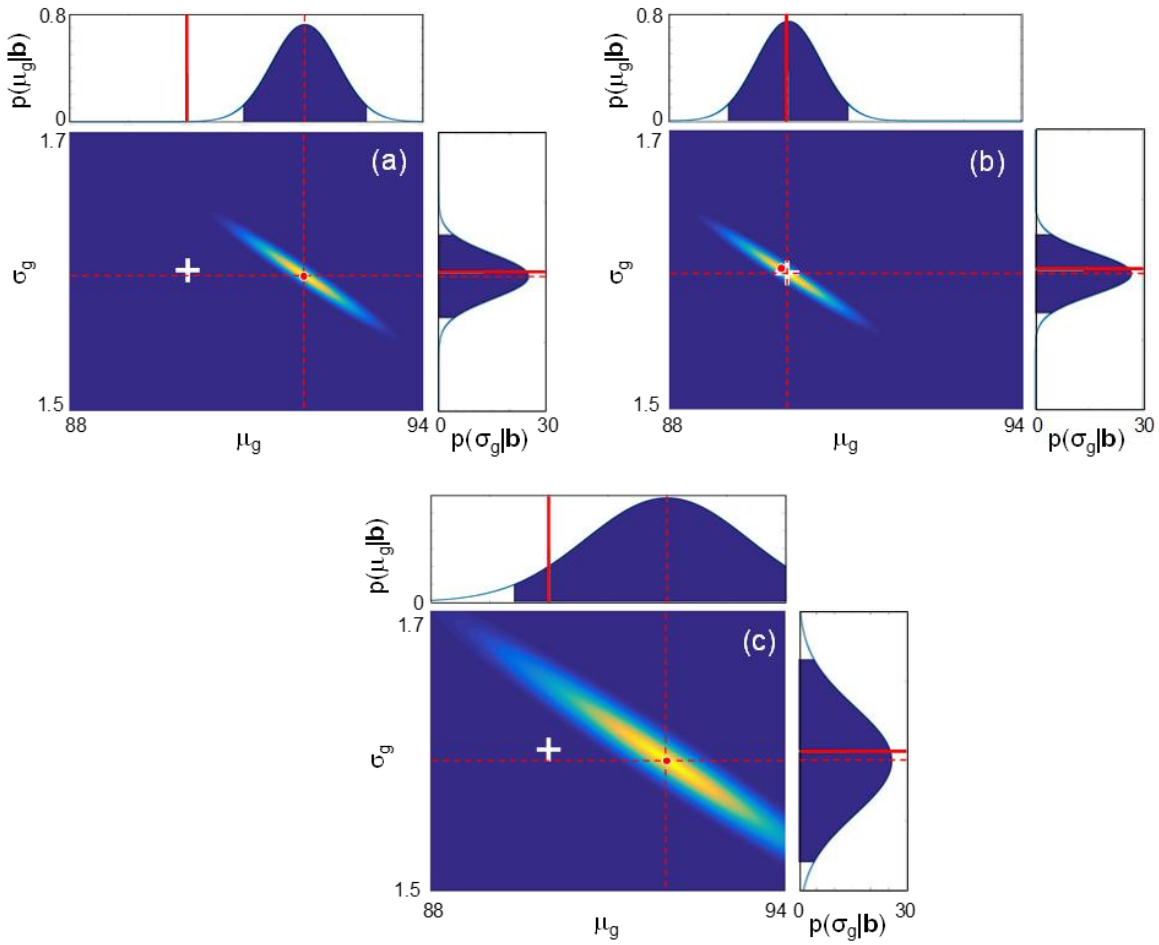

Figure 2-5 Posterior probability $p(\mu_g, \sigma_g|\mathbf{b})$, and 90% credibility intervals. (Exact data is contaminated with 2% Gaussian noise.) The exact and MAP solutions are denoted by the white cross and red circle, respectively. (*a*) The posterior distribution is calculated with the RDG-FA kernel. (*b*) The posterior distribution calculated with the exact numerical kernel (MSTM), *cf.* Figure 2-4 (a). (*c*) The posterior distribution is calculated with the usage of RDG-FA kernel with the addition of 8% normal noise to $\mathbf{a}(\mathbf{x}_{exa})$ to mask the model error.

The basis matrices, $\mathbf{K}_i$, are calculated from an ensemble of kernel error matrices. In particular, we consider the case where $d_p = 30$ nm, and $\mathbf{m} = 1.6 + 0.6i$ are constant and perfectly known, therefore the exact light scattering kernel in matrix form, $\mathbf{K}_{exact}(R_g, \theta, \mathbf{\Phi})$, is calculated for 62 morphological parameters sampled from $k_f \in [1.2, 2.3]$ and $D_f \in [1.4, 1.9]$ as shown in Figure 2-6, representative of the range of values reported in the literature.

The error vector in the light scattering structure factor for the i^{th} random sample $D_f^{(i)}$, $k_f^{(i)}$ is then

$$\begin{aligned}\boldsymbol{\delta}\mathbf{K}^{(i)}\left[\mathbf{r}\left(D_{\mathrm{f}}^{(i)},k_{\mathrm{f}}^{(i)}\right),\mathbf{m},d_{\mathrm{p}},\theta,R_{\mathrm{g}}\right]&=\mathbf{K}_{\text{exact}}\left[\mathbf{r}\left(D_{\mathrm{f}}^{(i)},k_{\mathrm{f}}^{(i)}\right),\mathbf{m},d_{\mathrm{p}},\theta,R_{\mathrm{g}}\right]\\&\quad-\mathbf{K}_{\text{RDG-FA}}\left(D_{\mathrm{f}}^{(i)},k_{\mathrm{f}}^{(i)},\mathbf{m},d_{\mathrm{p}},\theta,R_{\mathrm{g}}\right)\end{aligned}\tag{2.22}$$

where $\mathbf{r}(D_{\mathrm{f}}^{(i)},\ k_{\mathrm{f}}^{(i)})$ is a vector of random aggregate samples generated by the CCA algorithm. For convenience $\delta\mathbf{K}_{\mathrm{i}} \in \mathbb{R}^{\mathrm{Np}\times\mathrm{N}\Theta}$ is reshaped from a 2D matrix to a column vector, $\boldsymbol{\delta}\mathbf{k}_{\mathrm{i}} \in \mathbb{R}^{\mathrm{NpN}\Theta\times 1}$. The matrix of the error vectors is

$$\left\{\boldsymbol{\delta}\mathbf{k}\right\}=\left[\boldsymbol{\delta}\mathbf{k}_1,\boldsymbol{\delta}\mathbf{k}_2,\ldots,\boldsymbol{\delta}\mathbf{k}_{N_s}\right]\tag{2.23}$$

where the average vector of $\delta\mathbf{k}$ is calculated as

$$\overline{\boldsymbol{\delta}\mathbf{k}}=\frac{1}{N_s}\sum_{i=1}^{N_s}\boldsymbol{\delta}\mathbf{k}_i\tag{2.24}$$

The orthonormal basis vectors can be found by performing a singular value decomposition (SVD) on the error matrix as

$$\mathrm{SVD}\left(\boldsymbol{\delta}\mathbf{k}_c\right)=\mathbf{U}\boldsymbol{\Sigma}\mathbf{V}^T\tag{2.25}$$

where the matrix $\mathbf{U} = [\mathbf{u_1}, \mathbf{u_2}, \ldots, \mathbf{u_{Ns}}]$ consist of orthonormal column vectors. The covariance of $\{\delta\mathbf{k}_c\}$ is calculated by utilizing the SVD components

$$\boldsymbol{\Gamma}=\left\{\boldsymbol{\delta}\mathbf{k}_c\right\}\left\{\boldsymbol{\delta}\mathbf{k}_c\right\}^T=\mathbf{U}\boldsymbol{\Sigma}\mathbf{V}^T\mathbf{V}\boldsymbol{\Sigma}\mathbf{U}^T=\mathbf{U}\boldsymbol{\Sigma}^2\mathbf{U}^T\tag{2.26}$$

where $\boldsymbol{\Sigma} = \mathrm{diag}(\sigma_{s,1},\sigma_{s,2},\sigma_{s,3}\ldots\sigma_{s,Ns})$ are the singular values arranged in descending order. Finally, the basis matrices are defined by reshaping the orthonormal column vectors back into matrices, and the unknown β_i coefficients that have a prior probability density equal to an unbiased Gaussian distribution with a covariance $\boldsymbol{\Sigma}^2$ [124,139].

Incorporating the PCA approximation of the measurement model gives

$$\begin{aligned}\mathbf{b}&=\mathbf{a}_{\text{exact}}(\mathbf{x})+\boldsymbol{\delta}\mathbf{b}_{\text{noise}}\\&=\mathbf{a}_{\text{RDG-FA}}(\mathbf{x})+[\mathbf{a}_{\text{exa}}(\mathbf{x})-\mathbf{a}_{\text{RDG-FA}}(\mathbf{x})]+\boldsymbol{\delta}\mathbf{b}_{\text{noise}}\\&\approx\mathbf{a}_{\text{RDG-FA}}(\mathbf{x})+\boldsymbol{\delta}\mathbf{a}_{\text{PCA}}(\mathbf{x},\beta)+\boldsymbol{\delta}\mathbf{b}_{\text{noise}}\end{aligned}\tag{2.27}$$

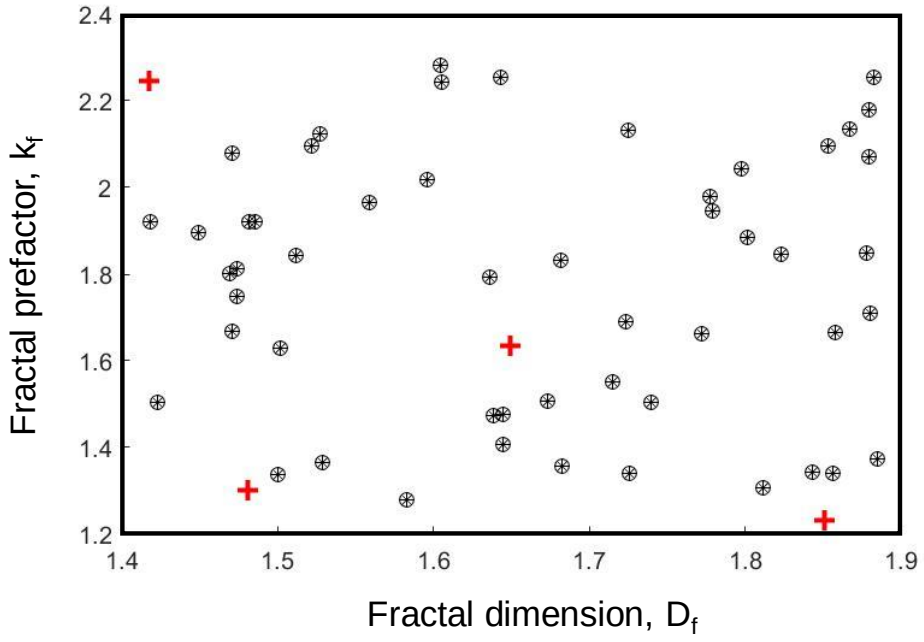

Figure 2-6 A "training set" of 62 randomly-sampled {D_f, k_f} pairs used to form the PCA basis matrices. The angular light scattering at each point found using the MSTM is averaged over 200 aggregates constructed according to the fractal parameters. The four points marked by "+" denote the test conditions used to evaluate the approximation error technique. These are excluded from the training set.

, where

$$\boldsymbol{\delta}\mathbf{a}_{\mathrm{PCA}}(\mathbf{x},\boldsymbol{\beta}) = C_{\exp}\left[\boldsymbol{\delta}\overline{\mathbf{K}} + \sum_{i=1}^{p}\beta_i\mathbf{U}_i\right]\mathbf{p}(\mathbf{x}). \tag{2.28}$$

When computing the posterior density the QoI are extended to include the unknown PCA weights, i.e. $\mathbf{x} = [\sigma_g, \mu_g, \beta_1, \beta_2, \ldots, \beta_{Ns}]^T$. The dependence of $\boldsymbol{\delta}\mathbf{a}_{\mathrm{PCA}}$ on D_f and k_f is now contained within the unknown $\{\beta\}$ coefficients, and by solving for these coefficients, the analyst is indirectly solving for the fractal parameters as well as μ_g and σ_g, although the relationship between D_f and k_f and $\{\boldsymbol{\beta}\}$ is not straightforward. The methodology can easily be extended to consider uncertainty in $\mathbf{m}_\lambda$, d_p, and other parameters.

2.6 Demonstration of the PCA technique

To demonstrate the basic concept of the PCA technique, we initially consider an "artificial" case where k_f and D_f values are perfectly known, so $\mathbf{x} = [\mu_g, \sigma_g, \boldsymbol{\beta}]^T$. We consider four different morphological parameter $\{D_f, k_f\}$ sets, indicated in Figure 2-6 with "+" signs, that are excluded from the training set used to derive the basis matrices $\{\mathbf{U}_i\}$. Synthetic MALS data is generated using $\mu_g = 90$ nm and $\sigma_g = 1.6$ using Eq. (2.8) with $\mathbf{K} = \mathbf{K}_{exact}$, and then contaminated with 2% Gaussian measurement noise, similar to Ref. [76]. (This noise is much larger than the refinement error of the trapezoidal integration scheme.) Gaussian priors having a standard deviation of 15% centered at $\boldsymbol{\mu}_{pri} = [85.5, 1.68]^T$ reflect the fact that the experimentalist may have imperfect foreknowledge of the distribution parameters.

The contour plots in Figure 2-7, each show two overlaid posterior densities: one calculated with a likelihood defined using only $\mathbf{a}_{RDG\text{-}FA}(\mathbf{x})$, and one derived with $\mathbf{a}_{RDG\text{-}FA}(\mathbf{x}) + \boldsymbol{\delta}\mathbf{a}_{PCA}(\mathbf{x},\boldsymbol{\beta})$. In both scenarios, the known values of k_f and D_f are used in the $\mathbf{a}_{RDG\text{-}FA}(\mathbf{x})$ models, while the unknown $\boldsymbol{\beta}$ parameters account for the variation in $\boldsymbol{\delta}\mathbf{a}_{PCA}$ with changes in D_f and k_f. In all cases, the posterior probability densities are narrow, but, as was the case in Figure 2-5 (*a*), the ones calculated using only $\mathbf{a}_{RDG}$ do not contain the exact solution. After applying the approximation error technique, however, the posterior distribution contains the exact point of the morphological parameters without any noticeable change to the shape of the posterior distribution, demonstrating that PCA effectively captures the RDG-FA model error without introducing any considerable computation power demand in the process of solving for posterior distribution using the more accurate MSTM method, beyond the one-time "overhead" needed to define $\boldsymbol{\delta}\overline{\mathbf{K}}$ and $\mathbf{U}$ in Eq. (2.21).

In reality, however, the fractal parameters will likely be imperfectly known at best, in which case they can be added to the parameters to be inferred, $\mathbf{x} = [\mu_g, \sigma_g, k_f, D_f]^T$. The exact solution is generated through Eq. (2.8) using $\sigma_g = 1.6$, $\mu_g = 90$ nm, $D_f = 1.60$, and $k_f = 2.28$. Since the experimentalist is likely to have some foreknowledge of these parameters based on previous experiments, TEM analysis, etc., we represent this knowledge with Gaussian priors centered at $\boldsymbol{\mu}_{pri} = [1.68, 85.5, 2.23, 1.64]^T$ with standard deviations of 15% all three parameters. The marginalized posterior probability distributions found using $\mathbf{a}_{RDG\text{-}FA}(\mathbf{x})$ and $\mathbf{a}_{RDG\text{-}FA}(\mathbf{x}) + \boldsymbol{\delta}\mathbf{a}_{PCA}(\mathbf{x}, \boldsymbol{\beta})$ are shown in Figure 2-8 (a) and (*b*) and Table 2-2. Defining the likelihood using $\boldsymbol{\delta}\mathbf{a}_{PCA}(\mathbf{x})$ by itself provides narrower distribution widths, but the exact solutions for μ_g, σ_g, and D_f are not contained within the 90% credibility intervals. Including the PCA correction increases the distribution widths due to the increased number of degrees-of-freedom (i.e. solving for the β coefficients), but the 90% credibility intervals now include the exact solution. The procedure was repeated 20 times using different random Gaussian noise $\boldsymbol{\delta}\mathbf{b}_{noise}$, and $\mathbf{x}_{exact}$ was always included in the 90% credibility intervals.

The effectiveness of the PCA error approximation can also be seen by inspecting the structure of the error. As discussed above, approximating the model error using unbiased white noise is the worst-case scenario, and represents "maximum information entropy"; it provides no information about the error beyond a rough estimate of its size, which one could obtain from literature studies that compare RDG-FA and MSTM predictions under a range of conditions. On the contrary, the model error calculated for a particular $\{D_f, k_f\}$ pair through the PCA approach in Eq. (2.21) is approximated by adding a fixed mean error to the sum of coefficients multiplied by basis matrices, where the basis matrices $\{\mathbf{U}_i|\}$contain the main portion of information for the covariance of the model error, $\mathbf{\Gamma}_{model}$. This makes the $\boldsymbol{\beta}$ estimation a major factor in the overall error estimate. Figure 2-9 shows the recovered β_i coefficients for $\{D_f, k_f\} = \{1.64, 1.63\}$, Figure 2-7 (d). This plot shows that only eight PCA modes (nontrivial β values) are needed to reconstruct the error. Figure 2-10 shows how the approximated error approaches the true structure factor error, $S_{exact}-S_{RDG\text{-}FA}$, as consecutive PCA summation terms are added to the mean error.

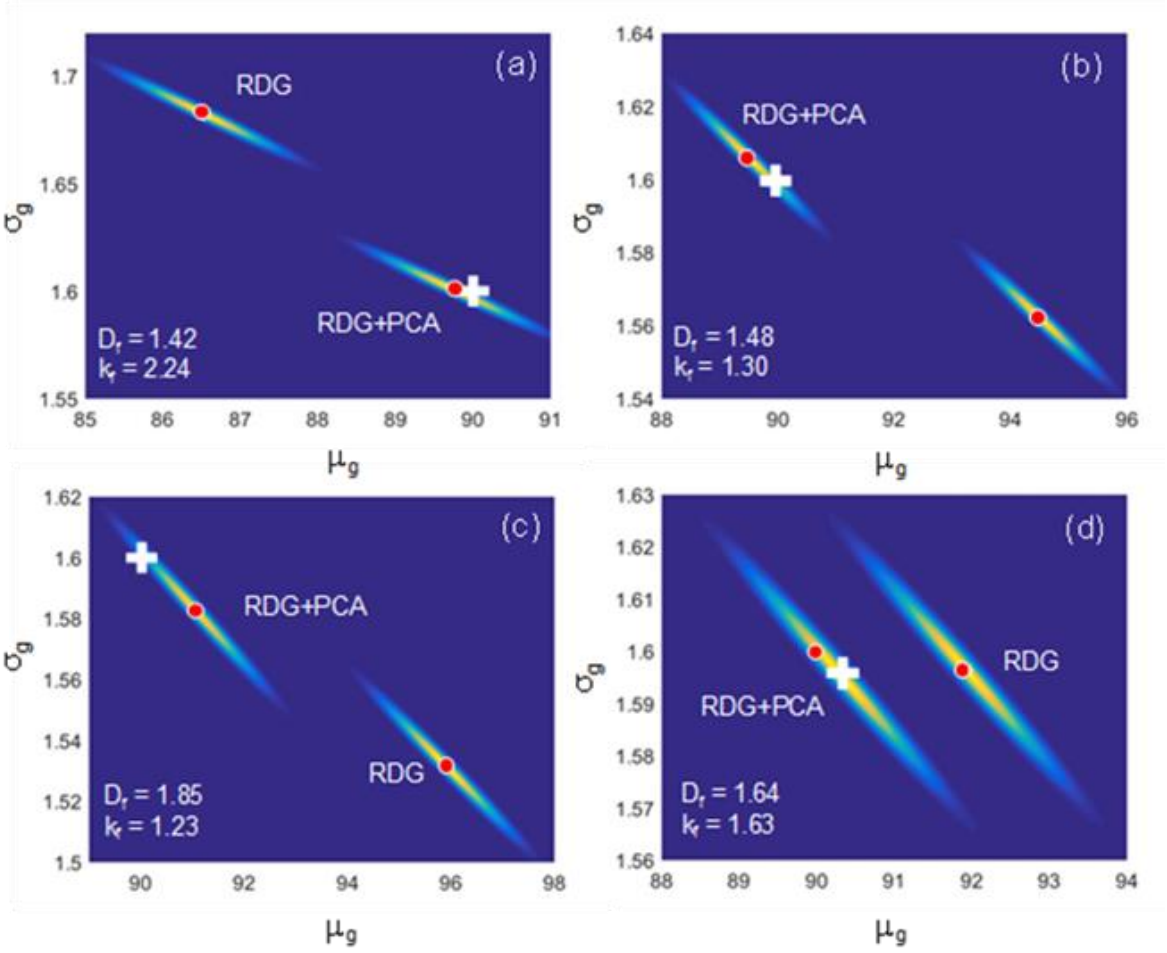

Figure 2-7 Posterior distributions calculated for four different {k_f, D_f} sets with and without the PCA correction/approximation error technique. Exact solution is shown with "+", and MAP estimates are red circles. In all cases, the MAP estimate obtained using the approximation error technique is close to the exact solution, while ignoring the RDG-FA model error produces a large bias. (Note the change in axes limits).

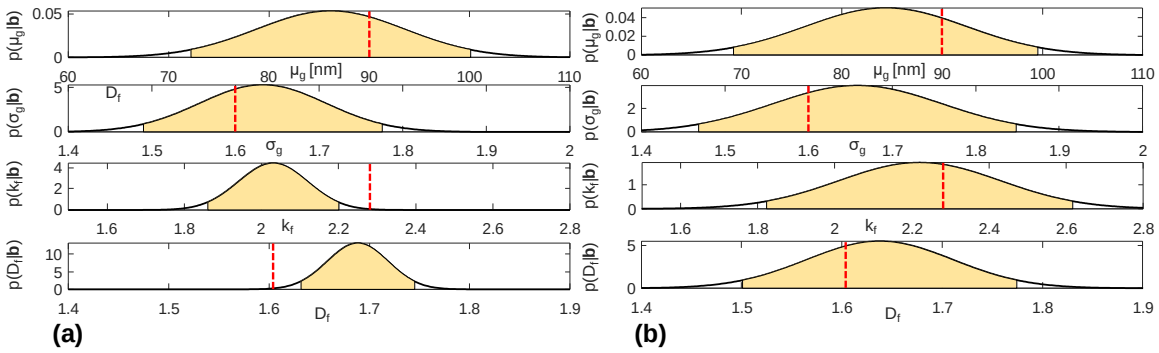

Figure 2-8 Marginalized probability distributions for μ_g, σ_g, k_f, and D_f, found using a Gaussian prior centered at $\boldsymbol{\mu}_{pri}$ = [1.68, 85.5, 2.23, 1.64]^T with standard deviations of 15%. The red line is the exact solution, and the shaded areas are 90% credibility intervals. (a) Using only $\mathbf{a}_{RDG\text{-}FA}(\mathbf{x})$ to define the likelihood results in a biased outcome. (b) Using $\mathbf{a}_{RDG\text{-}FA}(\mathbf{x}) + \boldsymbol{\delta}\mathbf{a}_{PCA}(\mathbf{x},\boldsymbol{\beta})$ gives wider posterior densities, but with less bias.

Table 2-2 90% credibility intervals for the posterior density shown in Figure 2-7 with and without PCA treatment.

	RDG-FA	RDG-FA + PCA	Exact Point
$\mu_{g,90\%}$ [nm]	86.14 ± 14.00	84.38 ± 15.21	90
$\sigma_{g,90\%}$	1.63 ± 0.14	1.66 ± 0.19	1.6
K_f	2.03 ± 0.17	2.22 ± 0.40	2.28
D_f	1.69 ± 0.06	1.64 ± 0.14	1.60

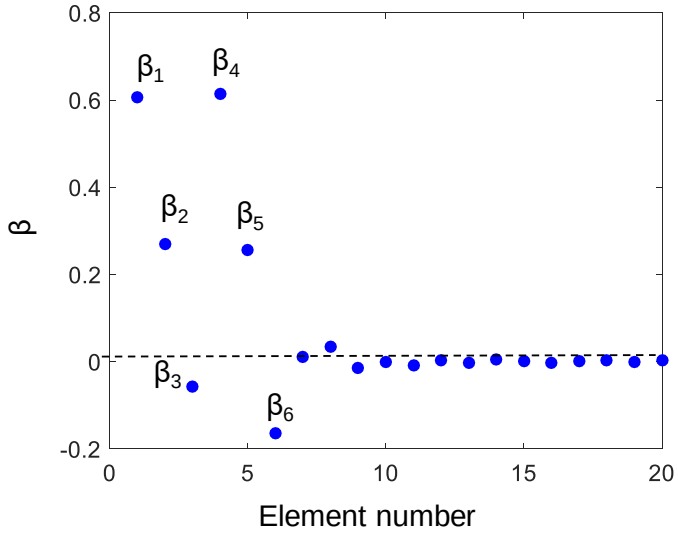

Figure 2-9 Twenty initial β coefficients solved for D_f = 1.64, k_f = 1.63, corresponding to Figure 2-7 (d). The results show that only the first eight PCA modes are needed to model the error.

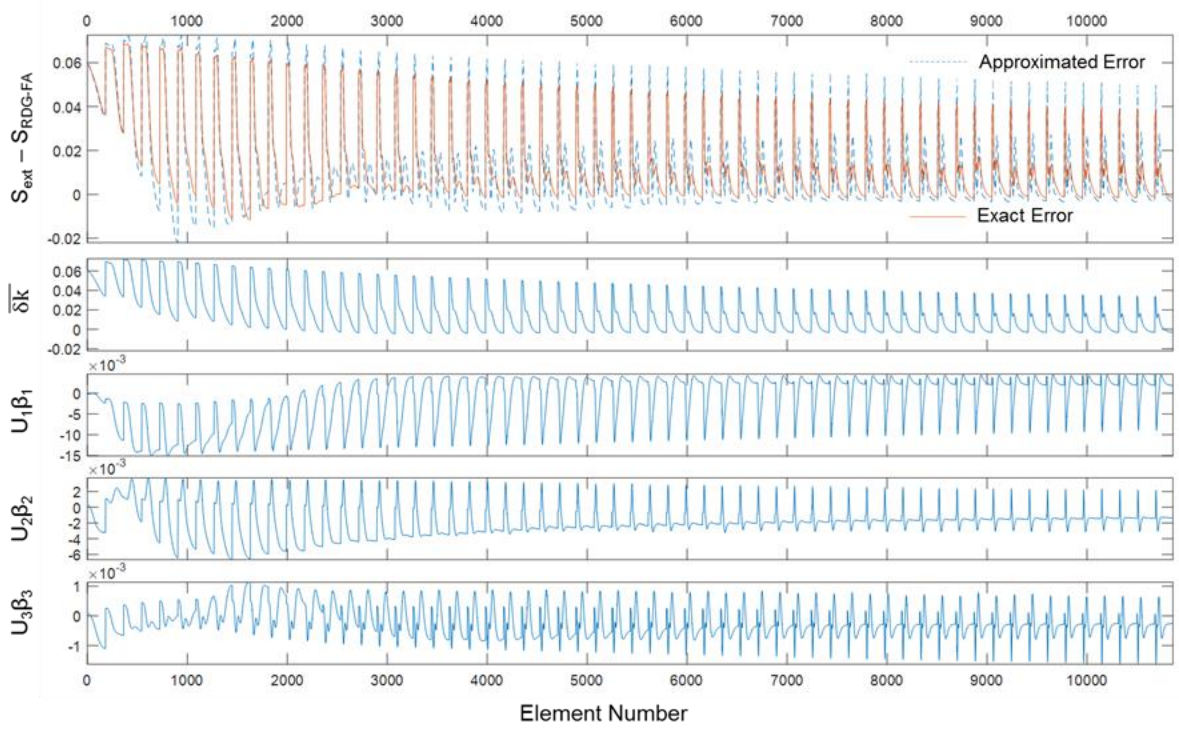

Figure 2-10 RDG-FA kernel error and approximated error through PCA. The kernel error is show in vectorized format. The averaged mean and initial three Uiβi are shown.

2.7 Conclusions

Multi-angle light scattering presents a promising technique for determining the size distribution and ancillary properties of aerosolized nanoaggregate, such as soot. The underlying problem is ill-posed, however, which sensitizes the inferred parameters to small errors in the data. While attention has focused mainly on the impact of measurement noise on the recovered solution parameters, the model error arising from Rayleigh-Debye-Gans Fractal-Aggregate theory introduces a significant bias in the recovered parameters. More accurate models, like the MSTM method, are too computationally-expensive to incorporate directly into the inference procedure. In principle, it is also possible to "mask" the RDG-FA model error with white noise, but this significantly increases the uncertainty in the recovered parameters.

The approximation error technique combines the computational efficiency of the RDG-FA technique with the accuracy of the MSTM method. This method builds a statistical (Gaussian) model of the model error by sampling the difference between the low order (RDG-FA) and high order (MSTM) schemes. Because of the high dimensionality of the problem and the computational expense of the MSTM method, the number of samples required to generate a "look-up table" for the model error over all the model parameters would be computationally-prohibitive. Instead, in this thesis, a small number of fractal parameter pairs are randomly-sampled over the range typical for soot aggregates, and the influence of these parameters on the scattering kernel is simulated through principal component analysis. The resulting measurement model consists of the RDG-FA scattering kernel, plus a second term that includes the unknown PCA coefficients that account for the uncertain fractal parameters. Bayesian inference is then used to recover the unknown parameters. While the posterior probability densities obtained through the approximation error technique are wider than those found using RDG-FA, the estimates are much less biased. Moreover, by accounting for the deterministic structure of the model error, the posterior probability densities found using the approximation error technique are far narrower than would be obtained by merely masking the model error with white noise. Aside from the one-time burden of computing the mean error and PCA basis, the computational effort required to carry out the Bayesian inference for the approximation error technique is virtually identical to that of ordinary RDG-FA, which is particularly attractive for applications involving real-time online analysis of light scattering.

While this chapter considered uncertain aggregate fractal parameters, in principle, it is straightforward to extend it to other model parameters, such as the primary particle diameter and the

complex index of refraction. Using a larger sample population to generate the PCA basis would also improve the accuracy of this approach.

Although the error approximation technique can function with increasing the model parameters, including the primary particle size in the inference process of MALS will increase the degree of the freedom of the ill-posed problem and consequently, the credibility intervals will be wider even in the case of a perfect model approximation.

Chapter 3
Artificial neural network for inferring soot morphology through multi-angle light scattering

The content of this chapter is an extension of an article accepted for publication in the *Journal of Quantitative Spectroscopy and Radiative Transfer* (JQSRT) entitled "Inferring soot morphology through multi-angle light scattering using an artificial neural network."

3.1 Introduction

In *Chapter 2* the applicability of Rayleigh-Debye-Gans fractal aggregate (RDG-FA) to multi-angle light scattering (MALS) problems is investigated. RDG-FA theory is based on the assumption that each primary particle scatters in the Rayleigh limit of Mie theory, and multiple scattering between the primary particles and scattering arising from self-interaction are neglected [23,118,120,129]. This approach is closed-form and computationally-efficient compared to MSTM and depends only on a set of morphological parameters, rather than a particular aggregate configuration. However, RDG-FA predictions can be expected to have errors of around 30% for typical soot aggregates [23,90,91,130], depending on the scattering angle, aggregate morphology, and bulk radiative properties of soot. The RDG-FA model error is manageable when predicting angular light scattering from an aerosol of well-characterized soot aggregates, but when light scattering data is used to infer aggregate size and morphology, the ill-posed nature of Eq. (1.6) amplifies small amounts of model error into significant variations in the inferred parameters. *Chapter 2* investigated an error approximation technique based on principal component analysis (PCA) to correct the RDG-FA model. And the Bayesian inference is used to find posterior PDFs for the lognormal size distribution and fractal morphological parameters. This is referred to as the *Bayesian/AE (Approximation Error)* approach in this chapter.

Alternatively, the quantities in **x** can be inferred directly using a multi-layer feed-forward artificial neural network (ANN) to invert Eq. (1.6) and then find parameters of interest from vector **b**. The ANN is developed through a training procedure using sampled high-order modeled data, e.g. from MSTM or DDA; although the training time might be significant, once the training is completed, the measurement model can be evaluated very quickly. Ulanowski et al. used neural networks to recover the size and refractive index of homogeneous spheres from angular light scattering measurements [140], while Ishimaru et al. [141] inferred the size distribution of spheres from single-angle backscattering measurements at three wavelengths. Both studies use the ANN as a regression tool, where the ANN takes the scattering measurements in **b** as an input and provides a single vector **x** as an output. While this approach is straightforward, it has two principal drawbacks: it does not provide an uncertainty estimate for **x**, and the prior information must be considered in the training process; therefore, if the prior information changes, the ANN must be retrained.

On the other hand, it is possible to approximate the MSTM kernel directly and then use this approximate model inside the Bayesian inference. Ericok et al. [142] approximated the MSTM kernel by applying the principles of supervised learning and design of experiments to build a surrogate model for estimating the optical properties of aggregates. Alternatively, an ANN can be used to approximate k. The ANN kernel as a black-box model is then incorporated into the Bayesian inference procedure to find $p(\mathbf{x}|\mathbf{b})$. In this scheme, the ANN is trained to approximate the light scattering kernel using the most accurate physical approximation (in this thesis MSTM solution) of the kernel and the prior information can be used to add information to the problem through Bayes' equation, cf. Eq. (2.1). This is referred to as the *Bayesian/ANN approach* throughout this thesis. The advantage of this method over previous approaches is that the ANN is not dependent on prior information, and uncertainty bounds can be defined over **x**.

In this chapter, candidate ANN structures are evaluated, and the effectiveness of the ANN approach to approximate the light scattering kernel is investigated. The Bayesian/ANN and Bayesian/AE approaches then are compared in a numerical study. The numerical study shows that Bayesian/ANN outperforms the Bayesian/AE in both accuracy and certainty in the credibility intervals regardless of the number of training samples, and the ANN approximation of the scattering kernel has less than 5% relative error over all scattering angles. Finally, the Bayesian/ANN method is used to predict in-flame soot morphology using data obtained from wide-angle light scattering (WALS [62,76,77]). In some cases the inferred credibility intervals for D_f and k_f contained values inferred from the TEM images. However, the inferred size distribution in all validation cases is smaller than the TEM

results. The measurement phenomenon can be due to remaining model error such as uncertainty in the refractive index of soot and ignoring its variation with measurement conditions; error in the algorithm used to simulate soot-like aggregates; approximating the primary particles as monodisperse and ignoring necking and sintering phenomenon in the aggregates.

3.2 Wide-angle light scattering measurements

While the techniques presented in this thesis can be applied to any multi-angle light scattering apparatus discussed in Section 1.1.1, we focus on the wide-angle light scattering (WALS) apparatus [62,76,77]. In this instrument, shown schematically in Figure 1-4, the aerosol is irradiated with a frequency-doubled continuous-wave ND:YVO_4 laser (CNI MLL-FN-532 DPSS laser, 532 nm, 1.5 W) with a beam diameter of about 500 μm; the beam is vertically polarized by a polarizing prism. The scattered light from the probe volume is imaged onto a secondary focal point using an elliptical mirror and subsequently imaged onto a charge-coupled device (CCD) camera (Allied vision technologies GmbH, Pike F-100B). A measurement resolution of less than 1° is possible, but for computational efficiency, the data is downsampled to a resolution of 2°. Measurement noise is often reduced through multi-shot averaging, in the case of a stable aerosol.

3.3 Artificial neural network

Feed-forward artificial neural networks (ANN) are ubiquitous due to their flexibility, excellent representational capabilities, and availability of a large number of training algorithms [143,144]. Once they are trained, they provide near-instantaneous solutions. Accordingly, while the fidelity of physics-based models must be sacrificed to achieve a computationally-efficient solution when they are used directly in inference problems, ANNs can avoid this compromise by "front-loading" the computational burden to a one-time training period, potentially reducing the model error.

Figure 3-1 shows an example of a feed-forward fully-connected ANN in which the network takes the input vector of $\mathbf{I} \in \mathbb{R}^{\zeta \times 1}$ and provides the output vector $\mathbf{O} \in \mathbb{R}^{\alpha \times 1}$, where ζ and α are the numbers of input and output elements. The input layer (L_{in}) units are used only to hold input values and to distribute these values to units in the next layer; thus, they do not implement a separate mapping or conversion of the input data and do not hold a function, bias, or weight [143]. The network can have an

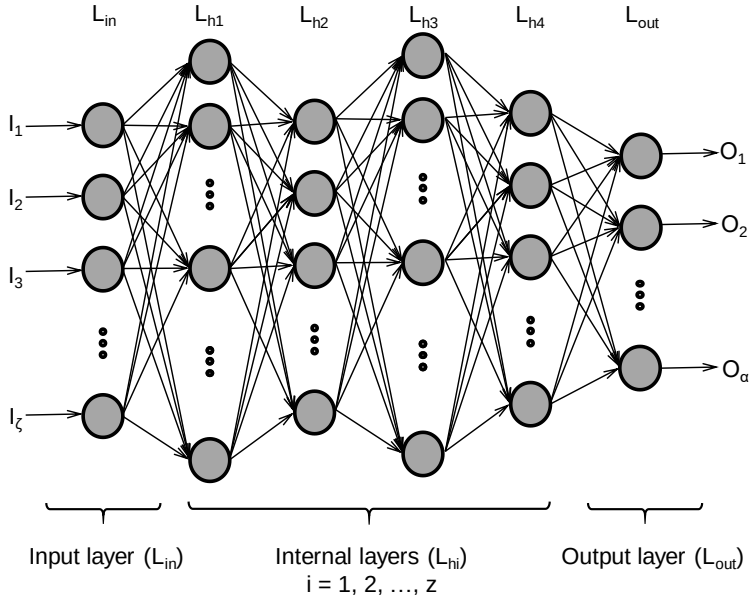

Figure 3-1 Structure of a sample feed-forward fully-connected ANN used in this work. The input layer (L_{in}) takes the input vector $\mathbf{I} \in \mathbb{R}^{\zeta \times 1}$ and the output layer (L_{out}) provides the output vector $\mathbf{O} \in \mathbb{R}^{\alpha \times 1}$. The internal layers start from L_{h_1} to L_{h_z} (z = 4 in this example but can be any positive integer) is fully connected to the next adjacent layer.

arbitrary number of internal layers ($z \geq 1$). The information in the network flows from the input, through successive layers, to the output. Each layer, based on its input, computes an output vector, and the information propagates to the next layer. In this chapter, L_{h_j} denotes the j^{th} internal layer, which can have an arbitrary number of nodes as shown by a superscript inside the parenthesis. Following the notation in Ref. [144], a hypothetical ANN that takes four input elements and provides two output elements and has two internal layers that each contain three and five neurons is shown as $L_{in}^{(4)} \times L_{h_1}^{(3)} \times L_{h_2}^{(5)} \times L_{out}^{(2)}$.

The mathematical characterization of a multilayer ANN network is a combined application of functions. Each of these functions represents a particular layer and may be specific to individual units in the layer. Each neuron receives a signal that is a linearly weighted sum of all the outputs from the neurons of the former layer. The output vector of the ANN as a function of the input vector can be written as

$$\mathbf{O} = \mathbf{f}^{L_{out}}\left(\mathbf{f}^{L_{h_w}} \cdots \left(\mathbf{f}^{L_{h_1}}(\mathbf{I})\cdots\right)\right). \tag{3.1}$$

In this chapter, a hyperbolic tangent transfer function [145] is used to model all internal layers neurons, and a linear transform function is used to the output layer to allow the node to send out the weighted sum itself.

The weights and biases of the ANN nodes are found through a training procedure. A cost function defined using the residual between the output vector and training data is minimized using the scaled conjugate gradient descent algorithm [146]. The training set is divided into three parts: (*i*) 75% of samples are "training data", which form the cost function; (*ii*) 10% is used to validate and assess network generalization, and to halt training when generalization stops improving; (*iii*) and the remaining 15% is used for testing (cross-validation), and have no effect on training to provide independent measure of network performance during and after training. If testing is not required, the testing samples are added to the training set.

While it is straightforward to train an ANN to find **x** as a function of **b**, this method does not provide uncertainty over the **x** parameters. Moreover, in this formulation, the prior information must be included in the training set. Therefore, if the prior information changes, the ANN would need to be retrained, which is a time-consuming process.

To overcome these drawbacks, we generate an ANN model for the light scattering kernel, $k(\theta, R_g, \mathbf{\Phi})$, which is then incorporated into the Bayesian inference algorithm. Therefore, ANN is independent of prior information on the QoI. The implemented ANN structure is shown in Figure 3-2. A separate ANN is trained for $N_p = 5, 10, 15, \ldots, 545$, each of which corresponds to one column of the $\mathbf{K}(R_g, \theta, \mathbf{\Phi})$ matrix in Eq. (2.9). Training vectors are generated using MSTM simulations on CCA-generated aggregates drawn from $D_f \sim \mathcal{U}(1.4, 1.9)$[1] and $k_f \sim \mathcal{U}(1.2, 3.0)$ and a fixed $\mathbf{m}_\lambda$, d_p and N_p over a finite set of angles $\boldsymbol{\theta} = [10°, 12°, \ldots, 160°]^T$. The ANN structure and training scheme used for training the ANN for different N_p values are identical. Training is stopped once the generalization stops improving, or when the number of epochs (the number of times the training vectors have passed through the learning algorithm) reaches 10^3.

The ANN structure (i.e. the number of hidden layers and nodes for each layer) must be chosen so that it can accurately represent the light scattering kernel without over-fitting. This depends on both the number of training samples and N_p. For large N_p the kernel becomes increasingly nonlinear due to a higher phase shift parameter, in which case a large number of neurons or additional layers may be

[1] $\mathcal{U}$ denotes a uniform probability density.

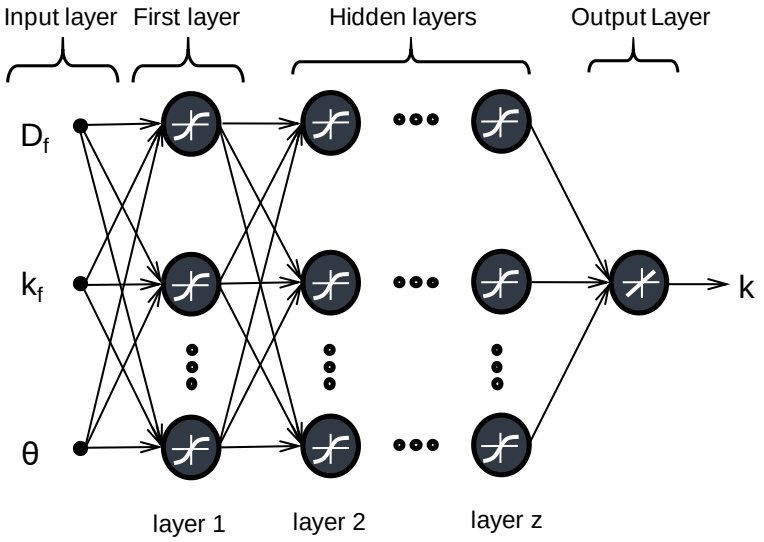

Figure 3-2 Schematic of the ANN used in this work. The inputs are D_f, k_f and θ, and the output values are the light scattering kernel evaluated at discrete R_g. This network is trained for discrete values of N_p and $\mathbf{\Phi}$ to approximate the complete light scattering kernel $\mathbf{K}(R_g, \theta, \mathbf{\Phi})$ in Eq. (2.9). A hyperbolic tangent transfer function [145] is used for all layers except the output and input layers. The output layer is modeled with a linear transform function, and the input layer acts as a holder for the input parameters.

needed, but using an ANN with too many degrees-of-freedom risks over-fitting errors. We evaluated several candidate ANN structures using various numbers of training samples; after each training period, the mean-squared error of the 15% test samples is calculated and compared as an independent test of the network performance. We repeated this procedure for training sample sets of 200, 1,400 and 2,700 consisting of randomly drawn values of $\{D_f, k_f\}$. In all cases, $d_p = 30$ nm and an equal number of neurons are considered on each layer. Figure 3-3 shows that ANN performance initially improves dramatically as the number of neurons approaches 6, but for large numbers of neurons, the performance deteriorates gradually, suggesting an overfitting region.

Moreover, the network shows a better performance for a higher number of $\{D_f, k_f\}$ training samples and lower N_p values. The results suggest that the best performance is achieved using 2 or 3 layers and between 7 to 14 neurons in each layer. In this study, we chose an ANN with two layers and each layer with 12 neurons for all different values of N_p. Therefore, the implemented ANN structure is $L_{in}^{(3)} \times L_{h_1}^{(12)} \times L_{h_2}^{(12)} \times L_{out}^{(1)}$ which takes a set $\{\theta, D_f, k_f\}$ as inputs and provides the output $\{k\}$. It should be noted that, while we only considered ANNs that have the same number of neurons per layer, it is also possible to vary the number of neurons in each layer. Also, in principle, instead of generating one ANN for each N_p, one could derive a single ANN that accepts inputs of $\{\theta, N_p, D_f, k_f\}$, but this would

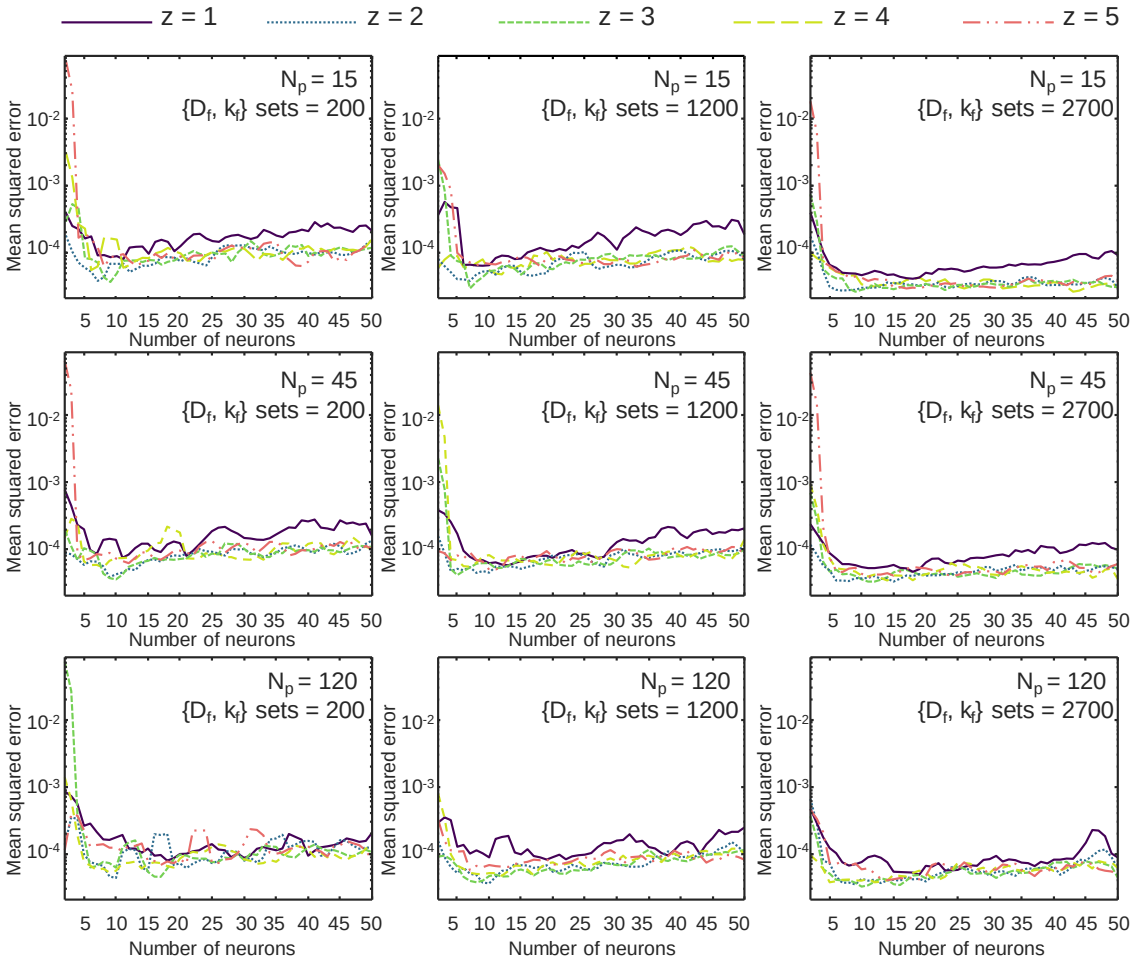

Figure 3-3 Mean squared error of the ANN on 15% of the test samples as a function of the number of internal layers, *z*, and the number of neurons per layer. The simulation is performed on three different numbers of primary particles and three different-sized training sets of {D_f, k_f}.

dramatically increase the size of the training samples, resulting in considerable memory overhead for batch mode training which limits the possibility of using a graphical processing unit for training. One could also include d_p or even $\mathbf{m}_\lambda$ as an input parameter to the ANN instead of treating these values as perfectly-known. A more rigorous study of the optimum ANN structure is required in the future.

Figure 3-4 compares the outcome of the ANN and RDG-FA approximations to the MSTM solution. The training set consisted of 1,500 samples of {D_f, k_f}, d_p = 30 nm and $\mathbf{m}_\lambda$ = 1.6 + 0.6i. The {D_f, k_f} pairs used to calculate the relative error are excluded from the ANN training set. Also, due to the structure of the measurement noise, measurements at smaller scattering angles have the greatest influence on the inferred parameters. The results demonstrate that the ANN accurately reproduces the

MSTM solution; for $\theta < 110°$ the ANN relative error was always below 3% and for $\theta \geq 110°$ the error was below 5% in most instances.

Next, the capability of the ANN to extrapolate over its training range is studied. Oh and Sorensen [147] have investigated the effect of overlap between primary particles on the fractal properties, concluding that D_f and particularly k_f may vary considerably with the rate of overlapping. Inferring k_f is particularly challenging if the aggregate size distribution is narrow [148], as evidenced by the wide range of reported fractal prefactors in the literature. The range chosen for the training samples is $1.2 \leq k_f \leq 3.0$, and k_f values higher than 3.0 have been reported in some studies [149]. The ANN capability for extrapolating over its training range is shown in Figure 3-5. For the case of $k_f = 3.18$ the relative error of the kernel is below 7% for all θ and N_p values and below 6% for $\theta \leq 60°$. Therefore, the ANN has the capability of extrapolating over its training range to some degree, particularly for small N_p and θ values.

3.4 Results and discussion

In principle, both the ANN kernel model and the PCA-based approximation error technique introduced in *Chapter 2* can mitigate the impact of model error on the posterior covariance. Initially, the performance of these techniques is assessed and compared using simulated MALS data, in terms of the accuracy of the MAP estimate and the size of the credible intervals. In the case of the Bayesian/AE approach, additional $\boldsymbol{\beta}$ parameters (unbiased stochastic coefficients in Eq. (2.21)) are inferred alongside the QoI as nuisance parameters (parameters of the measurement model that are not the focus of the study.) If we assume D_f and k_f to be perfectly known, the inferred parameters are $\mathbf{x} = [\mu_g, \sigma_g, \beta_1, \beta_2, \ldots, \beta_p]^T$. Previously, it was shown that the Bayesian/AE approach is highly effective when D_f and k_f are assumed deterministic. However, D_f and k_f can also be treated as stochastic parameters to be inferred from the measurements, which is a more reasonable scenario considering that the fractal parameters are not generally known in the absence of detailed electron microscopy data. When D_f and k_f are treated as stochastic variables with prior densities the credibility intervals become wider [122]. This is because the $\mathbf{U}_i$ basis are derived assuming $\{D_f, k_f\}$ as fixed variables; however in the solution they are treated as random variables, so the modeled kernel is incompatible with the physical data. Also, the previous study did not examine how the $\{D_f, k_f\}$ sample size affects the accuracy of the MAP estimate and credible interval width. In this thesis, we show that increasing the number of $\{D_f, k_f\}$ samples increases

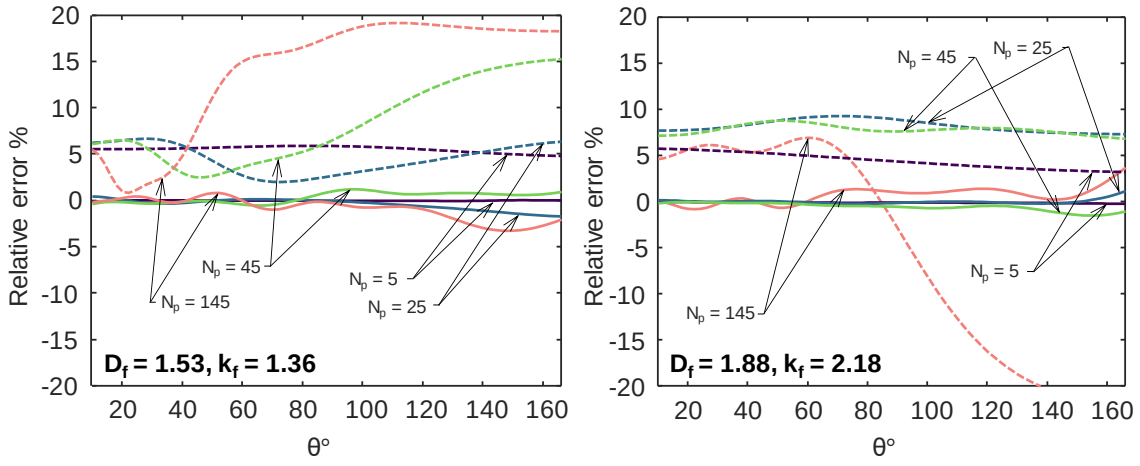

Figure 3-4 Relative error in the light scattering kernels predicted using the ANN (solid lines) and RDG-FA (dashed lines) compared to the MSTM solution for different number of primary particles (N_p) and two different {D_f, k_f} pairs.

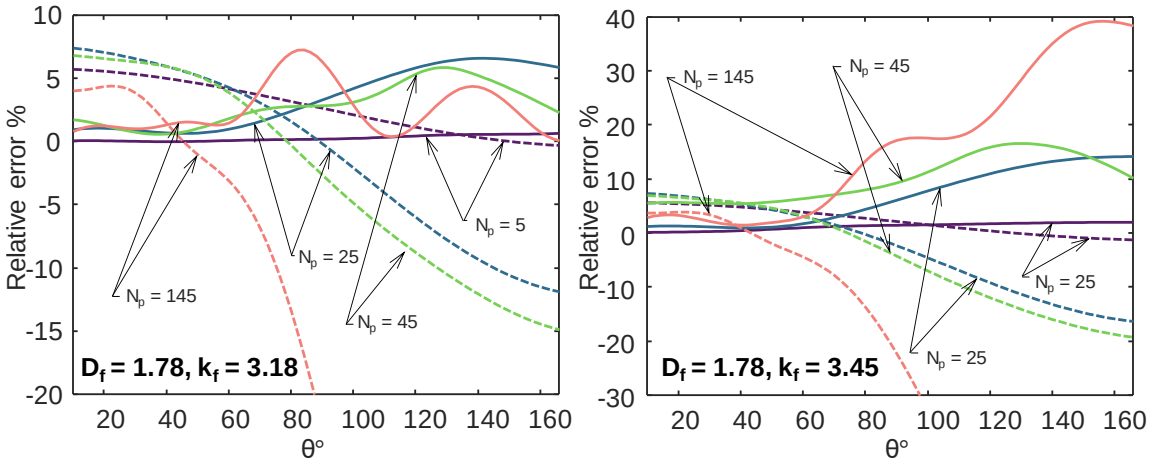

Figure 3-5 Relative error in the light scattering kernels predicted using the ANN (solid lines) and RDG-FA (dashed lines) compared to the MSTM solution for different number of primary particles (N_p) and two different {D_f, k_f} pairs. Fractal prefactor training range was from $k_f \sim \mathcal{U}(1.2, 3.0)$, therefore, the ANN is extrapolating the training set.

the accuracy of $\mathbf{U}_i$ bases and lowers kernel approximation error, but also increases the number of unknown β_i variables and consequently may increase the widths of the QoI credible intervals. These drawbacks do not apply to the ANN approach as increasing {D_f, k_f} samples will improve the training of the ANN (if the network structure is chosen correctly) and consequently reduce the kernel approximation error.

3.4.1 Demonstration on synthetic data

The performances of the Bayesian/AE and Bayesian/ANN algorithms are evaluated using simulated data generated using $\mathbf{x}_{exact} = [\mu_g, \sigma_g, k_f, D_f]^T = [90, 1.6, 1.52, 1.67]^T$, $\mathbf{m}_\lambda = 1.6 + 0.6i$ and $d_p = 30$ nm using the MSTM approach. The χ_{exp} term is excluded from the inference by assuming it to be perfectly known. The simulated data $\mathbf{b} = \mathbf{a}(\mathbf{x}_{exact})$ is contaminated with 2% random normal noise, and an identical noise structure is assumed for both algorithms. In the inversion process, $\mathbf{m}_\lambda = 1.6 + 0.6i$ and $d_p = 30$ nm are assumed and identical Gaussian priors having a standard deviation of 15% centered at $\boldsymbol{\mu}_{pri} = [\mu_{g,pri}, \sigma_{g,pri}, k_{f,pri}, D_{f,pri}]^T = [81, 1.76, 1.44, 1.74]^T$ over $\mathbf{x}$ is assumed for both Bayesian/AE and Bayesian/ANN. The exact $\{k_f, D_f\}$ sample is excluded from both the ANN and PCA training sets to avoid an inverse crime [150].

While the Bayesian/AE method requires the assumption of Gaussian PDFs (i.e. a linearized measurement model about $\mathbf{x}_{MAP}$) [133], the Bayesian/ANN method has no such restrictions, and the credibility intervals are calculated using MCMC [151]. While the posterior of the analytical solution is convex due to the linear measurement model, Eq. (1.6), the kernel approximation makes the posterior nonconvex as evidenced by artificial local minima in the credibility intervals. Therefore, the MAP is found using a hybrid minimization scheme: the negative log posterior is initially minimized using a genetic algorithm (GA), which acts as an initial point for an interior-point method algorithm. Equation (2.17) is then used to calculate marginalized probability densities.

The credibility intervals and MAP estimates are shown in Figure 3-6. The Bayesian/ANN approach outperforms the Bayesian/AE method both in terms of accuracy of the $\mathbf{x}_{MAP}$ and the width of the marginalized credibility intervals for all training samples. In the case of Bayesian/AE, as the number of training samples increases, the accuracy of the MAP estimate improves, especially for D_f and k_f. However, the 90% uncertainty interval also increases, as the number of inferred β_i coefficients is equal to the number of training samples.

In the case of Bayesian/ANN, both the accuracy of the MAP estimate and the width of the credibility intervals (considering all variables) improve as the number of training samples increases from 100 to 500, although precise estimates can be obtained using only 200 samples. The total performance (considering all four variables) is almost identical for 500 and 1000 samples. The superior performance of the Bayesian/ANN method is for two reasons: first, the higher degrees-of-freedom in the ANN method allows it to better approximate the kernel; and second, the Bayesian/AE method requires the presumption of normal distributions for the QoI due to very high number of inferred

parameters (due to presence of β_i coefficients), which is not correct because the measurement model is nonlinear.

Figure 3-7 shows the relative error of the PCA and ANN kernel approximations at the MAP for four different N_p values, as a function of the number of training samples. In the case of Bayesian/AE, once $\mathbf{x}_{MAP}$ is identified (including the β_i coefficients), an approximated kernel can be found through Eq. (2.21). The relative error of the ANN approximation is below 3% overall scattering angles and increases as N_p increases, which can be due to an increase in the nonlinearity of k for higher N_p. In contrast, the PCA kernel accurately models the light scattering kernel for low θ values but is subject to more substantial errors at larger scattering angles. These results imply that the kernel approximation is a significant contributor to the relative error of the MAP estimate in Figure 3-7.

In the above analysis, the only model error comes from the kernel approximation, which is mitigated through AE modeling or training the ANN, and both scenarios presume perfectly known d_p and $\mathbf{m}_\lambda$ values. A more realistic scenario is found by generating the AE or ANN using values of $\mathbf{m}_\lambda = 1.6 + 0.6i$ and $d_p = 30$ nm by MSTM solution, and then generating the measurement vector $\mathbf{b}$ using $\mathbf{m}_\lambda = 1.4 + 0.8i$ (another possible value for refractive index of soot [152]) and $d_p = 25$ nm. The number of training samples is 500, and the priors are the same as the previous study. The credibility intervals over parameters of interest are shown in Figure 3-8. Compared to the results in Figure 3-6 (with 500 training samples), the accuracy of the MAP estimate for both Bayesian/ANN and Bayesian/AE approaches deteriorates. Also, new local minimums emerge in the credibility intervals for Bayesian/ANN due to additional model error. The uncertainty for both Bayesian/ANN and Bayesian/AE methods changes insignificantly with increasing the model error.

3.4.2 Demonstration on WALS measurements

It is shown that an ANN can accurately model the light scattering kernel, as long as the training samples accurately represent the soot-laden aerosol. Accordingly, the Bayesian/ANN technique should provide accurate MAP estimates for the QoI, along with credible intervals that reflect the uncertainty introduced by the measurement noise and inherent uncertainty in the parameters. However, the analysis also shows that the ill-posedness of the measurement equation, caused by the smoothing action of the kernel in Eq. (1.6), amplifies small perturbations in the problem (measurement noise *and* model error) into significant variations in the QoI. Thus, the inference procedure will be less effective when considering

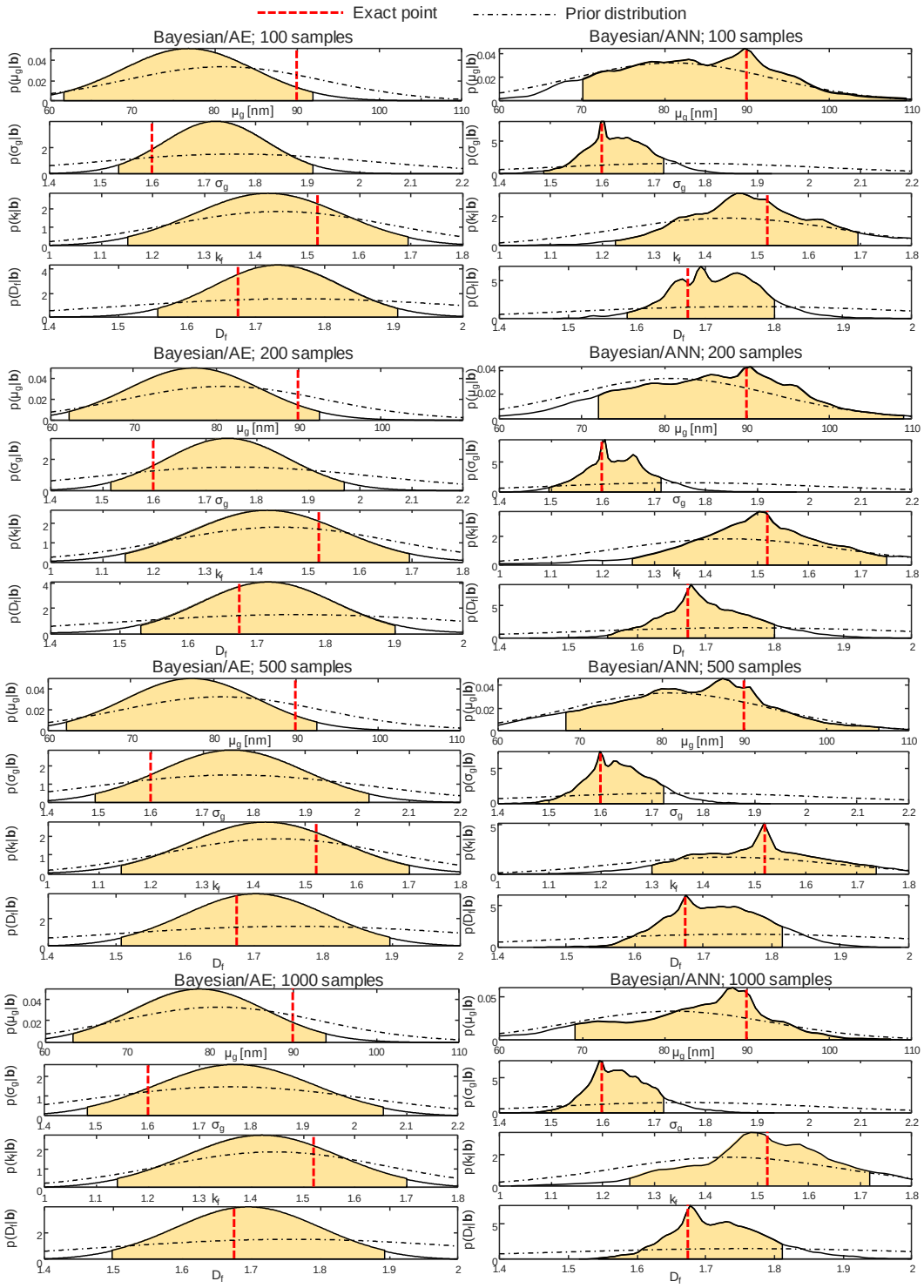

Figure 3-6 Comparing Bayesian/AE and Bayesian/ANN predictions for a different number of training samples. Identical **b** vector, training samples, and prior information are used in both approaches. Shaded areas are 90% credibility intervals.

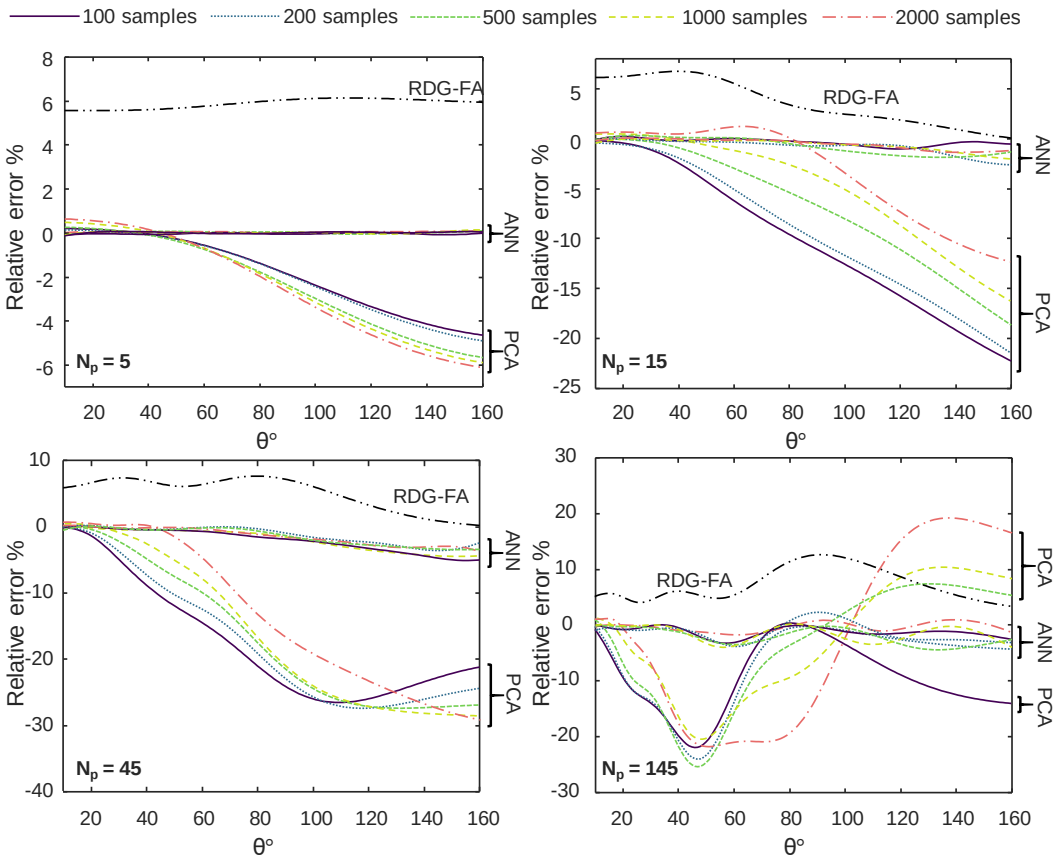

Figure 3-7 The relative error of PCA (used inside Bayesian/AE), RDG-FA and ANN scattering kernels compared to the exact (MSTM) solution as a function of the number of training samples. The PCA-derived kernel is estimated using the MAP estimate from Figure 3-6.

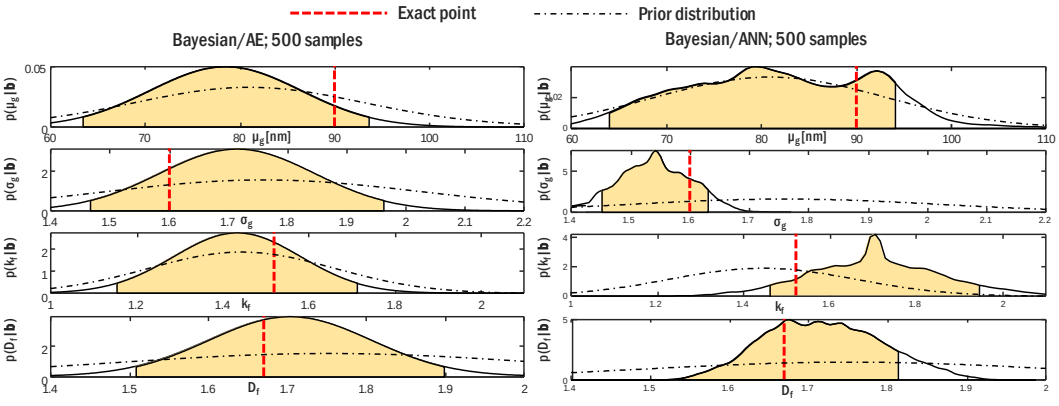

Figure 3-8 Comparing Bayesian/AE and Bayesian/ANN predictions. The same **b** vector, training samples, and prior information are used in both approaches. Shaded areas are 90% credibility intervals.

experimental data due to hidden model errors that may not have been included in the measurement model, Eq. (2.18).

The performance of the Bayesian/ANN and Bayesian/AE techniques were further assessed by analyzing WALS light scattering measurements made on a well-defined soot-laden aerosol. The aerosol is generated with a porous flat flame burner (McKenna type, Holthuis and Associates) with a bronze sintering plate of 60 mm in diameter. A premixed gas flow of air with ethene (C_2H_4, purity 3.0) or ethyne (C_2H_2, purity 2.5) is fed to the burner. The overall flow rate of fuel and air was set to 10.0 NLPM, and the equivalence ratio was varied between $2.3 \leq \varphi \leq 2.9$. The sintering plate of the burner is annularly enclosed by a shroud ring through which a co-flow of nitrogen (N_2, purity 5.0) at a rate of 15,0 normal liters per minute (NLPM) is passed. The flame was stabilized by a stainless steel cylinder with a diameter of 60 mm and a height of 20 mm was mounted at 26 mm HAB. The flat flame burner was cooled down using water at a temperature of 12°C and a volume flow rate of 0.8 standard litres per minute. One thousand single shot WALS images are recorded with an exposure time of ~ 60 µs and then averaged to produce a single measurement.

Altenhoff et al. [149] analyzed a large sample of TEM micrographs sampled from ethene and ethyne premixed flames for different φ and HAB values. All priors and the values reported as TEM predictions in this thesis are derived from these measurements. Two methods were employed by the authors to segment primary particles and aggregate areas from TEM images. First, the particles and aggregates were contoured manually using a graphical user interface. Second, semi-automatic segmentation was applied using Trainable Weka Segmentation (TWS) [153]. The primary particle diameter is evaluated from their projected areas under the assumption of spherical shape. While calculating $p(d_p)$ from the TEM images is straightforward, inferring $p(R_g)$ and k_f and D_f from the TEM images (which amount to 2D projections of the soot aggregates) is not straightforward and can be subject to bias. Various methods from the literature were applied to interpret the TEM images; $p(R_g)$ prediction is consistent between different methods. Both $p(R_g)$ and $p(d_p)$ can be approximated by lognormal distributions, and the PDF for d_p is narrow. Priors for μ_g and σ_g are chosen from their results found by using the method of Köylü et al. [26]. However, the k_f and D_f values varied significantly depending on the inference method. For the case of D_f and k_f, priors are derived from their results inferred by manual segmentation of primary particles and aggregate and using the box-counting algorithm [154], which is considered as the most robust inference method by the authors. These values are shown as D_f and k_f in the figures. However, inferred values based on the algorithms of Köylü [155] ($D_{f,LW,minarea}$ and $k_{f,LW,minarea}$) and Brasil et al. [156] ($D_{f,L}$ and $k_{f,L}$) are also shown to emphasize the

potential variation in the results. For the case of k_f, an uninformed prior is used as the TEM-inferred values had a large deviation depending on the algorithm. A standard deviation of 15% is used for all other prior distributions.

The ANN is trained for fixed d_p values of 15 nm, 20 nm, 25 nm, 30 nm and 35 nm with 545, 526, 624, 1200, 622 $\{D_f, k_f\}$ random samples, and assuming a fixed $\mathbf{m}_\lambda = 1.6 + 0.6i$. For other d_p values, the light scattering kernel is interpolated from the neighboring two ANNs predictions. In the present Bayesian/ANN analysis d_p is assumed to be perfectly-known and monodisperse, and is set equal to the volumetric mean $d_{p,v}$ from reported TEM analysis distribution. Liu et al. [157] showed that an equivalent volume diameter could approximate the soot aggregates optical behaviour more accurately compared to the geometric mean. In the case that μ_p and σ_p are the geometric mean and standard deviation of primary particles, $d_{p,v}$ can be calculated as [157]

$$d_{p,v} = \mu_p \left[\exp\left(\frac{9 \ln^2 \sigma_p}{2} \right) \right]^{1/3} . \tag{3.2}$$

The first measurement is carried out on an aerosol generated by burning ethyne with $\varphi = 2.7$ and at a HAB of 17 mm. Analysis of TEM micrographs showed that $\mu_p = 25.7$ nm and $\sigma_p = 1.16$ [149], therefore $d_{p,v} = 26.6$ nm is used as the primary particle size. The WALS (Bayesian/ANN) and the TEM inferred parameters are shown in Figure 3-9. The WALS inferred size parameters μ_g and σ_g are smaller than TEM results. However, the inferred k_f and D_f are close to those inferred from the TEM images (D_f and k_f values in the figure) and TEM values are inside the credibility interval found through MCMC.

The second set of measurements was carried out by burning ethene, with the same φ and HAB values ($\varphi = 2.7$, HAB = 17 mm). The TEM-inferred size distribution parameters for $p(d_p)$ were $\mu_p = 30.2$ nm and $\sigma_p = 1.20$ for this case [149], therefore $d_{p,v} = 31.7$ nm is used as the primary particle size when analyzing the WALS data. The results are shown in Figure 3-10 Credibility intervals found through MCMC analysis and TEM results (dashed vertical red lines) for the second measurement study (ethene, $\varphi = 2.7$, HAB of 17 mm). Dot dashed lines are the prior distributions. The inferred geometric mean μ_g is smaller than those shown in Figure 3-9, however, the WALS-inferred μ_g remains significantly smaller compared to the TEM results.

The third set of measurements was carried out using ethyne fuel $\varphi = 2.7$ and at a HAB of 12 mm. The HAB value is lower compared to the first measurement case, but other measurement conditions are identical. Analysis of TEM micrographs showed that $\mu_p = 22.7$ nm and $\sigma_p = 1.14$ [149], therefore $d_{p,v} = 23.3$ nm is used as the primary particle size. The initial solution inferred the MAP values

of D_f = 1.82 and k_f =3.48. These values do not agree with the TEM results. Also, compared to the first case the aggregate must be less compact (lower D_f and k_f values). Another problem is that the inferred k_f value lies considerably outside the ANN training range. Therefore, the MCMC solution is bounded with additional priors $p_{pri}(D_f) \sim \mathcal{U}(1.4, 1.9)$ and $p_{pri}(k_f) \sim \mathcal{U}(1.2, 3.2)$. The results are shown in Figure 3-11. Due to the uniform prior used in the solution, both D_f and k_f have very narrow distributions with a peak adjacent to their maximum permitted values. The TEM values are not included in the inferred credibility interval of μ_g and σ_g. Also, the inferred values are smaller compared to the TEM result. Measured signals **b** and the model fit to the signal $\mathbf{a}(\mathbf{x}_{MAP})$ for all three measurements mentioned above are shown in Figure 3-12.

The inconsistency between the WALS-inferred size parameters and those found from the TEM images suggest that there remains unaccounted-for model errors in the ANN predictions. The discrepancy cannot be attributed only to the ANN approximation error as the analysis of synthetic data demonstrates that the Bayesian/ANN approach accurately recovered the QoI from synthetic WALS data. Therefore, it is more plausible that the model error originates from the difference between the training samples, which consisted of MSTM-modeled light scattering using synthetic soot aggregates, and the behavior of real soot aggregates.

It is possible to mask the remaining model error as described in *Chapter 2*. Figure 3-13 shows the solution for the first case study (ethyne fuel with φ = 2.7 and at a HAB of 17 mm, cf. Figure 3-9) with 4% random noise. As observable $\mathbf{x}_{MAP}$ did negligible change compared to the solution with 2% noise, however, the posterior credibility intervals are wider. The assumed 2% measurement noise is originated from the nature of the experiments (calibration error) which translates into the solution uncertainty. Any additional masking of the model error reduces the uncertainty in the final solution without shifting the MAP estimate towards the TEM results.

A key suspect is the treatment of the refractive index, which is assumed to be constant in the training set, while, in reality, the refractive index of soot changes with fuel type and local combustion conditions. Another possible discrepancy could be due to the limited fidelity of the CCA algorithm used to construct the simulated aggregates especially for extreme soot morphological parameters [64,91], the fact that the primary particle sizes are assumed to be monodisperse, and in perfect point-contact. Chao et al. [157] studied the effect of primary particle size distribution on the radiative properties of soot in the forward model. The findings suggest that aggregates with different-sized monomers exhibit stronger scattering and absorption compared to the aggregates with monodisperse

monomers. The effect of the necking and sintering phenomenon between neighboring primary particles in the forward model has been investigated using DDA [158], but the influence of this error on MALS-inferred aggregate parameters has not been assessed. Finally, in reality, k_f and D_f values in the aerosol obey a Gaussian distribution, which is excluded from our forward model.

In the future, the effect of an uncertain $\mathbf{m}_\lambda$ will be addressed by including it as a nuisance parameter in the Bayesian inference procedure and ANN training algorithm. This will be done by generating training set data with $\mathbf{m}_\lambda$ values sampled over values from the literature [159]. One drawback of adding further parameters to the inference process (e.g. d_p or $\mathbf{m}_\lambda$) is that it will increase the uncertainty bounds. Therefore, refractive indices for soot reported in the literature can be used to derive maximum entropy priors, following Hadwin et al. [159]. The error induced by neglecting necking and sintering between the primary particles can be studied numerically in the inverse model using DDA simulations, and if it is significant, it can also be incorporated into the model. Another source of error is caused by the lognormal size distribution assumption over $p(R_g)$. Other distribution functions can be used to approximate $p(R_g)$. For example, a scaling distribution is used by Taylor et al. [160] to explain the radius of gyration size distribution. In the future, the effect of different distribution functions can be evaluated systematically by using Bayesian model selection [161]. Another improvement in the inference would be to use the correlation between k_f and D_f as prior information. Sorensen et al. [162] showed that the prefactor shows uniform trends with the fractal dimension. The information content of the experimental data can be improved by considering both the vertical and horizontal polarization modes of the scattered light, which should further reduce the ill-posedness of the underlying inverse problem. The performance of the ANN-kernel approximation can also be improved by tailoring the ANN structure to address the large approximation error for high N_p values.

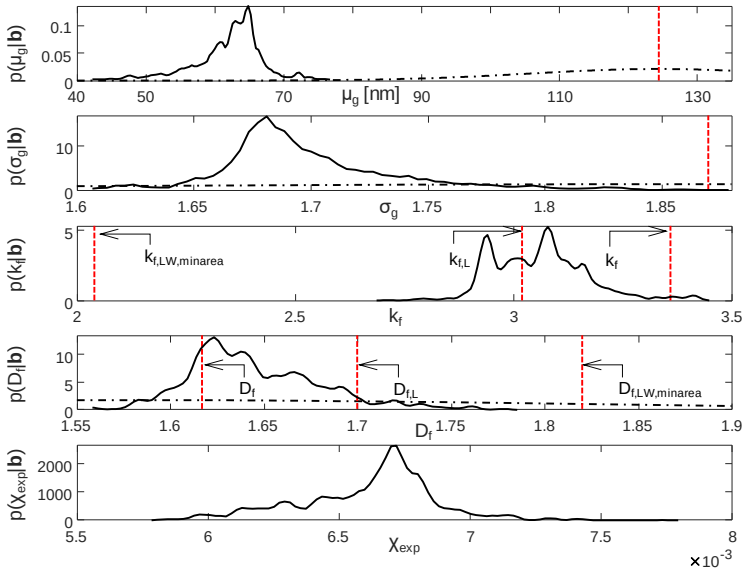

Figure 3-9 Credibility intervals found through MCMC analysis and TEM results (dashed vertical red lines) for first measurement study (ethyne, φ = 2.7, HAB of 17 mm). Dot dashed lines are the prior distributions.

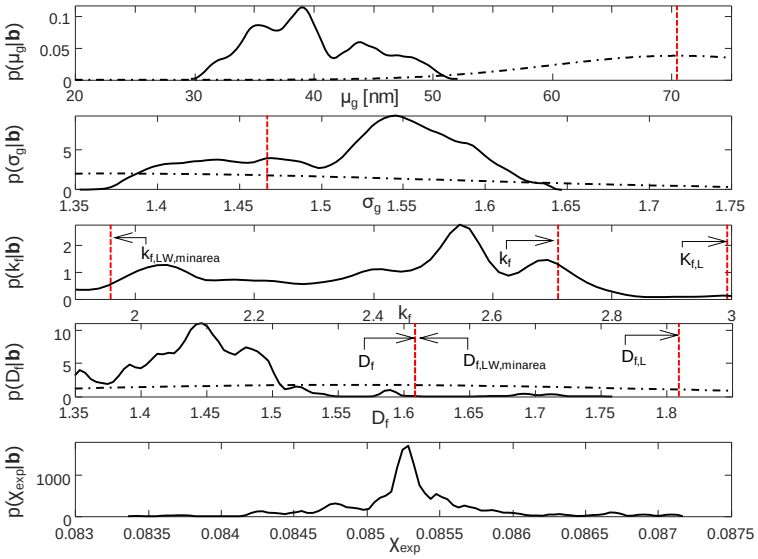

Figure 3-10 Credibility intervals found through MCMC analysis and TEM results (dashed vertical red lines) for the second measurement study (ethene, φ = 2.7, HAB of 17 mm). Dot dashed lines are the prior distributions.

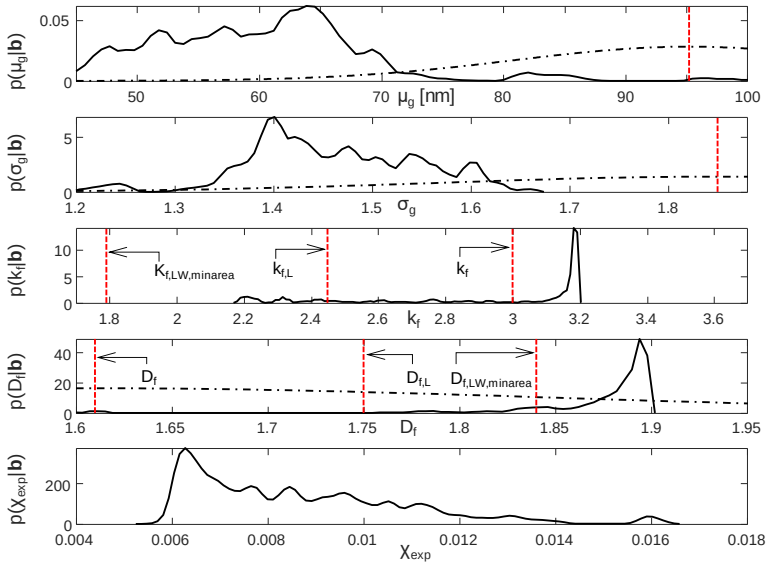

Figure 3-11 Credibility intervals found through MCMC analysis and TEM results (dashed vertical red lines) for the third study case (ethyne, φ = 2.7, HAB of 12 mm). Dot dashed lines are the prior distributions. The prior for D_f is 10 times larger than its actual value to be able to show properly in the figure. Additional priors are used to bound possible D_f and k_f values as $p_{pri}(D_f) \sim \mathcal{U}(1.4, 1.9)$ and $p_{pri}(k_f) \sim \mathcal{U}(1.2, 3.2)$.

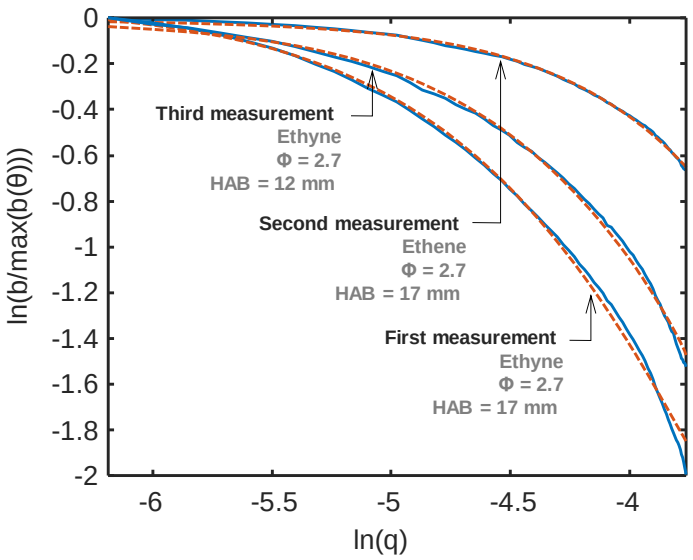

Figure 3-12 Normalized measured signals **b** (solid lines) and fit to the signal (dashed lines) using the $\mathbf{x}_{MAP}$ estimate $\mathbf{a}(\mathbf{x}_{MAP})$.

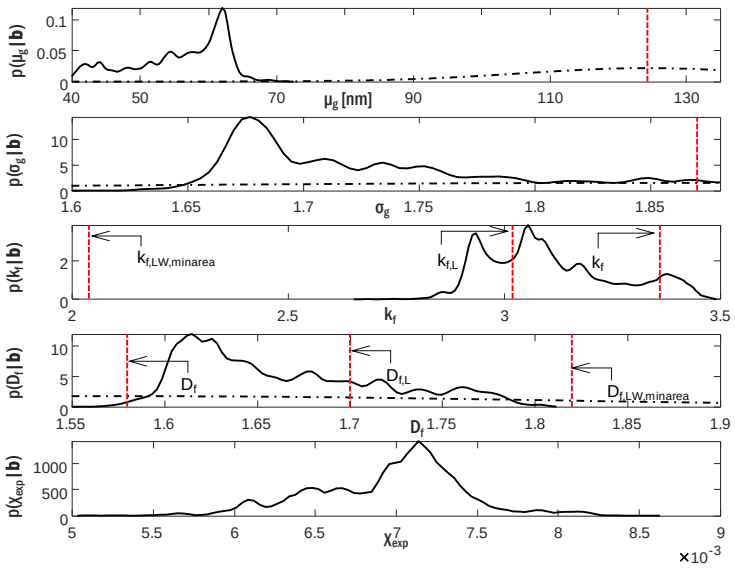

Figure 3-13 Credibility intervals found through MCMC analysis and TEM results (dashed vertical red lines) for the first measurement study (ethyne, φ = 2.7, HAB of 17 mm). Dot dashed lines are the prior distributions. The measurement noise is assumed to be 4%.

3.5 Conclusions

Multi-angle elastic light scattering is increasingly applied to infer the morphological parameters of aerosolized soot, but this requires a measurement model that relates the soot size and structure to the angular distribution of scattered light. While Rayleigh-Debye-Gans Fractal Aggregate (RDG-FA) theory is a convenient way to approximate the light scattering kernel, it is subject to as much as 30% model error, which is amplified by the ill-posedness of the inference process into large deviations in the inferred parameters. More accurate models are too computationally expensive and time-demanding to be used directly in the model equation. In this chapter, the light scattering kernel is approximated using a feed-forward multi-layered artificial neural network (ANN) to achieve an accurate and computationally-efficient kernel model. The ANN is trained using multi-sphere T-matrix (MSTM) scattering simulations on randomly-generated soot aggregates sampled from plausible morphological parameters. The ANN models the light scattering kernel within a relative error range within 5%. In the inverse model, the Bayesian/ANN approach is compared to Bayesian approximation error (AE) technique, which is based on modeling the RDG-FA model error using the Karhunen-Loève theorem. The Bayesian/ANN approach outperforms the Bayesian/AE method both in terms of accuracy of the maximum a posteriori estimate and the width of the marginalized credibility intervals for all training

samples. The Bayesian/ANN is then applied to wide angle light scattering (WALS) measurements carried out within a flame and the inferred parameters compared with results derived from transmission electron micrographs of extracted soot particles. The inferred geometric mean of the aggregate sizes is persistently under-predicted by the Bayesian/ANN compared to transmission electron microscopy (TEM) results. The inconsistency between the WALS-inferred size parameters and those found from the TEM images suggest that there remains unaccounted-for model error in the ANN predictions. These errors may be caused by the assumption of a deterministic refractive index for soot independent of measurement conditions, ignoring necking and sintering phenomena, and treating the primary particles as monodisperse. In the future, the effect of an uncertain refractive index will be addressed by including it in the inference process. Also, the effect of polydisperse monomer size and necking and sintering phenomena will be studied in the inverse model.

Chapter 4
Laser-induced incandescence on metal nanoparticles: validity of Rayleigh approximation

The content of this chapter is an extended version of a paper published in *Journal of Applied Physics B* entitled, "Laser-induced incandescence on metal nanoparticles: Validity of the Rayleigh approximation [118]."

4.1 Introduction

Chapter 2 and *Chapter 3* of the thesis discussed how multi-angle light scattering (MALS) can be used to infer the morphological parameters of soot. While MALS focuses on inferring the size of aggregates, TiRe-LII is about analyzing the primary particle size and thermophysical properties.

Time-resolved laser-induced incandescence (TiRe-LII) as was shown schematically in Figure 1-2, is mainly used to measure the primary particle size and volume fraction of soot in combustion-related applications. In this technique, a nanosecond laser pulse heats the nanoparticles within a sample volume of aerosol, and the subsequent emission (assumed to be purely incandescence) is collected at one or more wavelengths. The spectral intensity data is connected to the unknown nanoparticle volume fraction and size distribution via two coupled models: a spectroscopic model that relates the observed spectral incandescence to an instantaneous temperature of the nanoparticle ensemble, and a heat transfer model that relates the temperature decay to the nanoparticle size distribution and other thermophysical properties of interest. While much of the development of TiRe-LII has focused on soot, this technique is increasingly applied to non-carbonaceous nanoparticles, including metals [57,112,114,163–165], metalloids [166–168], and oxides [93,169,170]. It has also been expanded to infer the thermal

accommodation coefficient [93,95,116], radiative properties, and thermophysical properties under extreme temperatures.

Unfortunately, current measurement models cannot completely explain some commonly-observed phenomena in TiRe-LII signals. In the case of metal nanoparticles, this includes "excessive absorption" wherein an energy balance based on the peak pyrometrically-inferred nanoparticle temperature suggests that the nanoparticles absorb considerably more laser energy than can be accounted for based on the laser fluence and spectral absorption cross-section at the excitation wavelength, *cf*. Figure 4-1 [21]. Excessive absorption has been reported for iron, molybdenum, and silver nanoparticles [21,113]. Moreover, TiRe-LII measurements on iron nanoparticles must be interpreted by treating the complex refractive index of iron, $\mathbf{m}_\lambda$, as uniform [171] or nearly uniform [21] over the detection wavelengths in order to obtain the expected particle size distribution and peak nanoparticle temperature. This is contrary to the bulk property given in the literature, which varies significantly over the visible and near-infrared spectra. Another unexplained feature concerns the *intensity scaling factor* (ISF), a coefficient that relates the nanoparticle incandescence calculated using the spectral absorption cross-section and the blackbody intensity to the detected incandescence signal [172]. The ISF accounts for the efficiency and configuration of the collection optics and the aerosol volume fraction, so it should, in principle, remain constant during a single shot measurement provided the laser fluence is low enough to avoid significant particle vaporization. Nevertheless, the effective ISF inferred from TiRe-LII measurements on liquid silicon nanoparticles [168], iron, molybdenum, and silver nanoparticles [173], and soot [172,174,175] show that this quantity changes over time in a manner that cannot be explained by evaporation of the nanoparticle material alone.

Various hypotheses have been proposed to interpret these phenomena. Eremin et al. [113] use a size-dependent refractive index function for carbon and iron nanoparticles to explain the excessive absorption phenomenon. However, while the apparent refractive index may become size-dependent through electron scattering from the nanoparticle surface, this phenomenon only occurs for nanoparticle diameters that approach the mean-free electron path, which is typically only a few nanometers [176,177].

This chapter suggest that, for metal nanoparticles, many of these unexplained anomalies may originate from a misapplication of Rayleigh theory to model the spectral absorption cross-section of the nanoparticles. Rayleigh theory has been nearly universally applied to interpret TiRe-LII measurements on non-carbonaceous nanoparticles (e.g. [18,50,116,168,171,178,179]), with the justification that the size criterion is satisfied ($x_p = \pi d_p/\lambda << 1$). However, this rationale disregards the

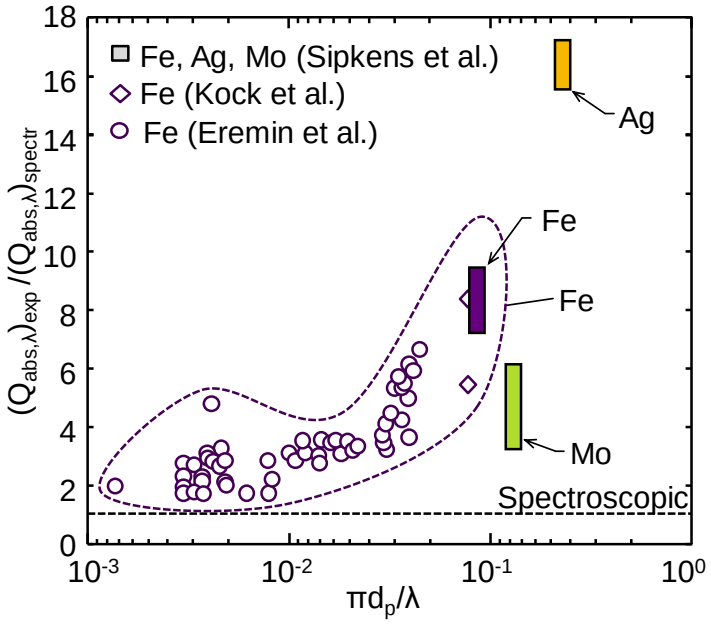

Figure 4-1 Excessive absorption phenomenon in metal nanoparticles adopted from Sipkens et al. [21], including experimental data from Sipkens et al. [21], Kock et al. [171], Eremin et al. [113] and Sipkens et al. [180]. The ordinate axis is the ratio of the absorption efficiency calculated from calorimetry, $(Q_{abs,\lambda})_{exp}$ to the one predicted from the spectroscopic model, $(Q_{abs,\lambda})_{spectr}$. The spectroscopic absorption efficiency is found by using Rayleigh approximation and assuming a monodisperse aerosol with a geometric mean of the size distribution as nanoparticle size, while $(Q_{abs,\lambda})_{exp}$ is found by using the peak pyrometry effective temperature in calorimetry. The excitation wavelength in all experiments was 1064 nm.

second criteria needed to ensure the validity of the electrostatic approximation: $|\mathbf{m}_\lambda| x_p << 1$. For metal nanoparticles, $|\mathbf{m}_\lambda|$ is usually much larger than for carbonaceous nanoparticles in the visible and near-infrared spectra, such that this criterion is generally *not* satisfied. In this case, the Rayleigh theory should not be applied to interpret TiRe-LII measurements. Errors induced by a misapplication of Rayleigh theory can be further exacerbated by modeling an aerosol containing polydisperse particle sizes as monodisperse, which is a common practice to simplify data analysis. Moreover, while most TiRe-LII models account for the temperature dependence of specific heat and density, radiative properties are almost always treated as invariant as the nanoparticles heat and then cool. This may be an inaccurate assumption for most metal nanoparticles, which change from solid to liquid during laser heating.

This chapter investigates how applying Mie theory, incorporating polydispersity of primary particle sizes, and accounting for the change in the refractive index about the melting point, may explain

anomalies in TiRe-LII measurements on metal nanoparticles. The chapter starts by introducing the spectroscopic and heat transfer models used in TiRe-LII analyses, including a summary of Mie theory as it applies to the absorption of E-M waves by silicon, iron, silver, and molybdenum nanoparticles. Synthetic signals are generated for monodisperse and polydisperse aerosols by applying Mie theory to modeled nanoparticle temperature decays. The signals are then interpreted using the Rayleigh approximation and a quadrupole approximation to Mie theory to investigate the effect that these approximations have on the inferred properties. It is shown that using Mie theory instead of the Rayleigh approximation and considering polydisperse particle sizes explains the discrepancy between the experimentally-derived and simulated ISF and may partially explain the apparent discrepancy in the $E(\mathbf{m}_\lambda)$ ratio at the detection wavelengths for iron nanoparticles, while these effects combined with the change in refractive index when the nanoparticles melt partially accounts for the apparent enhanced absorption cross-section. We also show that the nanoparticle charge state is unlikely to contribute to these anomalies. Remaining anomalies suggest that some other spectroscopic phenomena must also be occurring to explain the enhanced absorption of laser energy, particularly for silver nanoparticles.

4.2 TiRe-LII measurement model

4.2.1 Spectroscopic model

For a polydisperse, optically-thin aerosol, the total spectral incandescence, J_λ, emitted by heated nanoparticles within the probe volume is found by

$$J_\lambda(t) = \Lambda \int_0^\infty p(d_\mathrm{p}) \frac{\pi d_\mathrm{p}^2}{4} Q_{\mathrm{abs},\lambda}(d_\mathrm{p}, \mathbf{m}_\lambda) I_{\mathrm{b},\lambda}\left[T_\mathrm{p}(t, d_\mathrm{p})\right] \mathrm{d}(d_\mathrm{p}), \tag{4.1}$$

where Λ is the intensity scaling factor (ISF) [172]; $I_{\mathrm{b},\lambda}$ is the blackbody spectral intensity at the nanoparticle temperature, T_p; d_p is the nanoparticle size; $p(d_\mathrm{p})$ is the instantaneous nanoparticle size distribution; and $Q_{\mathrm{abs},\lambda}$ is the spectral absorption efficiency, which is discussed further in Section 3. While the particle sizes in most aerosols are polydisperse, many LII studies model the aerosol as monodisperse. In this case, Eq. (4.1) simplifies to

$$J_\lambda(t) = \Lambda \frac{\pi d_\mathrm{p}^2}{4} Q_{\mathrm{abs},\lambda}(d_\mathrm{p}, \mathbf{m}_\lambda) I_{\mathrm{b},\lambda}\left[T_\mathrm{p}(t, d_\mathrm{p})\right]. \tag{4.2}$$

Equations (4.1) and (4.2) connect the measured spectral incandescence from the probe volume, $J_\lambda(t)$, to the particle temperature. The spectral incandescence measured at two or more wavelengths is then used to infer an "effective" pyrometric temperature that is a point estimate of the distribution of nanoparticle temperatures within the probe volume at any instant. This calculation and its relationship with the spectroscopic properties of the nanoparticles is discussed further in Section 4.3. References [48,116] provide further details on the LII spectroscopic model.

4.2.2 Heat transfer model

The spectroscopic model is coupled with a heat transfer model that describes how the nanoparticle temperature (which indicates its sensible energy) changes with time. For each size class, the nanoparticle temperature is found by solving

$$\frac{\pi}{6} d_{\mathrm{p}}^3 \rho_{\mathrm{p}}(t) c_{\mathrm{p}}(t) \frac{dT_{\mathrm{p}}}{dt} = q_{\mathrm{laser}}(t) - q_{\mathrm{evap}}\left[T_{\mathrm{p}}(t)\right] - q_{\mathrm{cond}}\left[T_{\mathrm{p}}(t)\right], \tag{4.3}$$

where ρ_{p} and c_{p} are the density and specific heat of the nanoparticle, respectively, and q_{laser}, q_{evap} and q_{cond} are the laser absorption, evaporation and conduction heat transfer rates, respectively. Laser heating is given by

$$q_{\mathrm{laser}}(t) = F_0 f(t) \frac{\pi d_{\mathrm{p}}^2}{4} Q_{\mathrm{abs},\lambda_{\mathrm{laser}}} \tag{4.4}$$

where F_0 is the laser fluence, $f(t)$ is the temporal laser profile, and λ_{laser} is the laser wavelength. Since the diameters of the nanoparticles involved in TiRe-LII measurements are smaller than the mean free path of the buffer gas in most TiRe-LII experiments (>1 μm), evaporation typically occurs in the free-molecular (Knudsen) regime, and the evaporation heat transfer rate is given by

$$q_{\mathrm{evap}}(t) = \pi d_{\mathrm{p}}^2 N_{\mathrm{v}}'' \frac{\Delta H_{\mathrm{v}}}{N_{\mathrm{A}}} \tag{4.5}$$

where ΔH_{v} is the molar latent heat of vaporization, N_{A} is Avogadro's number

$$N_{\mathrm{v}}''(t) = \frac{n_{\mathrm{v}} v_{\mathrm{v}}}{4} = \underbrace{\frac{1}{4} \frac{p_{\mathrm{v}}}{k_{\mathrm{B}} T_{\mathrm{p}}}}_{n_{\mathrm{v}}} \underbrace{\left(\frac{8 k_{\mathrm{B}} T_p}{\pi m_{\mathrm{v}}} \right)^{1/2}}_{c_{\mathrm{v}}} \tag{4.6}$$

is the number flux of evaporated molecules from nanoparticle surface, n_{v} and c_{v} are the number density (in molecules/m^3) and the mean thermal speed of the evaporated species, p_{v} is the vapour partial

pressure of the evaporated species, k_B is Boltzmann's constant, and m_v is the molecule mass of the evaporated species. The Clausius-Clapeyron equation gives the partial pressure

$$p_v = p^* \exp\left[\frac{\Delta H_v\left(T_p - T^*\right)}{RT_pT^*}\right], \tag{4.7}$$

where p^* and T^* are the reference pressure and temperature, respectively, and R is the universal gas constant [179,181]. The evaporation rate also causes the nanoparticle mass to change according to

$$\frac{dm_p}{dt} = -\dot{m}_{evap}\left(T, d_p\right) = -m_v \frac{q_{evap}\left(t\right)}{\Delta H_v} \tag{4.8}$$

The instantaneous nanoparticle mass is then used to calculate the nanoparticle diameter given by

$$d_p\left(t\right) = \left\{\frac{6m_p\left(t\right)}{\pi\rho_p\left[T_p\left(t\right)\right]}\right\}^{\frac{1}{3}}. \tag{4.9}$$

Heat conduction also occurs within the free molecular regime and is given by [21,48]

$$q_{cond}\left(T_p, d_p\right) = \pi d_p^2 N_g'' \langle E_o - E_i\rangle = \pi d_p^2 \frac{n_g c_{g,t}}{4}\langle E_o - E_i\rangle \tag{4.10}$$

where N_g'' is the incident gas number flux; $n_g = p_g/(k_BT)$ is the molecular number density of the buffer gas; $c_{g,t} = [8k_BT_g/(\pi m_g)]^{1/2}$ is the mean thermal speed of the carrier gas; p_g, T_g, and m_g are the carrier gas pressure, temperature, and molecular mass, respectively; $\langle E_0 - E_i\rangle$ is the average energy transfer per collision, which can be written using the thermal accommodation coefficient, α,

$$\langle E_0 - E_i\rangle = \alpha\langle E_0 - E_i\rangle_{max} = \alpha\left(2 + \zeta_{rot}/2\right)k_B\left(T_p - T_g\right) \tag{4.11}$$

where ζ_{rot} is the number of rotational degrees of freedom of the buffer gas. In the present study, we consider monatomic gases such that $\zeta_{rot} = 0$. The conduction cooling term then reduces to

$$q_{cond}\left(T_p, d_p\right) = \frac{\pi}{2} d_p^2 n_g c_{g,t} \alpha k_B\left(T_p - T_g\right). \tag{4.12}$$

Other heat transfer terms, including radiation and thermionic emission, are typically much smaller than evaporation and conduction and can be excluded from the model. Further details on the LII heat transfer model can be found in Refs. [48,116].

4.3 Spectral absorption efficiency of nanoparticles

4.3.1 Optical properties

Equations (4.1) and (4.2) highlight the importance of the spectral absorption efficiency when interpreting TiRe-LII data. Assuming that the nanoparticles are large enough to ignore electron scattering effects [176,177], which only become important when nanoparticle diameters approach the mean free electron path of the bulk material, the spectral absorption cross-section of a nanoparticle depends exclusively on two parameters: the size parameter, $x_p = \pi d_p/\lambda$, and the electromagnetic properties of the bulk material, expressed in terms of the complex refractive index, $\mathbf{m}_\lambda = n_\lambda + k_\lambda i$, or complex dielectric permittivity, $\boldsymbol{\varepsilon}_\lambda = \varepsilon_{I,\lambda} + \varepsilon_{II,\lambda}\, i$. These latter quantities are related by

$$\varepsilon_{I,\lambda} = n_\lambda^2 - k_\lambda^2,\ \varepsilon_{II,\lambda} = 2n_\lambda k_\lambda . \tag{4.13}$$

The Lorentz-Drude model can describe some metal-dielectric functions. It is given by [182]

$$\boldsymbol{\varepsilon}_\lambda = \underbrace{1 - \frac{f_0\omega_p^2}{\omega\left[\omega - \Gamma_0 i\right]}}_{\text{Drude}} + \underbrace{\sum_{n=1}^{m} \frac{f_n\omega_p^2}{\left(\omega_n^2 - \omega^2\right) + \omega\Gamma_n i}}_{\text{Lorentz}} \tag{4.14}$$

where $\omega = 2\pi c_0/\lambda$ is the angular frequency of the incident wave, c_0 is the speed of light in a vacuum, ω_p is the plasma frequency of the electrons with an oscillator strength of f_n, and Γ_n is the damping coefficient, which is related to the collision frequency between electrons and atoms/ions by $\tau = 1/\Gamma_n$. The Drude term in Eq. (4.14) accounts for free-electron effects (intraband transitions) and the Lorentz term accounts for bound-electron effects (interband transitions).

In most LII experiments on metal aerosols reported in the literature, the nanoparticles start as a solid and melt as they are heated. Exceptions include molybdenum nanoparticles, which remain solid due to their comparatively high melting temperature, and silicon and germanium nanoparticles within a microwave plasma reactor, e.g. Ref. [167], in which the nanoparticles are in liquid state throughout the measurement. Accordingly, it is crucial to consider the electromagnetic properties of both the solid and liquid phases, which may differ significantly due mainly to changes in the electron band structure. The Drude model can also describe the optical properties of some liquid metals and metalloids, specifically those in which interband transition effects are not significant over the spectrum of interest. Values of ω_p, f_0, and Γ_0 for liquid silicon and silver are taken from Ref. [183] and [184], respectively. The refractive index of solid silver is calculated using Eq. (4.14) with model parameters

Table 4-1 Refractive index of metal nanoparticles examined in this thesis.

Material	λ = 442 nm	λ = 716 nm	λ = 1064 nm
Fe (solid, 30 °C) [185]	2.54 + 2.74*i*	2.86 + 3.21*i*	2.93 + 3.99*i*
Fe (liquid, 1616 °C) [186]	2.37 + 3.21*i*	3.48 + 4.13*i*	5.64 + 5.01*i*
Si (liquid, 1414 °C) [183]	2.11 + 4.53*i*	3.58 + 5.95*i*	5.06 + 7.18*i*
Mo (solid, 1926 °C) [187]	2.83 + 3.45*i*	3.83 + 4.09*i*	4.29 + 5.30*i*
Ag (solid, 30 °C) [182]	0.14 + 2.25*i*	0.16 + 4.42*i*	0.24 + 6.87*i*
Ag (liquid, 962 °C) [184]	0.10 + 2.92*i*	0.25 + 4.89*i*	0.55 + 7.31*i*

adapted from Ref. [182]. In cases where the Drude model is not valid (iron and molybdenum [188]), the optical properties are taken from ellipsometry measurements carried out on bulk samples, with the values summarized in Table 4-1.

4.3.2 Evaluating the absorption cross-section

The absorption efficiency of nanoparticles can be obtained from the optical properties of the bulk material using one of several candidate models. Most generally, the spectral absorption efficiency of a non-magnetic, uncharged, spherical nanoparticle embedded in a dielectric material can be found directly by Mie theory [83,120]. In this theory, extinction and scattering efficiencies, denoted by $Q_{\text{ext},\lambda}$ and $Q_{\text{sca},\lambda}$ respectively, are defined as the ratios between the corresponding radiative and geometrical cross-sections of the spherical particle. Assuming that the sphere is embedded within a vacuum or a medium having a refractive index of unity (e.g. most gases at visible and near-infrared), $Q_{\text{ext},\lambda}$ and $Q_{\text{sca},\lambda}$ are given by

$$Q_{\text{ext},\lambda} = \frac{2}{x_{\text{p}}^2}\sum_{l=1}^{\infty}(2l+1)\,\text{Re}\left(a_l + b_l\right) \tag{4.15}$$

and

$$Q_{\text{sca},\lambda} = \frac{2}{x_{\text{p}}^2}\sum_{l=1}^{\infty}(2l+1)\left(|a_l|^2 + |b_l|^2\right), \tag{4.16}$$

where

$$a_l = \frac{\mathbf{u}\psi_l(\mathbf{u}y)\psi'_l(y) - \psi_l(y)\psi'_l(\mathbf{u}y)}{\mathbf{u}\psi_l(\mathbf{u}y)\xi'_l(y) - \xi_l(y)\psi'_l(\mathbf{u}y)}, \tag{4.17}$$

and

$$b_l = \frac{\psi_l(\mathbf{u}y)\psi'_l(y) - \mathbf{u}\psi_l(y)\psi'_l(\mathbf{u}y)}{\psi_l(\mathbf{u}y)\xi'_l(y) - \mathbf{u}\xi_l(y)\psi'_l(\mathbf{u}y)} \tag{4.18}$$

are scattering coefficients; $\mathbf{u} = \boldsymbol{\varepsilon}_\lambda^{1/2}$; $\boldsymbol{\varepsilon}_\lambda$ is the relative complex permittivity of the nanoparticle; and ψ_l and ξ_l are the Riccati-Bessel functions of order l. Finally, the spectral absorption cross-section is inferred from

$$Q_{\text{abs},\lambda} = Q_{\text{ext},\lambda} - Q_{\text{sca},\lambda}. \tag{4.19}$$

While Mie theory provides an exact solution to the spectral absorption coefficient of spherical nanoparticles, it is rarely used to analyze LII data due to the computational effort associated with evaluating the Riccati-Bessel functions and because it requires knowledge of the nanoparticle diameter, which is typically unknown and the focus of the LII analysis.

Instead, practitioners use an approximation for the absorption cross-section. Invoking the *electrostatic approximation*, in which the variation of the electromagnetic field inside the nanoparticle is assumed to be negligible at any instant, is tantamount to neglecting the influence of electromagnetic field coupling [120]. This results in the Rayleigh approximation to Mie's equations, in which

$$Q_{\text{abs},\lambda} = 4x_{\text{p}}E(\mathbf{m}_\lambda), \tag{4.20}$$

where

$$E(\mathbf{m}_\lambda) = \text{Im}\left(\frac{\mathbf{m}_\lambda^2 - 1}{\mathbf{m}_\lambda^2 + 2}\right), \tag{4.21}$$

is the absorption function. This approach is appealing for two reasons: (*i*) this model is far simpler and much less computationally-expensive to implement compared to the full Mie equations, and (*ii*) the electrostatic assumption separates the influence of the bulk electromagnetic ($\mathbf{m}_\lambda$ or $\boldsymbol{\varepsilon}_\lambda$) and size ($x_{\text{p}} = \pi d_{\text{p}}/\lambda$) on $Q_{\text{abs},\lambda}$. Consequently, the peak effective temperature derived from the TiRe-LII data is nearly independent of size, and, for the monodisperse case, the spectroscopic and heat transfer submodels can be decoupled and solved sequentially. For these reasons, the Rayleigh approximation is almost universally applied to analyze LII data.

The validity of the Rayleigh approximation relies on two criteria: (*i*) $x_{\text{p}} << 1$, and (*ii*) that the phase shift parameter satisfies $x_{\text{p}}|\mathbf{m}_\lambda| << 1$. While the latter criterion is usually satisfied for

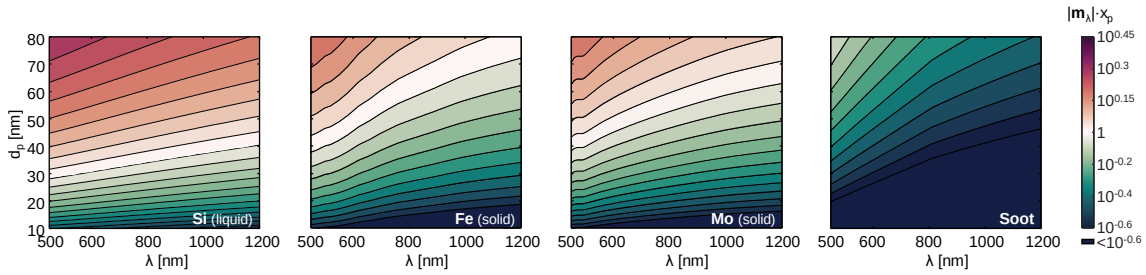

Figure 4-2 Comparison of $|m_\lambda|x_p$ values for different nanoparticles. Contours are logarithmic. The lightest region represents those values close to $|m_\lambda|x_p = 1$, and Rayleigh theory is expected to valid in those regions that are dark blue (bottom right corner of most plots). The refractive index of soot is adopted from Ref. [191].

carbonaceous nanoparticles (e.g. soot), this is not true for metal nanoparticles since they have a much larger refractive index, as shown in Figure 4-2. Consequently, the internal electric field of the nanoparticle during wave interaction is not sufficiently uniform to be approximated by a single dipole for the wavelengths important to LII. This finding conflicts somewhat with a recent paper by Sorensen et al. [189], who downplay the importance of the phase shift criteria because, they argue, absorption is an incoherent phenomenon. They also suggest that all spheres, regardless of size, display semi-quantitative Rayleigh behavior for the condition $x_p \cdot k < 0.3$. However, their study assumes a fixed value of $n = 1.5$, which is much smaller than values typical of metals in the visible and near infrared and ignores the fundamental correlation between k and n through the plasmon frequency and electron damping coefficient. Moreover, the Mie absorption, Eq. (4.19), is a linear combination of Mie scattering coefficients a_l and b_l which depend on both n and k through $\mathbf{u} = (\boldsymbol{\varepsilon}_p)^{1/2} = \mathbf{m}_\lambda$. This can be shown by examining the difference between Rayleigh and Mie absorption efficiency predictions and the phase shift parameter over a range of n and k values expected for non-plasmonic metal nanoparticles at 1064 nm ($n \in [1, 7]$, $k \in [1, 7]$). These differences are highly correlated with the phase shift parameter (Pearson correlation coefficients greater than 90% for nanoparticles with $d_p < 100$ nm), which can thus be used as an error metric.

The shortcomings of the Rayleigh approximation present a need for other $Q_{abs,\lambda}$ models that are more accurate but avoid the complexity and computational effort of the full Mie solution. Schebarchov et al. [190] recently presented a simple, computationally-efficient, closed-form approximation to the exact Mie solution for metal nanospheres under 100 nm:

$$Q_{ext}^{Mie,approx} = -\frac{2}{x_p^2}\mathrm{Re}\left[3b_1 + 3a_1 + 5b_2 + O\left(x_p^7\right)\right] \tag{4.22}$$

and

$$Q_{\mathrm{sca}}^{\mathrm{Mie,approx}} = \frac{2}{x_{\mathrm{p}}^2}\left[3|b_1|^2 + 3|a_1|^2 + 5|b_2|^2 + O\left(x_{\mathrm{p}}^7\right)\right]. \tag{4.23}$$

The extinction and scattering efficiencies can be approximated using the scattering coefficients, a_1 and b_1, as defined above. Equations (4.22) and (4.23) predict scattering and absorption spectra of metal nanospheres and account for localized surface plasmon resonances (LSPR) which depends mostly on b_1 (electric dipole), b_2 (electric quadrupole) and a_1 (magnetic dipole). The electric quadrupole, b_2, and magnetic dipole, a_1, contributions are of the order x_{p}^5. The remaining truncated terms are of order x_{p}^7 or higher.

4.3.3 Defining the effective temperature and intensity scaling factor

Most often the raw TiRe-LII data is converted into an effective temperature via a calibration (which relates the raw data to spectral incandescence measurements) and then a spectroscopic model, *cf.* Eq. (4.2). This approach is appealing for several reasons: it reduces the dimension of the inference problem; it avoids the need to infer the intensity scaling factor, which relates the measured LII signal to the spectral incandescence [172]; and it gives a temperature that provides some physical insight into the heat transfer processes that govern nanoparticle heating and cooling. In general, one can define an effective temperature at any given instant in time using a least squares analysis by assuming that all the detected radiation is due to nanoparticle incandescence,

$$\mathbf{x}(t) = \begin{bmatrix} T^{\mathrm{eff}}(t) \\ \Lambda^{\mathrm{eff}}(t) \end{bmatrix} = \underset{T,\Lambda}{\arg\min} \left\{ \left\| \begin{matrix} J_{\lambda_1} - \Lambda \cdot Q_{\mathrm{abs},\lambda_1} \cdot I_{\mathrm{b},\lambda_1}(T) \\ \vdots \\ J_{\lambda_{\mathrm{w}}} - \Lambda \cdot Q_{\mathrm{abs},\lambda_{\mathrm{w}}} \cdot I_{\mathrm{b},\lambda_{\mathrm{w}}}(T) \end{matrix} \right\|_2^2 \right\}. \tag{4.24}$$

In the above equation, all the terms are time-dependent, including the ISF and absorption efficiency. If Rayleigh theory is used to model $Q_{\mathrm{abs},\lambda}$, the inference becomes

$$\mathbf{x}^{\mathrm{Rayl}} = \begin{bmatrix} T^{\mathrm{eff,Rayl}} \\ \Lambda^{\mathrm{eff,Rayl}} \end{bmatrix} = \underset{T,\Lambda}{\arg\min} \left\{ \left\| \begin{matrix} J_{\lambda_1} - \Lambda \cdot E(\mathbf{m}_{\lambda 1}) \cdot I_{\mathrm{b},\lambda_1}(T) \\ \vdots \\ J_{\lambda_{\mathrm{w}}} - \Lambda \cdot E(\mathbf{m}_{\lambda 1}) \cdot I_{\mathrm{b},\lambda_{\mathrm{w}}}(T) \end{matrix} \right\|_2^2 \right\}. \tag{4.25}$$

The $\pi d_p^2/4$ and $\pi d_p^3/\lambda$ terms are merged into the Λ coefficient in Eq. (4.24) and Eq. (4.25), respectively. For the particular case of two-color pyrometry (w = 2), a closed-formed solution for T^{eff} is found by invoking Wien's approximation and taking the ratio of the signals

$$T^{\text{eff,Rayl}}\left(t\right)=\frac{hc_0}{k_B}\left(\frac{1}{\lambda_1}-\frac{1}{\lambda_2}\right)\left[\ln\left(\frac{J_{\lambda 1}\left(t\right)}{J_{\lambda 2}\left(t\right)}\frac{1}{E\left(\mathbf{m}\right)_{\text{r}}}\left(\frac{\lambda_1}{\lambda_2}\right)^6\right)\right]^{-1}, \tag{4.26}$$

and $E(\mathbf{m})_{\text{r}} = E(\mathbf{m}_{\lambda 1})/E(\mathbf{m}_{\lambda 2})$. This avoids calculating the ISF altogether, although the parameter can still be evaluated by substitution and contains useful information [172].

If one cannot invoke the Rayleigh approximation, the absorption cross section is a non-linear function of the nanoparticle diameter. Accordingly, defining an effective temperature now requires knowledge of d_{p}, which is not generally known *a priori*. One solution is to also define an effective diameter, $d_{\text{p,eff}}$, which can then be used to define an effective temperature,

$$\mathbf{x}^{\text{Mie}}\left(d_{\text{p,eff}}\right)=\begin{bmatrix}T^{\text{eff,Mie}}\left(d_{\text{p,eff}}\right)\\ \Lambda^{\text{eff,Mie}}\left(d_{\text{p,eff}}\right)\end{bmatrix}=\underset{T,\Lambda}{\arg\min}\left\{\left\|\begin{matrix}J_{\lambda_1}-\Lambda\cdot Q_{\text{abs},\lambda_1}\left(d_{\text{p,eff}}\right)\cdot I_{\text{b},\lambda_1}\left(T\right)\\ \vdots\\ J_{\lambda_{\text{w}}}-\Lambda\cdot Q_{\text{abs},\lambda_1}\left(d_{\text{p,eff}}\right)\cdot I_{\text{b},\lambda_1}\left(T\right)\end{matrix}\right\|_2^2\right\}. \tag{4.27}$$

This effective temperature corresponds to an ensemble average of the temperatures in the real aerosol and is equivalent to the temperature of a hypothetical monodisperse aerosol of the specified effective diameter that will produce an emission spectrum that most closely resembles the experimental emission spectrum. An identical treatment must be applied to simulated data in order to infer the effective temperature. One candidate effective diameter is the geometric mean, $d_{\text{p,g}}$, which is motivated by the fact that, when using Rayleigh theory to interpret laser absorption and incandescence from nanoparticles during conduction-dominated cooling, the pyrometric temperature would correspond to that of a hypothetical monodisperse aerosol containing nanoparticles having the geometric mean diameter of the polydisperse aerosol [49]. Alternatively, the volumetric diameter

$$d_{\text{p,v}}=\left(\int_0^\infty d_{\text{p}}^3 p\left(d_{\text{p}}\right)\text{d}d_{\text{p}}\right)^{1/3} \tag{4.28}$$

could be used.

The pyrometric temperature is often used to indicate the internal energy of the atoms and molecules in the nanoparticle, and the variation of peak pyrometric temperature with laser fluence is often related to evaporation and sublimation. In a strict thermodynamic sense, were the true

nanoparticle size distribution and corresponding size-dependent temperatures known, the instantaneous thermodynamic temperature (i.e. the temperature that indicates the average internal energy of the nanoparticles within the probe volume) could be calculated from

$$T^{\text{thermo}} = \frac{\int_0^\infty T\left(d_\text{p}\right) c_\text{p} \rho d_\text{p}^3 p\left(d_\text{p}\right) \text{d}d_\text{p}}{\int_0^\infty c_\text{p} \rho d_\text{p}^3 p\left(d_\text{p}\right) \text{d}d_\text{p}}, \tag{4.29}$$

where, as before, all of the terms can be a function of time.

4.4 Effect of the spectroscopic model assumption on TiRe-LII data interpretations

Consider now the kind of errors that will arise when the Rayleigh approximation is used to simulate the incandescence signals.

4.4.1 Effect of the spectroscopic model assumptions on the simulated nanoparticle temperature

Most TiRe-LII analyses assume that nanoparticles are heated to the same peak temperature regardless of their size, a consequence of the fact that the Rayleigh absorption cross-section and the sensible energy of the nanoparticle are both proportional to d_p^3. Consider simulated LII measurements on liquid silicon nanoparticles generated using model parameters adapted from Menser et al. [168]. Nanoparticles are heated using a spatially-uniform and temporally-Gaussian pulse at 1064 nm with a full-width half maximum of 15 ns at a fluence of 8 mJ/mm^2. The bath gas consists of 93% Ar and 7% H_2 at T_g = 1500 K and P_g = 10 kPa, and α = 0.2 is assumed for the heat transfer model. Figure 4-3a shows that the Rayleigh model predicts an approximately identical temperature profile for nanoparticles of different sizes, with the only differences stemming from a size-dependent nanoparticle dilation due to the temperature-dependent density, and a size-dependent evaporation rate. In contrast, Mie theory predicts a much broader range in peak temperatures, which results in a strong size-dependent decay rate in the nanoparticle temperature following the peak temperature, with large nanoparticles exhibiting rapid mass loss due to evaporation, *cf*. Figure 4-3b. This would result in significant errors that would propagate into inferred nanoparticle diameters. The quadrupole approximation, Eqs. (4.22) and (4.23), generally overpredicts the absorption cross-section of larger nanoparticles, increasing the range of

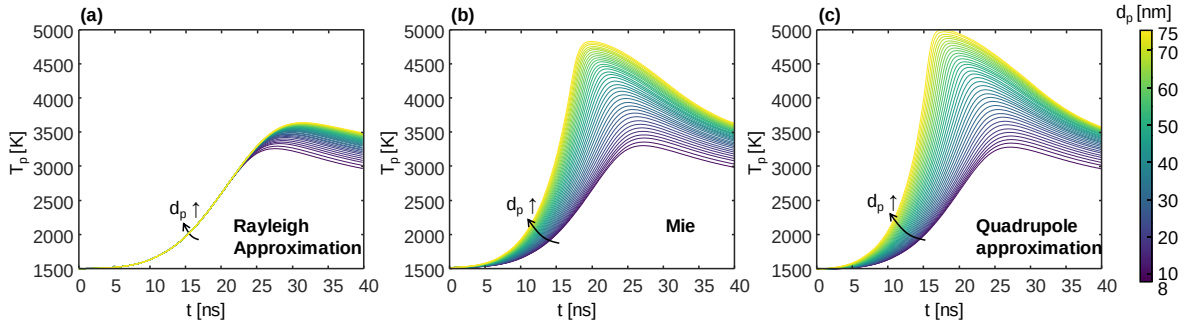

Figure 4-3 Temperature of liquid silicon nanoparticles obtained using a laser having a uniform spatial and Gaussian temporal profile. Results are shown for a range of spectroscopic models, including: (a) the Rayleigh approximation, Eq. (4.20); (b) Mie theory; Eqs. (4.15) and (4.16); and (c) the quadrupole approximation [190], Eq. (4.22).

modeled peak temperatures, *cf.* Figure 4-3c. Consequently, more mass loss is predicted for larger nanoparticles due to superheating relative to Mie theory, especially during the laser pulse period.

4.4.2 Effect of the spectroscopic model assumption on the prompt effective temperature

Consider the Mie theory results shown in Figure 4-3b as the ground truth. Incandescence signals are generated by integrating the incandescence emitted by each size class over a lognormal distribution having a geometric mean and standard deviation of 25 nm and 1.3, respectively, following Eq. (4.1). Spectral signals are generated by sampling the incandescence between 425 nm and 700 nm at 0.4 nm intervals, matching the resolution of the spectrometer used in Ref. [168]. The simulated incandescence signals are then used to calculate an effective temperature using either: (*i*) the Rayleigh approximation, Eq. (4.25); or (*ii*) Mie theory with $d_{p,g}$ or $d_{p,v}$ as effective diameter, Eq. (4.27). Figure 4-4 shows that the effective temperature obtained from the Rayleigh interpretation closely resembles the thermodynamic temperature and that the Rayleigh- and Mie-based temperatures are quite similar. This suggests that it may be reasonable to use the Rayleigh/monodisperse approximation in order to calculate a pyrometric temperature, even if the phase shift criterion is violated.

Figure 4-5 shows the nanoparticles temperature distribution at the peak incandescence signal when the absorption efficiency is calculated: (*i*) using Rayleigh approximation, $T_{peak}^{Rayl}(d_p)$; and (*ii*) using Mie theory, $T_{peak}^{Mie}(d_p)$. The simulation assumptions are identical to what is used to generate Figure 4-3. As previously discussed, the peak temperature predicted using Rayleigh theory is more

uniform compared to Mie theory. The $T_{peak}^{Rayl}(d_p)$ and $T_{peak}^{Mie}(d_p)$ distributions are then used to define a pyrometric temperature via the Rayleigh approximation, Eq. (4.25), to process the total incandescence signal calculated using $p(d_p)$ in Eq. (4.1). The error in predicting the peak temperature distribution, $T_{peak}^{Mie}(d_p)$ - $T_{peak}^{Rayl}(d_p)$ caused by using the Rayleigh approximation, propagates into the pyrometric temperature through the modeled incandescence signal. Furthermore, this error increases as the distribution becomes wider or as it shifts towards larger particles. Therefore, we expect that the pyrometric temperature difference further increases by increasing the geometric mean or geometric standard deviation in $p(d_p)$.

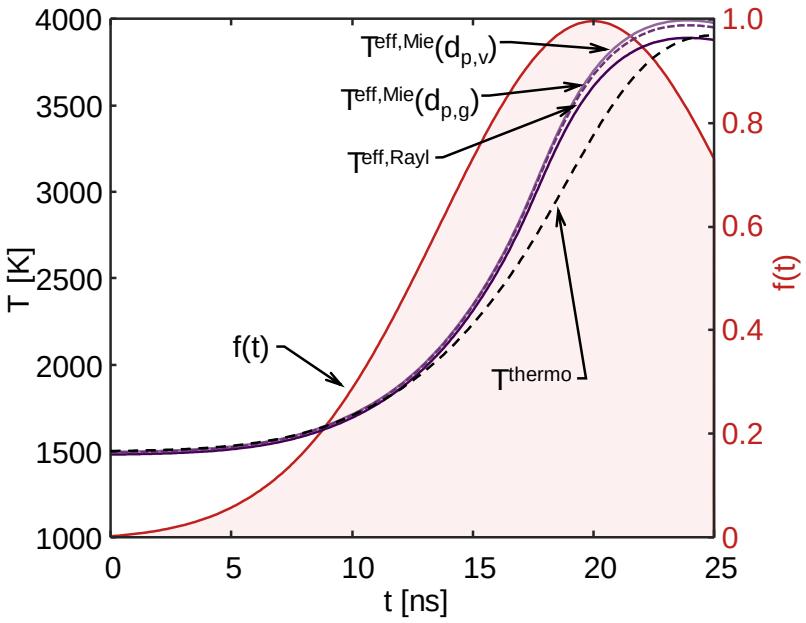

Figure 4-4 The effective temperature of silicon nanoparticles inferred by simulating the incandescence signal (using Mie theory and considering polydispersity) over a wavelengths between 425 nm and 700 nm. Effective temperatures are evaluated using the Rayleigh approximation, Mie theory assuming $d_{p,g}$, and Mie theory assuming $d_{p,v}$. The laser fluence, $f(t)$, is shown as a red line. The cross-sections predicted using Rayleigh and Mie theory produce very similar effective temperatures, all of which exceed the thermodynamic temperature during laser heating.

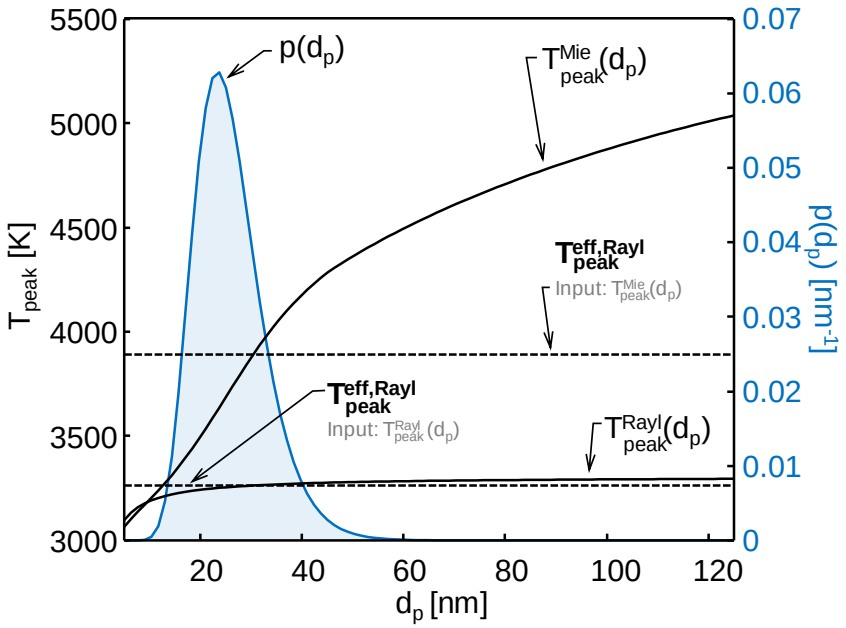

Figure 4-5 Pyrometric temperature of silicon nanoparticles at the peak incandescence as a function of nanoparticle diameter, calculated using either Mie theory, $T_{peak}^{Mie}(d_p)$, or Rayleigh theory, $T_{peak}^{Rayl}(d_p)$, to generate the incandescence. (These temperatures closely correspond to the maximum temperature reached by each size class in Figure 4-3 a and b). Dashed horizontal lines correspond to the pyrometrically-defined peak effective temperature inferred assuming Rayleigh theory (that is $T_{peak}^{eff,Rayl}$ from Eq. (4.26)) for incandescence generated using both methods and assuming the particle size distribution.

4.4.3 Anomalies in the intensity scaling factor

Next, consider the anomalies in the effective ISF for TiRe-LII measurements on silicon nanoparticles reported by Menser et al. [168]. In their study, the data collected by patching together streak camera (Hamamatsu C10910) images recorded with a temporal offset of 1μs and the temporal resolution of the camera was 5 ns. A streak camera operates by transforming the time variations of light pulse into a spatial profile on a detector which is achieved by producing time-varying deflection of the light across the width of the detector. A light pulse enters the instrument through a narrow slit along one direction gets deflected in the perpendicular direction so that photons that arrive first hit the detector at a different position compared to photons that arrive later [192].

Effective temperatures and ISFs are evaluated using Rayleigh theory and shown as circles in Figure 4-6b. While one would expect the effective ISF to be constant, analysis of experimental data shows that it varies with time, and decreases sharply after the laser pulse. Menser et al. [168] attributed

this trend, in part, to the fact that the streak camera data is "temporally blended" due to the finite width of the spectrograph slit. To understand the origin of this anomaly, we simulate the incandescence signal using Eq. (4.1), and progressively relax a range of assumptions in the spectroscopic model used to generate the signal. In all cases, Rayleigh theory is used to calculate the effective temperature from the simulated LII signals. The TiRe-LII data is produced following three scenarios: (*i*) Rayleigh theory for an aerosol composed of silicon nanoparticles having a diameter of 25 nm (matching the assumptions in the pyrometric model); Mie theory with a diameter of 25 nm; (*iii*) Mie theory with polydisperse particle diameters (lognormal with a geometric mean and standard deviation of 25 nm and 1.3, respectively); and finally (*iv*) with the quadrupole approximation, Eq. (4.22), with polydisperse particle diameters.

The pyrometrically-inferred effective ISF, shown in Figure 4-6, changes with the assumptions used to generate the TiRe-LII signals. Using Mie theory to model the laser absorption leads to a higher mass loss due to evaporation and a larger drop in the ISF. Including polydisperse particle sizes exacerbates this effect, since polydispersity broadens the distribution of nanoparticle temperatures, cf. Section 4.4.1. The resulting temporal variation in the ISF resembles the experimental trends reported by Menser et al. [168], suggesting that this effect could be attributed mostly to the use of the Rayleigh absorption cross-section combined with the assumption of monodisperse particle diameters.

These results indicate the need to couple the heat transfer and spectroscopic models in the case of metal aerosols. While this approach was previously necessary to simulate polydispersity during nanoparticle cooling using the Rayleigh model (e.g. [167]), the results shown in Figure 4-6 indicate that, for aerosols of metal nanoparticles Mie theory should be used to model both nanoparticle heating and cooling, in order to capture the nanoparticle temperature distribution at any instant. Figure 4-7 demonstrates the necessary steps for such an approach. Incandescence is simulated using the heat transfer and spectroscopic models, in this case evaluating the absorption efficiency using Mie theory, incorporating polydisperse sizes, and accounting for the change in the refractive index due to melting. At this point, simulated and modeled incandescence traces can be reduced to an effective temperature using Rayleigh theory, Eq. (4.25). The analysis then focuses on identifying the unknown aerosol attributes (e.g. size distribution parameters) by regressing the modeled effective temperatures to the measured effective temperatures, e.g. through Bayesian inference [159].

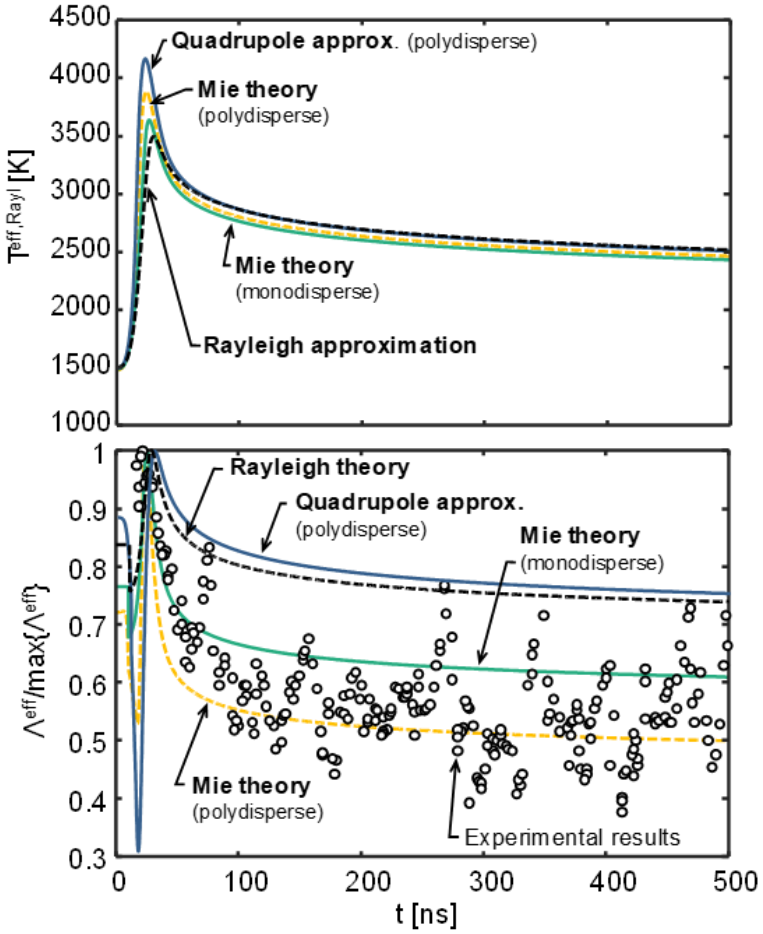

Figure 4-6 Comparing the normalized effective intensity scaling factor, Λ^{eff} /*max*(Λ^{eff}), and temperature, $T^{eff,Rayl}$, (*i*) inferred using Rayleigh theory, Eq. (4.25), after simulating the TiRe-LII signals using different spectroscopic models, and (*ii*) reported directly by Menser et al. [168]. Simulations model liquid silicon nanoparticles with T_g =1500 K, P_g = 100 kPa, α = 0.2, and nanoparticles sizes approximated with a lognormal size distribution having a geometric mean and standard deviation of 25 nm and 1.3, respectively. The nanoparticles are heated using a spatially-uniform and temporally-Gaussian pulse at 1064 nm with a full-width half maximum of 15 ns and a fluence of 8 mJ/mm^2.

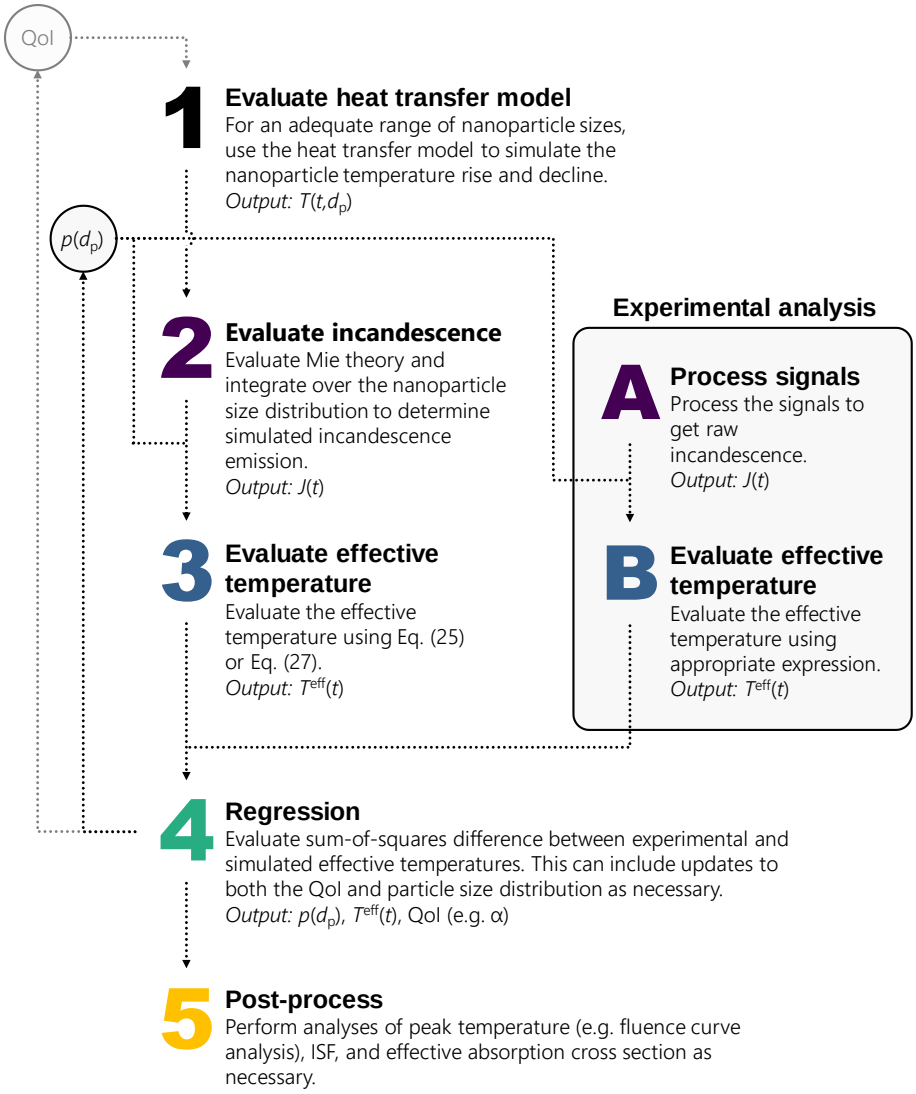

Figure 4-7 Algorithm for inferring nanoparticle quantities of interest (QoI) from TiRe-LII signals for coupled spectroscopic and heat transfer models. In this instance, the particle size distribution is used to evaluate the effective temperature from both simulated and experimental incandescence (i.e. steps 3 and B). In addition, the heat transfer and spectroscopic models in steps 1 and 2 are updated to incorporate the size-dependent absorption cross section predicted by Mie theory and a change in the refractive index when the particle melts.

The major drawbacks of this approach are that: (*i*) calculation of the pyrometric temperature now requires knowledge of the particle size; and (*ii*) the Mie absorption cross-section is computationally-costly to evaluate. The first issue is unavoidable as the above analysis shows that, in the case of metal aerosols, accurate TiRe-LII traces can only be generated if Mie theory is used to simulate incandescence. One may be tempted to circumvent the second issue by using the Mie

quadruple approximation, Eq. (4.22). Surprisingly, Figure 4-6 shows that, when the simulated data is generated with the quadrupole approximation, the pyrometric temperature and ISF differ significantly from those found using Mie theory. As shown in Figure 4-3c, the quadrupole approximation over-predicts the absorption cross-section of the nanoparticle, causing the largest nanoparticles to lose a significant percentage of their mass before the peak laser intensity and therefore less mass is lost after the peak compared to the Mie theory. This effect can be seen as a sharp drop in ISF during the heating process in Figure 4-6. This results in an under-prediction of $\Lambda^{\text{eff}}(t)$ after the signal peak. This finding indicates that the quadrupole approximation should not be used to interpret TiRe-LII measurements on metal nanoparticles.

4.4.4 Peak nanoparticle temperature and excessive absorption

Another anomaly reported in the literature concerns the effective absorption cross-section required for metal nanoparticles to reach the inferred peak temperature at a given laser fluence. Previous treatments by Eremin et al. [113] and Sipkens et al. [21,180] assumed a monodisperse aerosol and determined this quantity by considering the integration of the energy balance in Eq. (4.3) carried out from the start of laser heating until the peak pyrometric temperature, neglecting the cooling terms,

$$\rho\left(T_{\text{g}}\right)\frac{\pi d_{\text{p}}^3}{6}\left[H^{\circ}\left(T_{\text{peak}}^{\text{eff}}\right)-H^{\circ}\left(T_{\text{g}}\right)\right]\approx Q_{\text{laser}} \tag{4.30}$$

where $H^{\text{o}}(T_{\text{g}})$ and $H^{\text{o}}(T_{\text{peak}}{}^{\text{eff}})$ are the enthalpies of the material at the buffer gas temperature, T_{g}, and the peak effective temperature, $T_{\text{peak}}{}^{\text{eff}}$, and Q_{laser} is the total energy transferred to the nanoparticle due to laser absorption throughout the laser pulse. The total laser absorption at a given fluence is

$$Q_{\text{laser}}=F_0\,\frac{\pi d_{\text{p}}^2}{4}Q_{\text{abs},\lambda_{\text{laser}}}. \tag{4.31}$$

If the nanoparticle absorption cross section is modeled using Rayleigh theory, the total absorbed laser energy is

$$Q_{\text{laser}}=F_0\,\frac{\pi^2 d_{\text{p}}^3}{\lambda_{\text{l}}}E\left(\mathbf{m}_{\lambda}\right). \tag{4.32}$$

This expression can now be used to derive an effective "calorimetric" $E(\mathbf{m}_{\lambda})$ that would be necessary to reach the experimentally-derived peak effective temperature,

$$\left[E\left(\mathbf{m}_\lambda\right)\right]_{\text{exp}} = \frac{\lambda_1}{6\pi F_0}\rho\left(T_\text{g}\right)\left[H^\circ\left(T_{\text{peak}}^{\text{eff}}\right) - H^\circ\left(T_\text{g}\right)\right]. \tag{4.33}$$

The nanoparticle size now cancels out in Eq. (4.33). Sipkens et al. [21,180] defined the ratio of the calorimetrically-defined absorption efficiency to the one predicted using the spectroscopic model, which, assuming Rayleigh theory and an aerosol of uniform particle sizes, amounts to

$$\frac{\left(Q_{\text{abs},\lambda_{\text{laser}}}^{\text{eff}}\right)_{\text{exp}}}{\left(Q_{\text{abs},\lambda_{\text{laser}}}^{\text{eff}}\right)_{\text{spectr}}} = \frac{\left[E\left(\mathbf{m}_\lambda\right)\right]_{\text{exp}}}{\left[E\left(\mathbf{m}_\lambda\right)\right]_{\text{spectr}}} \tag{4.34}$$

where $E(\mathbf{m}_\lambda)_{\text{spectr}}$ is derived from the optical properties given in the literature.

Figure 4-1 shows the quantity in Eq. (4.34) derived from the TiRe-LII signals of Eremin et al. [113] and Sipkens et al. [21]. Eremin et al. [113] investigated aerosols of iron nanoparticles having lognormal size distributions with geometric means that varied between 2 and 15 nm and a geometric standard deviation of 1.2. TiRe-LII measurements were carried out using a 1064 nm laser at fluences between 3 to 5 mJ/mm^2 and a full-width half-maximum (FWHM) of 12 ns. Sipkens et al. [21] considered an aerosol of iron nanoparticles having diameters that obeyed a lognormal distribution with a geometric mean and standard deviation of 40 nm and 1.16, respectively; an aerosol of silver nanoparticles having diameters that obeyed a Weibull distribution with a mean of 64.4 nm and a standard deviation of 6.11; and an aerosol of molybdenum nanoparticles, having diameters that obeyed a lognormal distribution with a geometric mean and standard deviation of 45 nm and 1.49, respectively. Figure 4-1 demonstrates that the experimentally-derived cross-section greatly exceeds that predicted by Rayleigh theory, in some cases by more than an order-of-magnitude.

To examine this anomaly, we revisit the assumptions that underlie this calculation. For each of these cases, we generate simulated TiRe-LII signals using Mie theory and account for polydispersity and a change in the refractive index when the nanoparticles melt. The melting effect on the refractive index is assumed to be spontaneous for iron nanoparticles and is calculated using the information in Table 4.1. If we consider how polydispersity and variation in thermophysical properties of the nanoparticles with temperature affect the change to the internal energy of the nanoparticles, a more accurate version of the LHS of Eq. (4.30) is

Table 4.1 Comparing different effective absorption cross-sections inferred from simulated data, given in Figure 4-3b.

Case	**1**	**2**	**3**
Method of calculating T^{eff}	Rayleigh, Eq. (4.25)	Mie, Eq. (4.27)	N/A
Expression to evaluate $(Q_{\text{abs},\lambda})_{\text{exp}}$	Eq. (4.37)	Eq. (4.37)	Eq.
Includes polydispersity?	No (evaluated at $d_{\text{p,g}}$)	No (evaluated at $d_{\text{p,g}}$)	Yes
$(Q_{\text{abs},\lambda})_{\text{exp}}$	0.0113	0.0116	0.0119

$$U_{\text{peak}} - U_0 = \int_0^\infty \left\{ \rho \left[T \;\; d_{\text{p}}, t_{\text{peak}} \right] \frac{\pi d_{\text{p}}^3}{6} H^\circ \left[T \;\; d_{\text{p}}, t_{\text{peak}} \right] \right\} p \;\; d_{\text{p}}, t_{\text{peak}} \;\; \text{d}d_p - \int_0^\infty \left\{ \rho \;\; T_{\text{g}} \;\; \frac{\pi d_{\text{p}}^3}{6} H^\circ \;\; T_{\text{g}} \right\} p \;\; d_{\text{p}}, t_0 \;\; \text{d}d_p \tag{4.35}$$

where $p(d_{\text{p}}, t_0)$ and $p(d_{\text{p}}, t_{\text{peak}})$ are the initial particle size distributions and the size distribution at the peak pyrometric temperature, the latter determined by solving Eq. (4.3), and U_{peak} and U_0 are the total internal energy of the aerosolized particle at the peak and prior to the laser pulse, respectively. By combining Eq. (4.31) and Eq. (4.35) about the geometric mean diameter, the experimentally-derived absorption efficiency can be defined as

$$Q_{\text{abs},\lambda_{\text{laser}} \;\; \text{exp}}^{\text{eff}} \equiv \frac{4\left[U_{\text{peak}} - U_0\right]}{\pi F_0 d_{\text{p,g}}^2}. \tag{4.36}$$

This value can be compared to the one found from $[E(\mathbf{m}_\lambda)]_{\text{exp}}$ following the previous treatment by Eremin et al. [113] and Sipkens et al. [21] by evaluating

$$Q_{\text{abs},\lambda_{\text{laser}} \;\; \text{exp}}^{\text{eff}} = \frac{4\pi d_{\text{p,g}}}{\lambda} \left[E \;\; \mathbf{m}_\lambda \;\; \right]_{\text{exp}}. \tag{4.37}$$

Applying this approach to silicon nanoparticles (using the same simulation parameters as Section 4.4.1) shows that the error caused by neglecting polydisperse particle sizes is less than 5%, *cf.* Table 4.1. Therefore, Eq. (4.30) can be used as a physical approximation of aerosol absorption for both simulating data and for interpreting experiments results.

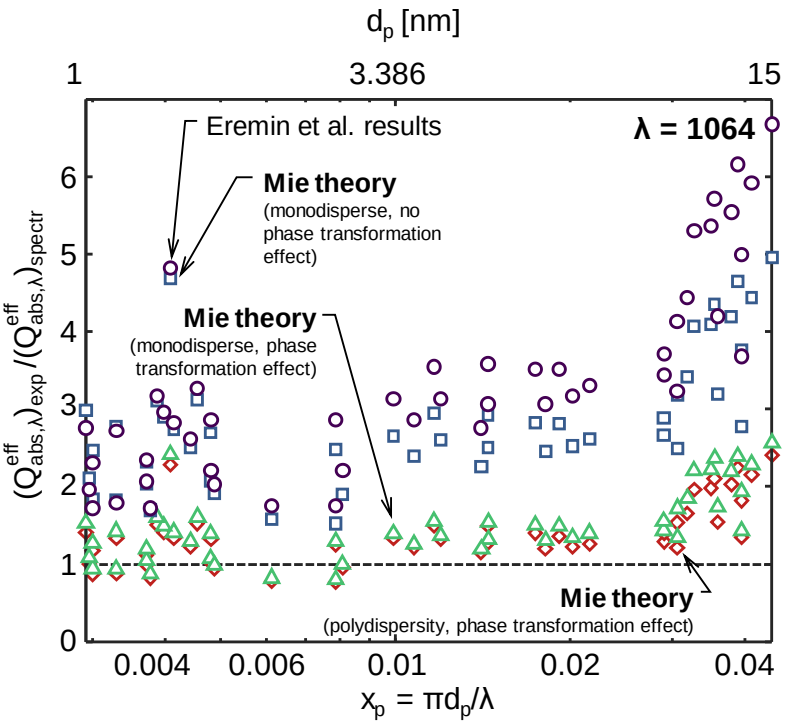

Figure 4-8 Ratio of the calorimetric and spectroscopic absorption cross-sections at the laser wavelength reported by Eremin et al. [113] for aerosols of solid iron nanoparticles. Purple circles are the original results calculated by comparing effective experimental absorption cross-section found from Eq. (4.37) using the peak pyrometric temperature, compared to the Rayleigh absorption cross-section at $d_{p,g}$, Eq. (4.32). The blue squares denote signals computed with Mie theory assuming a monodisperse aerosol ($d_p = d_{p,g}$) and ignoring the change in refractive index due to melting, and then inferring the effective absorption cross-section using Eq. (4.33). Green triangles are found by simulating the signals using Mie for a monodisperse aerosol but with considering the refractive index change due to melting. Red diamonds show results by considering Mie theory, polydispersity and refractive index change due to melting, which is the most accurate model. The largest effect comes from considering the change in refractive index upon melting, and, for larger nanoparticles, Mie theory and polydisperse sizes.

With this in mind, the experimentally-derived effective absorption cross-section, $(Q_{abs,\lambda laser}{}^{eff})_{exp}$, is found by multiplying the data in Figure 4-1 by the spectroscopically-derived Rayleigh absorption cross-section at $d_{p,g}$. The ratio can now be updated using a new spectroscopically-derived absorption cross-section obtained from the particle size distribution found using the algorithm depicted in Figure 4-7. Progressively more elaborate spectroscopic models can be used to simulate the laser heating of the nanoparticle and the emitted spectral incandescence. One should note that, according to Figure 4-7, the effective absorption cross-section used to define T^{eff} does not matter, as long as the simulated and measured signals are processed in the same way.

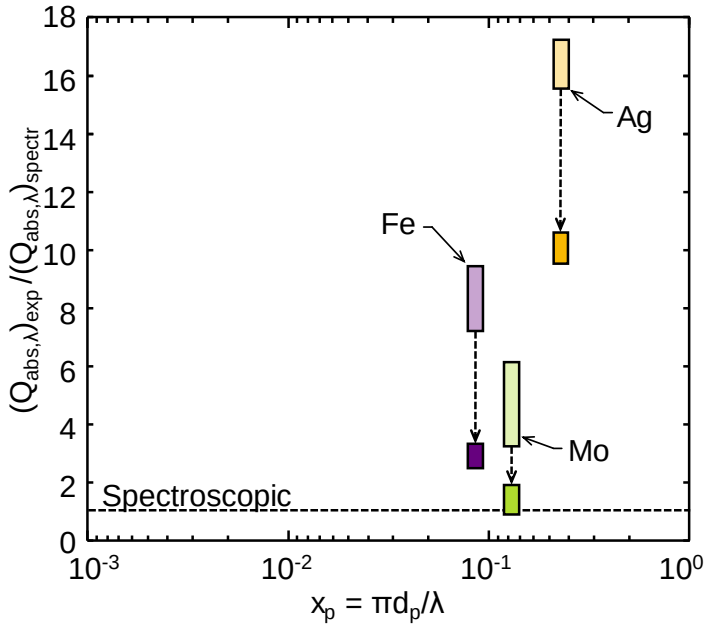

Figure 4-9 Ratio of the calorimetric and spectroscopic absorption cross-sections at the laser wavelength reported by Sipkens et al. [21] for aerosols of solid molybdenum, iron, and silver nanoparticles. Rectangles represent the uncertainty in the reported values. The lighter rectangles show the original values, and the darker rectangles indicate the results when accounting for Mie theory, polydisperse particle sizes, and the change in refractive index with melting.

For aerosols of iron nanoparticles, Figure 4-8 shows the ratio of calorimetrically-derived $(Q_{abs,\lambda_{laser}}^{eff})_{exp}$, reported by Eremin et al. [114] (originally in terms of an effective $E(\mathbf{m}_\lambda)$) to the one predicted using various spectroscopic models to compute the laser absorption and spectral incandescence, including when: (*i*) the absorption cross section is modelled using Mie theory and a monodisperse size distribution is assumed; (*ii*) Mie theory is used, accounting for polydisperse sizes; and, finally, (*iii*) one that accounts for the change in refractive index as the iron nanoparticles melt. The agreement between the experimental results and the modelled data improves considerably as additional effects are included in the simulation, largely resolving the discrepancy between spectroscopic and calorimetric absorption cross-sections. Closer inspection of Figure 4-8 suggests a possible size dependence for larger nanoparticles, although it is unclear whether this is significant in view of experimental uncertainties.

We repeat this analysis using calorimetrically-inferred absorption cross-sections for the iron, silver, and molybdenum nanoparticles reported by Sipkens et al. [21]. Following this procedure, Figure 4-9 shows that the effective absorption cross-sections predicted using the spectroscopic model are

generally more consistent with the calorimetrically-inferred values, particularly for the aerosol of molybdenum nanoparticles. For the iron nanoparticles, accounting for Mie theory, the change in refractive index upon melting, and polydisperse sizes in the spectroscopic cross-section brings it closer to the calorimetric cross-section, but the calorimetric cross-section is still larger by a factor of 2-3. This indicates that the effective temperature reached by the aerosol during the LII measurements is higher than the one predicted by the simulation using the most accurate physical model. This remaining discrepancy may suggest that the nanoparticle size distribution is larger than what Sipkens et al. [21] measured by dynamic light scattering. It is also possible that the aerosol contained aggregates, as opposed to isolated nanospheres, which would affect both the spectroscopic and heat transfer models. Rayleigh-Debye-Gans fractal aggregate (RDG-FA) theory does not apply to these aggregates because it is fundamentally dependent on primary particles to be in the Rayleigh regime. For aggregates, multiple internal scattering may increase the overall absorption efficiency of the aggregate compared to the individual nanoparticles [23,122,193,194]. Semi-analytical methods such as discrete dipole approximation (DDA) [87,136,195] or T-matrix [86,122,127] or fully numerical schemes such as finite-different time-domain (FDTD) [196] can be used to retrieve the optical properties of aggregates. Due to the heat up the aggregates will go through a sintering process which will change their morphology during the measurements [197,198]. Partial oxidation of the nanoparticle could also increase the absorption cross-section due to constructive electromagnetic field interference [199]. In the case the nanoparticles are synthesized in a colloidal solution, a surfactant must be used to stop agglomeration and growth of nanoparticles. The surfactant could remain on the nanoparticle after the aerosolization process and potentially change the nanoparticle to a core-shell nanoparticle. This could change the optical properties of the nanoparticle dependent upon the time which the surfactant remains on the surface during the heating process. Alternatively, the uncertainty in the Clausius-Clapeyron equation prediction of vapour partial pressure may contribute to the remaining discrepancies [168]. In the case of Mo nanoparticles, due to high melting temperature (~ 2,896 K) no evaporation occurs and the discrepancy is completely solved after applying the Mie theory and polydispersity.

For the silver nanoparticles, accounting for Mie theory, polydispersity, and the change in refractive index lowers the ratio of calorimetrically- to spectroscopically-defined absorption efficiencies from 16.4 ± 0.72 to 10.1 ± 0.45. The large ratio is a consequence of the relatively small absorption cross-section of silver nanoparticles. In principle, it should not be possible for the laser pulse to heat the silver nanoparticles more than 100 K above their initial temperature at the given fluences. This suggests that other phenomena may be involved (e.g. the observed signals are not incandescence,

but some other non-incandescent phenomena [200]). The TiRe-LII measurements on silver will discuss in details in *Chapter 6*.

4.4.5 Spectral distribution of E(m$_\lambda$) for iron nanoparticles

Finally, we consider the discrepancy between the experimentally-inferred and spectroscopically-derived values of $E(\mathbf{m})_r$, which is defined as

$$E\left(\mathbf{m}\right)_r \equiv \frac{E\left(\mathbf{m}_{\lambda_1}\right)}{E\left(\mathbf{m}_{\lambda_2}\right)}. \tag{4.38}$$

As expected the $E(\mathbf{m})_r$ from Rayleigh theory is independent of particle size. In contrast, the equivalent $E(\mathbf{m})_r$ calculated by Mie theory depends on particle size,

$$E\ \mathbf{m}\ _{r,\mathrm{Mie}} = \frac{\lambda_2\ Q_{\mathrm{abs},\lambda 1}}{\lambda_1\ Q_{\mathrm{abs},\lambda 2}} \tag{4.39}$$

Sipkens et al. [21] estimated an experimentally-implied value of $E(\mathbf{m})_r$ by assuming that the plateau in the peak effective temperature for higher fluences should only slightly exceed the boiling point of the material, T_{boil}. Under this assumption, the value of $E(\mathbf{m})_r$ implied by the experiments can be approximated as

$$\left[E\left(\mathbf{m}\right)_r\right]_{\mathrm{exp}} \approx \frac{J_{\lambda 1}(t)}{J_{\lambda 2}(t)}\left(\frac{\lambda_1}{\lambda_2}\right)^6 \exp\left[-\frac{hc_0}{k_B}\left(\frac{1}{\lambda_2}-\frac{1}{\lambda_1}\right)\frac{1}{T_{\mathrm{boil}}}\right]. \tag{4.40}$$

Using the boiling temperature of bulk iron ($T_b \approx 3073$ K), Sipkens et al. found $[E(\mathbf{m})_r]_{\mathrm{exp}} \approx 1.1$. This value is consistent with the assumption that $E(\mathbf{m})_r = 1.0$, which was universally adopted in previous LII studies on iron nanoparticles (e.g. Ref. [163]). However, this value is inconsistent with the value of $E(\mathbf{m})_r = 1.82$ derived from published ellipsometry measurements on molten iron, cf. Table 1. The $E(\mathbf{m})_{r,\mathrm{Mie}}$ approaches unity for nanoparticles larger than 50 nm, *cf*. Figure 4-10 therefore, the discrepancy might be partially attributed to the faulty assumption of Rayleigh theory.

Of course, if Rayleigh theory cannot be applied, $E(\mathbf{m})_r$ loses its physical meaning. In this case, one can attempt to reproduce this anomaly by defining an $[E(\mathbf{m})_r]_{\mathrm{sim}}$ by combining Eq. (4.40) with simulated incandescence that incorporates Mie theory, polydispersity and the change in the refractive index due to melting. Simulated TiRe-LII measurements for iron nanoparticles are generated for this purpose using the experimental parameters reported by Sipkens et al. [21] ($d_{p,g} = 40$ nm, $\sigma_{p,g} = 1.16$) at

a fluence of $F_0 = 2.9$ mJ/mm^2. Following this procedure results in $[E(\mathbf{m})_r]_{sim} = 11.17$. The magnitude of this value, which greatly exceeds what could be considered plausible, stems from the fact that $[E(\mathbf{m})_r]_{sim}$ must significantly enhance the incandescence from the nanoparticles, which only reach $T_{peak}^{eff,Rayl} = 1795$ K, to match the emission expected from nanoparticles at the boiling point ($T_{boil} = 3073$ K) used in Eq. (4.40).

To proceed, then, we next consider that the excessive absorption by the nanoparticle can be accommodated by artificially modifying $Q_{abs,\lambda}^{Mie}(d_p)$ to $yQ_{abs,\lambda}^{Mie}(d_p)$, where y coefficient accounts for some unknown mechanism that could enhance the absorption. Figure 4-11 shows that as y increases, the value of $T^{eff,Rayl}$ increases to T_{boil} and $[E(\mathbf{m})_r]_{sim}$ decreases to the value inferred by Sipkens et al. [21] (in fact, dropping below 1.1). This suggests that, if the excessive absorption is assumed to be physical, the difference between the spectroscopic value of $E(\mathbf{m})_r$ and the experimental $[E(\mathbf{m})_r]_{exp}$ from Sipkens et al. [21] could stem from a misapplication of Rayleigh theory. This is to say that the combination of: (*i*) Mie theory causing a distribution of nanoparticle temperatures; (*ii*) these temperatures being weighted more heading towards the larger, hotter particles (cf. Figure 4-5); and (*iii*) the inadequacy of Eq. (39) and using a single nanoparticle temperature to infer a value of $E(\mathbf{m})_r$ combine to suppress the perceived value of $[E(\mathbf{m})_r]_{exp}$.

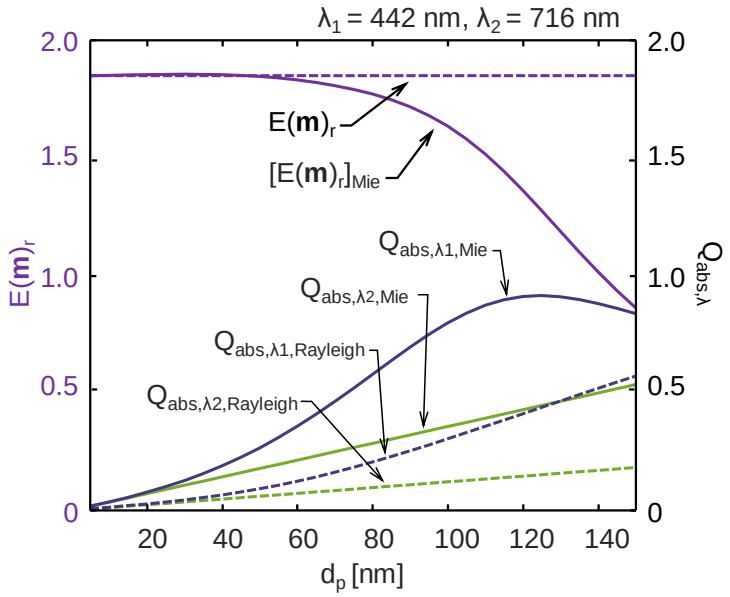

Figure 4-10 Comparing Rayleigh and Mie absorption at 442 nm and 716 nm for liquid iron nanoparticles.

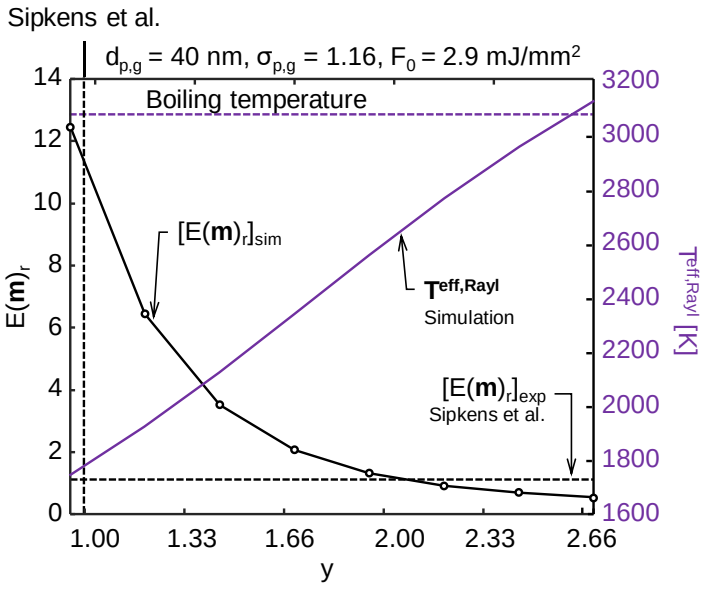

Figure 4-11 Comparison of $[E(\mathbf{m})_r]_{sim}$, which is inferred from simulations, as a function of y coefficient for the size distribution reported by Sipkens et al. [21] ($d_{p,g}$ = 40 nm, $\sigma_{p,g}$ = 1.16) to $[E(\mathbf{m})_r]_{exp}$ inferred from experimental data at F_0 = 2.9 mJ/mm^2.

Another possibility is that there is no need to artificially modify $Q_{abs,\lambda}^{Mie}(d_p)$ to reach lower values of $[E(\mathbf{m})_r]_{sim}$, but the size distribution differs from the ex-situ characterization. This could lead to higher nanoparticle temperatures and therefore a lower $[E(\mathbf{m})_r]_{sim}$. Figure 4-12 shows a contour plot

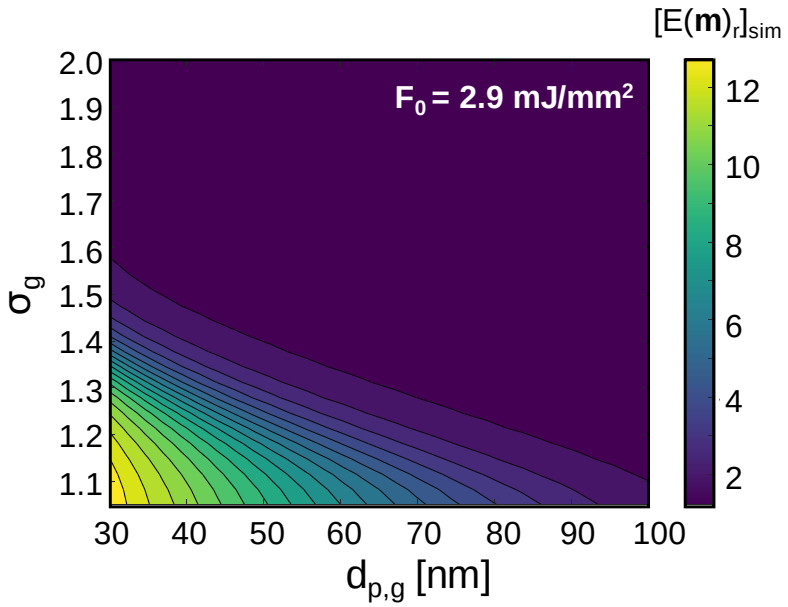

Figure 4-12 Simulation results as a function of $d_{p,g}$ and $\sigma_{p,g}$ for a fixed value of laser fluence. The minimum value of $[E(\mathbf{m})_r]_{sim}$ is 1.21 in the figure.

of $[E(\mathbf{m})_r]_{sim}$ as a function of $d_{p,g}$ and the geometric standard deviation, $\sigma_{p,g}$, respectively for a fixed fluence of $F_0 = 2.9$ mJ/mm^2. The results show that a value of 1.21 is reached only for extreme values of $d_{p,g}$ and $\sigma_{p,g}$, which is significantly different from the DLS size distribution reported by Sipkens et al. [21]. Accordingly, this scenario is unlikely.

4.4.6 Effect of nanoparticle charge

The Mie scattering coefficients in Eqs. (4.17) and (4.18) are derived by solving the Helmholtz wave equation for a non-charged and non-magnetic sphere suspended in a non-absorbing medium [83,120]. During the LII experiments, we expect the nanoparticles to accumulate a positive charge due to electron emission processes [201–203]. The synthesis process can also impart a charge on the nanoparticles. In the case of a nanoparticle colloid, for example, synthesis surfactants are used to protect the surface of the nanoparticles, stop their growth and prevent agglomeration by adding a positive or negative net charge to the nanoparticle [204].

In the case of a non-magnetic charged nanoparticle, the modified Mie scattering coefficients are [205–207]

$$a_l = \frac{\mathbf{u}\psi_l(\mathbf{u}y)\psi'_l(y) - \psi_l(y)\psi'_l(\mathbf{u}y) + g\mathbf{u}\psi'_l(\mathbf{u}y)\psi'_l(y)}{\mathbf{u}\psi_l(\mathbf{u}y)\xi'_l(y) - \xi_l(y)\psi'_l(\mathbf{u}y) + g\mathbf{u}\psi'_l(\mathbf{u}y)\xi'_l(y)}, \tag{4.41}$$

and

$$b_l = \frac{\psi_l(\mathbf{u}y)\psi'_l(y) - \mathbf{u}\psi_l(y)\psi'_l(\mathbf{u}y) - g\mathbf{u}\psi_l(y)\psi_l(\mathbf{u}y)}{\psi_l(\mathbf{u}y)\xi'_l(y) - \mathbf{u}\xi_l(y)\psi'_l(\mathbf{u}y) - g\mathbf{u}\xi_l(y)\psi_l(\mathbf{u}y)}, \tag{4.42}$$

where

$$g = -\frac{f_c|\Phi|}{x_p}\frac{\omega}{\omega + \gamma_s i}. \tag{4.43}$$

In Eq. (4.43) Φ is the electrostatic potential of the nanoparticle in volts defined as

$$\Phi = \frac{N_e e_{elec}}{2\pi\varepsilon_o d_p}\mathrm{sgn}(N_e), \tag{4.44}$$

where N_e is integer charge of the nanoparticle, e_{elec} is electron charge, sgn(·) is the signum function, $f_c = \varepsilon_0\mu_0 e_{elec}/m_{elec} = 1.96 \times 10^{-6}$, and the parameters $\gamma_s \approx 2\pi k_B T_p/h$ [208,209], h and k_B are Planck and Boltzmann constants, respectively. As shown in Eq. (4.44) the charge to size ratio of the nanoparticle alters the Mie scattering coefficients compared to the non-charged ones.

We consider absorption efficiencies calculated using the exact Mie coefficients, Eqs. (4.41) and (4.42), as well as an approximation by Wang et al. [208] for 442 nm, 716 nm and 1064 nm as a function of the nanoparticle charge and at $T_p = 2000$ K. Mitrani [201] et al. predicted a maximum of $N_e = 40$ for carbonaceous nanoparticles through thermionic emission during TiRe-LII experiments. Talebi-Moghaddam et al. [200] predicted a maximum value of $N_e = 12$ for liquid silicon nanoparticle. In all cases, our calculations show that the nanoparticle charge has a negligible impact on the absorption efficiency.

4.5 Conclusions

Time-resolved laser-induced incandescence is increasingly applied to measure metal nanoparticles, but there remain several anomalies that cannot be explained using standard LII models. Instead, a number of effects have been speculated in the literature, including size-dependent optical properties and signal

contamination by non-incandescent laser-induced emission (e.g. from a plasma). Our analysis showed that many of these discrepancies, including temporal variation in the intensity scaling factor during TiRe-LII measurements on molten (metal) silicon, enhanced absorption cross-sections of molybdenum and iron nanoparticles, and the $[E(\mathbf{m})_r]_{exp}$ ratio for iron nanoparticles, can be partially explained by: (*i*) the fact that the Rayleigh approximation of Mie theory is usually invalid for metal nanoparticles under TiRe-LII conditions; (*ii*) polydisperse particle sizes, coupled with Mie theory, increase temperature non-uniformity in the aerosol; (*iii*) and the fact that the radiative properties of iron change significantly upon melting. Our analysis also shows that the charge state of metal nanoparticles is unlikely to contribute to these phenomena.

While implementing Mie theory explains some of the observed anomalies, some problems remain. For example, the spectroscopically-defined absorption cross-section of silver nanoparticles restricts nanoparticle heating to only several hundred Kelvin, which would render incandescence undetectable. Also, in the case of iron nanoparticles, while the discrepancy between calorimetrically- and spectroscopically-derived absorption cross-sections has been reduced, it has not been eliminated fully. This may be connected to the discrepancy in the $E(\mathbf{m})_r$ value for iron nanoparticles, which is not completely explained by the faulty assumptions of Rayleigh approximation and monodisperse sizes. These results point to other deficiencies in the spectroscopic model, such as non-incandescent LIE contaminating the incandescence signals, uncertainty in the physical parameters used in the simulation, oxidation, or aggregation and sintering effects for iron nanoparticles.

Chapter 5
Plasma emission during time-resolved laser-induced incandescence measurements

The content of this chapter is an extended version of an article published in *Applied Physics B* titled, "Plasma emission during time-resolved laser-induced incandescence measurements of aerosolized metal nanoparticles [200]."

5.1 Introduction

In the previous chapter, it is shown that how using Mie theory within TiRe-LII spectroscopic model instead of the Rayleigh approximation and combining it with polydispersity and change of refractive index due to melting could at least partially explain the excessive absorption phenomenon as well as the temporal variation of the integral scaling factor (ISF) in the case of LII measurements on liquid silicon. However, these modifications do not completely address anomalous cooling and remaining excessive absorption for LII measurements on Fe and Ag nanoparticles.

A laser-induced aerosol plasma could potentially explain each of these observations. Anomalous cooling may be due to the corruption of spectral incandescence by bremsstrahlung emission, which would be most pronounced at short wavelengths, leading to an elevated pyrometric temperature lasting until the plasma dissipates [112,117]. Enhanced absorption of the laser pulse by metal nanoparticles could be caused by inverse bremsstrahlung absorption, which may also explain the increased extinction of the aerosol during and shortly after the laser pulse in LII/LOSA measurements. Also, while Saffaripour et al. [210] speculated that the change in extinction they observed in their combined LII/LOSA measurements on soot could be due to a change in the optical properties of soot induced by laser heating, these results could alternatively be explained (at least in part) by plasma absorption. Laser-induced plasmas surrounding nanoparticles have been observed in other scenarios,

albeit at higher fluences. For example, when carrying out laser-induced breakdown spectroscopy (LIBS) measurements on metal oxide nanoaerosols, Tse's group [211,212] discovered a fluence regime, typically ~30 mJ/mm^2, in which it is possible to break down the nanoparticle and not the enveloping gas, based on the presence of atomic line emission from the nanoparticle constituents and the absence of lines from the gas constituents. They hypothesize that the laser pulse induces a localized plasma that envelops and consumes the nanoparticle, without affecting the gas. Evidence for plasma formation at even lower fluences (~10 mJ/mm^2) is provided by Menser et al. [213], who observed spontaneous atomic emission from laser-heated silicon nanoparticles, lasting for hundreds of nanoseconds after the laser pulse, cf. Figure 5-1. This signal comes from a sustained source of excited silicon atoms, which implies the existence of laser-induced plasma. In another study, Maffi et al. [214] investigated laser-induced emission (LIE) from titania (TiO_2) aerosolized nanoparticles using a fluence of 6 mJ/mm^2. Their results indicated that in many cases, the radiation could not be purely presumed as incandescence and the perturbations in the signal caused by short-lived photoluminescence of titania and emission of molecular bands should be considered as incandescence signal contaminators.

The current chapter examines the physical phenomena that may underlie laser-induced plasma formation in LII experiments on the metallic nanoparticles, specifically molten Si, Fe, and Mo nanoparticles in argon, and quantifies how it may affect spectral intensity measurements. The different thermophysical properties of these nanoparticles, especially the boiling point, latent heat of vaporization, and refractive index, enables a comparative analysis that provides insight into the physics underlying this phenomenon. The results show that plasma formation depends strongly on the laser pulse fluence, nanoparticle material and size, and ambient gas conditions. While plasma absorption and emission could explain both anomalous cooling and excessive absorption phenomena for high-fluence LII experiments, the current model is unable to justify some of the discrepancies reported in the literature for low-fluence experiments. Suggestions to improve the current plasma model are proposed as future work.

5.2 Initial electron generation mechanisms

Plasma formation starts from a small number of "trigger electrons", which accelerate in the presence of the oscillating E-M wave and produce more electrons through impact ionization, thereby initiating an "electron cascade." Trigger electrons can potentially arise from two primary candidate sources for

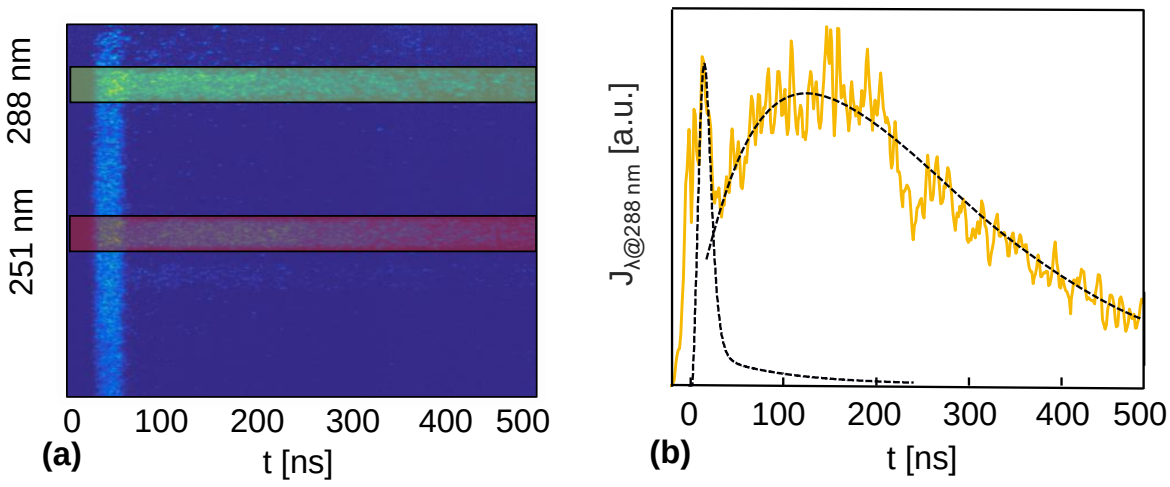

Figure 5-1 (a) Temporal versus spectral emission of atomic line emissions from Si. The observed lines are 251 nm and 288 nm (b) The observed signal composed of the "prompt" feature and the "delayed" component with a longer intensity decay. The figure is used with permission from Menser et al. study [213].

an aerosol: (*i*) the molecules in the gas phase surrounding the nanoparticle, including both evaporated nanoparticle molecules and bath gas molecules; and (*ii*) the metallic nanoparticle itself. The interaction of the laser pulse with the gas-phase molecules can release initial electrons due to multi-photon ionization (MPI), while electrons can be emitted by the nanoparticle through plasmonic decay photoemission [215], thermionic emission [216], and thermally-assisted photoemission [202]. We consider the plausibility of each scenario below.

5.2.1 Trigger electrons from the gas-phase

A molecule having an ionization potential of W_{ion} can be directly ionized by a photon having a larger energy $e_p = h\nu$. However, several photons with energies below the atomic ionization potential can also ionize the molecule via MPI if they interact with the molecule in a timescale shorter than the relaxation

time of the valence electron. The ionization rates for both the evaporated species and bath gas molecules are proportional to $I^{n_{ph}}$ [217]

$$W_{\mathrm{MPI}} = \sigma_{\mathrm{MPI}}\left(\lambda, W_{\mathrm{ion}}\right) I^{n_{\mathrm{ph}}} \tag{5.1}$$

where I is the pulse intensity, σ_{MPI} is the MPI cross-section of each species, and n_{ph} is the number of photons simultaneously required to ionize each species,

$$n_{\mathrm{ph}} = \mathrm{int}\left(\frac{W_{\mathrm{ion}}}{e_{\mathrm{p}}} + 1\right) = \mathrm{int}\left(\frac{W_{\mathrm{ion}}}{h\nu} + 1\right). \tag{5.2}$$

While MPI is a viable source of trigger electrons in LIBS experiments carried out at higher fluences [41], the laser intensities and pulse durations typical of LII experiments are insufficient to ionize the metal vapors. Moreover, experiments on bulk silicon irradiated by a 1064 nm laser pulse with intensities up to 10^7 W/cm^2, far higher than those typical of LII measurements, showed no evidence of MPI-generated electrons [218], and, since the ionization energy of the bath gas molecules exceed those of evaporated metal atoms (e.g., Ar has a first ionization energy of 15.57 eV [219] while that of Si is 8.15 eV [220]), this result would appear to immediately disallow MPI as a candidate source of trigger electrons in LII experiments.

However, some metallic nanoparticles act as "antennas" in the presence of an oscillating E-M field due to plasmonic effects, which causes high-intensity near-field regions to form in the vicinity of the nanoparticle [221,222]. In such cases, a molecule located within the near-field region may encounter a much higher intensity field compared to one that is further away. This phenomenon has been exploited to reduce the fluence threshold needed to produce a laser-induced plasma surrounding gold nanoparticles in water [177,223]. The near-field electric/magnetic spatial intensity profile is given by $n_{\mathrm{NF}}(\mathbf{r}) = E(\mathbf{r})/E_0$, where E_0 is the incident-field electrical intensity, and $E(\mathbf{r})$ is the electric field in the vicinity of the nanoparticle. This quantity can be readily found using Mie theory [177,199,224] for isolated nanospheres. Figure 5-2*a* shows $n_{\mathrm{NF}}(\mathbf{r})$ contours for a 30 nm liquid silicon nanoparticle, and maximum field enhancements for Fe, Mo, Si, and Ag nanoparticles are plotted in Figure 5-2*b* as a function of nanoparticle size. Incorporating these near-field enhancements into Eq. (5.1), using pulses up to 10 mJ/mm^2 with a 10 ns top-hat pulse ($I < 10^9$ W/cm^2), and assuming that evaporated atoms remain within the enhanced region during the entire laser pulse duration resulted in an insignificant amount of MPI ionization. Therefore, MPI ionization can be discounted as a candidate source of trigger electrons in 1064 nm LII experiments for Fe, Mo, Ag, and Si nanoparticles. This conclusion may not

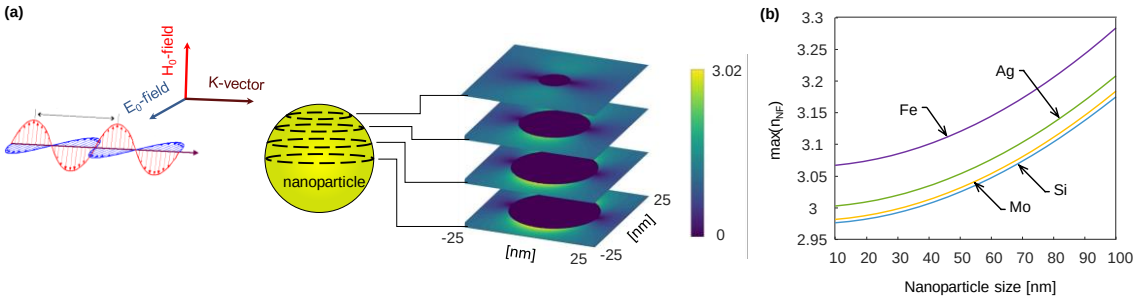

Figure 5-2 (a) Near-field enhancement around a 30 nm molten silicon nanoparticle interacting with 1064 nm incident wavelength. (b) Maximum near-field profile as a function of nanoparticle size for different nanoparticles.

hold at a shorter excitation wavelength, for example, 532 nm, due to the higher photon energy. Also, in the case of aggregation, the near field could intensify drastically due to the near-field coupling phenomenon [225,226].

5.2.2 Trigger electrons from the nanoparticle

Electron emission from the nanoparticle may also be enhanced through plasmonics. Following plasmon excitation due to light absorption, electromagnetic decay occurs on a femtosecond time scale, either radiatively through photon re-emission or non-radiatively by emitting hot electrons [227]. In the non-radiative process, surface plasmons first decay into single-electron excited states. This may be followed by photoemission if the electron exceeds the work function of the material, which specifies the energy needed for an electron to escape the metallic surface. Electron emission may originate from the conduction band. Valence bands could also contribute to the emission (e.g., d-band) in the case of plasmonic nanoparticles [228–230]. Plasmonic decay has been used extensively for enhancing the efficiency of photovoltaics using noble metals nanoparticles such as Au and Ag [231–233]. However, our analysis of Fe, Mo and Si nanoparticles between 10-100 nm, irradiated by 1064 nm pulse, did not exhibit any plasmonic decay photoemission. Nevertheless, this phenomenon could be a contributing factor for trigger electron emission in LII experiments on Ag and Au nanoparticles (e.g., Refs. [21,57]), which will be discussed in *Chapter 6*.

Thermionic emission [216] represents another candidate source of trigger electrons from the nanoparticle. It arises from the fact that electron energies within a metal obey a Boltzmann distribution,

and a fraction will thus have an energy exceeding the work function. The rate of electron emission J_{th} is governed by the Richardson-Dushman equation [216]

$$J_{th} = A_R T_p^{\,2} \exp\left[\frac{-W - \Phi_e}{k_B T_p}\right], \tag{5.3}$$

where $A_R = 7.503 \times 10^6$ electrons/(nm^{2}sK^2), W is the work function, and k_B is Boltzmann constant. The ionization potential, Φ_e, depends on the spontaneous charge of the nanoparticle N_e and its size according to [234]

$$\Phi_e(t) = \frac{N_e^{\,2}(t) e^2}{4\pi\varepsilon_0 d_p(t)} \mathrm{sgn}(N_e), \tag{5.4}$$

where ε_0 is the vacuum permittivity and sgn(·) is the sign of the nanoparticle accumulated charge. Thermionic emission has been included in some LII models, but only in the context of how it affects nanoparticle cooling [201,235].

The number flux of ionized atoms evaporated from the nanoparticle surface can be found from the Saha-Langmuir equation, which is derived assuming local thermal equilibrium across the phase interface of the nanoparticle [216]. The ratio of the number density of evaporated ionized species n_1 to neutrals n_0 is

$$\frac{n_1}{n_0} = \frac{Z_1}{Z_0} \exp\left[\frac{-W_i + W + \Phi_e}{k_B T_p}\right], \tag{5.5}$$

where Z_1 and Z_0 are associated partition functions. In the case of silicon nanoparticles at 4,000K (a typical peak LII temperature) these are 5.6 and 9.1 respectively [236], and W_i is the ionization potential. Ion emission will change the ionization potential, Φ_e, and consequently augment the electron emission rate, J_{th}.

The accumulated number of electrons emitted by the nanoparticle is limited by ionization potential growth due to positive charge build-up of the nanoparticle, *cf*. Eq. (5.4). As an example, Mitrani et al. [201] predicted that approximately 25 accumulative electrons would be emitted from a 32 nm diameter graphite nanoparticle during an LII measurement, which would likely be inadequate to initiate a plasma. However, most metallic nanoparticles have significantly higher evaporation rates compared to carbonaceous nanoparticles, resulting in more ion emission via the Saha-Langmuir equation. Ion emission reduces the positive charge potential and induces more electron emission from

the nanoparticle. This assumption is valid for the case of a low ion density accumulation in the vicinity of the nanoparticle so that the emission of ions does not affect the Richardson-Dushman equation [216]. The emission of thermal electrons strongly depends on the rate of atom and ion evaporation, which, in turn, depends on absorption efficiency of the nanoparticle as well as the enthalpy of vaporization and atomic mass.

Accumulative thermionic electron emission from a 40 nm diameter Si nanoparticle is shown in Figure 5-3 (a) for different fluences. The accumulative electron emission increases at high fluences due to higher temperatures and evaporation rates, which collectively result in a greater rate of ion emission from the nanoparticle. Also, the ratio of the total number of emitted ions to the total emitted molecules (taken to be single Si atoms [237]) is less than 2.5% as shown in Figure 5-3 (a). If the effect of ion emission on the nanoparticle charge state is neglected, on the other hand, only 12 electrons are emitted. Low electron emission, in this case, is due to the positive charge built-up that halts the emission of thermal electrons early during the pulse, as shown in Figure 5-3b. This analysis suggests that, for low melting-point metals, thermionic emission is the most likely candidate source of trigger electrons.

Finally, thermally-assisted multiphoton photoelectric emission [202,238,239] arises from the fact that the work function drops by increasing the plasmon electron energy over the Fermi level due to the elevated temperature of the material. This, in turn, increases the probability of multiphoton ionization from the nanoparticle. During a laser-pulse lasting on the order of nanoseconds, one would expect electrons emitted through thermally-assisted multiphoton photoelectric emission to precede thermionic emission, since the former scenario can occur at lower temperatures. Modeling this phenomenon requires several empirically-derived coefficients [240], which are unavailable for liquid Fe, Mo, and Si in the literature. Accordingly, this phenomenon is excluded from this study.

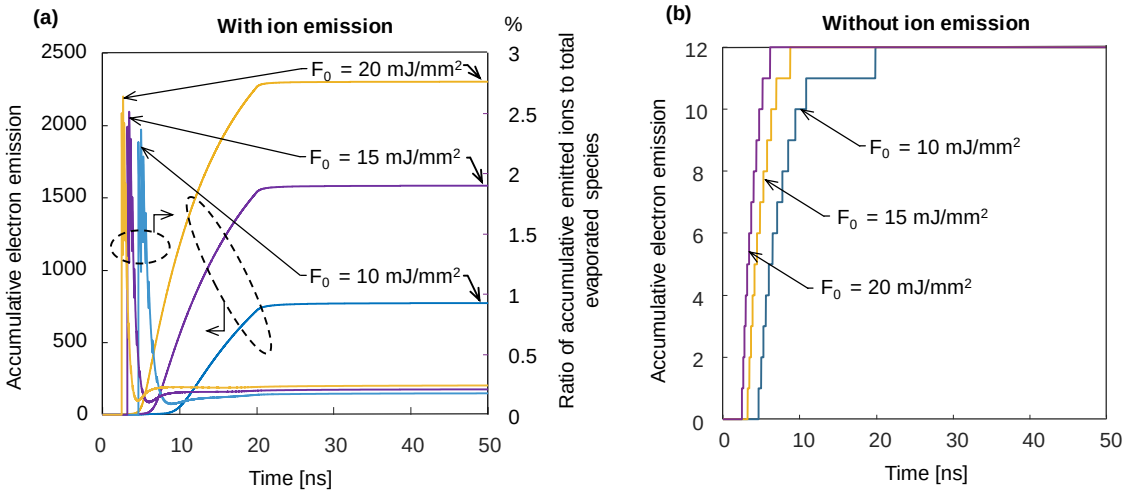

Figure 5-3 Accumulative electron emission, and ratio of emitted ions to total evaporated species, from a Si nanoparticle during a 20 ns top-hat laser pulse for three different fluences with: (a) the influence of ion emission on the charge state of the nanoparticle; and (b) neglecting this effect.

5.3 Laser-induced aerosol plasma generation

A plasma forms when trigger electrons accelerate in the presence of the oscillating E-M field of the laser and collide with the bath gas molecules and evaporated nanoparticle neutrals and ions. The number density of neutral bath gas molecules far exceeds the evaporated nanoparticle atoms in LII experiments, so one may expect that the primary interaction between the E-M wave and the plasma is via inverse neutral bremsstrahlung absorption as the electrons scatter from the neutral bath gas species. Further ions and electrons are generated from the interaction of electrons with metallic evaporated molecules via impact ionization. Some of the free electrons combine with the ions to produce neutrals.

The initial 100 ns of plasma formation and growth is called the "early plasma" problem [241]. The characteristic time constant for gas-phase collisional processes is much longer than those governing processes that control transport across the nanoparticle phase boundary. Accordingly, local thermal equilibrium (LTE), which underlies both the Saha equation, describing the ionization states of gas-phase species, and Boltzmann kinetic theory, which governs the distribution of atomic energy levels [241], is unlikely to hold. Instead, empirical relations are used to model the initial breakdown event [242]. Unfortunately, the few models reported in the literature apply to lower laser wavelengths and higher pulse intensities compared to those used in LII experiments, which result in significantly higher

MPI-driven electron emission [242–244]. Therefore, we must derive empirical electron growth equations appropriate to LII experiments [245].

In order to simplify the analysis, electron and ion growth models neglect electron diffusion and recombination. Moreover, the electron impact ionization rate is assumed to be sufficiently high to ionize all the evaporated species. The net effect of these assumptions and simplifications is to provide the maximum possible number density of electrons and ions, and thus the maximum possible influence of laser-induced plasma emission on LII measurements. We also assume that the electrons are not sufficiently energetic to ionize the LII bath gas species, which has a much higher ionization potential. This treatment is supported by the fact that typical LII fluences are less than those used in PS-LIBS [212], in which no bath gas ionization was observed. Double ionization of the evaporated species is similarly unlikely, since Si^{++}, Fe^{++} and Mo^{++} ionization potentials are approximately equal to the Ar^{+} ionization potential.

The duration of the LII laser pulse is usually less than 30 ns. Early plasma dynamics suggest that there is an insufficient opportunity for the plasma to equilibrate with the LII bath gas molecules [243,246]. Therefore, it can be assumed that the electrons and ions emitted by the nanoparticle are at a much higher temperature compared to the bath gas. Accordingly, the LII plasma submodel consists of two distinct systems: (*i*) the bath gas, which is assumed to be in local thermal equilibrium (LTE) at T_g; (*ii*) and ions and electrons emitted by the nanoparticle having speeds that approximately obey Maxwellian distributions corresponding to the plasma temperature T_{pl} and their respective masses.

5.4 Thermal emission from a laser-induced plasma

Broadband emission and absorption of a plasma is a consequence of the non-quantized (“free-free”) transitions in electronic translational energy states [247]. Continuum emission originates from non-quantized deceleration of free electrons as they interact with charged particles or the atomic field of neutrals. Likewise, photons are absorbed by free electrons undergoing sudden acceleration around ions and neutrals via inverse bremsstrahlung. Accordingly, plasma emission depends on the instantaneous spatial distribution of the electrons, ions, and neutrals, as well as their temperatures.

Bremsstrahlung radiation due to scattering of electrons from ions per unit volume, time, solid angle, and wavelength is given by [248,249]

$$E_{\text{e-i},\lambda}\left(T_{\text{pl}},\mathbf{r},\lambda,t\right)=\underbrace{\frac{16}{3}\left(\frac{\pi}{6}\right)^{1/2}\frac{q_{\text{e}}^{6}}{{c_0}^{2}{m_{\text{e}}}^{2}}\left(\frac{m_{\text{e}}}{k_{\text{B}}}\right)^{1/2}}_{C_{e-i}}\frac{n_{\text{e}}\left(t\right)n_{\text{i}}\left(\mathbf{r},t\right)}{\lambda^{2}T_{\text{pl}}^{1/2}\left(t\right)}Z^{2}g_{\text{e-i}}\exp\left(\frac{-hc_0}{k_{\text{B}}\lambda T_{\text{pl}}\left(t\right)}\right),\tag{5.6}$$

assuming a Maxwellian distribution over electron and ion velocities. The quantum-mechanical correction factor $g_{\text{e-i}}$ (Gaunt factor) is assumed to be unity due to the low number density of ions, n_{i}, and electrons, n_{e}, and ionic charge number Z^2 is also unity due to the single ionization state. The constant $C_{\text{e-i}}$ is related to the electron mass, m_{e}, electron charge, q_{e}, Boltzmann constant, k_{B}, and speed of light in a vacuum, c_0. Equation (5.6) is averaged over the LII probe volume to account for spatial variation in the plasma temperature and density.

Neutral bremsstrahlung emission and absorption is calculated using the emission cross-section from Dalgarno and Lane [250,251]

$$\frac{d\sigma_{\nu}\left(E\right)}{d\nu}=\frac{8r_{\text{e}}}{3c_0}\frac{E}{h\nu}\left(1-\frac{h\nu}{E}\right)^{1/2}\left[q_0\left(E-h\nu\right)+\left(1-\frac{h\nu}{E}\right)q_0\left(E\right)\right],\tag{5.7}$$

where r_{e} is the classical electron radius, E is the initial electron energy, $\nu = c_0/\lambda$ is the frequency, $h\nu$ is the photon energy, and q_0 is the electron momentum cross-section as a function of electron energy. Equation (5.7) expresses the neutral bremsstrahlung cross-section arising from electron-neutral elastic scattering in the limit of low-energy photons using the phase-shift approximation [252]. The energy radiated from neutral bremsstrahlung per unit time, unit volume, solid angle, and wavelength is then found by integrating Eq. (5.7) over the electron energy distribution,

$$E_{\text{NB},\lambda}\left(t,T_{\text{pl}}\right)=\frac{n_n n_{\text{e}}\left(t\right)h\nu}{4\pi}\int_{h\nu}^{\infty}v_e\left(E,T_{\text{pl}}\right)\left[\frac{d\sigma_{\nu}\left(E\right)}{d\nu}\frac{c_0}{\lambda^{2}}\right]f\left(E,T_{\text{pl}}\right)dE\tag{5.8}$$

where n_n is the number density of LII bath gas neutrals and $v_{\text{e}}(E)$ is the initial velocity of the electron as a function of electron energy. The c_o/λ^2 term changes the unit of the neutral bremsstrahlung cross-section from frequency to wavelength, and $f(E)$ is the electron energy distribution in the gas medium. Neutral bremsstrahlung emission is calculated by numerically-integrating Eq. (5.8) using a value of $d\sigma_{\nu}/d\nu$ derived from a momentum cross-section reported the literature [253], and a Maxwellian distribution over $f(E)$ at an electron temperature of T_{pl}. Finally, the total contribution of plasma emission to the detected LII signal is found by

$$J_{\text{pl}}=J_{\text{NB},\lambda}+J_{\text{e-i},\lambda}=C_{\text{exp}}\left(E_{\text{NB},\lambda}+E_{\text{e-i},\lambda}\right).\tag{5.9}$$

The plasma temperature can increase considerably during the laser pulse due to inverse bremsstrahlung heating, but this is difficult to calculate. Under near threshold breakdown conditions, the plasma temperature is typically between 1/3 to 1/4 of the ionization potential of the ionized species [254], which corresponds to approximately $T_{pl} \sim 2$ eV, so this value is adopted unless otherwise noted.

The distribution of electrons within the probe volume is assumed to be spatially-uniform due to their low mass, high speeds, and small Coulomb attraction force between ions and electrons [245]. In contrast, the distribution of the ions is limited by their considerably slower speeds and the limited diffusion rate through the ambient enveloping gas. Based on transient Direct Simulation Monte Carlo (DSMC) simulations on the dispersion of C_3 (a type of molecular carbon) species around a laser-heated soot aggregate [255,256], and given the spacing of the aerosol considered here (~3.2×10^3 nm for f_v = 2 ppm, d_p = 50 nm) we can assume that the clouds of evaporated species around each nanoparticle do not overlap. Therefore, the number of ions in each microplasma, N_i, is equal to the evaporated species from a single nanoparticle, while molecular diffusion governs the spatial distribution of ions, and roughly follows $1/r^2$ at any instant. The exact distribution does not matter, however; integration of Eq. (5.6) with any proposed ion distribution and uniform electron distribution results in

$$J_{e\text{-}i,\lambda} = c_{exp} c_{e-i} n_p^2 \frac{N_e N_i}{\lambda^2 T_{pl}^{1/2}} Z^2 \exp\left(\frac{-hc_0}{k_B \lambda T_{pl}}\right). \tag{5.10}$$

Equation (5.10) shows that electron-ion plasma emission depends only on the total number of emitted ions, N_i. Also, $J_{e\text{-}i,\lambda}$ depends on n_p^2, while neutral bremsstrahlung depends on n_p. Moreover, we should consider that a higher n_p value results in a higher initial electron population density and therefore a higher MPI ratio, which leads to a higher final electron population at the end of the pulse. However, in this thesis, we assume that the evaporated neutrals are completely ionized in the gas surrounding the nanoparticle, so this does not affect the plasma absorption or emission.

Since the evaporated species are assumed to be completely ionized, the population of neutral atoms surrounding the nanoparticle remains constant and consists exclusively of gas molecules. The evaporation rate, which defines the accumulative number density of electrons and ions, is found by solving Eq. (4.3) and Eq. (4.8) simultaneously.

5.5 Results and discussion

The model described above is used to predict plasma formation and emission from laser-heated Si, Fe, and Mo nanoparticles to determine how this effect is influenced by nanoparticle size and composition, ambient temperature, and laser fluence. In all cases, the initial nanoparticle temperature is that of the bath gas, taken to be 300 K for Mo and Fe nanoparticles, following Ref. [180], and 1500 K for the liquid Si nanoparticles, as in Ref. [168]. The refractive indices and thermophysical properties of nanoparticles are identical 4.3.1. While in reality, the time-averaged laser temporal profile is usually Gaussian, to simplify our analysis we instead assume a top-hat temporal profile of 10 ns duration.

Figure 5-4 shows how plasma emission corrupts the nanoparticle incandescence signal for Si and Fe nanoparticles. (One would expect the radiative properties of molten iron to be a smooth function of wavelength, and the spectral features are likely artifacts of the ellipsometry technique used to derive $\mathbf{m}_\lambda$ [186]). Note that the plasma emission is "blue shifted" compared to the incandescence signal, and, consequently, the bremsstrahlung-contaminated incandescence signal has a peak at a wavelength shorter than the incandescence signal by itself.

Figure 5-5 (a) and (b) shows that neutral bremsstrahlung emission is an order-of-magnitude larger than electron-ion bremsstrahlung for all electron temperatures and laser fluences. This is due to the high density of neutral LII bath gas atoms compared to electrons and ions, which is consistent with experiments on weak plasmas [257,258]. Electron-ion bremsstrahlung emission is related to the number density of electrons and ions by Eq. (5.6), and is independent of the bath gas type and number density. In contrast, neutral bremsstrahlung emission depends on the number density of electrons and neutrals in the gas-phase. Therefore, both the pressure and temperature of the bath gas strongly influence neutral bremsstrahlung emission.

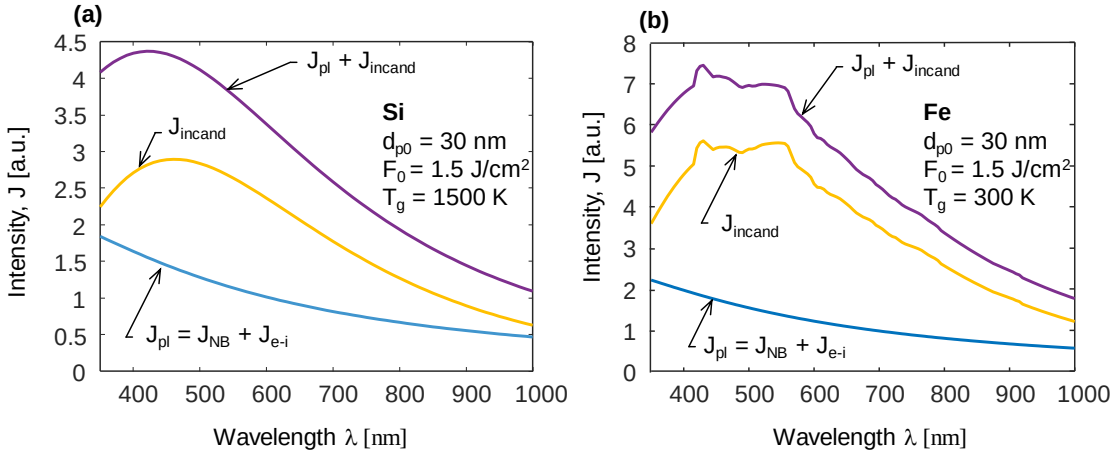

Figure 5-4 Comparison of bremsstrahlung emission with nanoparticle incandescence, J_{incad}, at the peak temperature of the nanoparticle, (a) Si nanoparticle and (b) Fe nanoparticle. The non-smooth features of the Fe nanoparticle emission arise from artifacts in the ellipsometry data used to calculate the refractive index of molten iron.

To assess how plasma emission affects the inferred nanoparticle temperatures, pyrometry is carried out on the modeled spectral intensity, erroneously assuming that the detected signal is purely incandescence at $\lambda_1 = 442$ nm and $\lambda_2 = 716$ nm. Initially, we calculate the pyrometric temperature through nonlinear least-squares regression of the incandescence model at two wavelengths to the corresponding spectral intensities calculated using the incandescence+plasma model. In all cases, the maximum error increases with fluence due to increased evaporation, although, as one may expect, the influence of the plasma on the pyrometric temperature depends strongly on the nanoparticle type, initial diameter, d_{p0}, and laser fluence, *cf.* Figure 5-6. The peak temperature error for the Mo nanoparticles is lower than the others due to its higher boiling point and lower evaporation rate. In general, the error is most significant for the smallest nanoparticles, since the ratio of the plasma and nanoparticle absorption cross-sections is largest. If one uses Wien's approximation to carry out ratio pyrometry, the error is generally less, and varies strongly with the material. This effect could, in some circumstances, explain anomalous cooling, since one would expect the pyrometry error to drop as the plasma dissipates over time, but confirmation of this effect requires a detailed transport model for the plasma species.

Due to the dominance of neutral bremsstrahlung over electron-ion bremsstrahlung, the linear relationship between neutral bremsstrahlung emission and electron density in Eq. (5.8), and the fact that the neutral density n_N remains constant, the pyrometry error is independent of the nanoparticle loading since it scales both incandescence and neutral bremsstrahlung emissions in the same way, as shown in Figure 5-6. However, the electron-ion bremsstrahlung ratio increases with the particle loading.

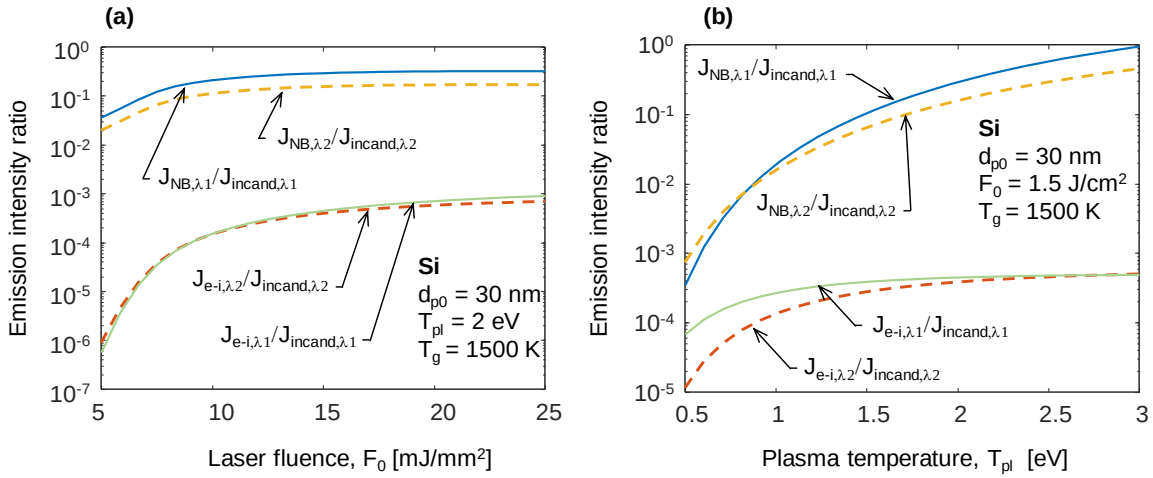

Figure 5-5 Neutral bremsstrahlung, $J_{NB,\lambda}$, and electron-ion bremsstrahlung, $J_{e\text{-}i,\lambda}$, ratios to nanoparticle incandescence, $J_{incand,\lambda}$, at nanopaticle peak temperature for detection wavelengths λ_1 = 442 nm and λ_2 = 716 nm: (a) Intensities as a function of laser fluence at a constant plasma temperature; (b) Intensities as a function of plasma temperature at a constant laser fluence

The variation of pyrometric temperature with laser fluence is shown in Figure 5-7 as a function of type and size of the nanoparticle.

The electron momentum cross-section q_0 in Eq. (5.7) is largest for molecules having high polarizability [257]. Therefore we expect to see a more substantial pyrometry error for experiments with LII bath gas species having higher polarizabilities, *cf*. Figure 5-8. Although the LII bath gas species type influences the nanoparticle cooling rate through conduction heat transfer, the peak nanoparticle temperature is determined by a balance between the energy added by the laser and the energy lost due to evaporation, which are both independent of the bath gas. Therefore, a change in the peak temperature for different LII bath gas species indicates neutral bremsstrahlung emission.

Figure 5-9 (a) and (b) shows that the pyrometrically-inferred peak temperature error for an iron nanoparticle is sensitive to both bath gas pressure and temperature. The peak temperature error increases approximately linearly with increasing bath gas pressure, which is proportional to n_N. The relationship with gas temperature is more complex: the error initially decreases with increasing bath gas temperature, since $n_N \propto 1/T_g$, but increases at higher temperatures, since higher bath gas temperatures lead to higher nanoparticle peak temperatures and greater evaporation rates for a given fluence.

The plasma also absorbs the laser pulse through inverse-bremsstrahlung, through a combination of neutral and electron-ion interactions. The ratio of the IB absorption efficiency, Q_{pl}, at

1064 nm, and the nanoparticle absorption efficiency calculated using Mie theory, Q_{NP}, is shown in Figure 5-10 as a function of fluence. The plasma cross-section is less than the nanoparticle cross-section up to 30 mJ/mm^2, at which point Q_{pl} begins to dominate the absorption cross-section. This is for two reasons: first, the physical cross-section of the nanoparticle drops at higher fluences due to evaporation; and second, the evaporated species ionizes and generates a higher-density plasma. Therefore, Q_{pl}/Q_{NP} is expected to be larger for higher fluences, and also for shorter pulses. This effect is most significant for highly-conducting metallic nanoparticles, which have a low nanoparticle absorption cross-section. As a specific example, Ag nanoparticles at 1064 nm have an even lower absorption cross-section compared to the metallic nanoparticles considered in this study [21], and one would expect the neutral bremsstrahlung cross-section, calculated from Eq. (5.8), to dominate nanoparticle incandescence. This may be the explanation for the fact that, in their LII measurements of Ag nanoparticles, Sipkens et al. [21] reported peak temperatures around 2,800 K, which is much higher than the Ag boiling temperature of 2,130 K. Were this temperature to reflect the true peak nanoparticle temperature, the nanoparticle absorption cross-section would need to be at least 16 times higher compared to the one predicted by Mie-Drude theory in order to absorb enough laser energy. Accordingly, we also do not expect to induce a plasma in the system, however, any electron emission from the nanoparticle still can emit neutral bremsstrahlung which may be the source of the observed radiation.

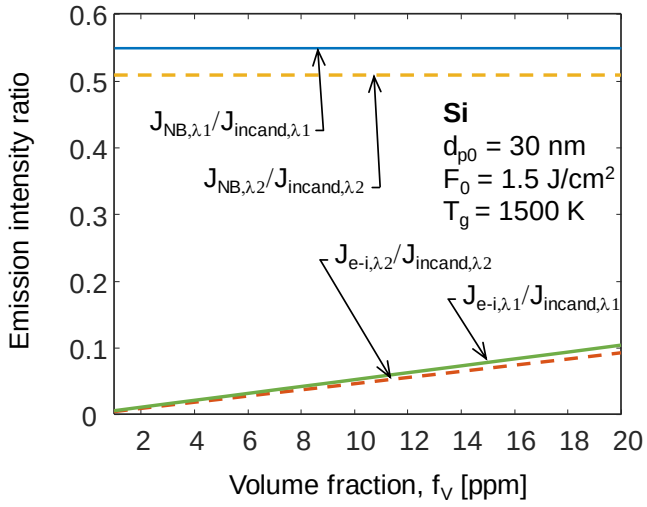

Figure 5-6 Neutral bremsstrahlung, $J_{NB,\lambda}$, and electron-ion bremsstrahlung, $J_{e\text{-}i,\lambda}$, ratios to nanoparticle incandescence, $J_{incand,\lambda}$, at nanopaticle peak temperature for detection wavelengths λ_1 = 442 nm and λ_2 = 716 nm as a function of nanoparticle loading.

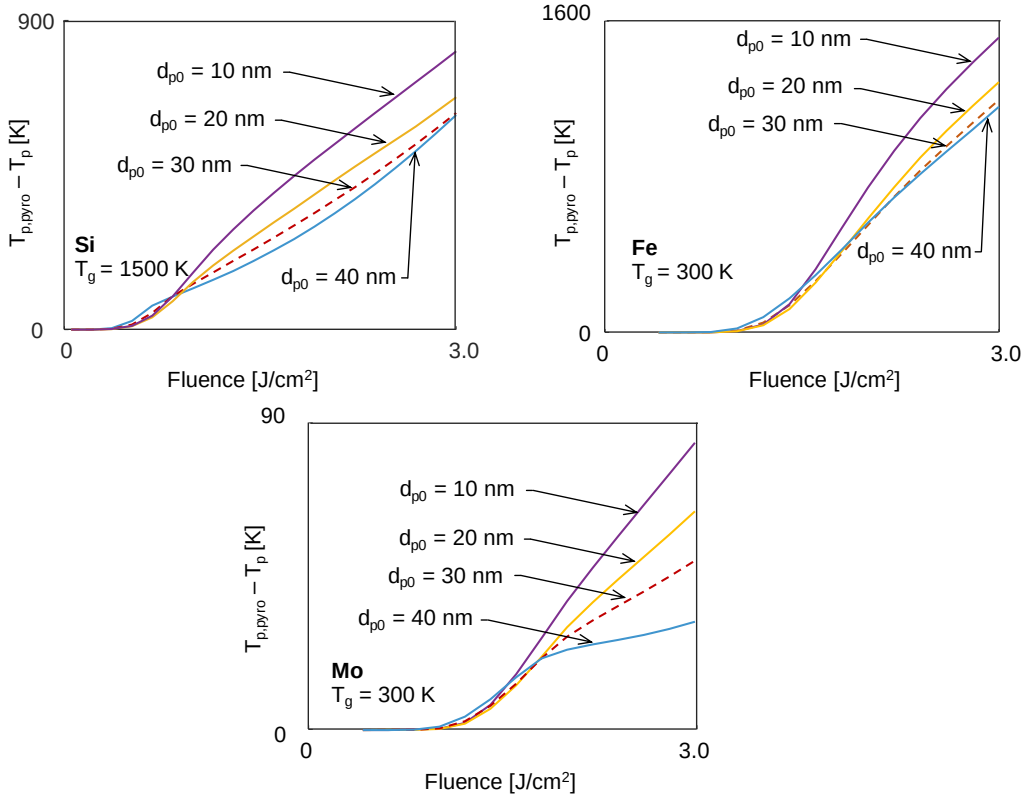

Figure 5-7 Difference between real and pyrometrically-inferred peak temperatures for different nanoparticle materials. In the analysis, particle loading is 2 ppm, T_{pl} = 2 eV, P_g = 101 kPa.

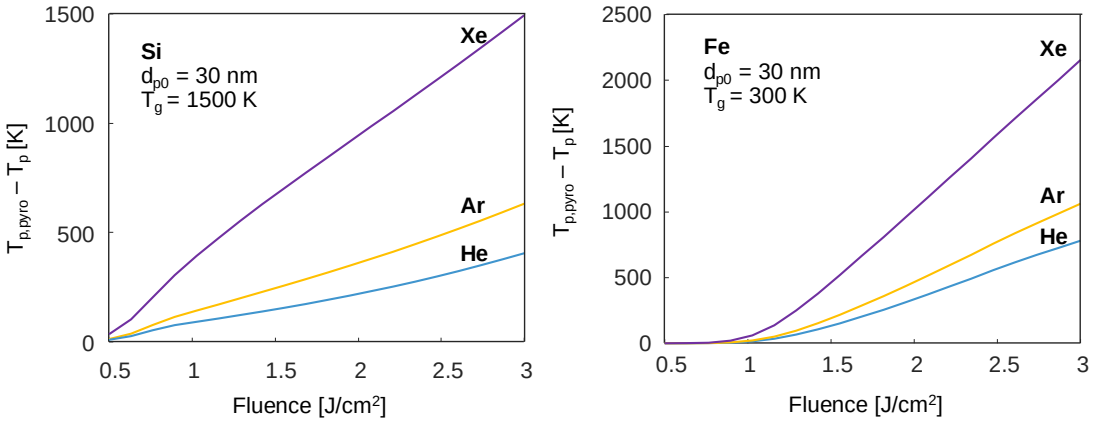

Figure 5-8 Difference between real and pyrometrically-inferred peak temperatures for different nanoparticle materials with different LII bath gas species. In the analysis, particle loading is 2 ppm, T_{pl} = 2 eV, P_g = 101 kPa.

Finally, it should be remarked that the fluence range in which neutral bremsstrahlung is comparable in magnitude with the incandescence is higher than the fluence range at which many of the unexplained LII phenomena described in the introduction occured. Excessive absorption in LII experiments has been observed over 1 to 5 mJ/mm^2 [21,113], while anomalous cooling usually occurs between 1 mJ/mm^2 to 3 mJ/mm^2 [21,117,259,260]. The exception is the unexplained secondary Si atomic emission lines observed by Menser et al. at fluences above 10 mJ/mm^2 [213] as was shown in Figure 5-1, which is consistent with the fluence range considered in this study. The secondary lines are distinct from the primary lines that coincide with the laser pulse, and are attributed to evaporation of thermally-excited Si atoms. The secondary lines have their peak about two hundred nanoseconds after the peak laser fluence, and the total length of the signal is about 700 ns. This timescale points to a gas-phase collisional process (possibly electron/neutral recombination) as a source of excited Si atoms, which fluoresce as they relax. The plasma predicted by the proposed model may, in turn, be the source of the electrons.

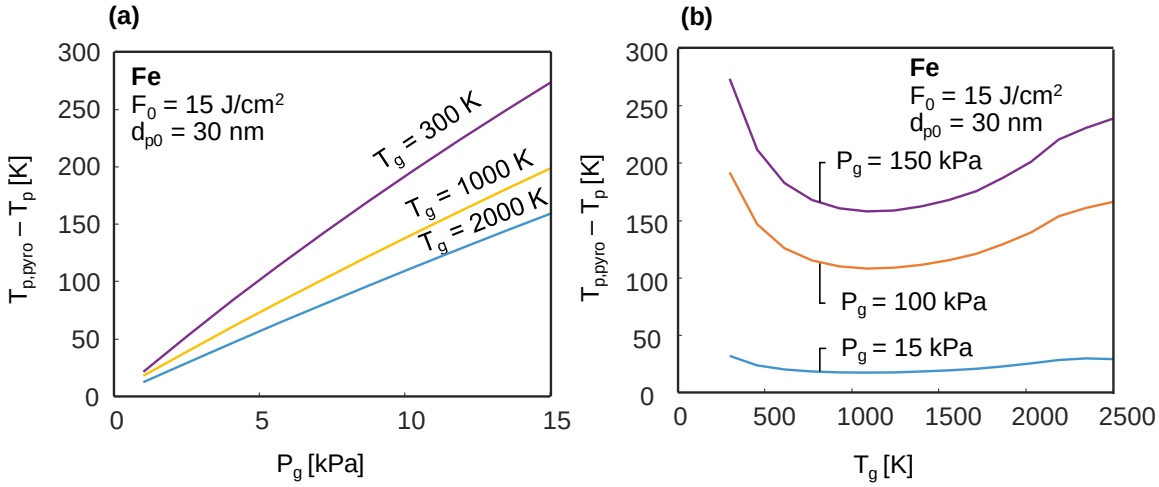

Figure 5-9 (a) Peak temperature inference error due to bremsstrahlung emission as a function of LII bath gas pressure. (b) Peak temperature inference error as a function of LII bath gas temperature.

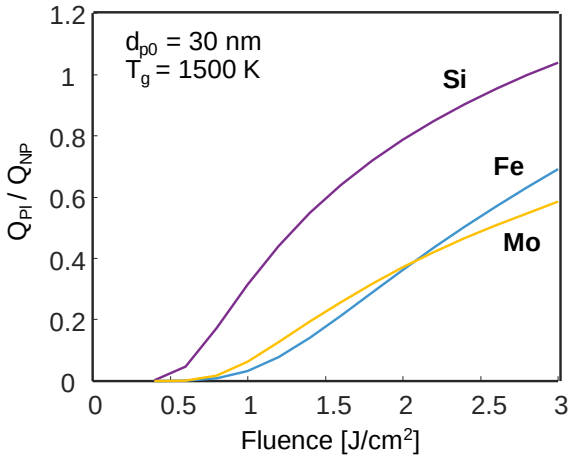

Figure 5-10 Absorption of the nanoparticle (Q_{NP}) compared with the absorption of the plasma (Q_{PI}) for different nanoparticle materials at λ = 1064 nm.

5.6 Conclusions

There has been speculation that some commonly-observed and as-yet unexplained LII phenomena may be caused by a laser-induced plasma linked to nanoparticle evaporation. This chapter attempts to define a theoretical basis for plasma formation around a metallic nanoparticle during laser-induced incandescence. This chapters examined several candidate sources for the trigger-electrons needed to initiate the plasma cascade, and found that, for excitation wavelengths of 1064 nm, thermionic emission remains the most probable source, due to the influence of ion evaporation on the nanoparticle charge state. The cascade then occurs through electron impact ionization of evaporated species into a singly-ionized state. The plasma model presented in this chapter shows that, under normal LII conditions, neutral bremsstrahlung dominates over electron-ion bremsstrahlung due to the low number density of electrons and ions.

Broadband plasma emission contaminates the background incandescence from the nanoparticle at fluences greater than 8 mJ/mm^2, and is most pronounced for metallic nanoparticles having a low melting point, due to the enhancement of thermionically-emitted electrons, and nanoparticles having small spectral absorption cross-sections, which leads to a weak background incandescent emission. Since plasma emission is most pronounced at short wavelengths, contamination of the LII signal leads to overestimation of the nanoparticle temperature. Inverse bremsstrahlung absorption may also explain the enhanced absorption cross-section observed in LII measurements on metal nanoparticles and, potentially, the increased extinction observed in combined LII/LOSA studies.

While the present analysis suggests that the formation of laser-induced plasmas is unlikely in low-fluence LII experiments, it is important to note that many of the phenomena observed by LII practitioners appear to be consistent with the bremsstrahlung-contaminated incandescence signals predicted at higher fluences. Anomalous cooling, for example, is more pronounced in LII experiments carried out on aerosols at ambient temperatures and pressures, which is consistent with model predictions. It may be that the simplifications needed to derive the plasma model (e.g. uniform electron density) do not capture key mechanisms underlying plasma formation, although neglecting electron diffusion and recombination, and assuming total ionization of the evaporated species likely overestimate the possibility of plasma formation and not the other way around. It may also be that the unexplained LII phenomena may originate from electron/neutral bremsstrahlung, but without the electron cascade/impact ionization associated with plasma formation. For example, preliminary calculations show that bremsstrahlung caused by plasmonically-enhanced electron emission and the

neutral gas species could account for the detected LII signal from silver nanoparticles. Further theoretical and experimental analysis, including comparative LII measurements on a range of aerosols and over a broad set of wavelengths, to understand this phenomenon.

Chapter 6
Electron neutral bremsstrahlung emission during time-resolved laser-induced incandescence on plasmonic nanoparticles

6.1 Introduction

The previous chapter demonstrated how a laser-induced plasma could explain the excessive absorption and anomalous cooling phenomena observed in high fluence TiRe-LII experiments ($F_0 > 8$ mJ/mm^2). In low fluence TiRe-LII, the nanoparticle incandescence signal should mask the plasma neutral bremsstrahlung signal. However, if the incandescence signal is negligible, the neutral bremsstrahlung signal should be detectable in the case that free electrons are present in the gas phase. This is likely to be the case in LII measurements on silver nanoparticles, due to their extremely small absorption cross-section relative to other materials in the near-infrared spectrum.

Filippov et al. [57] applied TiRe-LII to silver (Ag) nanoparticles to measure nanoparticle size distribution and compare it with *ex-situ* measurements. In their experiments, silver nanoparticles produced by a metal evaporation/condensation process and argon (Ar) with 99.999% purity was used as the buffer gas. An Nd:YAG laser operating at 355 nm (third harmonic excitation wavelength) was introduced to provide UV pulses, and the signals were detected at a broad wavelength band around 500 nm within a visible range. The laser energy is reported to be 1.5 mJ with a beam diameter of approximately 5 mm (laser fluence $F_0 = 0.76$ mJ/mm^2). In contrast to LII measurements carried out at 1064 nm excitation, the Ag nanoparticle has a high absorption cross-section at 355 nm due to the proximity of the excitation wavelength to its localized surface plasmonic resonance (LSPR) peak. The

measured signal showed a rapid rise to maximum in between 20 ns followed by an exponential decay in less than approximately 70 ns. The reported TEM micrographs analysis showed nanoparticle to have a mean of 6 nm with no smaller than 2 nm and no larger than 15 nm. Analysis reported based on TiRe-LII modeling of the signal suggested that the nanoparticle sizes obeyed a narrow distribution with geometric mean of 10 nm. However, in their study, the authors did not mention the possibility of interference of 355 nm laser pulse with Ar and Ag electronic bands. Also, the possibility of multiphoton electron ionization from the nanoparticle phase and gas phase resulting in plasma [200].

Measured signals reported by Filippov et al. [57] could be attributed to nanoparticle incandescence due to rapid heating of the nanoparticle, while the rapid decay of the signal may be due to the low melting temperature of silver and small size of the nanoparticles and nanoparticle evaporation (reported to be around 10%). In another study by Sipkens et al. [21], a 1064 nm laser pulse was used to measure silver nanoparticles within a Weibull-type size distribution with a mean diameter of 69.4 nm and a standard deviation of 6.11. In the synthesis of silver nanoparticles, a citrate agent was used as a surfactant to stop further growth and agglomeration. Due to the negative zeta potential of the citrate agent, the net charge of the nanoparticle will also be negative. Experiments were conducted at atmospheric pressure and room temperature and the scanning electron microscopy (SEM) on samples from the aerosol showed single spherical nanoparticles. Pyrometric temperatures calculated from the LII signals assuming that the detected signals originated from nanoparticle incandescence showed a rapid decay from 2750 K to 2250 K in less than 70 ns. The peak pyrometric temperature showed no difference for a narrow fluence range between 2.5 mJ/mm^2 to 2.9 mJ/mm^2. The calculated calorimetric absorption efficiency of the aerosol was about 10 times higher than what is predicted by using the Mie theory and considering the polydispersity effect as was previously discussed in *Chapter 4*, *cf*. Figure 4-9. Heat transfer model shows that the nanoparticle could heat up to approximately 100 K assuming the maximum laser fluence. Therefore, the calculated peak pyrometric temperature of 2800 K could not be originated from nanoparticle incandescence.

As discussed in *Chapter 5*, these observations could be due to non-incandescent laser-induced emission (LIE) that contaminates the incandesce signals and act as a model error as this phenomenon is not considered in the TiRe-LII standard model. Furthermore, due to the broadband nature of both nanoparticle incandescence and the observed non-incandescent LIE, it is challenging to detect the contamination.

In *Chapter 5*, the influence of a laser-induced plasma on the TiRe-LII experiments is investigated. It is shown that the electron emission is due to a combination of thermionic emission and

ion emission due to nanoparticle evaporation. Also, the momentum of free electrons could increase due to inverse neutral bremsstrahlung absorption, which could lead to electron impact ionization of molecules evaporated from the nanoparticle and an increase in free electrons population. However, it is shown that the electron neutral bremsstrahlung emission is relevant to nanoparticle incandescent at high-fluence LII experiments.

Another possible scenario is the absent of the nanoparticle incandescent. In the case of the presence of free electrons in the gas phase the neutral bremsstrahlung emission should be detectable. Thermionic emission could not be the source of the free electrons in this scenario. In this chapter, it is proposed that the origin of the observed signal from silver aerosol is due to electron inverse neutral bremsstrahlung due to the scattering of hot free electrons of gas-phase molecules. The hypothesis are validated in a systematic approach. Initially, it is assumed that the signals originate from liquid silver nanoparticles and a peak pyrometric temperature is found. The results showed that the peak temperature is a function of the buffer gas used during the experiments and is above the boiling point of silver. Therefore, the origin of the observed signal should be from the gas phase. Also, plasmonic-decay photoemission is proposed as the origin of the observed electrons. The models show that the electron emission to the buffer gas by this model is a strong function of nanoparticle charge, which proves another validation criterion. No signals observed for positively charged gold (Au) nanoparticle and Ag nanoparticle synthesized with a polyvinylpyrrolidone (PVP) agent.

6.2 Laser-induced incandescence experiments

The experiments are performed on nanoparticles using the apparatus shown in Figure 6-1. A colloidal solution is aerosolized using a pneumatic atomizer (Model 3067 Constant Output Atomizer) supplied with a buffer gas. The wet aerosol then flows through a diffusion dryer before entering the LII measurement chamber. A sample volume of the aerosol is irradiated with an Nd:YAG laser at 1064 nm and a 20 Hz pulse rate. The nominal laser fluence is found to be 2.4 ± 0.4 mJ/mm^2 by measuring the pulse energy with a Coherent J-25MB-IR pyroelectric sensor. The laser fluence is adjusted by changing the polarization state of the beam by a half-wave plate and then passing the beam through a polarizer. The resulting spectral incandescence from the probe volume was imaged onto two photomultiplier tubes equipped with bandpass filters centred at 448 nm and 750 nm, having a full width/half maximum (FWHM) of 60 nm and 50 nm, respectively.

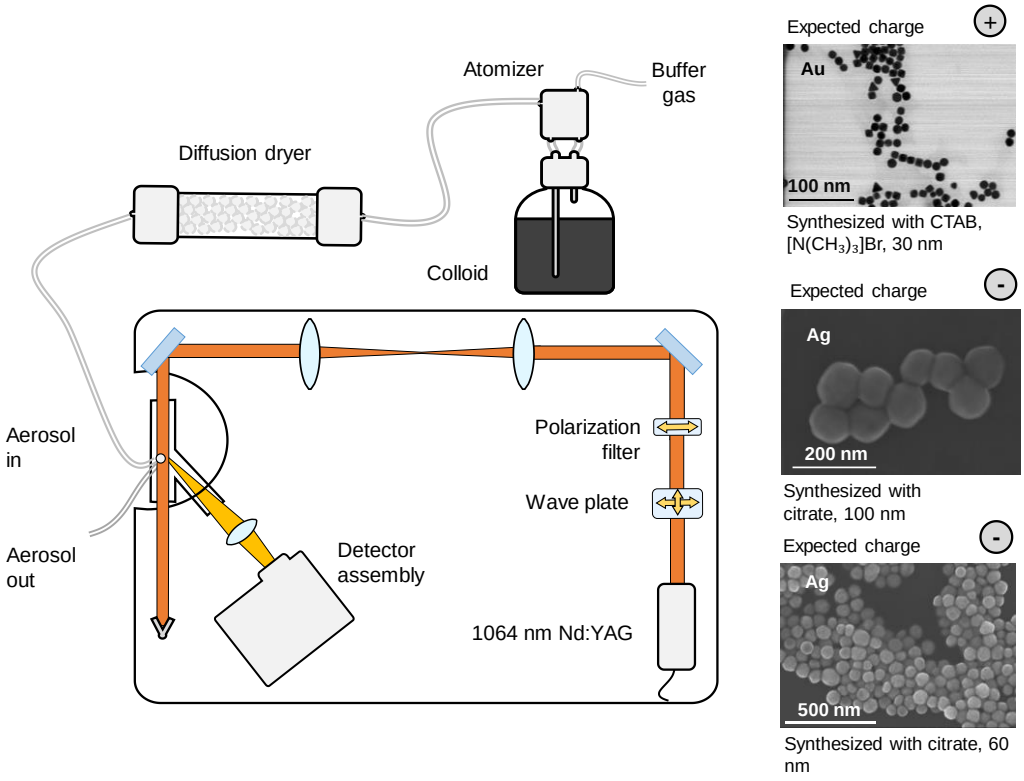

Figure 6-1 Schematics of TiRe-LII setup and SEM/TEM images of sampled aerosolized nanoparticles.

One of the gold nanocolloids used in this study was prepared following the procedure in Ref. [204], which uses CTAB (cetrimonium bromide, $[(C_{16}H_{33})N(CH_3)_3]Br$.) Because CTAB is a cationic capping agent, the net charge of the gold nanoparticles is positive. In addition to the CTAB-synthesized gold nanocolloid, three additional colloids were acquired from a commercial source (Nanocomposix, Inc.) Two of these colloids contained 60 ± 6 nm in diameter gold nanoparticles and 60 ± 4 nm in diameter silver nanoparticles. Both silver and gold nanoparticles produced via a citrate capping agent, resulting in negatively-charged nanoparticles. A third colloid contained 60 ± 6 nm silver nanoparticles using 40 kDa PVP as a surfactant agent which has a negative zeta potential but higher (more positive) compared to citrate.

Scanning and transmission electron microscopy (SEM/TEM) was carried out on Au and Ag nanoparticles sampled from both colloid and the aerosol, and the morphology found to be identical in both cases. No agglomeration between the primary particles is observed. (Observable aggregate clusters are due to the drying of colloid droplets on the grid and because no sintering is observed there is no aggregation in the colloidal form). Colloidal samples were prepared by wetting copper TEM grips with

drops of the nanocolloid and allowing the grids to dry in air. Some of the images are shown in Figure 6-1.

The duration of measurable LII signals were consistent with those reported by Sipkens et al. [21], in which the signals decay to 90% of its peak value in approximately 60 ns, *cf*. Figure 6-2. The signal goes duration exceeds the laser temporal profile, suggesting the signal is due to thermal emission and not multi-photon luminescence and inelastic light scattering that would be due to the laser [261–263]. If we assume that the LII signals arise from incandescence, a peak pyrometric temperature can be found using Eq. (4.26). In the pyrometry, $E(\mathbf{m})_r = 2.916$ is used which is found by using Drude parameters of liquid silver ($\omega_p = 1.3175\times10^{16}$ rad/s, $\Gamma_0 = 2.6439\times10^{14}$ 1/s [184,264]) in Eq. (4.14). Figure 6-3 shows the peak pyrometric temperature of liquid Ag nanoparticles. Each point is an average of 1,000 laser shots. Previous experiments have shown that the standard deviation of the mean is small for 1000 shots. The inferred temperatures are above the boiling point of the Ag and show a correlation with the buffer gas type. However, the variation with the laser fluence could be due to the low intensity of the signal, which amplifies the influence of electronic noise. The heat transfer model predicts that the laser should only heat the Ag nanoparticles up to 100 K above ambient due to their small absorption cross-section at 1064 nm. In the case of that large aggregate clusters of silver form in the aerosol, the emission could be attributed to incandescence due to localized-surface plasmon resonance (LSPR) [265]. In this process, a region of the aggregate goes through LSPR, and the aggregate cools down due to evaporation and conduction to the gas phase but also conduction to the cold regions of the aggregate which accelerates the cooling rate furthermore.

Although TEM/SEM images suggest that the aerosolized particles are not aggregated it is possible that some aggregates do exist in the aerosol and they were not captured on the analyzed grids due to the sparsity of the aerosol. Therefore, supplementary TEM/SEM analysis is required to rule out this scenario in the future. From the current observations, on could conclude that the TiRe-LII signals from the Ag aerosols do not originate from the nanoparticle incandescence, and it is doubtful that the pyrometric temperatures reflect the true temperature of the nanoparticle.

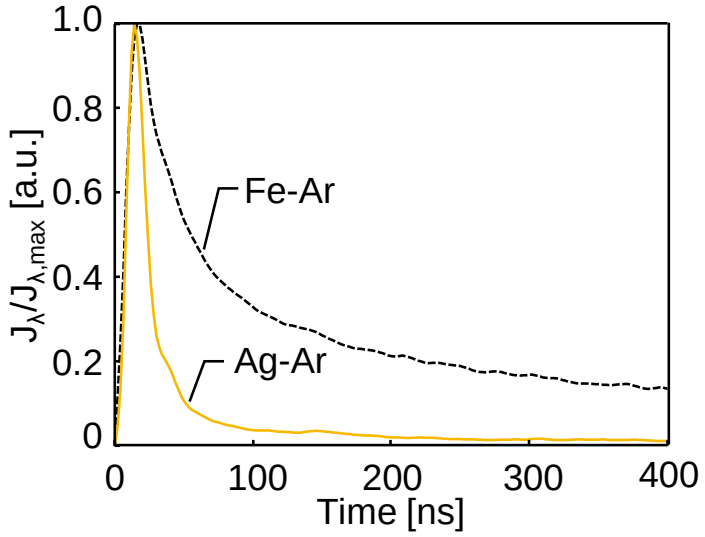

Figure 6-2 Sample of a detected signal from silver and iron aerosolized nanoparticles.

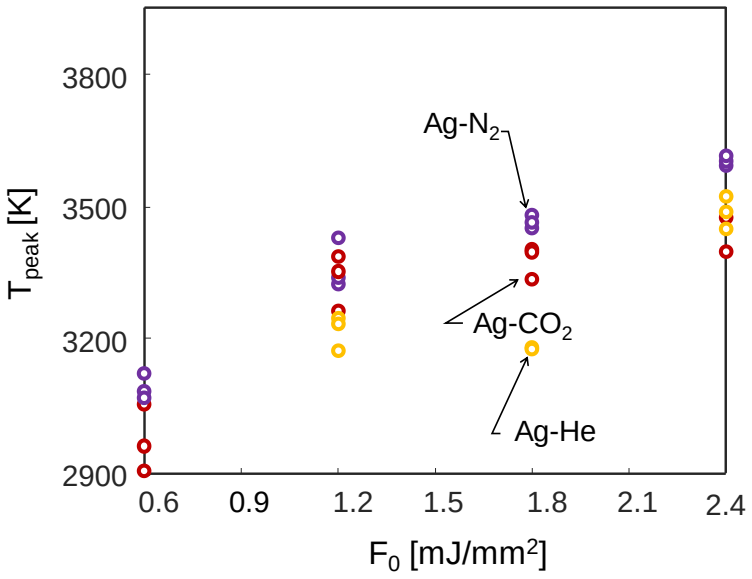

Figure 6-3 Peak silver nanoparticle temperature inferred as a function of fluence and buffer gas. Every point is averaged over 1000 laser shots.

6.3 Plasmonic decay photoemission

Central to electron neutral bremsstrahlung is the production of free "trigger" electrons from the nanoparticles. Under laser intensities typical of TiRe-LII (~ 10^8 J/cm^2) at 1064 nm, no nanoparticle phase or gas phase multi-photon ionization is expected, even considering nanoparticle nearfield enhancement as discussed in *Chapter 5*, *cf*. Figure 5-2. While thermionic emission has been included in some TiRe-LII models [200,201], this effect is unlikely to be the source of the free electrons in this case, especially if the true nanoparticle temperatures are much lower than the pyrometric temperature.

Alternatively, hot free electrons can be generated from a metal nanoparticle through the photoelectric effect [266]. Photoelectric emission from plasmonic nanostructures was initially investigated by Tamm and Schubin [231,267], who defined two mechanisms. In surface photoemission, an electron on the surface of the metal absorbs a photon and is then emitted if the final electron energy after the collision is sufficient to overcome the potential barrier. The metal boundary is approximated as a 1-D potential barrier $U_b(t) = E_F + W + \Phi_e(t)$, where E_F is the Fermi energy in metal (assumed 5.1 eV and 4.26 eV for gold and silver, respectively [268]) and W is the work function, which is assumed to be 5.47 eV and 4.64 eV for gold and silver, respectively [269]. Finally, Φ_e is the ionization potential, which depends on the spontaneous charge of the nanoparticle $N_{e,np}$ and its size [234] which is previously defined in Eq. (5.4).

In volumetric photoemission, an electron within the metal absorbs a photon and then moves to the boundary of the metal, during which time it loses energy through collisions with cold electrons or phonons. However, if the electron reaches the surface with sufficient energy to overcome the potential barrier, it could be emitted to the surrounding medium. This thesis considers only the surface mechanism, with the understanding that this may underestimate the true electron emission flux. However, the number of electrons that can be emitted by a nanoparticle depends on its charge to size ratio. Moreover, all possible electron emissions occur in a timescale less than a nanosecond. Therefore, excluding the volumetric mechanism does not change the final population of free electrons in the gas phase.

By assuming the field inside the sphere as homogeneous, the spontaneous photoelectron emission rate from a single nanoparticle due to the surface mechanism, J_e'' in units of electrons per second is

$$J_e^{"} = C_{\text{sur}}\left(U_{\text{b}}, \varepsilon_{\text{i}}, \varepsilon_{\text{m}}, \lambda, d_{\text{p}}\right)\pi d_{\text{p}}^2 \,|\, \underbrace{\frac{2\varepsilon_{\text{m}}(\lambda)}{\varepsilon_{\text{i}}(\lambda)+2\varepsilon_{\text{m}}(\lambda)}E_{\text{o}}}_{E_{\text{i}}} \,|^2 \,/3. \tag{6.1}$$

The field within the nanoparticle, E_{i}, is parallel to the external field E_{o}, and ε_{m} and ε_{i} are the relative permittivity of the external medium (here taken as unity) and the nanoparticle (for solid silver and solid gold taken from Ref. [182] and Ref. [270], respectively), respectively. The coefficient C_{sur} can be found by solving the quantum-mechanical problem for the collision of a single electron with the metal boundary, and then successively summing over all conduction band electrons undergoing such collisions with the surface [231]. The coefficient C_{sur} depends, in particular, on the electron density in the metal, on the irradiated photon wavelength (1064 nm in the experiments described here) and U_{b} for electrons at the nanoparticle boundary which is a function of metal and surrounding medium work functions and nanoparticle size and charge. In the case of Ag and Au, the Broglie electron wavelength $\lambda_{\text{e}} \sim 0.5$ nm is much smaller than the characteristic nanoparticle size expected for the present case ($d_{\text{p}} >$ 30 nm), and therefore quantum confinement effects can safely be neglected [209].

The C_{sur} coefficient in Eq. (6.1) is calculated using the potential barrier function (approximated to be 1-D), which depends on the nanoparticle charge and with the assumption that $h\nu < E_{\text{F}}$ [231,271]

$$C_{\text{sur}} = \frac{16\varepsilon_0\alpha_{\text{f-s}}c_0}{\pi(h\nu)^3}U_{\text{b}}^3\int_{1-h\nu/U_b}^{\varepsilon_F/U_b}\left\{\text{Re}\left[\left(E'-1+\frac{h\nu}{U_b}\right)^{1/2}\right]\frac{G(E')}{\sqrt{E'}}\left|K_{\Delta\varepsilon}(E')\right|^2\left(\frac{E_F}{U_b}-E'\right)\right\}dE' \tag{6.2}$$

,where $\alpha_{\text{f-s}} \sim 1/137$ is the fine structure constant and

$$G(E) = E\cdot\frac{\left|\sqrt{(E)}-\sqrt{(E-1)}\right|^2}{\left|\sqrt{E+h\nu/U_b}+\sqrt{E+h\nu/U_b-1}\right|} \tag{6.3}$$

The coefficient $K_{\Delta\varepsilon}$ describes the effect of the discontinuity between the nanoparticle and the surrounding medium. In our case $\varepsilon_{\text{m}} = 1$, $K_{\Delta\varepsilon}$ is

$$K_{\Delta\varepsilon}(E) = \frac{1}{2}\left[(\varepsilon_{\text{i}}+1)-(\varepsilon_{\text{i}}+1)\left(\sqrt{E+\frac{h\nu}{U_b}}+\sqrt{E-1}\right)^2\right]. \tag{6.4}$$

The photoelectron emission rate divided by irradiated field intensity is shown in Figure 6-4. The white region is where the potential barrier $U_{\text{b}} < 0$. As expected from the photoelectric phenomenon, there is a nanoparticle charge threshold beyond which we expect electron emission, depending on the nanoparticle diameter. The quasi-static approximation error used in Eq. (6.1) to connect E_0 to E_{i} only

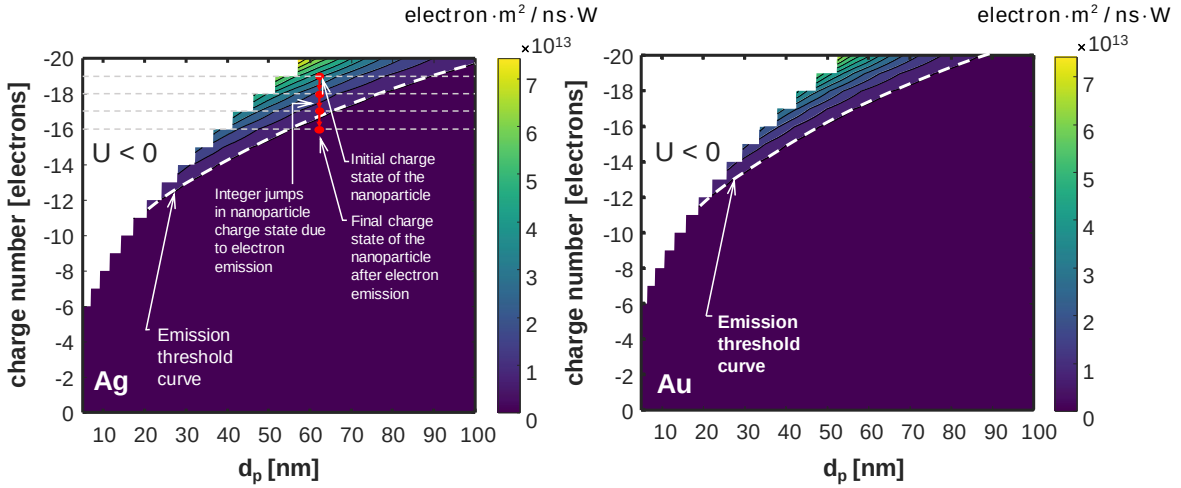

Figure 6-4 Surface electron photoemission rate normalized by collimated beam irradiated field intensity N_e''/I_0 as a function of nanoparticle size and integer charge irradiated by a 1064 polarized plane wave.

changes the rate of electron emission and not the emission threshold, which only depends on C_{sur}. We expect the charge to size ratio threshold to be lower than what is depicted in Eq. (6.2) due to nanoparticle defects and the possibility of two photon absorption process in which a secondary photon interacts with the excited plasmon in a timescale shorter than its relaxation time.

The effect of the negative charge on the photoemission is comparable to having a semiconductor as the surrounding medium of the metallic nanoparticle (Schottky barrier) in which the nonzero work function of the semiconductor reduces the total potential function, U_b. This analysis shows that irradiating a neutral Ag or Au nanoparticle with a 1064 nm pulse results in no photoemission, which is consistent with the findings of Manjavacas et al. [272]. However, a negatively charged Au or Ag nanoparticle could produce significant electron emission flux depending on whether the size to charge ratio is satisfied. After the emission of these electrons to the buffer gas in sub-nanosecond timescale, free electrons will evolve by absorbing the incoming irradiation by inverse neutral bremsstrahlung, and lose energy by two mechanics: (*i*) neutral bremsstrahlung emission; and (*ii*) elastic and non-elastic impact with buffer gas molecules. The number density of the electrons depends on the number density of the nanoparticles in the aerosol. We expect no recombination between the electrons and nanoparticles, and the number density of the electron only declines due to volumetric diffusion. However, the mean temperature of the electrons will reduce due to neutral bremsstrahlung and momentum transfer to the free molecules.

6.4 Results and discussion

No signals were observed for LII measurements on positively charged Au nanoparticles (synthesized using CTAB) and silver nanoparticles synthesized with PVP. This could be due to the termination of electron emission to the gas phase because U_b is higher for these two cases compared to silver synthesized with citrate. Also, no signals observed with propane as a buffer gas, which is another indication that the observed signals depend on the buffer gas type.

By using the equations of neutral bremsstrahlung defined in the previous chapter, an average electron temperature could be found from the detected signals (assuming that the signals are purely neutral bremsstrahlung). Neutral bremsstrahlung emission is calculated by numerically-integrating Eq. (5.8) using a value of $d\sigma_\nu/d\nu$ derived from a momentum cross-section reported the literature [253], and a Maxwellian distribution over $f(E,T_e,t)$. In the case of two-wavelength LII, the average electron temperature, T_e, can be found implicitly by solving

$$T_e(t) = \arg\min_{T_e} \left\| \frac{J_{NB,\lambda_1}^{exp}(t)}{J_{NB,\lambda_2}^{exp}(t)} - \frac{\nu_1 \int_{h\nu_1}^{\infty} \nu_e(E,T_e) \left[\frac{d\sigma_\nu(E)}{d\nu} \frac{c_0}{\lambda_1^2} \right] f(E,T_e,t)\, dE}{\nu_2 \int_{h\nu_2}^{\infty} \nu_e(E,T_e) \left[\frac{d\sigma_\nu(E)}{d\nu} \frac{c_0}{\lambda_2^2} \right] f(E,T_e,t)\, dE} \right\|_2^2, \quad (6.5)$$

where $J_{NB,\lambda1}^{exp}$ and $J_{NB,\lambda2}^{exp}$ are detected signals, and the integrals are evaluated numerically. Note that the N_e and N_e in Eq. (5.8) cancel out.

Electron peak temperatures as a function of fluence and buffer gas type are shown in Figure 6-5. A linear trend is observed between the electron peak temperature and fluence for the studied laser fluence range, in which the slope of the linear fit depends on the buffer gas. The peak electron temperature is much lower than the ionization potential of the nanoparticle species or the buffer gas species, and therefore no electron impact ionization is expected. In the case of increasing the fluence, we expect to reach the fluence regime of laser-induced breakdown spectroscopy (LIBS) in which a full plasma is developed due to initial electron emission and electron cascade production.

The average normalized number density of electrons can be inferred by using the T_e value calculated from Eq. (5.8) which is shown in Figure 6-6. No electron temperature is evaluated for Ag-He and Au-He experiments due to the very low detected signal intensity. The number density shows a

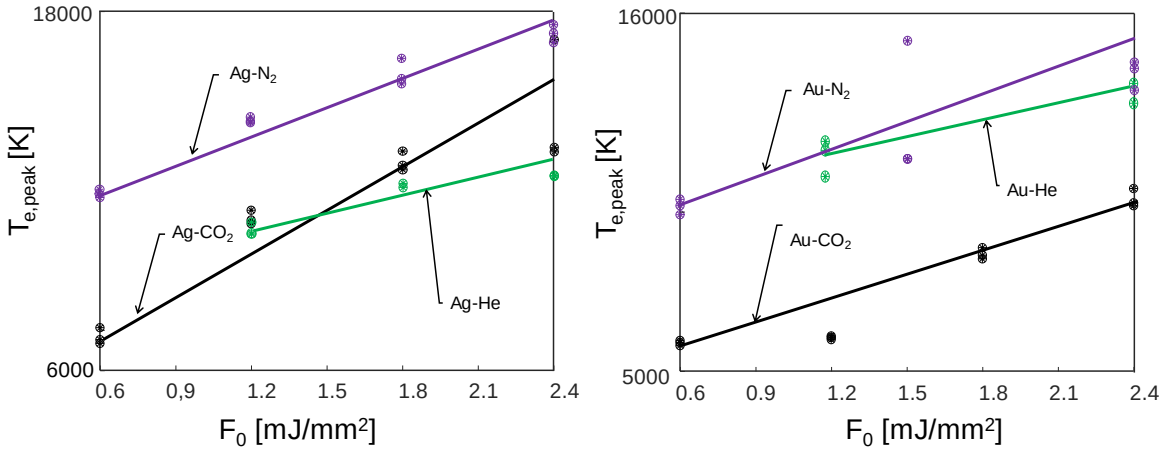

Figure 6-5 Free electron temperature found from the neutral bremsstrahlung.

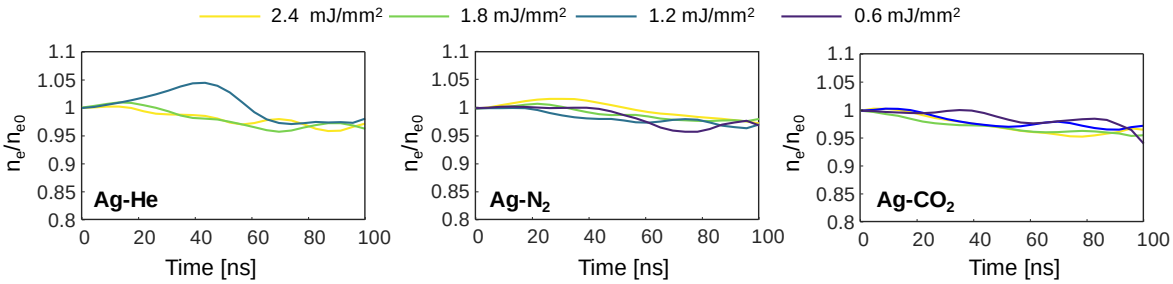

Figure 6-6 Normalized electron density to the initial electron density at the peak of the signal as a function of buffer gas type and laser fluence, found by using the inferred T_e, and normalized to the max N_e value.

negligible correlation with time and no correlation with buffer gas type and laser fluence. Therefore, the decay of the detected signal should be due to electron temperature decay exclusively.

To test the electron diffusion from the probe volume, we assumed a 1-D cylindrical probe volume as shown in Figure 6-7. Electron diffusivity is defined as $D_e = (k_B T_e/m_e \nu_e)$, where ν_e is the electron-gas collision frequency found for the mean T_e and T_g value from Ref. [273]. The diffusion equation for the electron cloud can then be solved in 1-D cylindrical coordinates as

$$\frac{\partial n_e}{\partial t} = \frac{1}{r}\frac{\partial}{\partial r}\left(D_e r \frac{\partial n_e}{\partial r} \right) \tag{6.6}$$

with the boundary conditions are assumed to be

$$t = 0 \begin{cases} n_e(r < r_0) = n_{e0} \\ n_e(r > r_0) = 0 \end{cases}, \quad \lim_{r\to\infty} n_e(t,r) = 0 \tag{6.7}$$

The analytical solution to Eq. (6.6) with boundary conditions defined in Eq. (6.7) for a constant D_e is

$$n_e(r,t) = n_{e0}\left\{1+\frac{2}{\pi}\int_0^{\infty}\exp\left(-\lambda'^2\tau_0\right)\left[\frac{J_0(\lambda' R)Y_0(\lambda') - J_0(\lambda')Y_0(\lambda' R)}{J_0^2(\lambda') + Y_0^2(\lambda')}\right]\right\}\frac{d\lambda'}{\lambda'}, \tag{6.8}$$

where $R = 2r/d_p$; $\tau_0 = 2tD_e/d_p$; J_0 and Y_0 are Bessel functions of first kind and second kind, respectively Although D_e varies considerably for different buffer gases used in the experiment as shown in Figure 6-8, the model shows that the electron diffusion from the probe volume is negligible for the timescale of the observed signal and maximum value of D_e.

In this study, a Maxwellian distribution is assumed for the electron energy distribution, $f(E)$, but in reality, this distribution only applies as an initial condition, and when the system reaches thermal equilibrium. At intermediate times, the system is far from equilibrium, and the electron energy distribution may depart from a Maxwellian distribution. This, in turn, could influence the nature of the laser-induced nanoparticle emission. In future studies, this transformation should be modeled explicitly by performing a Monte Carlo simulation for the electron emission, inverse neutral bremsstrahlung absorption, and neutral bremsstrahlung emission.

While this chapter shows that neutral bremsstrahlung initiated by electrons emitted by plasmonically-enhanced photoemission could account for laser-induced emission from silver and gold nanoparticles, it may also be the case that a different, as-yet identified phenomenon is responsible. One possibility could be nonradiative plasmon decay originated from the nanoparticle. A detailed discussion for the elimination of other sources of emission will be part of the future work.

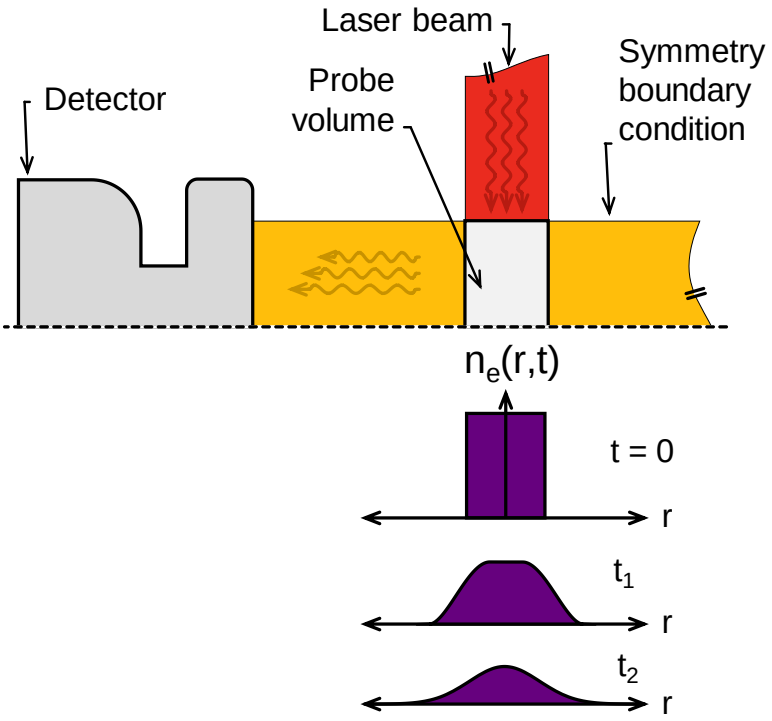

Figure 6-7 Schematic of 1-D cylindrical electron diffusion through the probe volume. Initially, we assume a uniform electron density in the probe volume.

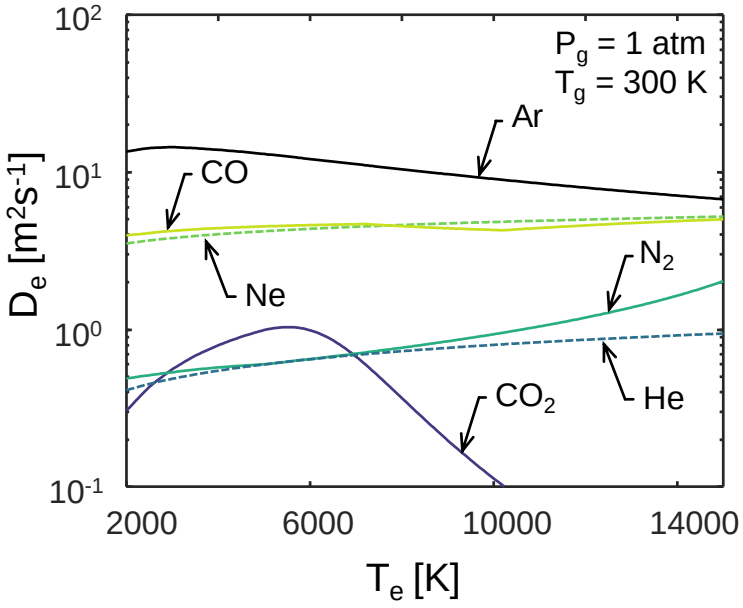

Figure 6-8 Electron diffusivity as a function of electron temperature and buffer gas which is at atmospheric pressure and room temperature. The temprature of the buffer is T_g = 300 K.

6.5 Conclusions and future work

The observed signal from aerosolized negatively charged silver and gold nanoparticles during TiRe-LII experiments could be explained by inverse neutral bremsstrahlung emission due to the collision of hot carriers to the buffer gas molecules. This hypothesis is supported by experimental TiRe-LII measurements, which show that the peak inferred temperature depends on the buffer gas, contrary to what would occur if the nanoparticles were heated directly by the laser. Plasmonic decay photoemission is proposed as the source of the electrons in the probe volume, in which the emission depends strongly on the wavelength of the pulse and the charge to size ratio of the nanoparticle. No signal is observed for the net positively charged Au nanoparticles and Ag nanoparticle synthesized with polyvinylpyrrolidone (PVP), which is consistent with this hypothesis. Peak electron temperatures inferred are not high enough to ionize both nanoparticle phase and the gas phase. Therefore, no electron growth due to electron impact ionization is expected. In the future, more experimental results are required to further validate the hypothesis, including uncertainty analysis in the inferred temperature with different buffer gases, and a detailed TEM/SEM analysis.

Chapter 7
Conclusions and future work

Both time-resolved laser-induced incandescence (TiRe-LII) and multi-angle light scattering (MALS) are powerful diagnostics for characterizing aerosolized nanoparticles. This thesis explores how improving the spectral models that underlie these techniques may improve the robustness of aerosol characteristics inferred from the measurements.

7.1 Summary and key findings

7.1.1 Multi-angle light scattering

In the case of MALS, the primary challenge is the complexity and time required to compute an exact solution to the light scattering kernel. This is critical since the kernel must be evaluated repeatedly, particularly if the uncertainty of the derived estimates is to be evaluated through Bayesian inference. This motivates the use of approximate models such as Rayleigh-Debye-Gans fractal aggregate (RDG-FA) to avoid time-consuming and computationally-demanding numerical solutions to the kernel. However, as shown previously in the literature [76] and also in this thesis (*Chapter 2*), model errors inherent in these approximations may be amplified into large errors in the inferred aerosol parameters due to the underlying ill-posed nature of the problem.

This thesis proposes the approximation error (AE) technique and artificial neural networks (ANN) to address this problem. In the case of AE, a statistical model is constructed by using the difference between sample solutions from low order (RDG-FA) and high order (multi-sphere T-matrix, MSTM) solutions. The final kernel is presented as a summation of RDG-FA scattering kernel plus a second term that includes the unknown coefficients and principal directions of the RDG-FA model found by through principal component analysis (PCA). Finally, the aggregate parameters and associated uncertainties are found through Bayesian inference. While the posterior probability densities obtained through the approximation error technique are wider than those found using RDG-FA, the estimates

are nearly unbiased. Moreover, by accounting for the deterministic structure of the model error, the posterior probability densities found using the AE technique are far narrower than would be obtained by merely masking the model error with white noise. Aside from the one-time burden of computing the mean error and PCA basis, the computational effort required to carry out the Bayesian inference for the approximation error technique is virtually identical to that of ordinary RDG-FA.

In the case of ANN, the light scattering kernel is approximated using a feed-forward multi-layered ANN to achieve an accurate and computationally-efficient kernel model. The ANN is trained using multi-sphere T-matrix (MSTM) scattering simulations on randomly-generated soot aggregates sampled from plausible morphological parameters. The ANN models the light scattering kernel within a relative error range of 5%. The Bayesian/ANN approach outperforms the Bayesian/AE method both in terms of accuracy of the maximum a posteriori estimate and the width of the marginalized credibility intervals for all training samples. The Bayesian/ANN is then applied to wide-angle light scattering (WALS) measurements carried out within a flame and the inferred parameters compared with results derived from transmission electron micrographs of extracted soot particles.

7.1.2 Laser-induced incandescence

While in MALS, the primary problem was the complexity of the light scattering kernel, in TiRe-LII, the central challenge concerns commonly-observed experimental features that cannot be explained using existing measurement models.

This thesis showed that many of these discrepancies, including temporal variation in the intensity scaling factor during TiRe-LII measurements on molten (metallic) silicon, enhanced absorption cross-sections of molybdenum and iron nanoparticles, and the $[E(\mathbf{m})_r]_{exp}$ ratio for iron nanoparticles, can be partially explained by: (*i*) the fact that the Rayleigh approximation of Mie theory is usually invalid for metal nanoparticles under TiRe-LII conditions; (*ii*) polydisperse particle sizes, coupled with Mie theory, increase temperature non-uniformity in the aerosol, and; (*iii*) the fact that the radiative properties of iron change significantly upon melting.

While incorporating Mie theory into the measurement model explains some of the observed anomalies, some problems remain. For example, the spectroscopically-defined absorption cross-section of silver nanoparticles restricts nanoparticle heating to only one hundred Kelvin, which would render incandescence undetectable. Also, in the case of iron nanoparticles, while the discrepancy between

calorimetrically- and spectroscopically-derived absorption cross-sections has been decreased, it has not been eliminated.

Accordingly, this indicates that additional physical phenomena remain unaccounted for in the spectroscopic model. For example, there has been speculation that some remaining TiRe-LII measurement phenomena may be caused by a laser-induced plasma linked to nanoparticle evaporation. Therefore this thesis attempted to define a theoretical basis for plasma formation around a metallic nanoparticle during laser-induced incandescence. In order for a laser-induced plasma to form, initial "trigger" electrons are required to initiate a electron cascade growth. Therefore several candidate sources for the trigger-electrons needed to initiate the electron cascade are investigated. It is found that in the case of nanoparticles that can absorb apprciable amounts of laser energy (Si, Mo, Fe) thermionic emission is the most probable source due to the influence of ion evaporation on the nanoparticle charge state. Electron population cascade growth occurs through electron impact ionization of evaporated species into a singly-ionized state. The plasma model presented in this thesis shows that, under normal LII conditions, neutral bremsstrahlung dominates over electron-ion bremsstrahlung due to the low number density of electrons and ions.

Broadband plasma emission contaminates the background incandescence from the nanoparticle at fluences approximately higher than 8 mJ/mm^2, and is most pronounced for metallic nanoparticles having a low melting point, due to the enhancement of thermionically-emitted electrons, and those having low spectral absorptions, which leads to a weak background incandescent emission. Since plasma emission is most pronounced at short wavelengths, contamination of the LII signal leads to an overestimation of the nanoparticle temperature. Inverse bremsstrahlung absorption may also explain the enhanced absorption cross-section observed in LII measurements on metal nanoparticles and, potentially, the increased extinction observed in combined LII/LOSA studies. It may also be that the unexplained LII phenomena may originate from electron/neutral bremsstrahlung but without the electron cascade/impact ionization associated with plasma formation. For example, preliminary calculations show that bremsstrahlung caused by plasmonically-enhanced electron emission and the neutral gas species could account for the detected LII signal from silver nanoparticles.

In the case of TiRe-LII experiments on silver nanoparticles, the experimentally inferred absorption cross section is ten times greater than the one calculated using the Mie theory. Therefore, the detected signal could not be attributed to nanoparticle incandescence. For experimental validation, TiRe-LII measurements were conducted on Ag and Au nanoparticle with different buffer gases. Signals were observed for aerosols of Ag and Au nanoparticles that were synthesized with citrate, which

induces a negative charge on the nanoparticles. Furthermore, no signal is observed for aerosols of Ag nanoparticles synthesized with PVP (polyvinylpyrrolidone), nor aerosols of positively charged Au nanoparticles synthesized with CTAB (cetrimonium bromide). Also, using propane as a buffer gas completely diminished previously observed signals. Pyrometrically-inferred peak temperatures showed that the nanoparticle should be well above the boiling temperature of the silver and also showed a dependence on the buffer gas type.

The observed signal from aerosolized negatively charged silver and gold nanoparticles during TiRe-LII experiments could be explained by inverse neutral bremsstrahlung emission due to the collision of hot carriers to the buffer gas molecules. This hypothesis is supported by experimental LII measurements, which show that the peak inferred temperature depends on the buffer gas, contrary to what would occur if the nanoparticles were heated directly by the laser. Plasmonic decay photoemission is proposed as the source of the electrons in the probe volume, in which case emission would depend strongly on the wavelength of the pulse and the charge to size ratio of the nanoparticle.

7.2 Future work

7.2.1 Multi-angle light scattering

Although the Bayesian/ANN process investigated in this work showed promising results on synthetic data, when this technique was applied to experimental data, the inferred size parameters were inconsistent with TEM-derived values. This is attributed to unaccounted model errors, perhaps due to the simplified aggregate structure and the limited range of refractive indices used to train the ANN. A more realistic light scattering database could be generated considering the necking and sintering phenomena, the polydispersity of primary particles, and the range of refractive indices for soot. This database could be used to train an artificial neural network (ANN), which can be used as the kernel of the light scattering model. Then the effect of any of these new assumptions could be evaluated in the inverse model.

The MALS model in this thesis assumed a deterministic primary particle size which was adopted from TEM inferred results. However, a more realistic assumption is to account for the uncertainty of d_p as a probabilistic estimate, and then this uncertainty will propagate through the Bayesian inference to inferred parameters.

The MALS measurements are usually have been done for vv-polarization (vertical emission-vertical detection). However, vh-polarization could also be measured. The addition of a secondary signal includes new information to the problem and reduces the ill-posedness of the problem.

7.2.2 Time-resolved laser-induced incandescence

As discussed in *Chapter 4*, Mie theory should replace the Rayleigh approximation for spectroscopic modeling of metal nanoparticles.

On the other hand, it is possible that metal nanoparticles go through an agglomeration process such as the case of molybdenum nanoparticle studied by Sipkens et al. [21] as was shown in Figure 1-1. The agglomeration could drastically change the spectroscopic model. Also, during the laser heat up process, different phenomena such as sintering or collapse could happen, leading to a change in morphology and optical properties. Investigating TiRe-LII on aggregated metal nanoparticles could connect the LII research to nanoantenna design and sintering at nanoscale research.

Also, the effect of partial oxidation of metal nanoparticles needs to be investigated. Partial oxidation could increase the absorption cross-section of the nanoparticle and fully or partially explain the excessive absorption in metal nanoparticles. Kinetic models for oxidation could be used to generate core-shell nanoparticles in TiRe-LII systems, which could then be analyzed using Mie theory.

The LII community usually treats soot as separate primary particles without considering the effect of the aggregates. Ignoring agglomeration results in overprediction of the cooling rate [50,54]. Also, RDG-FA is used to find the optical properties of the aggregates which is prone to model error, as is discussed in *Chapters 2* and *3*. The study of approximation model error or using an ANN to approximate soot optical properties can be used inside LII standard model for soot. Therefore, the methodology used in MALS setups (proposed in *Chapters 2* and *3*) can directly be used in the LII modeling.

The TiRe-LII microplasma model presented in *Chapter 5* must be validated by carrying out further experiments on a range of metallic aerosols at high fluences.

Thompson scattering has been used in the literature for plasma analysis and LIBS research [274–276]. However, to the best of author's knowledge, it has not been used in LII research. Thompson scattering occurs when electromagnetic radiation interacts with charged particles (electrons or ions) in the plasma, leading to an acceleration of the free charges and thus the emission. Thompson scattering

should be detectable in the case of the production of high-energy plasma, which makes it more useful for high-fluence LII research [243].

Direct light plasma imaging and Thompson light scattering using a secondary 532 nm laser could be employed to elucidate the plasma dynamics during the early plasma evolution. Temporal changes in the Thompson scattering signal during the laser pulse could be used to quantify the magnitude of the ionization and ion temperatures and neutral densities in the system, and to examine the equilibrium considerations. Also this could provide a direct technique of measuring electron/ion properties inside the plasma as compared to other techniques such as Langmuir probes [277]. The magnitude of the bremsstrahlung signal can also be increased in the case of a higher plasma density concentration.

The study on laser-induced breakdown spectroscopy using static magnets in the setup to induce a constant magnetic flux to the laser-induced plasma has shown to increase the spontaneous atomic emission by a factor of two in some experiments [278]. The same concept could be implemented in an LII experiment, to investigate the possibility of plasma formation. This would be especially useful to increase the detectability of the bremstralung emission from a weak plasma, which is otherwise difficult to discent from the black-body emission from the nanoparticle. Moreover, the magnetic flux will increase the final spontaneous atomic-emission [178] as the LIBS experiment suggested. The relation between the constant magnetic flux and the increase in the bremsstrahlung radiation and the spontaneous atomic-emissions could be used to collect information about the density and distribution of the microplasma.

References

[1] Kruis FE, Fissan H, Peled A. Synthesis of nanoparticles in the gas phase for electronic, optical and magnetic applications—a review. J Aerosol Sci 1998;29:511–35. https://doi.org/10.1016/S0021-8502(97)10032-5.

[2] Luo YL, Shiao YS, Huang YF. Release of photoactivatable drugs from plasmonic nanoparticles for targeted cancer therapy. ACS Nano 2011;5:7796–804. https://doi.org/10.1021/nn201592s.

[3] O'Neal DP, Hirsch LR, Halas NJ, Payne JD, West JL. Photo-thermal tumor ablation in mice using near infrared-absorbing nanoparticles. Cancer Lett 2004;209:171–6. https://doi.org/10.1016/j.canlet.2004.02.004.

[4] Xu H, Bjerneld EJ, Käll M, Börjesson L. Spectroscopy of single hemoglobin molecules by surface enhanced Raman scattering. Phys Rev Lett 1999;83:4357–60. https://doi.org/10.1103/PhysRevLett.83.4357.

[5] Atwater HA, Polman A. Plasmonics for improved photovoltaic devices. Nat Mater 2010;9:205–13. https://doi.org/10.1038/nmat2629.

[6] Benelmekki M. An introduction to nanoparticles and nanotechnology. Des. Hybrid Nanoparticles, Morgan & Claypool Publishers; 2014. https://doi.org/10.1088/978-1-6270-5469-0ch1.

[7] Schwartzberg AM, Olson TY, Talley CE, Zhang JZ. Synthesis, characterization, and tunable optical properties of hollow gold nanospheres. J Phys Chem B 2006;110:19935–44. https://doi.org/10.1021/jp062136a.

[8] Huang X, El-Sayed M a. Gold nanoparticles: Optical properties and implementations in cancer diagnosis and photothermal therapy. J Adv Res 2010;1:13–28. https://doi.org/10.1016/j.jare.2010.02.002.

[9] Vinogradov S, Wei X. Cancer stem cells and drug resistance: the potential of nanomedicine. Nanomedicine 2012;7:597–615. https://doi.org/10.2217/nnm.12.22.

[10] Watson AY, Valberg PA. Carbon Black and Soot: Two Different Substances. AIHAJ - Am Ind Hyg Assoc 2010;62:218–28. https://doi.org/10.1080/15298660108984625.

[11] Hayashi J, Hashimoto N, Nakatsuka N, Tsuji H, Watanabe H, Makino H, et al. Soot formation characteristics in a lab-scale turbulent pulverized coal flame with simultaneous planar measurements of laser induced incandescence of soot and Mie scattering of pulverized coal. Proc Combust Inst 2013;34:2435–43. https://doi.org/10.1016/j.proci.2012.10.002.

[12] Menon S, Hansen J, Nazarenko L, Luo Y. Climate Effects of Black Carbon Aerosols in China and India. Science (80-) 2002;297:2250–3. https://doi.org/10.1126/science.1075159.

[13] Jacobson MZ. Strong radiative heating due to the mixing state of black carbon in atmospheric aerosols. Nature 2001;409:695–7. https://doi.org/10.1038/35055518.

[14] Lighty JS, Veranth JM, Sarofim a F. Combustion aerosols: factors governing their size and composition and implications to human health. J Air Waste Manag Assoc 2000;50:1565–618. https://doi.org/10.1080/10473289.2000.10464197.

[15] Stieb DM, Chen L, Eshoul M, Judek S. Ambient air pollution, birth weight and preterm birth: A systematic review and meta-analysis. Environ Res 2012;117:100–11. https://doi.org/10.1016/j.envres.2012.05.007.

[16] Smith RB, Fecht D, Gulliver J, Beevers SD, Dajnak D, Blangiardo M, et al. Impact of London's road traffic air and noise pollution on birth weight: Retrospective population based cohort study. BMJ 2017;359. https://doi.org/10.1136/bmj.j5299.

[17] Gehring U, Wijga AH, Hoek G, Bellander T, Berdel D, Brüske I, et al. Exposure to air pollution and development of asthma and rhinoconjunctivitis throughout childhood and adolescence: A population-based birth cohort study. Lancet Respir Med 2015;3:933–42. https://doi.org/10.1016/S2213-2600(15)00426-9.

[18] Dreier T, Schulz C. Laser-based diagnostics in the gas-phase synthesis of inorganic nanoparticles. Powder Technol 2016;287:226–38. https://doi.org/10.1016/j.powtec.2015.10.015.

[19] Alexander DTL, Crozier P a, Anderson JR. Brown Carbon Spheres in East Asian Outflow and Their Optical Properties. Science (80-) 2008;321:833–6. https://doi.org/10.1126/science.1155296.

[20] Lack DA, Cappa CD, Division CS. and Physics Impact of brown and clear carbon on light absorption enhancement , single scatter albedo and absorption wavelength dependence of black carbon 2010:4207–20. https://doi.org/10.5194/acp-10-4207-2010.

[21] Sipkens TA, Singh NR, Daun KJ. Time-resolved laser-induced incandescence characterization of metal nanoparticles. Appl Phys B Lasers 2017;123:14. https://doi.org/10.1007/s00340-016-6593-7.

[22] Sorensen CM, Cai J, Lu N. Light-scattering measurements of monomer size , monomers per aggregate , and fractal dimension for soot aggregates in flames. Appl Opt 1992;31:6547–57. https://doi.org/https://doi.org/10.1364/ao.31.006547.

[23] Sorensen CM. Light Scattering by Fractal Aggregates: A Review. vol. 35. 2001. https://doi.org/10.1080/027868201316900007.

[24] Forrest SR, Witten TA. Long-range correlations in smoke-particle aggregates. J Phys A Math Gen 1979;12:L109. https://doi.org/10.1088/0305-4470/12/5/008.

[25] Brasil AM, Farias TL, Carvalho MG. Evaluation of the Fractal Properties of Cluster? Cluster Aggregates. Aerosol Sci Technol 2000;33:440–54. https://doi.org/10.1080/02786820050204682.

[26] Köylü ÜÖ, Faeth GM, Farias TL, Carvalho MG. Fractal and projected structure properties of soot aggregates. Combust Flame 1995;100:621–33. https://doi.org/10.1016/0010-2180(94)00147-K.

[27] Li Z, Song C, Song J, Lv G, Dong S, Zhao Z. Evolution of the nanostructure, fractal dimension and size of in-cylinder soot during diesel combustion process. Combust Flame 2011;158:1624–30. https://doi.org/10.1016/j.combustflame.2010.12.006.

[28] Dobbins RA. Hydrocarbon Nanoparticles Formed in Flames and Diesel Engines. Aerosol Sci Technol 2007;41:485–96. https://doi.org/10.1080/02786820701225820.

[29] Gwaze P, Schmid O, Annegarn HJ, Andreae MO, Huth J, Helas G. Comparison of three methods of fractal analysis applied to soot aggregates from wood combustion. J Aerosol Sci 2006;37:820–38. https://doi.org/10.1016/j.jaerosci.2005.06.007.

[30] Sorensen CM, Feke GD. The Morphology of Macroscopic Soot. Aerosol Sci Tech 1996;25:328–37. https://doi.org/10.1080/02786829608965399.

[31] Pyrz WD, Buttrey DJ. Particle Size Determination Using TEM: A Discussion of Image Acquisition and Analysis for the Novice Microscopist. Langmuir 2008;24:11350–60. https://doi.org/10.1021/la801367j.

[32] Neer A, Koylu UO. Effect of operating conditions on the size, morphology, and concentration of submicrometer particulates emitted from a diesel engine. Combust Flame 2006;146:142–54. https://doi.org/10.1016/j.combustflame.2006.04.003.

[33] Bescond A, Yon J, Ouf FX, Ferry D, Delhaye D, Gaffié D, et al. Automated Determination of Aggregate Primary Particle Size Distribution by TEM Image Analysis: Application to Soot. Aerosol Sci Technol 2014;48:831–41. https://doi.org/10.1080/02786826.2014.932896.

[34] Einar Kruisa F, Fissana H, Peleda A. Synthesis of nanoparticles in the gas phase for electronic, optical and magnetic applications—a review. J Aerosol Sci 1998;29:511–35. https://doi.org/10.1016/S0021-8502(97)10032-5.

[35] Vander Wal RL, Weiland KJ. Laser-induced incandescence: development and characterization towards a measurement of soot-volume fraction. Appl Phys B 1994;59:445–52. https://doi.org/10.1007/BF01081067.

[36] Tishkoff, J. M., D. C. Hammond Jr ARC. Diagnostic measurements of fuel spray dispersion. J Fluids Eng 1982:313–7. https://doi.org/https://doi.org/10.1115/1.3241839.

[37] Coderre AR, Thomson KA, Snelling DR, Johnson MR. Spectrally resolved light absorption properties of cooled soot from a methane flame. Appl Phys B 2011;104:175–88. https://doi.org/10.1007/s00340-011-4448-9.

[38] Ma B, Long MB. Combined soot optical characterization using 2-D multi-angle light scattering and spectrally resolved line-of-sight attenuation and its implication on soot color-ratio pyrometry. Appl Phys B Lasers Opt 2014;117:287–303. https://doi.org/10.1007/s00340-014-5834-x.

[39] Scherer JJ, Paul JB, O'Keefe A, Saykally RJ. Cavity Ringdown Laser Absorption Spectroscopy: History, Development, and Application to Pulsed Molecular Beams. Chem Rev 1997;97:25–52. https://doi.org/10.1021/cr930048d.

[40] Vander Wal RL. Calibration and comparison of laser-induced incandescence with cavity ring-down. Symp Combust 1998;27:59–67. https://doi.org/https://doi.org/10.1016/s0082-0784(98)80390-1.

[41] Miziolek AW, Palleschi V, Schechter I. LIBS Fundamentials and Applications. Cambridge University Press; 2006. https://doi.org/10.1017/CBO9780511541261.

[42] Cremers D a., Radziemski LJ. Handbook of Laser-Induced Breakdown Spectroscopy. 2006. https://doi.org/10.1002/0470093013.

[43] Hessler JP, Seifert S, Winans RE. Spatially resolved small-angle X-ray scattering studies of soot inception and growth. Twenty-Ninth Symp Combust 2002;29:395–407. https://doi.org/10.1016/S1540-7489(02)80334-0.

[44] Xu R. Light scattering: A review of particle characterization applications. Particuology 2015;18:11–21. https://doi.org/10.1016/j.partic.2014.05.002.

[45] Sivaprakasam V, Lin H-B, Huston AL, Eversole JD. Spectral characterization of biological aerosol

particles using two-wavelength excited laser-induced fluorescence and elastic scattering measurements. Opt Express 2011;19:6191–208. https://doi.org/10.1364/oe.19.006191.

[46] Clark RJH, Long DA. Raman spectroscopy. New York: McGraw-Hill; 1977.

[47] A. ST. Advances in the Modeling of Time-Resolved Laser-Induced Incandescence. University of Waterloo, 2018.

[48] Michelsen HA, Liu F, Kock BF, Bladh H, Boiarciuc A, Charwath M, et al. Modeling laser-induced incandescence of soot: A summary and comparison of LII models. Appl Phys B Lasers Opt 2007;87:503–21. https://doi.org/10.1007/s00340-007-2619-5.

[49] Schulz C, Kock BF, Hofmann M, Michelsen H, Will S, Bougie B, et al. Laser-induced incandescence: recent trends and current questions. Appl Phys B 2006;83:333–54. https://doi.org/10.1007/s00340-006-2260-8.

[50] Snelling DR, Thomson KA, Liu F, Smallwood GJ. Comparison of LII derived soot temperature measurements with LII model predictions for soot in a laminar diffusion flame. Appl Phys B Lasers Opt 2009;96:657–69. https://doi.org/10.1007/s00340-009-3614-9.

[51] Lehre T, Jungfleisch B, Suntz R, Bockhorn H. Size distributions of nanoscaled particles and gas temperatures from time-resolved laser-induced-incandescence measurements. Appl Opt 2003;42:2021–30. https://doi.org/10.1364/AO.42.002021.

[52] Case MK, Hofeldt DL. Soot Mass Concentration Measurements in Diesel Engine Exhaust Using Laser-Induced Incandescence. Aerosol Sci Technol 1996;25:46–60. https://doi.org/10.1080/02786829608965378.

[53] Dankers S, Leipertz A. Determination of primary particle size distributions from time-resolved laser-induced incandescence measurements. Appl Opt 2004;43:3726–31. https://doi.org/10.1364/AO.43.003726.

[54] Liu F, Yang M, Hill FA, Smallwood GJ, Snelling DR. Influence of polydisperse distributions of both primary particle and aggregate sizes on soot temperature in low-fluence laser-induced incandescence. CEUR Workshop Proc 2005;195:14. https://doi.org/10.1007/s00340-006-2196-z.

[55] Vander Wal RL, Dietrich DL. Laser-induced incandescence applied to droplet combustion. Appl Opt 1995;34:1103. https://doi.org/10.1364/AO.34.001103.

[56] Shaddix CR, Smyth KC. Laser-induced incandescence measurements of soot production in steady and flickering methane, propane, and ethylene diffusion flames. Combust Flame 1996;107:418–52. https://doi.org/10.1016/S0010-2180(96)00107-1.

[57] Filippov A V, Markus MW, Roth P. In-situ characterization of ultrafine particles by laser-induced incandescence: sizing and particle structure determination. J Aerosol Sci 1999;30:71–87. https://doi.org/https://doi.org/10.1016/s0021-8502(98)00021-4.

[58] Dec JE, zur Loye AO, Siebers DL. Soot Distribution in a D.I. Diesel Engine Using 2-D Laser-Induced Incandescence Imaging, 1991. https://doi.org/10.4271/910224.

[59] Wal R. Vander, Weiland KJ. Laser-induced incandescence: Development and characterization towards a measurment of soo-volume fraction 1994.

[60] Chang H, Biswas P. In Situ light scattering dissymmetry measurements of the evolution of the aerosol size distribution in flames. J Colloid Interface Sci 1992;153:157–66. https://doi.org/10.1016/0021-9797(92)90307-8.

[61] Manickavasagam S, Mengüç MP. Scattering matrix elements of fractal-like soot agglomerates. Appl Opt 1997;36:1337–51. https://doi.org/10.1364/AO.36.001337.

[62] Oltmann H, Reimann J, Will S. Wide-angle light scattering (WALS) for soot aggregate characterization. Combust Flame 2010;157:516–22. https://doi.org/10.1016/j.combustflame.2009.10.011.

[63] Huber FJT, Altenhoff M, Will S. A mobile system for a comprehensive online-characterization of nanoparticle aggregates based on wide-angle light scattering and laser-induced incandescence. Rev Sci Instrum 2016;87:053102. https://doi.org/10.1063/1.4948288.

[64] Filippov A V., Zurita M, Rosner DE. Fractal-like Aggregates: Relation between Morphology and Physical Properties. J Colloid Interface Sci 2000;229:261–73. https://doi.org/10.1006/jcis.2000.7027.

[65] Burr DW, Daun KJ, Link O, Thomson KA, Smallwood GJ. Determination of the soot aggregate size distribution from elastic light scattering through Bayesian inference. J Quant Spectrosc Radiat Transf 2011;112:1099–107. https://doi.org/10.1016/j.jqsrt.2010.12.001.

[66] Gangopadhyay S, Elminyawi I, Sorensen CM. Optical structure factor measurements of soot particles in a premixed flame. Appl Opt 1991;30:4859. https://doi.org/10.1364/ao.30.004859.

[67] Sorensen CM, Cai J, Lu N. Light-scattering measurements of monomer size, monomers per aggregate, and fractal dimension for soot aggregates in flames. Appl Opt 1992;31:6547. https://doi.org/https://doi.org/10.1364/ao.31.006547.

[68] Köylü ÜÖ, Faeth GM. Optical Properties of Soot in Buoyant Laminar Diffusion Flames. J Heat Transfer 1994;116:971–9. https://doi.org/10.1115/1.2911473.

[69] Tsutsui K, Koya K, Kato T. An investigation of continuous-angle laser light scattering. Rev Sci Instrum 1998;69:3482–6. https://doi.org/10.1063/1.1149124.

[70] Santoro RJ, Semerjian HG, Dobbins RA. Soot particle measurements in diffusion flames. Combust Flame 1983;51:203–18. https://doi.org/10.1016/0010-2180(83)90099-8.

[71] Puri R, Richardson TF, Santoro RJ, Dobbins RA. Aerosol dynamic processes of soot aggregates in a laminar ethene diffusion flame. Combust Flame 1993;92:320–33. https://doi.org/10.1016/0010-2180(93)90043-3.

[72] Haller HR, Destor C, Cannell DS. Photometer for quasielastic and classical light scattering. Rev Sci Instrum 1983;54:973–83. https://doi.org/10.1063/1.1137512.

[73] Salzman GC, Crowell JM, Martin JC, Trujillo TT, Romero A, Mullaney PF, et al. Cell classification by laser light scattering: identification and separation of unstained leukocytes. Acta Cytol 1975;19:374–7.

[74] Bartholdi M, Salzman GC, Hiebert RD, Kerker M. Differential light scattering photometer for rapid analysis of single particles in flow. Appl Opt 1980;19:1573. https://doi.org/10.1364/ao.19.001573.

[75] Huber FJT, Will S. Characterization of a silica-aerosol in a sintering process by wide-angle light scattering and principal component analysis. J Aerosol Sci 2018;119:62–76. https://doi.org/10.1016/J.JAEROSCI.2018.02.006.

[76] Huber FJT, Will S, Daun KJ. Sizing aerosolized fractal nanoparticle aggregates through Bayesian analysis of wide-angle light scattering (WALS) data. J Quant Spectrosc Radiat Transf 2016;184:27–39. https://doi.org/10.1016/j.jqsrt.2016.06.030.

[77] Oltmann H, Reimann J, Will S. Single-shot measurement of soot aggregate sizes by wide-angle light scattering (WALS). Appl Phys B Lasers Opt 2012;106:171–83. https://doi.org/10.1007/s00340-011-4781-z.

[78] Altenhoff M, Aßmann S, Perlitz JFA, Huber FJT, Will S. Soot aggregate sizing in an extended premixed flame by high-resolution two-dimensional multi-angle light scattering (2D-MALS). Appl Phys B 2019;125:1–15. https://doi.org/10.1007/s00340-019-7282-0.

[79] Stanley, H Eugene; Ostrowsky N. An Introduction to Self-Similarity and Fractal Behavior. Springer; 1986. https://doi.org/https://doi.org/10.1007/978-94-009-5165-5_2.

[80] Chang H, Lin WY, Biswas P. An Inversion Technique to Determine the Aerosol Size Distribution in Multicomponent Systems from In Situ Light Scattering Measurements. Aerosol Sci Technol 1995;22:24–32. https://doi.org/10.1080/02786829408959725.

[81] Eriçok OB, Ertürk H. Inverse Characterization of Nanoparticle Clusters Using Unpolarized Optical Scattering Without Ex-Situ Measurements 2017. https://doi.org/10.1016/j.jqsrt.2017.04.029.

[82] Hadamard J. Sur les Problemes Aux Derivees Partielles et Leur Signification Physique. Princet Univ Bull 1902:45–52.

[83] Mie G. Beiträge zur Optik trüber Medien, speziell kolloidaler Metallösungen. Ann Phys 1908;330:377–445. https://doi.org/10.1002/andp.19083300302.

[84] T. L. MDGF, Ü. Ö. K, Carvalho. Effects of polydispersity of aggregates and primary particles on radiative properties of simulated soot. J Quant Spectrosc Radiat Transf 1996;55:357–71. https://doi.org/10.1016/0022-4073(95)00166-2.

[85] Xu Y. Electromagnetic scattering by an aggregate of spheres : far field. Appl Opt 1997;36:9496–508. https://doi.org/https://doi.org/10.1364/ao.36.009496.

[86] Machowski DW., Mishchenko MI. A multiple sphere T-matrix Fortran code for use on parallel computer clusters. J Quant Spectrosc Radiat Transf 2013;112:2182–92. https://doi.org/https://doi.org/10.1016/j.jqsrt.2011.02.019.

[87] Purcell EM., Pennypacker CR. Scattering and absorption of light by nonspherical dielectric grains. Astrophys J 1973;186:705–14. https://doi.org/10.1086/152538.

[88] Gouesbet G, Gréhan G. Generalized Lorenz-Mie Theories. Cham: Springer International Publishing; 2017. https://doi.org/10.1007/978-3-319-46873-0.

[89] Burr DW, Daun KJ, Thomson KA, Smallwood GJ. Optimization of measurement angles for soot aggregate sizing by elastic light scattering, through design-of-experiment theory. J Quant Spectrosc Radiat Transf 2012;113:355–65. https://doi.org/10.1016/j.jqsrt.2011.12.004.

[90] Liu F, Wong C. Investigation of Absorption and Scattering Properties of Soot Aggregates of Different Fractal Dimension at 532 nm Using RDG and GMM. Aerosol Sci Technol 2013;47:1393–405. https://doi.org/10.1080/02786826.2013.847525.

[91] Liu F, Snelling D. Evaluation of the accuracy of the RDG approximation for the absorption and scattering properties of fractal aggregates of flame- generated soot. 40th Thermophys. Conf., 2008.

[92] Liu F, Yon J, Bescond A. On the radiative properties of soot aggregates - Part 2: Effects of coating. J Quant Spectrosc Radiat Transf 2016;172:134–45. https://doi.org/10.1016/j.jqsrt.2015.08.005.

[93] Weeks RW, Duley WW. Aerosol-particle sizes from light emission during excitation by TEA CO2 laser pulses. J Appl Phys 1974;45:4661–2. https://doi.org/10.1063/1.1663111.

[94] Eckbreth AC. Effects of laser-modulated particulate incandescence on Raman scattering diagnostics. J Appl Phys 1977;48:4473–9. https://doi.org/10.1063/1.323458.

[95] Melton LA. Soot diagnostics based on laser heating. Appl Opt 1984;23:2201. https://doi.org/10.1364/AO.23.002201.

[96] Rohlfing EA. Optical emission studies of atomic, molecular, and particulate carbon produced from a laser vaporization cluster source. J Chem Phys 1988;89:6103–12. https://doi.org/https://doi.org/10.1063/1.455426.

[97] Schraml S, Will S, Leipertz A. Simultaneous measurement of soot mass concentration and primary particle size in the exhaust of a di diesel engine by time-resolved laser-induced incandescence (TIRE-LII). SAE Tech Pap 1999;108:82–9. https://doi.org/10.4271/1999-01-0146.

[98] Dec JE, Espey C. Soot and fuel distributions in a D.I. diesel engine via 2-D imaging. SAE Tech. Pap., SAE International; 1992. https://doi.org/10.4271/922307.

[99] Dec JE. Soot distribution in a D.I. Diesel engine using 2-D imaging of laser-induced incandescence, elastic scattering, and flame luminosity. SAE Tech. Pap., SAE International; 1992. https://doi.org/10.4271/920115.

[100] Wainner RT, Seitzman JM, Martin SR. Soot measurements in a simulated engine exhaust using laser-induced incandescence. AIAA J 1999;37:738–43. https://doi.org/https://doi.org/10.2514/2.782.

[101] Mitrovic A, Lee TW. Soot formation characteristics of laminar partially premixed flames. Combust Flame 1998;115:437–42. https://doi.org/10.1016/S0010-2180(98)00004-2.

[102] Snelling DR, Thomson KA, Smallwood GJ, Gülder ÖL. Two-dimensional imaging of soot volume fraction in laminar diffusion flames. Appl Opt 1999;38:2478–85. https://doi.org/10.1364/AO.38.002478.

[103] Geitlinger H, Streibel T, Suntz R, Bockhorn H. Two-dimensional imaging of soot volume fractions, particle number densities, and particle radii in laminar and turbulent diffusion flames. Symp Combust 1998;27:1613–21. https://doi.org/https://doi.org/10.1016/S0082-0784(98)80571-7.

[104] Vander Wal RL. LIF-LII measurements in a turbulent gas-jet flame. Exp Fluids 1997;23:281–7. https://doi.org/10.1007/s003480050112.

[105] Shaddix CR, Harrington JE, Smyth KC. Quantitative measurements of enhanced soot production in a flickering methane/air diffusion flame. Combust Flame 1994;99:723–32.

[106] Brookes SJ, Moss JB. Predictions of soot and thermal radiation properties in confined turbulent jet diffusion flames. Combust Flame 1999;116:486–503. https://doi.org/10.1016/S0010-2180(98)00056-X.

[107] Ni T, Pinson JA, Gupta S, Santoro RJ. Two-dimensional imaging of soot volume fraction by the use of laser-induced incandescence. Appl Opt 1995;34:7083. https://doi.org/10.1364/AO.34.007083.

[108] Snelling DR, Thomson KA, Smallwood GJ, Gülder ÖL. Two-dimensional imaging of soot volume fraction in laminar diffusion flames. Appl Opt 1999;38:2478. https://doi.org/10.1364/ao.38.002478.

[109] Vander Wal RL. Soot precursor carbonization: Visualization using LIF and LII and comparison using bright and dark field TEM. Combust Flame 1998;112:607–16. https://doi.org/10.1016/S0010-

2180(97)00171-5.

[110] Vander Wal RL. Soot precursor material: Visualization via simultaneous lIF-LII and characterization via tem. Symp Combust 1996;26:2269–75. https://doi.org/10.1016/S0082-0784(96)80054-3.

[111] Cignoli F, Benecchi S, Zizak G. Time-delayed detection of laser-induced incandescence for the two-dimensional visualization of soot in flames. Appl Opt 1994;33:5778–82. https://doi.org/10.1364/AO.33.005778.

[112] Vander Wal RL, Ticich TM, West JR. Laser-induced incandescence applied to metal nanostructures. Appl Opt 1999;38:5867–79. https://doi.org/10.1364/AO.38.005867.

[113] Eremin A, Gurentsov E, Popova E, Priemchenko K. Size dependence of complex refractive index function of growing nanoparticles. Appl Phys B Lasers Opt 2011;104:285–95. https://doi.org/10.1007/s00340-011-4420-8.

[114] Gurentsov E V., Eremin A V. Size measurement of carbon and iron nanoparticles by laser induced incadescence. High Temp 2011;49:667–73. https://doi.org/10.1134/S0018151X11050087.

[115] Sipkens TA, Singh NR, Daun KJ. Time-resolved laser-induced incandescence characterization of metal nanoparticles. Appl Phys B 2017;123:14–30. https://doi.org/10.1007/s00340-016-6593-7.

[116] Michelsen HA, Schulz C, Smallwood GJ, Will S. Laser-induced incandescence: Particulate diagnostics for combustion, atmospheric, and industrial applications. Prog Energy Combust Sci 2015;51:2–48. https://doi.org/10.1016/j.pecs.2015.07.001.

[117] Daun KJ, Smallwood GJ, Liu F. Investigation of Thermal Accommodation Coefficients in Time-Resolved Laser-Induced Incandescence. J Heat Transfer 2008;130:121201. https://doi.org/10.1115/1.2977549.

[118] Talebi-Moghaddam S, Sipkens TA, Daun KJ. Laser - induced incandescence on metal nanoparticles : validity of the Rayleigh approximation. Appl Phys B 2019;125:214. https://doi.org/10.1007/s00340-019-7325-6.

[119] Jolliffe IT. Principal Component Analysis, Second Edition. John Wiley & Sons, Ltd; 2002. https://doi.org/10.2307/1270093.

[120] Bohren CF, Huffman DR. Absorption and Scattering of Light by Small Particles. Inc: John Wiley & Sons; 1983. https://doi.org/ttps://doi.org/10.1002/9783527618156.

[121] Bohren CF. Light scattering by an aribitrary particle: the scattering-order formulation of the coupled-dipole method. J Opt Soc Am A 1988;5:1867. https://doi.org/https://doi.org/10.1364/josaa.5.001867.

[122] Talebi Moghaddam S, Hadwin PJ, Daun KJ. Soot aggregate sizing through multiangle elastic light scattering: Influence of model error. J Aerosol Sci 2017;111:36–50. https://doi.org/10.1016/j.jaerosci.2017.06.003.

[123] Hadwin PJ. Stochastic Boundary Operators and Model Uncertainties in Electrical Impedance Tomography. University of Auckland, 2015.

[124] Calvetti D, Hadwin PJ, Huttunen JMJ, Isaacson D, Kaipio JP, McGivney D, et al. Artificial boundary conditions and domain truncation in electrical impedance tomography. Part I: Theory and preliminary results. Inverse Probl Imaging 2015;9:749–66. https://doi.org/10.3934/ipi.2015.9.749.

[125] Barber D. Bayesian Reasoning and Machine Learning. Cambridge university press; 2012.

https://doi.org/https://doi.org/10.1017/cbo9780511804779.

[126] Kaipio J, Somersalo E. Statistical inverse problems: Discretization, model reduction and inverse crimes. J Comput Appl Math 2007;198:493–504. https://doi.org/10.1016/J.CAM.2005.09.027.

[127] Mackowski DW, Mishchenko MI. Calculation of the T matrix and the scattering matrix for ensembles of spheres. J Opt Soc Am A 1996;13:2266–78. https://doi.org/https://doi.org/10.1364/josaa.13.002266.

[128] Mackowski DW. Calculation of total cross sections of multiple-sphere clusters. J Opt Soc Am A 1994;11:2851. https://doi.org/10.1364/JOSAA.11.002851.

[129] Dobbins RA, Megaridis CM. Absorption and scattering of light by polydisperse aggregates. Appl Opt 1991;30:4747–54. https://doi.org/10.1364/AO.30.004747.

[130] Chakrabarty RK, Moosmüller H, Arnott WP, Garro MA, Slowik JG, Cross ES, et al. Light scattering and absorption by fractal-like carbonaceous chain aggregates: comparison of theories and experiment. Appl Opt 2007;46:6990–7006. https://doi.org/10.1364/AO.46.006990.

[131] Yon J, Liu F, Bescond A, Caumont-Prim C, Rozé C, Ouf FX, et al. Effects of multiple scattering on radiative properties of soot fractal aggregates. J Quant Spectrosc Radiat Transf 2014;133:374–81. https://doi.org/10.1016/j.jqsrt.2013.08.022.

[132] Yon J, Rozé C, Girasole T, Coppalle A, Méès L. Extension of RDG-FA for scattering prediction of aggregates of soot taking into account interactions of large monomers. Part Part Syst Charact 2008;25:54–67. https://doi.org/10.1002/ppsc.200700011.

[133] Kaipio, J. and Somersalo E. Statistical and Computational Inverse Problems. vol. 160. 2006. https://doi.org/10.1007/b138659.

[134] Lin MY, Klein R, Lindsay HM, Weitz DA, Ball RC, Meakin P. The structure of fractal colloidal aggregates of finite extent. J Colloid Interface Sci 1990;137:263–80. https://doi.org/10.1016/0021-9797(90)90061-R.

[135] Liu F, Smallwood GJ. Radiative Properties of Numerically Generated Fractal Soot Aggregates : The Importance of Configuration Averaging. J Heat Transfer 2010;132:023308. https://doi.org/10.1115/1.4000245.

[136] Draine BT, Flatau PJ. Discrete-dipole approximation for scattering calculations. J Opt Soc Am A 1994;11:1491–9. https://doi.org/10.1364/JOSAA.11.001491.

[137] Jaynes ET. Prior Probabilities. IEEE Trans Syst Sci Cybern 1968;4:227–41. https://doi.org/10.1109/TSSC.1968.300117.

[138] Jaynes ET. Information theory and statistical mechanics. II. Phys Rev 1957;108:171. https://doi.org/10.1103/PhysRev.106.620.

[139] Nissinen A, Kolehmainen V, Kaipio JP. Reconstruction of domain boundary and conductivity in electrical impedance tomography using the approximation error approach. Int J Uncertain Quantif 2011;1. https://doi.org/10.1615/Int.J.UncertaintyQuantification.v1.i3.20.

[140] Ulanowski Z, Wang Z, Kaye PH, Ludlow IK. Application of neural networks to the inverse light scattering problem for spheres. Appl Opt 2008;37:4027. https://doi.org/10.1364/ao.37.004027.

[141] Ishimaru A, Kitamura S, Marks RJ, Tsang L, Lam CM, Park DC. Particle-size distribution determination using optical sensing and neural networks. Opt Lett 1990;15:1221–3. https://doi.org/10.1364/ol.15.001221.

[142] Ericok OB, Ozbek AK, Cemgil AT, Erturk H. Gaussian Process and Design of Experiments for Surrogate Modeling of Optical Properties of Fractal Aggregates. J Quant Spectrosc Radiat Transf 2019;239:106643. https://doi.org/10.1016/j.jqsrt.2019.106643.

[143] Haykin S. Neural Networks: a comprehensive foundation. Prentice Hall PTR; 1994. https://doi.org/10.1145/272874.1067696.

[144] Schalkoff RJ. Artificial neural networks. McGraw-Hill Higher Education; 1997.

[145] de Harrington PB. Sigmoid transfer functions in backpropagation neural networks. Analytica 1993;65:2167–8. https://doi.org/doi/pdf/10.1021.

[146] Møller MF. A scaled conjugate gradient algorithm for fast supervised learning. Neural Networks 1993;6:525–33. https://doi.org/10.1016/S0893-6080(05)80056-5.

[147] Oh C, Sorensen CM. Light scattering study of fractal cluster aggregation near the free molecular regime. J Aerosol Sci 1997;28:937–57. https://doi.org/10.1016/S0021-8502(96)00488-0.

[148] Skorupski K, Mroczka J, Riefler N, Oltmann H, Will S, Wriedt T. Impact of morphological parameters onto simulated light scattering patterns. J Quant Spectrosc Radiat Transf 2013;119:53–66. https://doi.org/10.1016/j.jqsrt.2012.12.014.

[149] Altenhoff M, Aßmann S, Teige C, Huber FJT, Will S. An optimized evaluation strategy for a comprehensive morphological soot nanoparticle aggregate characterization by electron microscopy. J Aerosol Sci 2019;139. https://doi.org/10.1016/j.jaerosci.2019.105470.

[150] Kaipio J, Somersalo E. Statistical and Computational Inverse Problems. New York: Springer Science and Business Media; 2005. https://doi.org/10.1007/b138659.

[151] K. HW. Monte carlo sampling methods using Markov chains and their applications. Biometrika 1970;57:97–109. https://doi.org/10.1093/biomet/57.1.97.

[152] Sorensen CM, Yon J, Liu F, Maughan J, Heinson WR, Berg MJ. Light scattering and absorption by fractal aggregates including soot. J Quant Spectrosc Radiat Transf 2018;217:459–73. https://doi.org/10.1016/j.jqsrt.2018.05.016.

[153] Arganda-Carreras I, Kaynig V, Rueden C, Eliceiri KW, Schindelin J, Cardona A, et al. Trainable Weka Segmentation: a machine learning tool for microscopy pixel classification. Bioinformatics 2017;33:2424–6. https://doi.org/10.1093/bioinformatics/btx180.

[154] Wozniak M, Onofri FRA, Barbosa S, Yon J, Mroczka J. Comparison of methods to derive morphological parameters of multi-fractal samples of particle aggregates from TEM images. J Aerosol Sci 2011;47:12–26. https://doi.org/10.1016/j.jaerosci.2011.12.008.

[155] Köylü ÜÖ. Quantitative analysis of in situ optical diagnostics for inferring particle/aggregate parameters in flames: Implications for soot surface growth and total emissivity. Combust Flame 1997;109:488–500. https://doi.org/10.1016/S0010-2180(96)00179-4.

[156] Brasil AM, Farias TL, Koylu UO, Carvalho MG. A recipe for image characterization of fractal-like aggregates. J Aerosol Sci 1999;29:1379–89. https://doi.org/10.1016/S0021-8502(98)90820-5.

[157] Liu C, Yin Y, Hu F, Jin H, Sorensen CM. The Effects of Monomer Size Distribution on the Radiative Properties of Black Carbon Aggregates. Aerosol Sci Technol 2015;49:928–40.

https://doi.org/10.1080/02786826.2015.1085953.

[158] Yon J, Bescond A, Liu F. On the radiative properties of soot aggregates part 1: Necking and overlapping. J Quant Spectrosc Radiat Transf 2015;162:197–206. https://doi.org/10.1016/j.jqsrt.2015.03.027.

[159] Hadwin PJ, Sipkens TA, Thomson KA, Liu F, Daun KJ. Quantifying uncertainty in soot volume fraction estimates using Bayesian inference of auto-correlated laser-induced incandescence measurements. Appl Phys B 2016;122:1. https://doi.org/10.1007/s00340-015-6287-6.

[160] Taylor, Thomas W. CMS. Moment analysis of the cluster-size-distribution approach to scaling during coagulation. Phys Rev A 1987;36:5415. https://doi.org/10.1017/CBO9781107415324.004.

[161] Wasserman L. Bayesian Model Selection and Model Averaging. J Math Psychol 2000;44:92–107. https://doi.org/10.1006/JMPS.1999.1278.

[162] Sorensen CM, Roberts GC. The prefactor of fractal aggregates. J Colloid Interface Sci 1997;186:447–52. https://doi.org/10.1006/jcis.1996.4664.

[163] Starke R, Kock B, Roth P. Nano-particle sizing by laser-induced-incandescence (LII) in a shock wave reactor. Shock Waves 2003;12:351–60. https://doi.org/10.1007/s00193-003-0178-1.

[164] Sipkens T, Joshi G, Daun KJ, Murakami Y. Sizing of Molybdenum Nanoparticles Using Time-Resolved Laser-Induced Incandescence. J Heat Transfer 2013;135:052401. https://doi.org/10.1115/1.4023227.

[165] Sipkens TA, Hadwin PJ, Grauer SJ, Daun KJ. General error model for analysis of laser-induced incandescence signals. Appl Opt 2017;56:8436–45. https://doi.org/https://doi.org/10.1364/ao.56.008436.

[166] Eom GS, Park CW, Shin YH, Chung KH, Park S, Choe W, et al. Size determination of nanoparticles in low-pressure plasma with laser-induced incandescence technique. Appl Phys Lett 2003;83:1261–3. https://doi.org/10.1063/1.1599965.

[167] Sipkens TA, Mansmann R, Daun KJ, Petermann N, Titantah JT, Karttunen M, et al. In situ nanoparticle size measurements of gas-borne silicon nanoparticles by time-resolved laser-induced incandescence. Appl Phys B Lasers Opt 2014;116:623–36. https://doi.org/10.1007/s00340-013-5745-2.

[168] Menser J, Daun K, Dreier T, Schulz C. Laser-induced incandescence from laser-heated silicon nanoparticles. Appl Phys B 2016;122:277. https://doi.org/10.1007/s00340-016-6551-4.

[169] Altman IS, Lee D, Chung JD, Song J, Choi M. Light absorption of silica nanoparticles. Phys Rev B 2001;63:161402. https://doi.org/10.1103/PhysRevB.63.161402.

[170] Maffi S, De Iuliis S, Cignoli F, Zizak G. Investigation on thermal accommodation coefficient and soot absorption function with two-color Tire-LII technique in rich premixed flames. Appl Phys B Lasers Opt 2011;104:357–66. https://doi.org/10.1007/s00340-011-4536-x.

[171] Kock BF, Kayan C, Knipping J, Orthner HR, Roth P. Comparison of LII and TEM sizing during synthesis of iron particle chains. Proc Combust Inst 2005;30:1689–96. https://doi.org/10.1016/j.proci.2004.07.034.

[172] Sipkens TA, Menser J, Mansmann R, Schulz C, Daun KJ. Investigating temporal variation in the apparent volume fraction measured by time-resolved laser-induced incandescence. Appl Phys B 2019;125:140. https://doi.org/10.1007/s00340-019-7251-7.

[173] Sipkens TA. Advances in the modeling of time-resolved laser-induced incandescence. University of Waterloo, 2018.

[174] Migliorini F, De Iuliis S, Maffi S, Zizak G. Saturation curves of two-color laser-induced incandescence measurements for the investigation of soot optical properties. Appl Phys B Lasers Opt 2015;120:417–27. https://doi.org/10.1007/s00340-015-6151-8.

[175] Liu F, Rogak S, Snelling DR, Saffaripour M, Thomson KA, Smallwood GJ. Effects of laser fluence non-uniformity on ambient-temperature soot measurements using the auto-compensating laser-induced incandescence technique. Appl Phys B Lasers Opt 2016;122:1–13. https://doi.org/10.1007/s00340-016-6553-2.

[176] Scaffardi LB, Tocho JO. Size dependence of refractive index of gold nanoparticles. Nanotechnology 2006;17:1309–15. https://doi.org/10.1088/0957-4484/17/5/024.

[177] Bisker G, Yelin D. Noble-metal nanoparticles and short pulses for nanomanipulations: theoretical analysis. J Opt Soc Am B 2012;29:1383–1383. https://doi.org/10.1364/JOSAB.29.001383.

[178] Daun K, Menser J, Mansmann R, Moghaddam ST, Dreier T, Schulz C. Spectroscopic models for laser-heated silicon and copper nanoparticles. J Quant Spectrosc Radiat Transf 2017;197:3–11. https://doi.org/10.1016/j.jqsrt.2016.10.006.

[179] Michelsen HA, Linne MA, Kock BF, Hofmann M, Tribalet B, Schulz C. Modeling laser-induced incandescence of soot: Enthalpy changes during sublimation, conduction, and oxidation. Appl Phys B Lasers Opt 2008;93:645–56. https://doi.org/10.1007/s00340-008-3181-5.

[180] Sipkens TA, Singh NR, Daun KJ, Bizmark N, Ioannidis M. Examination of the thermal accommodation coefficient used in the sizing of iron nanoparticles by time-resolved laser-induced incandescence. Appl Phys B Lasers Opt 2015;119:561–75. https://doi.org/10.1007/s00340-015-6022-3.

[181] Pan H, Ritter JA, Balbuena PB. Examination of the approximations used in determining the isosteric heat of adsorption from the Clausius-Clapeyron equation. Langmuir 1998;14:6323–7. https://doi.org/10.1021/la9803373.

[182] Rakic AD, Djurisic AB, Elazar JM, Majewski ML. Optical properties of metallic films for vertical-cavity optoelectronic devices. Appl Opt 1998;37:5271–83. https://doi.org/10.1364/AO.37.005271.

[183] Li KD, Fauchet PM. Drude parameters of liquid silicon at the melting temperature. Appl Phys Lett 1987;51:1747–9. https://doi.org/10.1063/1.98511.

[184] Miller JC. Optical properties of liquid metals at high temperatures. Philos Mag 1969;20:1115–32. https://doi.org/10.1080/14786436908228198.

[185] Johnson P, Christy R. Optical constants of transition metals: Ti, V, Cr, Mn, Fe, Co, Ni, and Pd. Phys Rev B 1974;9:5056–70. https://doi.org/10.1103/PhysRevB.9.5056.

[186] Krishnan S, Yugawa KJ, Nordine PC. Optical properties of liquid nickel and iron. Phys Rev B 1997;55:8201. https://doi.org/https://doi.org/10.1103/PhysRevB.55.8201.

[187] BARNES BT. Optical Constants of Incandescent Refractory Metals. J Opt Soc Am 1966;56:1546. https://doi.org/10.1364/JOSA.56.001546.

[188] Kobatake H, Fukuyama H. Amendments to the Discussion on the Paper Entitled "Normal Spectral Emissivity Measurement of Liquid Iron and Nickel Using Electromagnetic Levitation in Direct Current Magnetic Field." Metall Mater Trans A 2016;47:3303–4. https://doi.org/10.1007/s11661-016-3529-0.

[189] Sorensen CM, Maughan JB, Moosmüller H. Spherical particle absorption over a broad range of imaginary refractive index. J Quant Spectrosc Radiat Transf 2019;226:81–6. https://doi.org/10.1016/j.jqsrt.2019.01.011.

[190] Schebarchov D, Auguié B, Le Ru EC. Simple accurate approximations for the optical properties of metallic nanospheres and nanoshells. Phys Chem Chem Phys 2013;15:4233–42. https://doi.org/10.1039/c3cp44124e.

[191] Dalzell WH, Sarofim AF. Optical Constants of Soot and Their Application to Heat-Flux Calculations. J Heat Transfer 1969;91:100–4. https://doi.org/10.1115/1.3580063.

[192] Lankhuijzen GM, Noordam LD. Atomic streak camera. Opt Commun 1996;129:361–8. https://doi.org/10.1016/S0030-4018(96)00166-6.

[193] Talebi Moghaddam S, Ertürk H, Mengüç MP. Enhancing local absorption within a gold nano-sphere on a dielectric surface under an AFM probe. J Quant Spectrosc Radiat Transf 2016;178:124–33. https://doi.org/10.1016/j.jqsrt.2016.02.011.

[194] Talebi Moghaddam S, Avşar D, Ertürk H, Pınar Mengüç M. Effect of the probe location on the absorption by an array of gold nano-particles on a dielectric surface. J Quant Spectrosc Radiat Transf 2017;197:106–13. https://doi.org/10.1016/j.jqsrt.2017.02.004.

[195] Avşar D, Ertürk H, Mengüç MP. Plasmonic responses of metallic/dielectric core-shell nanoparticles on a dielectric substrate. Mater Res Express 2019;6:065006. https://doi.org/10.1088/2053-1591/ab07fd.

[196] Mur G. Absorbing Boundary Conditions for the Finite-Difference Approximation of the Time-Domain Electromagnetic-Field Equations. IEEE Trans Electromagn Compat 1981;EMC-23:377–82. https://doi.org/10.1109/TEMC.1981.303970.

[197] Eggersdorfer ML, Kadau D, Herrmann HJ, Pratsinis SE. Multiparticle sintering dynamics: From fractal-like aggregates to compact structures. Langmuir 2011;27:6358–67. https://doi.org/10.1021/la200546g.

[198] Peterson NL. Self-diffusion in pure metals. J Nucl Mater 1978;69–70:3–37. https://doi.org/10.1016/0022-3115(78)90234-9.

[199] Suzuki H, I-Yin S. Calculation of the Mie scattering field inside and outside a coated spherical particle. Int J Phys Sci 2008;3:38–41. https://doi.org/https://doi.org/10.1117/12.2549918.

[200] Talebi Moghaddam S, Daun KJ. Plasma emission during time-resolved laser-induced incandescence measurements of aerosolized metal nanoparticles. Appl Phys B 2018;124:159. https://doi.org/10.1007/s00340-018-7028-4.

[201] Mitrani JM, Shneider MN, Stratton BC, Raitses Y. Modeling thermionic emission from laser-heated nanoparticles. Appl Phys Lett 2016;108:054101. https://doi.org/10.1063/1.4940992.

[202] Yen R, Liu J, Gloembergen N. Thermally Assisted Multiphoton Photoelectric Emission From Tungsten. Opt Commun 1980;35:277–82. https://doi.org/10.1016/0030-4018(80)90228-X.

[203] Sundararaman R, Narang P, Jermyn AS, Goddard W a., Atwater H a. Theoretical predictions for hot-carrier generation from surface plasmon decay. Nat Commun 2014;5:5788. https://doi.org/10.1038/ncomms6788.

[204] Gole A, Murphy CJ. Seed-mediated synthesis of gold nanorods: Role of the size and nature of the seed. Chem Mater 2004;16:3633–40. https://doi.org/10.1021/cm0492336.

[205] Bohren CF, Hunt AJ. Scattering of electromagnetic waves by a charged sphere. Can J Phys 1977;55:1930–5. https://doi.org/10.1139/p77-235.

[206] Klacka J, Kocifaj M. Scattering of electromagnetic waves by charged spheres and some physical consequences. J Quant Spectrosc Radiat Transf 2007;106:170–83. https://doi.org/10.1016/j.jqsrt.2007.01.016.

[207] Li X, Xie L, Zheng X. The comparison between the Mie theory and the Rayleigh approximation to calculate the EM scattering by partially charged sand. J Quant Spectrosc Radiat Transf 2012;113:251–8. https://doi.org/10.1016/j.jqsrt.2011.09.020.

[208] Wang N, Liu S, Lin Z. Tailoring optical properties of surface charged dielectric nanoparticles based on an effective medium theory. Opt Express 2013;21:20387. https://doi.org/10.1364/OE.21.020387.

[209] Klacka J, Kocifaj M. On the Scattering of Electromagnetic Waves By a Charged Sphere. Prog Electromagn Res 2010;109:17–35. https://doi.org/10.2528/pier10072708.

[210] Saffaripour M, Geigle KP, Snelling DR, Smallwood GJ, Thomson KA. Influence of rapid laser heating on the optical properties of in-flame soot. Appl Phys B Lasers Opt 2015;119:621–42. https://doi.org/10.1007/s00340-015-6072-6.

[211] Xiong G, Li S, Zhang Y, Buckley SG, Tse SD. Phase-selective laser-induced breakdown spectroscopy of metal-oxide nanoparticle aerosols with secondary resonant excitation during flame synthesis. J Anal At Spectrom 2016;31:482–91. https://doi.org/10.1039/C5JA00186B.

[212] Zhang Y, Xiong G, Li S, Dong Z, Buckley SG, Tse SD. Novel low-intensity phase-selective laser-induced breakdown spectroscopy of TiO2 nanoparticle aerosols during flame synthesis. Combust Flame 2013;160:725–33. https://doi.org/10.1016/j.combustflame.2012.11.007.

[213] Menser J, Daun K, Dreier T, Schulz C. Laser-induced atomic emission of silicon nanoparticles during laser-induced heating. Appl Opt 2017;56:50–7.

[214] Maffi S, Cignoli F, Bellomunno C, De Iuliis S, Zizak G. Spectral effects in laser induced incandescence application to flame-made titania nanoparticles. Spectrochim Acta - Part B At Spectrosc 2008;63:202–9. https://doi.org/10.1016/j.sab.2007.11.022.

[215] Clavero C. Plasmon-induced hot-electron generation at nanoparticle/metal-oxide interfaces for photovoltaic and photocatalytic devices. Nat Photonics 2014;8:95–103. https://doi.org/10.1038/nphoton.2013.238.

[216] Dresser MJ. The Saha-Langmuir equation and its application. J Appl Phys 1968;39:338–9. https://doi.org/10.1063/1.1655755.

[217] Chin SL. Multiphoton lonization of Atoms. Elsevier Science; 1984. https://doi.org/https://doi.org/10.1016/b978-0-12-172780-2.50006-9.

[218] Leung TLF, Van Driel HM. Time-resolved thermionic and photoemission from nanosecond, pulsed laser excited germanium and silicon. Appl Phys Lett 1984;45:683–5. https://doi.org/10.1063/1.95356.

[219] Found CG. Ionization potentials of argon, nitrogen, carbon monoxide, helium, hydrogen and mercury and iodine vapors. Phys Rev 1920;16:41–53. https://doi.org/10.1103/PhysRev.16.41.

[220] Chynoweth AG. Ionization Rates for Electrons and Holes in Silicon. Phys Rev 1958;109:1537–40.

https://doi.org/10.1103/PhysRev.109.1537.

[221] Maier SA. Plasmonics: Fundamentals and Applications. Springer Science & Business Media; 2007. https://doi.org/10.1007/0-387-37825-1.

[222] Talebi Moghaddam S, Ertürk H, Mengüç MP. Enhancing local absorption within a gold nano-sphere on a dielectric surface under an AFM probe. J Quant Spectrosc Radiat Transf 2016;178. https://doi.org/10.1016/j.jqsrt.2016.02.011.

[223] Hatef A, Meunier M. Plasma-mediated photothermal effects in ultrafast laser irradiation of gold nanoparticle dimers in water. Opt Express 2015;23:1967. https://doi.org/10.1364/OE.23.001967.

[224] Schäfer J, Lee SC, Kienle A. Calculation of the near fields for the scattering of electromagnetic waves by multiple infinite cylinders at perpendicular incidence. J Quant Spectrosc Radiat Transf 2012;113:2113–23. https://doi.org/10.1016/j.jqsrt.2012.05.019.

[225] Krenn JR, Dereux A, Weeber JC, Bourillot E, Lacroute Y, Goudonnet JP. Squeezing the optical near-field zone by plasmon coupling of metallic nanoparticles. Phys Rev Lett 1999;82:2590–3. https://doi.org/https://doi.org/10.1103/physrevlett.82.2590.

[226] Jain PK, Eustis S, El-Sayed M a. Plasmon coupling in nanorod assemblies: optical absorption, discrete dipole approximation simulation, and exciton-coupling model. J Phys Chem B 2006;110:18243–53. https://doi.org/10.1021/jp063879z.

[227] Sönnichsen C, Franzl T, Wilk T, von Plessen G, Feldmann J, Wilson O, et al. Drastic Reduction of Plasmon Damping in Gold Nanorods. Phys Rev Lett 2002;88:077402. https://doi.org/10.1103/PhysRevLett.88.077402.

[228] Hofmann J, Steinmann W. Plasma Resonance in the Photoemission of Silver. Phys Status Solidi 1968;30:K53–6. https://doi.org/https://doi.org/10.1002/pssb.19680300160.

[229] Endriz JG, Spicer WE. Surface-Plasmon-One-Electron Decay and its Observation in Photoemission. Phys Rev Lett 1970;24:64–8. https://doi.org/10.1103/PhysRevLett.24.64.

[230] Inagaki T, Kagami K, Arakawa ET. Photoacoustic observation of nonradiative decay of surface plasmons in silver. Phys Rev B 1981;24:3644–6. https://doi.org/10.1103/PhysRevB.24.3644.

[231] Uskov A V, Protsenko IE, Ikhsanov RS, Babicheva VE, Zhukovsky S V, Lavrinenko A V, et al. Internal photoemission from plasmonic nanoparticles: comparison between surface and volume photoelectric effects. Nanoscale 2014;6:4716–27. https://doi.org/10.1039/c3nr06679g.

[232] Knight MW, Wang Y, Urban A, Sobhani A, Zheng B, Nordlander P, et al. Embedding Plasmonic Nanostructure-diodes enhances Hot Electron Emission. Nano Lett 2013;13:1687–92. https://doi.org/10.1021/nl400196z.

[233] Ropers C, Elsaesser T, Cerullo G, Zavelani-Rossi M, Lienau C. Ultrafast optical excitations of metallic nanostructures: From light confinement to a novel electron source. New J Phys 2007;9. https://doi.org/10.1088/1367-2630/9/10/397.

[234] Perdew JP. Energetics of charged metallic particles: From atom to bulk solid. Phys Rev B 1988;37:6175–80. https://doi.org/10.1103/PhysRevB.37.6175.

[235] Landström L, Heszler P. Analysis of blackbody-like radiation from laser-heated gas-phase tungsten

nanoparticles. J Phys Chem B 2004;108:6216–21. https://doi.org/10.1021/jp0367629.

[236] Reader KAYRJ. No Title. NIST At Spectra Database (Ver 52) 2015.

[237] Sevast'yanov VG, Nosatenko PY, Gorskii V V., Ezhov YS, Sevast'yanov D V., Simonenko EP, et al. Experimental and theoretical determination of the saturation vapor pressure of silicon in a wide range of temperatures. Russ J Inorg Chem 2010;55:2073–88. https://doi.org/10.1134/S0036023610130036.

[238] Bechtel JH, Lee Smith W, Bloembergen N. Two-photon photoemission from metals induced by picosecond laser pulses. Phys Rev B 1977;15:4557–63. https://doi.org/10.1103/PhysRevB.15.4557.

[239] Malvezzi AM, Kurz H, Bloembergen N. Nonlinear photoemission from picosecond irradiated silicon. Appl Phys A Solids Surfaces 1985;36:143–6. https://doi.org/10.1007/BF00624934.

[240] Brogle RP. Studies of linear and nonlinear photoemission processes in metals and semiconductors. University of California, 1996.

[241] Jackson PB. Numerical Modeling of the Plasma-Particle Interactions of Aerosol Vaporization in a Laser-Induced Plasma. University of Florida, 2011.

[242] Carls JC, Brock JR. Propagation of laser breakdown and detonation waves in transparent droplets. Opt Lett 1988;13:273–5. https://doi.org/10.1364/OL.13.000273.

[243] Diwakar PK, Hahn DW. Study of early laser-induced plasma dynamics: Transient electron density gradients via Thomson scattering and Stark Broadening, and the implications on laser-induced breakdown spectroscopy measurements. Spectrochim Acta Part B 2008;63:1038–46. https://doi.org/10.1016/j.sab.2008.07.003.

[244] Beduneau JL, Ikeda Y. Spatial characterization of laser-induced sparks in air. J Quant Spectrosc Radiat Transf 2004;84:123–39. https://doi.org/10.1016/S0022-4073(03)00136-5.

[245] Oh Y, Zahaf R, Zachariah MR, Lee D. Nanosecond laser induced energetic ion formation from a nanoparticle: The origin of ion detection loss in a single particle mass spectrometry. Jpn J Appl Phys 2014;53:05HA10.

[246] PRASOON K DIWAKAR. Laser-Induced Plasmas As an Analytical Source for Quantitative Analysis of Gaseous and Aerosol Systems: Fundamentals of Plasma-Particle Interactions. University of Florida, 2009.

[247] Lochte-Holtgreven W. Plasma Diagnostics. AIP Press; 1995. https://doi.org/https://doi.org/10.1063/1.3022256.

[248] Rybicki GB, Lightman AP. Radiative processes in astrophysics. John Wiley & Sons; 2008. https://doi.org/https://doi.org/10.1002/9783527618170.

[249] Cox AN. Allen's Astrophysical Quantities. Springer; 2015. https://doi.org/https://doi.org/10.1007/978-1-4612-1186-0.

[250] Johnston RR. Free-free radiative transitions-a of theoretical results. J Quant Spectrosc Radiat Transf 1967;7:815–35. https://doi.org/https://doi.org/10.1016/0022-4073(67)90001-5.

[251] Park J, Henins I, Herrmann HW, Selwyn GS. Neutral bremsstrahlung measurement in an atmospheric-pressure radio frequency discharge. Phys Plasmas 2000;7:3141–4. https://doi.org/10.1063/1.874220.

[252] Ohmura T, Ohmura H. Continuous absorption due to free-free transitions in hydrogen. Phys Rev

1961;121:513–7. https://doi.org/10.1103/PhysRev.121.513.

[253] Itikawa Y. Momentum-transfer cross sections for electron collisions with atoms and molecules. At Data Nucl Data Tables 1974;14:1–10. https://doi.org/10.1016/S0092-640X(74)80026-4.

[254] Radziemski LJ, Cremers DA. Laser-induced plasmas and applications. M. Dekker; 1989. https://doi.org/https://doi.org/10.1117/1.oe.30.9.bkrvw2.

[255] Memarian F, Daun KJ. Gas Dynamics of Sublimed Nanoclusters in High-Fluence Time-Resolved Laser-Induced Incandescence. Numer Heat Transf Part B Fundam 2014;65:393–409. https://doi.org/https://doi.org/10.1080/10407790.2013.869098.

[256] Memarian F, Liu F, Thomson KA, Daun KJ, Snelling DR, Smallwood GJ. Effect of recondensation of sublimed species on nanoparticle temperature evolution in time-resolved laser-induced incandescence. Appl Phys B Lasers Opt 2015;119:607–20. https://doi.org/10.1007/s00340-015-6077-1.

[257] Taylor RL, Caledonia G. Experimental determination of the cross-sections for neutral bremsstrahlung I. Ne, Ar and Xe. J Quant Spectrosc Radiat Transf 1969;9:657–79. https://doi.org/10.1016/0022-4073(69)90014-4.

[258] Kung RT V, Changs CH. Neutral bremsstrahlung radiation of Ne, Ar and O. J Quant Spectrosc Radiat Transf 1976;16:579–86. https://doi.org/https://doi.org/10.1016/0022-4073(76)90024-8.

[259] Vander Wal RL, Choi MY, Lee K. The effects of rapid heating of soot: Implications when using laser-induced incandescence for soot diagnostics. Combust Flame 1995;102:200–4. https://doi.org/10.1016/0010-2180(95)00071-D.

[260] Bladh H, Bengtsson PE. Characteristics of laser-induced incandescence from soot in studies of a time-dependent heat- and mass-transfer model. Appl Phys B Lasers Opt 2004;78:241–8. https://doi.org/10.1007/s00340-003-1362-9.

[261] Farrer RA, Butterfield FL, Chen VW, Fourkas JT. Highly Efficient Multiphoton-Absorption-Induced Luminescence from Gold Nanoparticles. Nano Lett 2005;5:1139–42. https://doi.org/10.1021/nl050687r.

[262] Haug T, Klemm P, Bange S, Lupton JM. Hot-Electron Intraband Luminescence from Single Hot Spots in Noble-Metal Nanoparticle Films. Phys Rev Lett 2015;115:067403. https://doi.org/10.1103/PhysRevLett.115.067403.

[263] Hartland G V. Optical studies of dynamics in noble metal nanostructures. Chem Rev 2011;111:3858–87. https://doi.org/10.1021/cr1002547.

[264] Krishnan S. Emissivities and optical constants of electromagnetically levitated liquid metals as functions of temperature and wavelength. Mater Chem High Temp 1990:143–64. https://doi.org/https://doi.org/10.1007/978-1-4612-0481-7_11.

[265] Safonov VP, Shalaev VM, Markel VA, Danilova YE, Lepeshkin NN, Kim W, et al. Spectral dependence of selective photomodification in fractal aggregates of colloidal particles. Phys Rev Lett 1998;80:1102–5. https://doi.org/10.1103/PhysRevLett.80.1102.

[266] Hertz H. Ueber einen Einfluss des ultravioletten Lichtes auf die electrische Entladung. Ann Phys 1887;267:983–1000. https://doi.org/https://doi.org/10.1002/andp.18872670827.

[267] Tamm I, Schubin S. Zur theorie des photoeffektes an metallen. Zeitschrift Für Phys 1931;68:97–113.

https://doi.org/https://doi.org/10.1007/BF01392730.

[268] Ashcroft NW, Mermin ND. Solid state physics. Saunders; 1976.

[269] Hölzl J, Schulte FK. Work function of metals. Solid Surf Phys 1979:1–150. https://doi.org/https://doi.org/10.1007/BFb0048919.

[270] Christy PBBJ and RW. Optical Constants of the Noble Metals. Phys Rev B 1972;6:4370–9. https://doi.org/10.1103/PhysRevB.6.4370.

[271] Protsenko IE, Uskov A V. Photoemission from metal nanoparticles Photoemission from metal nanoparticles 2012;55:508. https://doi.org/10.3367/UFNe.0182.201205e.0543.

[272] Manjavacas A, Liu JG, Kulkarni V, Nordlander P. Plasmon-induced hot carriers in metallic nanoparticles. ACS Nano 2014;8:7630–8. https://doi.org/10.1021/nn502445f.

[273] Itikawa Y. Effective collision frequency of electrons in atmospheric gases. Planet Space Sci 1971;19:993–1007. https://doi.org/10.1016/0032-0633(71)90149-8.

[274] Keldysh L V. Ionization in the field of a strong electromagnetic wave. Sov Phys JETP 1965;20:1307–14. https://doi.org/10.1234/12345678.

[275] Bernard JE, Baldis HA, Villeneuve DM, Estabrook K. Time resolved Thomson scattering measurements of the electron and ion temperatures in a high intensity laser-plasma interaction. Phys Fluids 1987;30:3616. https://doi.org/10.1063/1.866443.

[276] Amini B, Chen FF. Thomson-Scattering Detection of Plasma Waves Excited by Two Laser Beams. Phys Rev Lett 1984;53:1441–4. https://doi.org/10.1103/PhysRevLett.53.1441.

[277] Bowden MD, Kogano M, Suetome Y, Hori T, Uchino K, Muraoka K. Comparison of electron property measurements in an inductively coupled plasma made by Langmuir probe and laser Thomson scattering techniques. Ournal Vac Sci Technol A 1999;17:493–9. https://doi.org/10.1116/1.581610.

[278] Rai VN, Rai AK, Yueh F-Y, Singh JP. Optical emission from laser-induced breakdown plasma of solid and liquid samples in the presence of a magnetic field. Appl Opt 2003;42:2085. https://doi.org/10.1364/AO.42.002085.